Biomechanical study of cells in microfluidic flow : application to sorting and platelet production

Doriane Vesperini

Par **Doriane VESPERINI**

Biomechanical study of cells in microfluidic flow: application to sorting and platelet production

Thèse présentée
pour l'obtention du grade
de Docteur de l'UTC

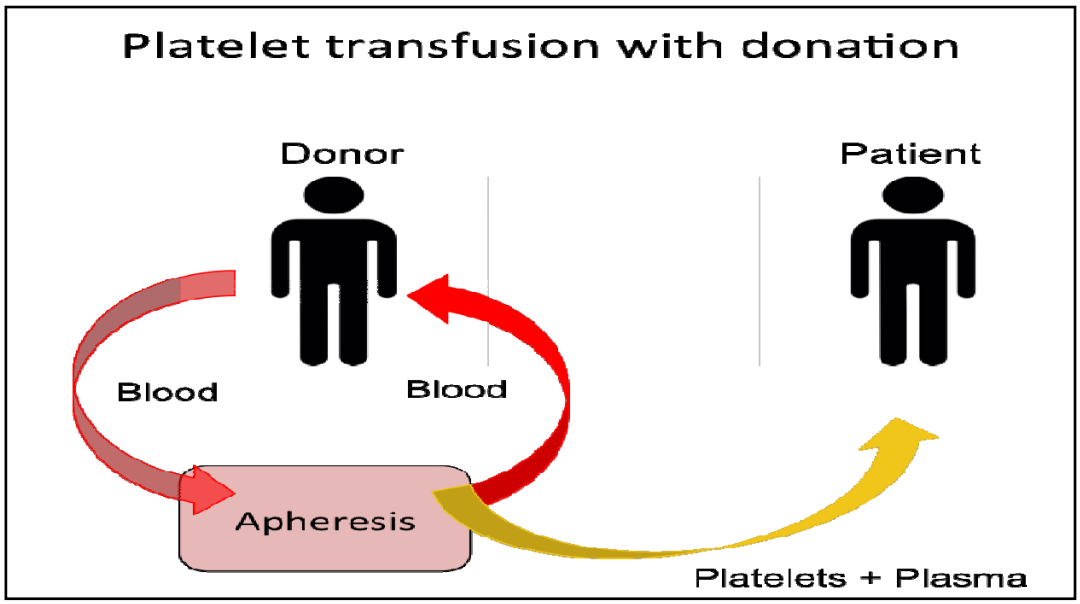

Soutenue le 10 octobre 2018
Spécialité : Biomécanique : Unité de Recherche Biomécanique et Bio-ingénierie (UMR-7338)
D2437

École doctorale n° 71 : Sciences pour l'Ingénieur

Thèse

Biomechanical study of cells in microfluidic flow: application to sorting and platelet production

pour obtenir le grade de docteur délivré par

Université de Technologie de Compiègne

Spécialité doctorale "Biomécanique"

présentée et soutenue publiquement par

Doriane Vesperini

le 10 octobre 2018
Directrice de thèse : **Anne Le Goff**

Jury

Dominique Collard,	Directeur de recherche CNRS-LIMMS-IIS, Tokyo, Japon	Examinateur
Gwennou Coupier,	Chargé de recherche CNRS-LIPhy, Grenoble, France	Rapporteur
Hamid Kokabi,	Professeur, UPMC, Paris, France	Examinateur
Franziska Lautenschläger,	Jun. Prof. Dr., INM, Sarrebrück, Allemagne	Examinatrice
Anne Le Goff,	Maître de conférence, UTC, BMBI, Compiègne, France	Directrice de thèse
Olivier Théodoly,	Directeur de recherche CNRS-INSERM, Marseille, France	Rapporteur
Muriel Vayssade,	Professeur, UTC, BMBI, Compiègne, France	Présidente

Contents

Abstract

When they mature in the bone marrow, the precursors of platelets, called megakaryocytes, grow and extend protrusions able to join blood circulation. There these protrusions elongate and break into platelets. Microfluidic techniques for *in vitro* platelet production represent a promising alternative to donation. In order to enhance platelet production and match the needs of clinical applications such as transfusion, we need to better understand the fragmentation of megakaryocytes into platelets. Our contribution will be described in this manuscript in two main axes.

First, in order to know if mechanical properties of megakaryocytes can indicate their maturity stage, we develop a cell sorting method based on deformability. The method is first validated with microcapsules. Their mechanical properties are determined by inverse analysis from their shape under flow in straight microchannels. Then the device is downscaled. The characterization of cell mechanical properties are performed using inverse analysis and tipless atomic force microscopy.

Second, we study megakaryocyte elongation and rupture in a microfluidic device. We quantify the spatial and temporal variations of the elongation rate and develop a laser ablation protocol to trigger and study the rupture of elongating cells.

Keywords :
Microfluidics, Microcapsules, Megakaryocytes, Platelets, Sorting, Flow-focusing, Deformability, Laser ablation, AFM

Résumé

Les mégacaryocytes sont des cellules de la moelle osseuse, à l'origine de la production des plaquettes sanguines. Quand elles arrivent à maturité, elles grossissent et émettent des prolongements de cytoplasme à travers la paroi des vaisseaux irriguant la moelle. Dans la circulation sanguine, ces prolongements, soumis aux forces de l'écoulement, s'allongent et se rompent pour former des plaquettes. Des techniques microfluidiques capables de produire des plaquettes *in vitro* existent et sont une alternative prometteuse au don. Mais le rendement reste à améliorer. Pour cela, il est nécessaire de mieux comprendre la fragmentation des mégacaryocytes en plaquettes. Ce travail de doctorat s'inscrit dans ce contexte et sera développé en deux axes principaux dans ce manuscrit.

Dans une première partie nous développons une méthode pour trier des cellules en fonction de leur déformabilité, afin de savoir si les propriétés mécaniques d'un mégacaryocyte sont liées à leur stade de maturité. La méthode a d'abord été mise au point avec des microcapsules. Leurs propriétés mécaniques sont déterminées par analyse inverse à partir de la mesure de leur forme en écoulement dans des constrictions droites. Puis le dispositif utilisé a été miniaturisé pour s'adapter à la taille des cellules. Pour la caractérisation de leurs propriétés mécaniques, deux outils ont été utilisés: l'analyse inverse et la microscopie à force atomique sans pointe.

Une deuxième partie porte sur l'étude de l'élongation et de la rupture de mégacaryocytes soumis écoulement. Nous avons quantifié les variations spatiotemporelles du taux d'élongation et développé un protocole d'ablation laser pour étudier les mécanismes de rupture de cellules en élongation.

Mots clefs :
Microfluidique, Microcapsules, Megacaryocytes, Plaquettes, Tri, Flow-focusing, Deformabilité, Ablation laser, AFM

Acknowledgement / Mille mercis !!!

Je souhaite remercier les membres de mon jury de thèse d'avoir accepté de faire de longs déplacements jusqu'à Compiègne pour évaluer mes travaux de doctorat. Particulièrement Olivier Théodoly et Gwennou Coupier, pour leurs rapports et discussions d'experts avisés, qui m'ont permis d'améliorer la qualité de mon manuscrit. Hamid Kokabi, Dominique Collard, Franziska Lautenschläger, merci pour vos expertises au moment de la soutenance. Muriel Vayssade, merci beaucoup d'avoir proposé d'être la présidente du jury.

Anne Le Goff, je te remercie de tout coeur de m'avoir accompagnée depuis le début. Il y a 3 ans, j'avais hâte d'avoir le feu vert pour commencer l'aventure avec toi. Ta passion et ta gentillesse me mettaient déjà en confiance. Au fur et à mesure, tes conseils et nos discussions scientifiques m'ont aidée à toujours vouloir comprendre davantage. Je te remercie de m'avoir permis d'aller en école d'été et en conférences. Cargèse, Milan, Sarrebruck, Dublin, Paris ont été des expériences incroyables où j'ai appris beaucoup d'un point de vue scientifique mais également sur moi même. J'y ai fait de très belles rencontres qui construisent mon parcours pour la suite et c'est grâce à toi. Mais tu es pour moi bien plus qu'un modèle en science et en recherche, bien plus que ma directrice de thèse. Ton écoute et tes valeurs m'ont permis de surmonter les difficultés personnelles que j'ai pu rencontrer pendant ces trois années. Tu m'as très souvent rendu de grands services, merci beaucoup. Aussi je suis ravie d'être la première doctorante à avoir eu la chance de travailler avec toi, c'était un réel plaisir. En un mot: MERCI. Pour les futurs doctorants, je dirais simplement: foncez et profitez, l'aventure en vaut la peine.

Franziska Lautenschläger, when I first met you in Cargèse in 2016 your presentation interested me so much. During lunch time I remember we had an interesting talk about optical stretchers and cell motility. When I came back in Compiègne, I discussed with Anne the possibilities to initiate a collaboration with you to characterize my cell mechanical properties. Finally the project with laser ablation emerged and supported by you and Anne I applied to the DAAD grant and came at INM in your team for three months. I thank you very much for the experience. I learned a lot about laser ablation and AFM with all the team and particularly: Emmanuel Terriac, Daniel Flormann and Luiza Stankevicins. I am glad I had the chance and opportunity to meet you. I am looking forward to join the group for the postdoc.

J'aimerais également remercier toutes les personnes avec qui j'ai eu la chance de collaborer pen-

dant ces trois dernières années. A commencer par l'IRT Bioaster avec qui nous avons co-encadré plusieurs stagiaires afin de mettre au point un trieur de cellules. Christophe Védrine, Yacine Bounab, merci pour votre expertise en biologie et votre implication dans le projet. Un grand merci également à Mathilde Reyssat de l'ESPCI avec qui j'ai réalisé ma première photolithographie. Sonia Chassac à l'INSERM , Kamel Khelloufi, Géraldine Sicot et Dominique Baruch à Platod, avec qui nous avons souvent interagi pour étudier les élongations de MK. I want also to thank Edgar Häner and Anne Juel for all of our discussions about physics involved in capsule sorting. I have always appreciated our Skype meetings. The research of truth takes time but it is such a pleasure when we succeed understanding complex physical processes.

A tous les membres de l'équipe Interactions Fluides Structures Biologiques avec qui nous avons partagé toutes les réunions d'équipe, les repas de midi et les pauses café. Dominique Barthès-Biesel, Isabelle Claude, Rachid Jellali, Agnès Drochon, Badr Kaoui, Cédric Dewas, Nicolas Grandmaison, Xingyi Wang, Bruno Sarkis, Claire Baranger, Clément Bielinski, merci d'avoir été là et d'avoir contribué fortement à mon épanouissement dans l'équipe. En particulier je voudrais remercier : Anne-Virginie Salsac pour ses conseils et encouragements. Ilyesse Bihi avec qui j'ai beaucoup apprécié travailler au quotidien. J'adore ton positivisme, tes bons conseils, notre entre-aide... et merci encore pour la visite guidée de Rabat quelques heures avant ton mariage. Les stagiaires qui ont travaillés sur le projet : Oriane Chaput, tu as été la première et c'était un tel plaisir de travailler avec toi. Loréline Dubois, Meriem Lebsir, Dongsheng Shi, Lucile Olive, vous n'étiez là qu'à mi-temps mais merci du travail accompli et des moments de partage très agréables. Mes derniers co-bureaux: Thibaut, ah ces longues heures de calcul vont me manquer ainsi que tes coups de "boost"; Baptiste, il nous reste encore beaucoup de Harry Potter à regarder, et de gâteaux à déguster, alors à très vite et bonne route vers le doctorat; Diane, merci pour ta bonne humeur et les découvertes rigolotes de Yuka et Cash show; Audrey, à tes quadro et ta gentillesse, tu es là depuis peu mais tu as déjà une grande place au bureau et dans l'équipe. Vous avez été présents pour la période de pression qui accompagne la fin du doctorat. Merci pour votre bonne humeur et les moments partagés souvent autour de biscuits, de thé ou au Pic les jours de Cac' Carotte. Je vous souhaite tout le meilleur pour la suite.

A tout le laboratoire BMBI sans qui l'expérience de doctorat aurait forcément été très différente. En particulier, merci à Ulysse Pereira et Murielle Dufresne qui se sont toujours montrés disponibles pour les questions diverses que j'ai pu avoir sur la biologie. Marie-Christine Ho Ba Tho pour la direction du laboratoire pendant mes premières années à Compiègne. Cécile Legallais pour ta direction du labo avec une écoute fidèle et une volonté de préserver des moments conviviaux. Merci à Catherine Lacourt et Alexandra Cousin, pour tous les ordres de mission signés. A tous les doctorants, et postdoctorants du labo avec qui nous avons partagé plein de petits moments très sympathiques: Alejandro, mon binôme de TP, Mégane, Lilandra, Mattia, Delphine, Elodie, Augustin, Amal, Firas, Malek, Kévin, Félix, Adrien, Jolanthe, Halim, Ines, vous allez me manquer les amis. Bon courage à tous pour la suite. Et pour finir tous ceux que je n'aurais pas cités ou cités plus tôt et qui ont contribué d'une façon ou d'une autre à mon épanouissement au sein du laboratoire.

Merci à la région des Hauts de France qui a financé le projet FORPLAQ : Biomechanical study

of platelet formation, dans le cadre duquel j'ai réalisé mes travaux de doctorat. Merci également à la bourse DAAD qui a financé mon séjour de recherche en Allemagne à l'INM dans l'équipe de Jun. Prof. Dr. Franziska Lautenschläger.

Mais l'expérience doctorale ne se borne pas aux frontières du laboratoire et je souhaite remercier tous ceux d'horizons différents avec qui nous avons pris du plaisir à collaborer et/ou à sortir : Aurélien, Raquel, Alejandra, Gérald, Lorine, Cristina, Franco, Nadja, Florian, Dimitri, Maxime, Chunmei, Sophie, Pierre, Gaëtan, Benjamin, Kayla, Risa, Vittoria... Bien sûr je ne peux pas ne pas mentionner le côté associatif lié à mon doctorat. Je remercie tous les doctorants qui ont fait partie à un moment ou à un autre de l'aventure du RED^2 pour fédérer tous les stagiaires, doctorants et postdocs de l'UTC. Merci à tous, on aura passé de l'énergie à motiver les docs de l'UTC à se connaître : barbeuc, repas de Noël, bowling, laser game, les soirées pizzas et la journée de visites des laboratoires pour les étudiants ingénieurs, ont été de super moments. Je remercie aussi le CA de Doc'up, où j'ai rencontré tant de personnes volontaires avec qui j'ai eu plaisir à partager de formidables évènements entre science et loisir.

Merci à tous les amis qui m'ont soutenue tout au long de mon doctorat, particulièrement à ceux qui sont venus jusqu'à Compiègne pour m'encourager: Laureen du lycée au supérieur, des rires aux larmes, toujours présente! Nicolas, des projets plein la tête, je te souhaite de transformer les rêves en réalité. Matthieu, à nos prochains rendez-vous de théâtre et bien d'autres. François, à très bientôt à Sarrebruck, merci d'avoir fait ce long voyage. Rishab, thanks for coming from Saarbrücken, such a nice surprise. See you soon my friend.

Pour finir, je remercie mes parents sans qui tout ce parcours n'aurait jamais vu le jour. Merci pour votre soutien, vos encouragements et votre amour au quotidien. A mon frère également, Titi, toi aussi tu finis dans très peu de temps. Je suis si fière de toi, poursuivre tes rêves avec autant de ténacité est très remarquable. Sam je te remercie de toujours faire de ton mieux pour être là tout simplement. Je vous aime très très fort.

Le mieux est le mortel ennemi du bien.
Montesquieu

A mes grand-parents

List of Figures

List of Tables

List of abbreviations

AFM Atomic Force Microscopy

BBI Blebbistatin

BF Bright Field

BSA Bovin serum albumin

BT Trypan Blue

CTC Cancer and Circulated Tumor Cells

CalA Calyculin A

CytoB Cytochalasin B

CytoD Cytochalasin D

DLD Deterministic Lateral Displacement

DMSO Dimethyl sulfoxide

Dext-500 Dextran 500 kDa

ER Enrichment ratio

FACS Fluorescence Activated Cell Sorting

FADS Fluorescence Activated Droplet Sorting

FBS Fetal bovine serum

FSC Front Scatter Detector

IMDM-BIT Iscove Modified Dulbecco Medium - BSA Insulin Transferrin

LatA Latranculin A

MACS Magnetic Activated Cell Sorting

MEM Minimum Essencial Medium

MK Megakaryocyte

NR Neutral Red

NS Non significant

PBMC Peripheral Blood Mononuclear Cells

PBS Phosphate buffered saline

PCR Polymerase Chain Reaction

PDMS Polydimethylsiloxane

PEEK Polyether ether ketone

PFF Pinch Flow Fractionation

PLT Platelet

PTFE Polytetrafluoroethylene

RBC Red Blood Cells

ROI Region of interest

SPM Scanning Probe Microscopy

SSC Side Scatter Detector

TPO Thrombopoietin

VWF von Willebrand Factor

Introduction

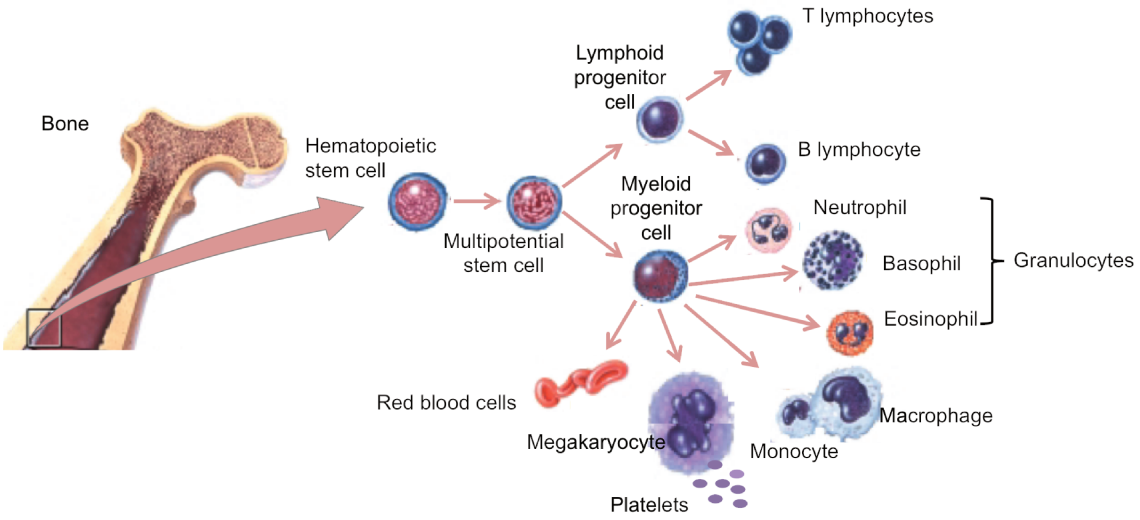

Figure 1: **Sketch of hematopoiesis.** Hematopoietic stem cells located in the bone marrow differentiate into blood cells: red blood cells, white blood cells (T lymphocytes, B lymphocytes, neutrophils, basophils, eosinophils and monocytes), and platelets. Figure adapted from [1].

Blood is composed of 55 % of plasma, 44 % of red blood cells and 1 % of white blood cells and platelets. The function of red blood cells is to transport oxygen and carbon dioxide through all the organs. White blood cells or leukocytes are immune cells that contribute to the protection of the organism against pathogens. Finally, platelets are involved in coagulation. Depending on their nature, blood cells have different life times, which are highly variable (but on average) a few days for white blood cells, 10 days for platelets and 100 days for red blood cells. Blood cells are therefore constantly renewed throughout the life. They all originate from hematopoietic stem cells located in the bone marrow. The formation of blood cells is called hematopoiesis (Figure 1). The perivascular environment in bone marrow supporting migration and differentiation of hematopoietic stem cells is often called the vascular niche [2]. In this work we focus on the pathway leading to platelet production.

Platelets are non nucleated cells circulating in blood and involved in coagulation and healing. Physiologically platelets come from megakaryocytes (MK) located in the bone marrow [3]. When they grow mature, MK become larger, their ploidy increases and their membrane invaginates. Then

they produce extensions of cytoplasm, called proplatelets, able to cross the endothelium of the bone marrow sinusoids (Figure 3). In the blood flow, these proplatelets elongate thanks to hydrodynamic forces and finally detach from the MK body. The released fragments, called preplatelets, undergo further ruptures in the blood circulation until they form platelets. High shear forces encountered in capillary beds have long been suspected to contribute to this late fragmentation. For instance, it is known that platelets count is higher downstream of the lungs than upstream. This hypothesis was confirmed recently by intravital microscopy observations of the production of platelets in the narrow capillaries of mouse lung [4].

Platelet production is impaired in several diseases such as genetic diseases and cancer. Thrombocytopenia, or lack of platelets, induces a risk of hemorrhage whereas thrombocytosis, an abnormally high platelet count, leads to clot formation. Thrombocytopenic patients are sometimes treated with platelet transfusion. The only source of platelets for transfusion therapy is donation. Figure 2 illustrates the principle of platelet donation: the whole blood of a donor is collected in an apheresis machine that separates platelets from other cells by continuous centrifugation, and returns whole blood to the patient. This operation lasts at least two hours; it is expensive because of the specific equipment needed and staff mobilization; and platelet shelf-life is limited to 5 days.

In this context, alternative methods are explored. Artificial platelet substitutes have been engineered but these products seem to induce clotting in a non-specific and uncontrolled way [5]. Recent advances in stem cell culture and tissue engineering have opened perspectives for the production of bioartificial platelets from cultured MK [6]. In this work we focus on the very last stage of thrombopoiesis, during which mature MK break into preplatelets. It was shown in earlier studies that this phenomenon can be reproduced *in vitro* in microfluidic systems coated with a protein, von Willebrand factor (VWF), that specifically binds MK and platelets [7, 8]. Although the quality of produced platelets is encouraging, the yield is still around 4 platelets/MK, much lower than *in vivo*. Not all MK elongate in these systems and a possible strategy for improving the platelet yield would be to improve MK elongation. Two hypotheses can explain the diversity of behavior of MK in bioreactors:

- The cell population is heterogeneous, with only a small fraction that has the capacity to deform in the flow. In this case it would be interesting to sort the MK suspension in order to isolate only the mature ones.
- All MK are deformable, but elongation is triggered by an external signal. All cells in the bioreactor are not exposed to the same stimuli and only a fraction of them elongates.

In order to address this question, we develop two strategies in this manuscript.

In the first three chapters, we seek to develop a method for sorting cells according to their deformability. Mature MK are characterized by a well-organized membrane demarcation system and cytoskeleton. They are not easy to separate by conventional techniques but could be identified in a biomechanical test. In chapter 1 we review existing microfluidic sorting techniques and present a device capable of sorting microcapsules according to their size. We also show that ,when used at high

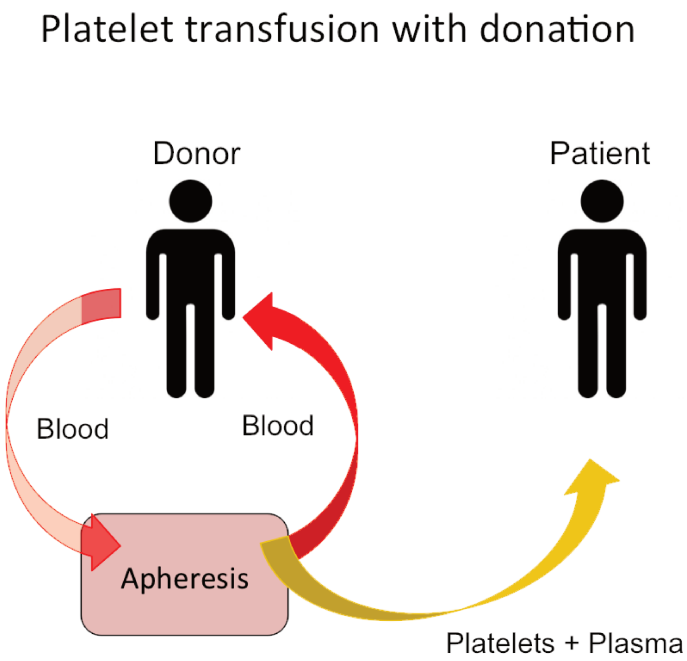

Figure 2: **Platelet transfusion with blood donation**. The blood of a donor is collected in an apheresis machine which sorts platelets and plasma from whole blood. The blood is then re-injected to the donor and platelet rich plasma collected is available for transfusion of a patient.

flow rates, this system allows to separate capsules based on their deformability. We discuss in chapter 2 the application of this system for deformability-based cell sorting. Microfluidic cell separation techniques are presented. We discuss the challenges of sorting cells compare to capsules according to their size and mechanical properties and present experimental results obtained in a downscaled version of our microcapsule sorter. Applications to the sorting of other cell types, in particular leukocytes, are also considered. In order to validate these systems, we need to characterize the mechanical properties of the cells and microcapsules used in the experiments. Chapter 3 presents a review of the common techniques usually used to characterize mechanical properties at the microscale. We focus on the two techniques used in this work: flow through a microfluidic constriction and tipless atomic force microscopy, to characterize capsules and cells respectively.

In the last two chapters, we develop tools to expose MK to well-controlled conditions in VWF-coated microfluidic chambers dedicated to the observation of isolated cells. In chapter 4, after reviewing methods to produce *in vitro* platelets, we characterize the spatiotemporal heterogeneity of MK elongation in microfluidic devices. Finally chapter 5 is dedicated to the elaboration of a laser ablation protocol in order to trigger and observe the rupture of elongating MK and the prelease of preplatelets. Conclusions and perspectives of this project are then exposed.

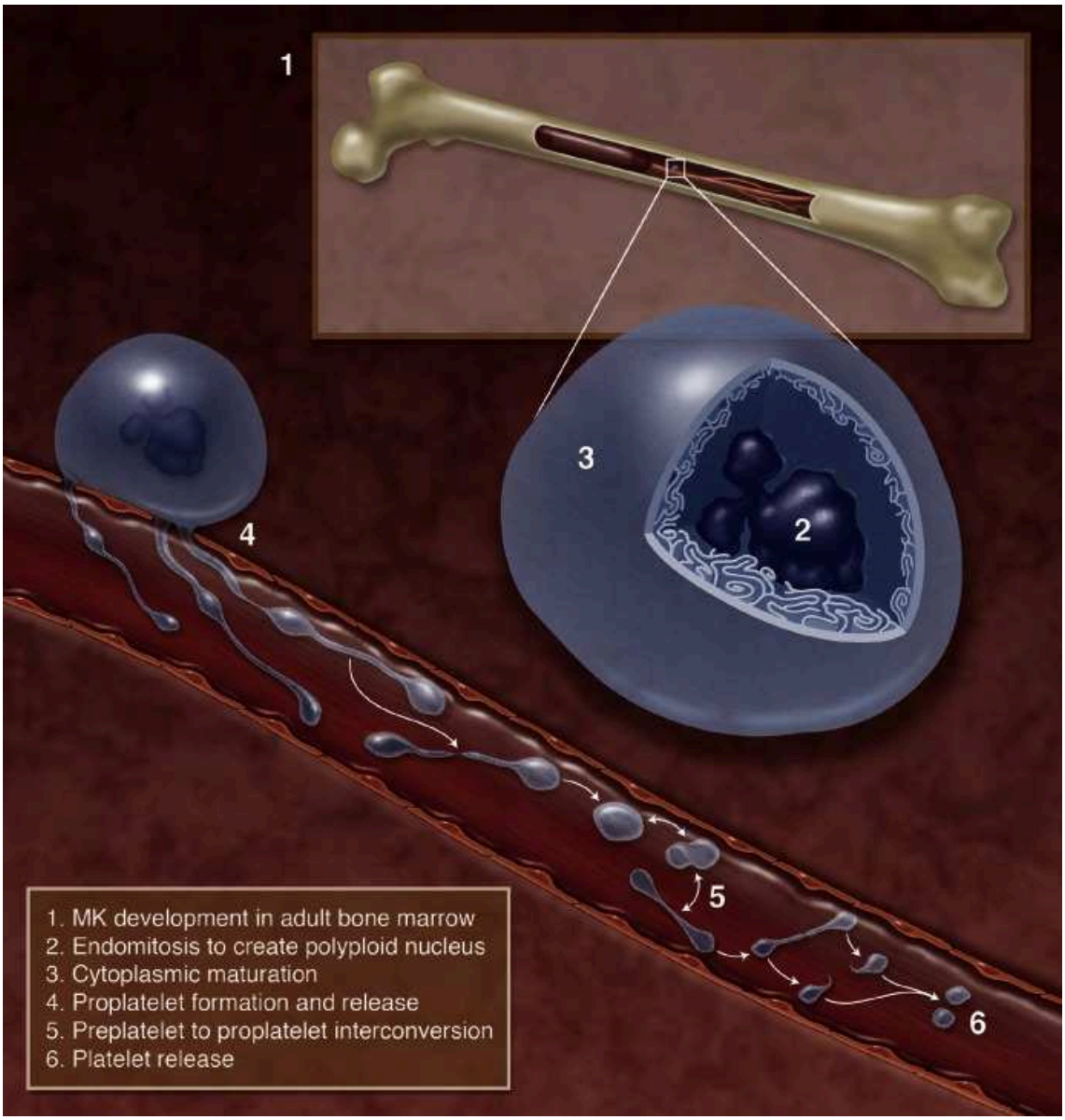

Figure 3: **Sketch of megakaryopoiesis.** (1) MK differentiates in the bone marrow. (2) MK undergo endomitosis and polyploidization . (3) The membrane invaginates in the cytoplasm and forms a reservoir for future proplatelets. (4) Proplatelets pass through the endothelium and join the blood flow. (5) Shear induces rupture of the proplatelets to form preplatelets. (6) Preplatelets further break and form platelets. Image adapted from [9].

Chapter 1

Capsule sorting

Contents

1.1 Introduction

1.1.1 Capsules: definition and applications

Capsules consist of a core medium enclosed with a membrane that controls exchanges between the internal content and the external environment [10]. The membrane protects, and prevents loss, dispersion and degradation of the sensitive products such as : perfume, flavor, or drugs, until their targeted delivery. Artificial capsules can be fabricated in a variety of materials and their size goes from nanometer to millimeter scale. For biological applications, we find biocompatible polymers such as poly-L-lysine-alginate [11] and polyamide [12]; and proteins [13, 14]. In bioengineering, capsules are considered, as simplified models for cells [15], whose intrinsic properties can be controlled.

Cells are much more complex but represent a natural example of capsules, as they consist of a cytoplasm and a nucleus enclosed in a lipid shell called membrane. Their core is a highly heterogeneous structure composed of the cytosol; the cytoskeleton: actin stress fibers, microtubules and intermediate filaments; and organelles such as the nucleus and the mitochondria [16]. Their membrane is made up with lipids and proteins [17]. Cells differ in stiffness, migration and adherence depending on their functions. Sorting cells according to their mechanical properties presents a real potential for many medical applications. In order to first avoid heterogeneities due to cell complexity, we will focus this chapter on capsule sorting. That presents its own applications in cosmetics [18], food [19] and medicine [20]. Thus sorting microcapsules according to their stiffness presents the advantage of controlling the properties of the final targeted capsules collected.

Several methods exist to sort capsules according to their physical and chemical properties such as : density, size, shape, deformability, electrical impedance, and biochemical markers. Microfluidics is a technique able to manipulate micro-objects according to their intrinsic properties. We can classify separating techniques into two categories : active and passive techniques. Active techniques require an external field, while passive techniques only rely on the device design and hydrodynamic forces. In the following section, we will review existing microfluidic systems. Among size-based sorting devices, we focus on the ones that are the most extensively described in the literature. The development of deformability-based sorting devices is much less advanced, but we present a state of the art.

1.1.2 Size-based sorting methods

Deterministic lateral displacement

Deterministic lateral displacement (DLD) is a passive method introduced by Huang et al [22]. The device consists of a chamber containing several rows of micro-pillars as shown in figure 1.1. Each row is shifted from the previous one with an angle. The gap between two pillars is chosen larger than particle size. Small particles (in green) follow the fluid streamline around each obstacle whereas large particles are deviated with a certain angle (in red). The trajectory of objects is disturbed as a function of the size of the particle. With this method it is possible to accurately separate particles whose size

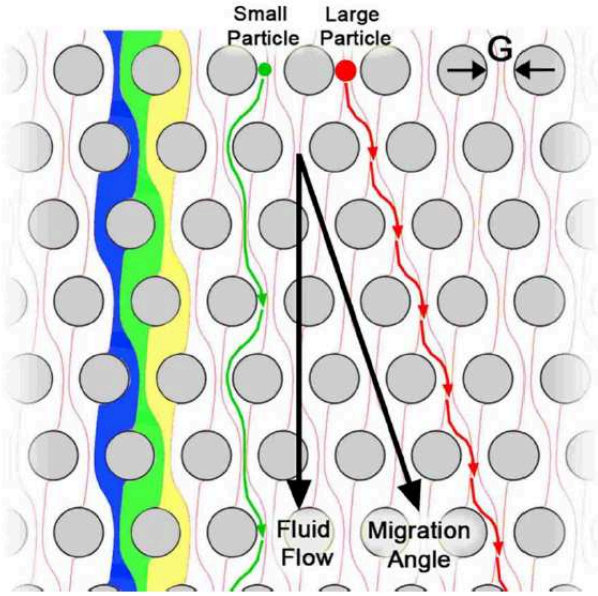

Figure 1.1: **Deterministic lateral displacement** Image from [21]. The fluid flows around the obstacles following different streamlines shown in blue, yellow, and green. Small particles (in green) are able to follow fluid flow and have, on average, a linear trajectory. On the contrary, large particles (in red) are deviated with a migration angle.

differs by 2 % [21]. The accuracy of the process increases with channel length. In order to be fully functional, the device needs to have well-defined dimensions. At microscale, defect of fabrication such as non defined pillars can occur. Also, after a while some gaps of the system may be clogged with the objects to be sorted.

Pinch flow fractionation

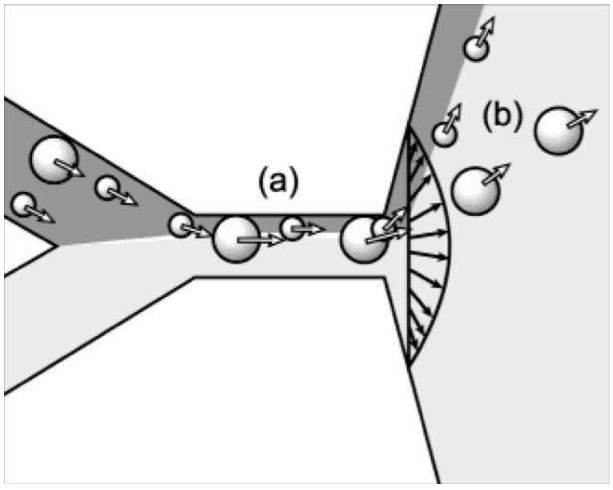

Figure 1.2: **Pinch flow fractionation.** Particles are all pushed on the sidewall whatever their size, controlling the flow strengths. Particles are perfused in the upper fluid (dark grey). In the diffuser, particles are separated according to their size. Small particles follow a trajectory closer to the wall than larger particles. Image from [23].

A method to avoid clogging is to have no obstacles. Pinch flow fractionation (PFF) is based on

continuous flow in a channel. The geometry consists of two inlets, a bifurcation, a diffuser and several outlets. One entrance is used for the suspension and the other one for another fluid devoid of particles. This external fluid is used to pinch all the particles in the filament as close to the wall as possible. Figure 1.2 shows two particles of different size. The trajectory of particles in the diffuser is dictated by the position of their center of mass in the constriction, where small particles are pushed closer to the wall than larger ones. The role of the diffuser is to amplify these differences of position in order to collect small and large particles in separate outlets. The system can be made more efficient by increasing the flow rate until inertial forces become comparable with viscous drag [24].

Inertial microfluidics

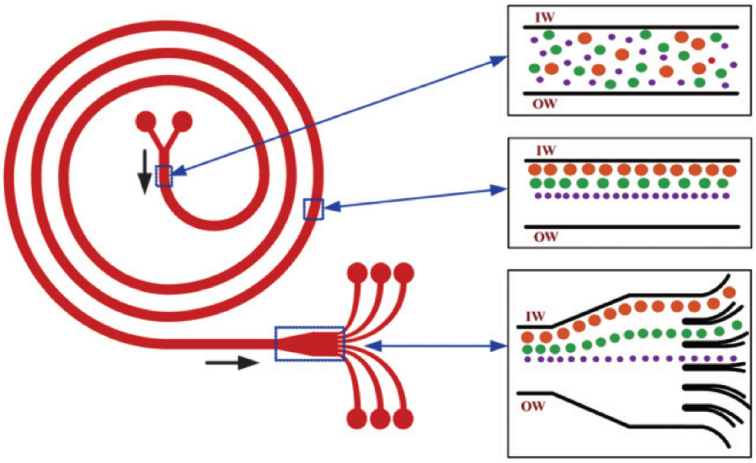

Figure 1.3: **Inertial microscopy.** Spiral microfluidic channel used to sort particles according to their size. In order to separate individual particles stream, the channel widens at the end and several outlets allow to collect the different populations. Image from [25].

Due to the small size of the channels, we often neglect inertial effects in microfluidic flow [26]. We can estimate the Reynolds number ($Re = \rho UH/\mu$). Where ρ is the density (kg/m^3), U the flow velocity (m/s), H the characteristic length of the channel (μm) and μ the viscosity (Pa.s). The Reynolds number is the ratio between inertial and viscous forces. At the microscale, H is small and high velocity U is required to have an effect of both viscous and inertial forces. Among inertial effects, the lift force exerted on a particle flowing in a curved channel has been studied as a tool to focus [27] and sort [28] microscopic particles. Inertial effect is most of the time used with curvatures (coil or spirals). In a curvature an additional force is exerted on particles and is called the inertial lift force. The lift effect is directed perpendicularly to the flow in the direction to the wall. Small particles are more sensitive to lift effect. Thus they find their equilibrium in a off-centered streamline close to the wall in a linear channel (Figure 1.4, c). As the length needed to separate the objects is long, a spiral shape, such as the one presented in figure 1.3, is often used to save space and minimize the total dimensions of the sorting system. The spiral allows margination of particles. Small particles follow the center line, when larger cells follow the wall line.

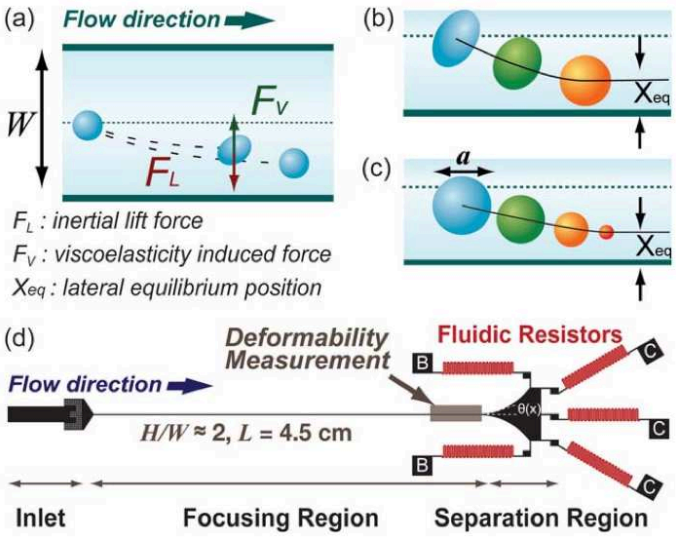

Figure 1.4: **Inertial effect on deformation of particles**. **(a)** The inertial lift force and the viscoelasticity induced force compete and lead to a unique lateral inertial focusing equilibrium position depending on deformability **(b)** and size of particles **(c)**. **(d)** The microfluidic device based on this principle consists of a very long channel to focus the particles in their equilibrium position and a gradually expanding chamber ending on several outlet to collect the different populations of capsules. Image from [35].

1.1.3 Deformability-based sorting methods

The logic behind the methods presented in the previous section is that small particles are collected at the end of streamlines originating from positions that are not accessible to large particles. Trajectories can be deduced from the velocity field by taking into account excluded volume effects. This is true for stiff particles but not always for deformable capsules or cells. For soft particles, hydrodynamic forces generate not only displacements but also deformation. Deformation has been extensively studied in the case of: margination [29, 30], deformation in a constriction [31, 32] and release [33, 34]. The sorting of deformable objects is a fluid-structure problem which has been extensively studied numerically and experimentally. Deformability-based methods for sorting have been less studied than size-based sorting. However they present many advantages for several medical applications where cell mechanical properties are modified cause of diseases. We are here focusing on deformability-based sorting methods for capsules.

Inertial microfluidics

We have already seen that inertial microfluidics can be used to separate capsules according to their size. Lift forces not only depend on particles size and position, but also on their compliance and shape [36]. When they deform, capsules have different shapes which induces different lift forces and different equilibrium positions in a channel [37, 38]. Lift forces tend to push capsules close to the wall when the deformation compete to stay as centered as possible. The effect of the competition between inertial lift forces and viscoelastic induced forces is presented in figure 1.4. Small and non deformable capsules flow along the wall while deformed and large capsules follow the centerline [35]. The limit of using inertial effect for sorting particles according to their mechanical properties is the length (4

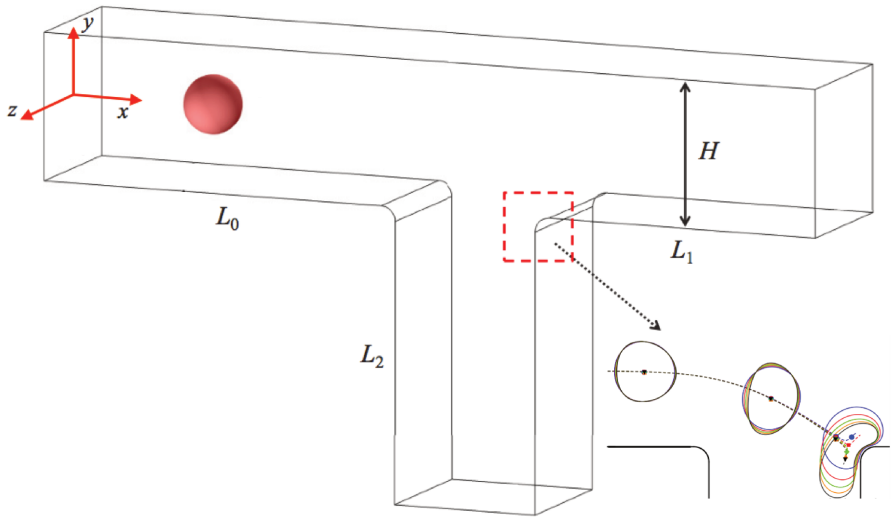

Figure 1.5: **Flowing through a bifurcation.** Capsules are flowing in a T-shape device. Capsules are first suspended in the center of the channel. Zoom on the 90° curvature where the capsule deforms and passes in the straight channel or in the bifurcation. Image adapted from [39].

cm) needed to reach equilibrium.

Flow through a bifurcation

In a recent numerical work, Villone et al. [39] propose a geometry based on a T-shape bifurcation. In figure 1.5, capsules are suspended well centered in the channel and the pressures are chosen to have the same flow rate in both outlet channels. Thus the centerline arrives on an equilibrium point trapped onto the curvature (zoomed zone in the red square). Perfectly centered capsules deform around the corner and the position of their center of mass determines the channel where they will flow. Stiff capsules deform weakly on the corner and flow in the straight channel. Soft capsules deform more against the corner and the position of their center of mass is deviated in the direction of the 90° curved channel. The capsules sorting can be achieved according to their deformability. However, the principle is very sensitive to capsule centering and needs very high viscosity and velocities to be efficient.

Flow through a constriction

Another technique using mechanical properties consists in flowing microcapsules through ridges structures [42] and constrictions. In their patent, Sulcheck et al. have described a microfluidic device consisting of several tilted ridges [43]. Figure 1.6 presents how capsules are confined between the beams and the wall [40]. The trajectories followed by the particles depend on their deformability. Soft particles , in blue in figure 1.6 (b), deform and are deflected in the channel. Stiff particles, in green, weakly deform in the constrictions and their trajectory deviates with a different angle caused by the presence of the ridges. This passive method efficiency will be decreased with the microfabrication limits, and after some uses, ridges could present defects. Until now the technique has only been

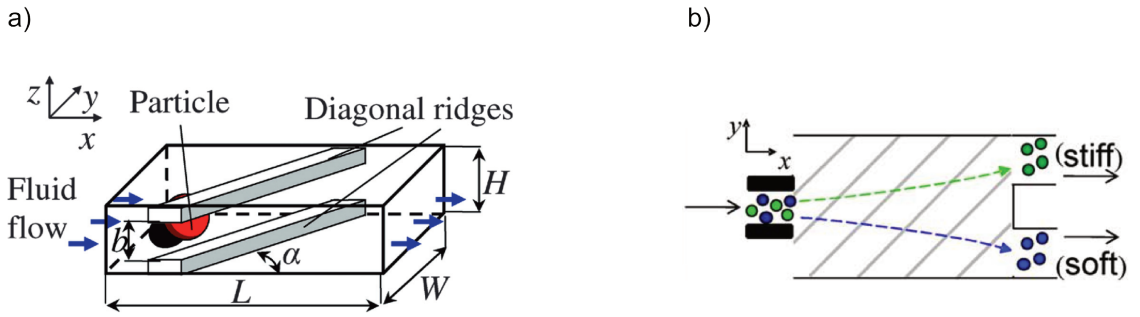

Figure 1.6: **Flowing through constrictions. (a)** Capsules are flowing through successive diagonal ridges. Ridges are present in the top and the bottom and confine the capsules when they are flowing through the constriction. Image adapted from [40]. **(b)** Stiff particles weakly deform in the constriction and have a straight trajectory in the device. On the contrary, soft particles deform and are deflected following the angle of the ridge. Image adapted from [41].

validated for large stiffness contrasts of 57.

1.1.4 Objectives of our microsystem

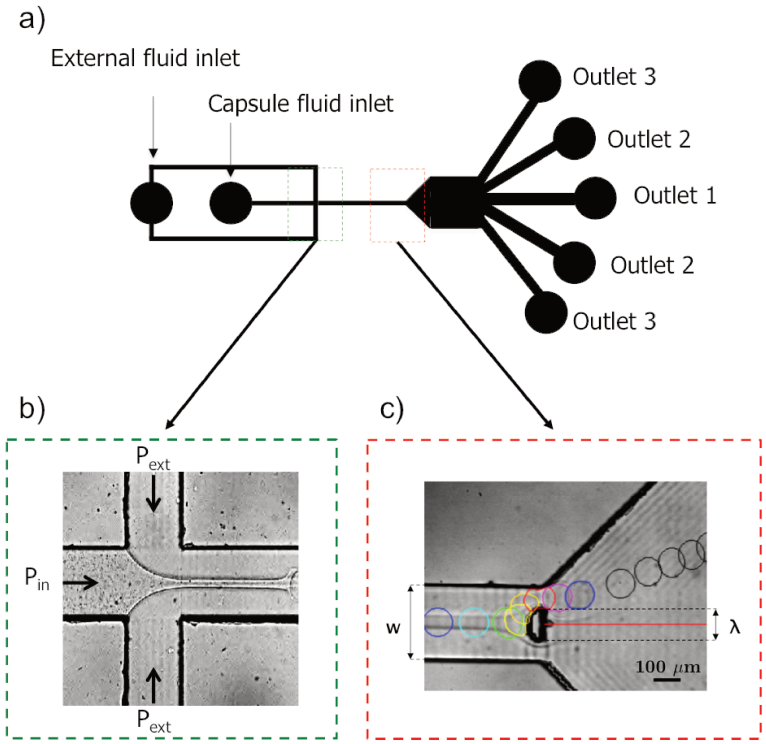

Figure 1.7: **Sketch of the experimental device.** The fluids flow from left to right. (**a**) Sketch of the microfluidic device geometry. The system presents two entrances for the flow focusing, a diffuser and five outlets to collect capsules. **(b)** Zoom of the green delimited zone is a picture of the flow focusing module. The external fluid is perfused at P_{ext} and pinches the internal fluid which contains the capsules in order to focus them onto the obstacle. **(c)** Zoom of the red delimited zone. It is a picture of the half-cylinder obstacle at the end of the straight channel. Here a capsule of diameter 80 μm moves to the obstacle, deforms, passes into the constriction and follows a trajectory in the diffuser.

We propose in this chapter to separate microcapsules whose stiffness is known and differs only by a factor three. The method consists of squeezing microcapsules through a constriction and study their trajectories into a diffuser (Figure 1.7, c). The geometry, inspired by a numerical work [44], consists of an obstacle at the end of a straight channel. The gap between the wall and the obstacle constrains the capsules to deform. Zhu et al. [44] have shown that for well centered capsules with different stiffness the trajectories differ after the constriction. In order to adapt numerical work to experimental study, we need to add some modules to make the experiment feasible. We design a flow-focusing at the entrance of the channel to center the capsules (Figure 1.7 b). Two fluids are perfused at the same time in the channel. The internal one contains microcapsules. It is pinched in the center of the channel by controlling the pressures, as for pinch flow fractionation. When the channel widens, the trajectories separate. We can follow trajectories in the diffuser by drawing all the successive positions of a capsule as presented figure 1.7 (c). To collect the capsules in different reservoirs, we design five symmetrical outlets (Figure 1.7 a).

The objectives are (i) to understand how the pressure-driven flow of fluids is controlled in this geometry; (ii) to separate capsules according to their size and deformability; and (iii) define the main parameters of sorting. The results of this work may have significant impact on label-free micro-objects sorting device based on deformation.

This chapter is organized as follows. A first section (1.2) presents the geometry of the microfluidic channel, the preparation of capsules and the experimental set-up. A second section (1.3) introduces coflow experiments without capsules in order to characterize the flow in the geometry of the device. A third section (section 1.4) presents the trajectories followed by lycopods and microcapsules in the microfluidic system, at low and high flow strengths. A forth section (section 1.5) presents the parameters involved in deformability- and/or size-based sorting.

1.2 Material and Methods

1.2.1 Microchannel design and fabrication

Our microfluidic device is symmetric and consists of a rectangular straight channel of width w and depth h partially obstructed by a half-cylinder obstacle of diameter λ (Figure 1.7 c). Upstream of the main channel, a flow-focusing module is added to focus the capsules onto the center of the obstacle (Figure 1.7 b). Downstream of the obstacle, the channel widens (Figure 1.7 a) and splits into several exits to collect capsules. The width of the confined zone between the side wall and the obstacle is chosen to be smaller than the capsule size.

Microfluidic systems are fabricated in PDMS (Polydimethylsiloxane). To fabricate the chips, we use standard soft lithography techniques [45]. PDMS presents many advantages for microfluidic observation: it is transparent, flexible, easily cast and bounded. Silicon oil and curing agent (Sylgard) are mixed together in a 10:1 ratio and cast onto a master. The master is a silicon wafer with SU8-

photoresist microstructures (Microfactory, Paris). To avoid air bubbles, the master covered with non cross-linked mixture is placed under vacuum until the air bubbles have all disappeared from PDMS. After baking for 2 hours at 70°C the PDMS is cross-linked and can be peeled off from the SU8 master. Holes are punched at the inlet and outlet places. The PDMS chip is then plasma-bounded together with a glass slide using air plasma generated by a plasma-oxidizer (HARRICK, NY 14850, USA). The chip is sealed when the two surfaces are placed in contact. After 2 hours in stove at 70°C the device is ready to be used.

1.2.2 Capsule preparation

Microcapsules consist of a thin cross-linked membrane of ovalbumin around a liquid core. They are prepared by the team of Florence Edwards-L, with the method of interfacial cross-linking as described in [14]. Briefly, an aqueous solution of 10 % ovalbumin solution in a phosphate buffer (pH 5.9 or pH 8) is mixed with an organic solution of cyclohexane added with 2 % m/V sorbitan trioleate, to form an emulsion. Adding 2.5 % (w/v) terephtaloyl chloride to the organic phase induces the cross-linking reaction at the surface of the droplets, and the formation of the membrane. After 5 minutes, the chemical reaction is stopped by dilution, adding a solution of chloroform:cyclohexane (1:4, v/v). Capsules are then rinsed with an aqueous solution of polysorbate, and then with pure water. The result is a suspension of microcapsules in water; that is stored at 4°C. The average diameter D and polydispersity of the capsule population is estimated by acquiring pictures of a large number of capsules under the microscope and performing image analysis. In the whole chapter D is determined with the Image J software using a circular fit, and expressed as the mean $\pm$ the standard deviation.

1.2.3 Capsule treatments

In order to have different populations of capsules with different mechanical properties, we exposed capsules to different treatments. We observed the capsules between slide and cover slip spaced with three layers of tape (total thickness 150 μm), with an inverted microscope (DMIL LED, Leica Microsystems GmbH, Germany). The aim is to have two populations of capsules with comparable average size, round shape and able to resist mechanical solicitations. In this section we will present images of capsules exposed to different treatments, before being perfused in the constriction, and in the diffuser when they should have recover their round shape.

Ethanol treatment

Ethanol has been observed to favor membrane stiffening by accumulating saturated fatty acids [46]. Moreover, it is a known solvent used for protein precipitation [47]. So, we expect ethanol to stiffen microcapsules. Capsules are suspended in a 70 % ethanol solution for two hours then rinsed with pure water. Non-treated capsules are observed between slide and coverslip. At rest their shape are round (Figure 1.8 a). After treatment with ethanol, the capsules seem to have similar size but ellipsoidal shape when compared to non-treated capsules (Figure 1.8 b). When flowing through the microsystem, we expect capsules to deform around the obstacle and recover a round shape in the diffuser. That is what we observed for non-treated capsules (Figure 1.8 c). But the membrane of ethanol

treated capsules seems to retract and does not present a spherical shape.

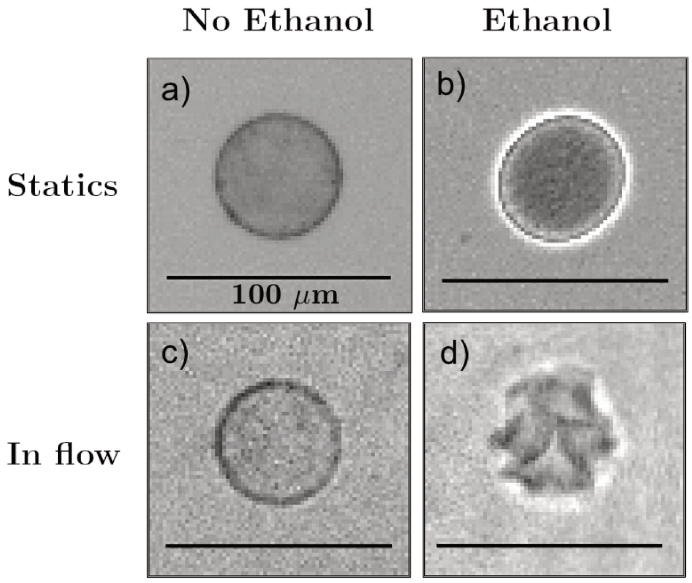

Figure 1.8: **Ethanol treatment effect on microcapsule shape**. Observation of an ovalbumin capsule fabricated at pH 5.9, (**a**) without any treatment between slide and coverslip. (**b**) treated with ethanol between slide and coverslip, they present an ellipsoidal shape. (**c**) without any treatment in the divergent chamber. (**d**) treated with ethanol in the divergent chamber, the membrane retracts. Scale bar 100 μm.

Our system is expected to sort spherical micro-objects. Ethanol treatment modifies capsule shape, so we will not use this treatment to artificially modify capsule mechanical properties.

Diamide treatment

In the literature, diamide has often been used to stiffen red blood cells (RBCs) [48–50]. Diamide is a chemical thiol-cross linking agent and ovalbumin capsule membrane contains thiol groups. Thus we expect diamide to stiffen capsules. We treat capsules with diamide (55 μM) during 25 min at 37°C. After the 25 min exposition, capsules are rinsed and centrifuged three times, 5 min at 250 rcf, in pure water, to eliminate diamide excess. After the last centrifugation they are resuspended in pure glycerol and perfused into the device with the conditions exposed in section 1.2.4.

In order to keep the sphericity of the capsule after treatment, we test several diamide concentrations, exposition duration, and centrifugation speed and duration. We finally manage to obtain a spherical shape for capsules treated with 55 μM for 25 minutes and rinsed 3 times in water by 3 successive centrifugation of 5 minutes at 250 rcf. However, finding the right parameters to have round treated capsules takes time. When we perfuse the corresponding non-treated capsules in the PTFE (polytetrafluoroethylene) tubes they are damaged by the flow (Figure 1.9 c). We observe that aging impacts capsule fragility. Mechanical solicitations of the flow in the capillaries irreversibly damages the capsules. They are already impaired at the entrance of the channel (Figure 1.9 c). Treated capsules appear to be round between slide and coverslip and in flow, in the diffuser (Figure 1.9 b, d). Diamide has probably stiffened the capsule membrane which remains spherical. But even if non-treated cap-

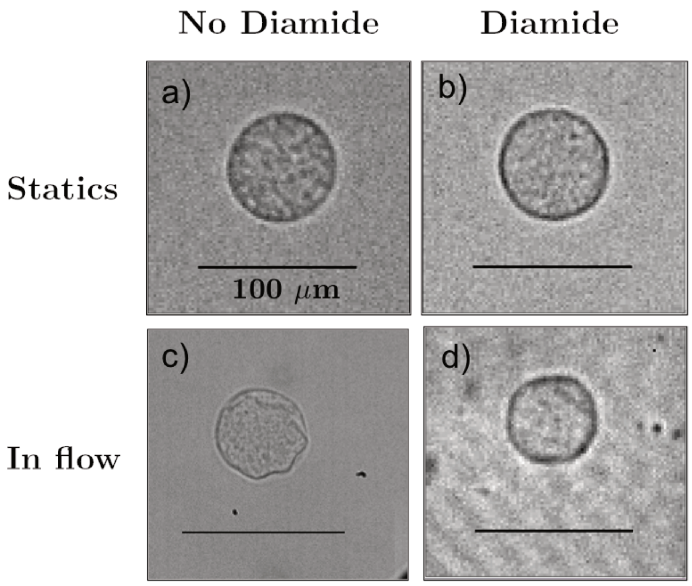

Figure 1.9: **Diamide treatment effect on microcapsule shape**. Observation of an ovalbumin capsule fabricated at pH 5.9, (**a**) without any treatment between slide and coverslip. (**b**) treated with diamide between slide and coverslip. (**c**) without any treatment after perfusion in a PTFE tube before perfusion in the microfluidic system.(**d**) treated with diamide in the divergent chamber.

sules are round when observed between slide and coverslip before perfusion, their membrane became too weak to stay spherical in flow. It is then not possible to compare treated and non-treated capsule trajectories when capsules from one batch are not spherical. With these capsules we can not conclude about capsule behavior in a constriction. We will not use these capsules in the following sections.

Modification of fabrication conditions

In the literature Chu et al. [51] have shown that fabrication conditions of microcapsules (protocol detailed in section 1.2.2) influence their mechanical properties and deformability. In particular, the pH of the buffer solution containing ovalbumin modifies capsule stiffness. Capsules prepared at low pH are softer than those prepared in more basic conditions [51]. We have worked with capsules fabricated at two different pH (pH 5.9 and pH 8). Capsules fabricated at pH 5.9 are expected to be softer than those fabricated at pH 8.

First, we observe the two batches of capsules between slide and coverslip, and it appears that they are spherical at rest (Figure 1.10 a and b). When flowing through the microfluidic device, downstream of the obstacle in the diffuser they remain spherical (Figure 1.10 c and d). This is the case whatever the pH used during capsule production. We will use these capsules for perfusion and analyze their trajectories when they pass through a constriction. Having capsules fabricated with different conditions is our best chance to distinguish capsules by their stiffness without further treatments. As presented earlier in this section, chemical treatments made on capsules interfere with their shape and it is difficult to control precisely their mechanical properties.

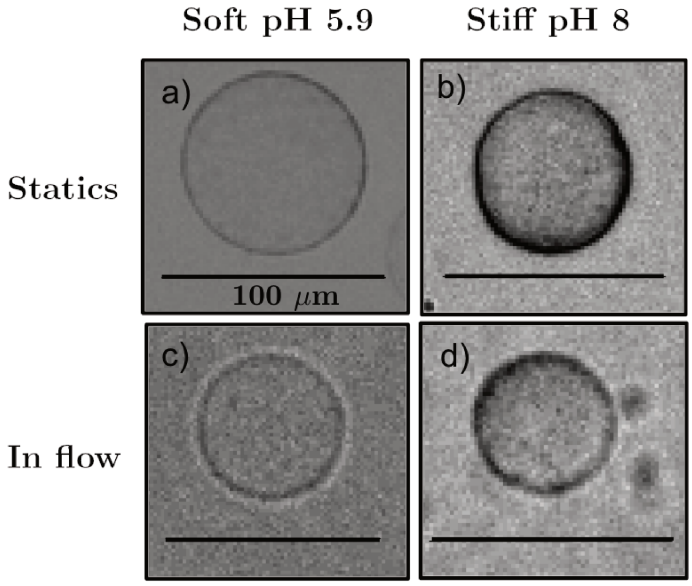

Figure 1.10: **Shape of microcapsules produced at two different pH**. Observation of an ovalbumin capsule, (**a**) fabricated at pH 5.9 between slide and coverslip. (**b**) fabricated at pH 5.9 in the divergent chamber in flow. (**c**) fabricated at pH 8 between slide and coverslip. (**d**) fabricated at pH 8 in the divergent chamber in flow.

1.2.4 Experimental setup

The schematic of my experimental setup is shown in figure 1.7, its geometry is described in section 1.2.1. We fill the channel with two fluids. The internal one, of viscosity $\mu_{in} = 800$ cP, is composed of 20 μL of the capsule suspension and 1 g of pure glycerol. The second one, perfused as the external fluid is pure glycerol (Figure 1.7 a), of viscosity $\mu_{ext} = 1300$ cP. The reservoirs respectively containing the external and internal fluids are connected to the microsystem using PTFE tubes with an internal diameter of 0.3 mm. We impose a pressure P_{in} to the internal reservoir and P_{ext} to the external reservoir, with a pressure controller (MFCS, Fluigent, France). Videos are recorded using a high-speed camera (Fastcam SA3, Photron, USA) whose pixel size is 17 μm. Image analysis is performed with the Image J software. In order to accurately capture capsule trajectories in the diverging chamber, we operate at 250 frames per second with a resolution of 1024×768 pixels, with a $10\times$ magnification for all the videos and images. We measure the capsule velocity U in the straight channel upstream of the obstacle, before any deformation, and the trajectory followed by the capsule in the divergent chamber, at different pressures. Varying the pressures P_{in} and P_{ext} modifies capsule velocity U. The chip is placed on the stage of an inverted microscope (DMIL LED, Leica Microsystems GmbH, Germany).

1.3 Coflow configuration in the device

Prior to perfuse any microcapsule, it is necessary to understand how fluids behave in the microfluidic chip. At the entrance of our device, a flow focusing module is used to center capsules. There, the internal fluid is pinched by the external one. When the more viscous fluid is the core fluid, it forms a thread extruded by the external fluid and moving in a solid-like manner. When the core fluid is the less viscous one, it is referred to as a jet. The coflow of immiscible fluids has been stud-

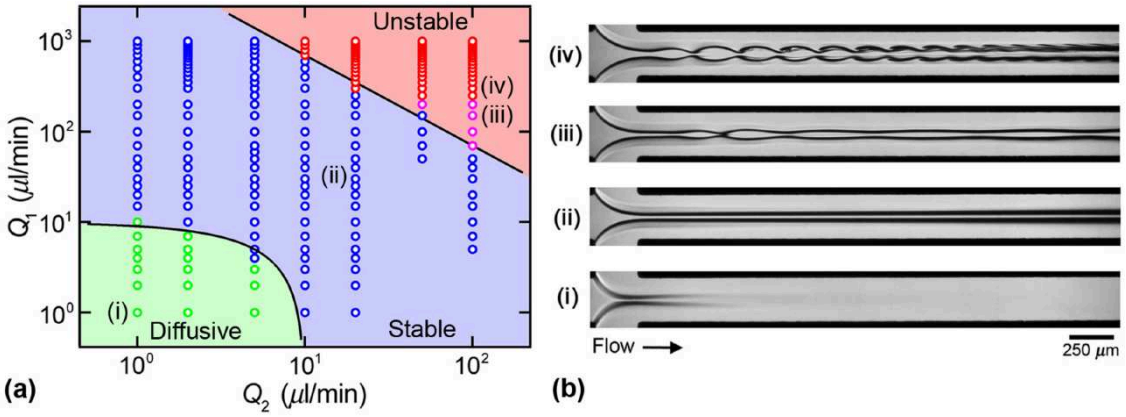

Figure 1.11: **Phase diagram of a jet exposed to different flow rates**. **(a)** Dimensional flow map to predict diffusive, stable and unstable behaviors of the jet. **(b)** Corresponding pictures (i) diffusive regime, (ii) stable regime, (iii) transitional regime, (iv) unstable regime. Image from [52].

ied for droplet [53, 54], foam production [55], and chemistry extractor [56]. Among the few studies on miscible coflows, most address liquid threads and focus on the stability of the pseudo-interface [57, 58]. Recently, Hu and Cubaud [52] describe miscible jets formed by the coflow of a viscous fluid surrounding a less viscous one in a square non deformable channel. They define three behaviors depending on flow rate imposed : diffusive regime, stable and non stable regimes (Figure 1.11).

In our case, we are also working with a jet between two miscible fluids. We use a deformable, rectangular channel for the experiments. So the dimensional phase diagram (Figure 1.11 a) is not applicable to our geometry. We are, in this section, studying the coflow of different fluid pairs in order to determine a relation between the conditions of perfusion and the width ϵ. For the centering of capsules, we need to control the core width ϵ with precision. We perform experiments to determine which inlet pressures allow to be in a stable regime and with a width ϵ smaller than capsule diameter.

1.3.1 Coflow experiment

Table 1.1: **Fluid properties for different coflow experiments** with μ_{in} (resp. μ_{ext}) as the viscosity of the inner fluid (resp. external fluid), and an order of magnitude of the viscosity contrast $\chi^{-1} = \mu_{ext}/\mu_{in}$.

Fluid pair	Internal fluid	External Fluid	μ_{in}[cP]	μ_{ext}[cP]	χ^{-1}
A	Pure water	Glycerol 70%	1	30	30
B	Alginate solution	Glycerol 70%	7	30	4
C	Capsule suspension	Pure glycerol	800	1300	2

The reservoirs containing the external and internal fluids are connected to the microfluidic device using PEEK (polyether ether ketone) tubes with an internal diameter of 0.25 mm. For variable values of the internal and external pressures, we measure the external and internal flow rates, q_{ext} and q_{in}, in the two inlets of the flow-focusing module thanks to a flowmeter (Flowell, Fluigent, France). The value of the flow rate ratio $\phi = q_{in}/q_{ext}$ is deduced. The internal fluid of viscosity μ_{in} is perfused at pressure P_{in} into another fluid of viscosity μ_{ext} moved at pressure P_{ext} ($\mu_{in} < \mu_{ext}$). The pressures ap-

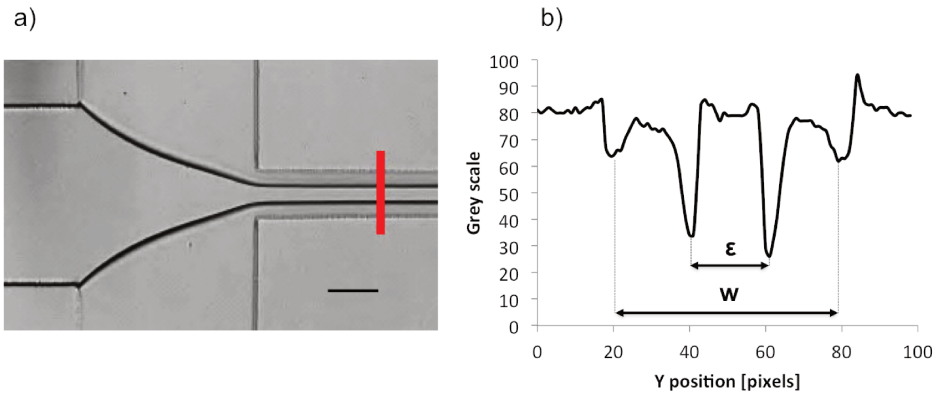

Figure 1.12: **Determination of the core width**. **(a)** Picture of a coflow of an internal flow of pure water injected into a solution of 70 % of glycerol (Fluid pair A, Table 1.1). Scale bar 50 μm. **(b)** Grayscale profile along the red line. The width of the channel w and the core width ϵ are determined by measuring the distance between two pics.

plied to each entrance are adjusted, varying P_{in}/P_{ext}, in order to control the core flow width ϵ (Figure 1.12 b). Different fluid pairs (Table 1.1) are used to calibrate the flow and establish the relationship between the flow rate ratio ϕ and the width ϵ.

Coflow experiments are performed with different fluids, whose properties are summarized in Table 1.1. The aim is to characterize the jet formation in our channels, with different pressure pairs and different viscosity ratios. We prepare a 70 % glycerol/water mixture (VWR, France) and a 1 % (w/w) low viscosity alginate (A1112, Sigma-Aldrich, St Louis, MO, USA) solution in water containing 0.9% NaCl and 0.2% Hepes. The alginate solution is agitated at least two days at $4°C$.

Images are post-processed with the software Image J. A ROI (Region of Interest) line is drawn across the main channel, and grey levels are plotted along this line (Figure 1.12 a). The core flow width ϵ is defined as the distance between the two minima of the grey curve plot (Figure 1.12 b).

1.3.2 The width of the core flow controlled by pressures applied

In order to characterize the width ϵ of the jet, we carry out experiments fixing the viscosity ratio (for each fluid pair described in table 1.1) and the external pressure P_{ext}. We only modify the internal pressure P_{in}, in a range which avoids backward surge in one or the other inlet. We measure the flow rates q_{ext} and q_{in} with the flowmeter and ϵ with the method described in the previous subsection. We observe that the width ϵ increases with the internal pressure P_{in} (Figure 1.13). We use several channels with the same geometry but different aspect ratios of the straight part upstream of the obstacle. In figure 1.13 the devices are smaller than those used for capsule sorting but the evolution of core width with pressure is kept.

Modifying the pressure ratio induces a modification of the core width. Keeping one of the pressure P_{ext} or (resp. P_{in}) constant and modifying the other implicates a larger jet width when P_{in} increases (resp. a smaller jet width when P_{ext} increases). In the other hand, playing with P_{ext} and P_{in} at the

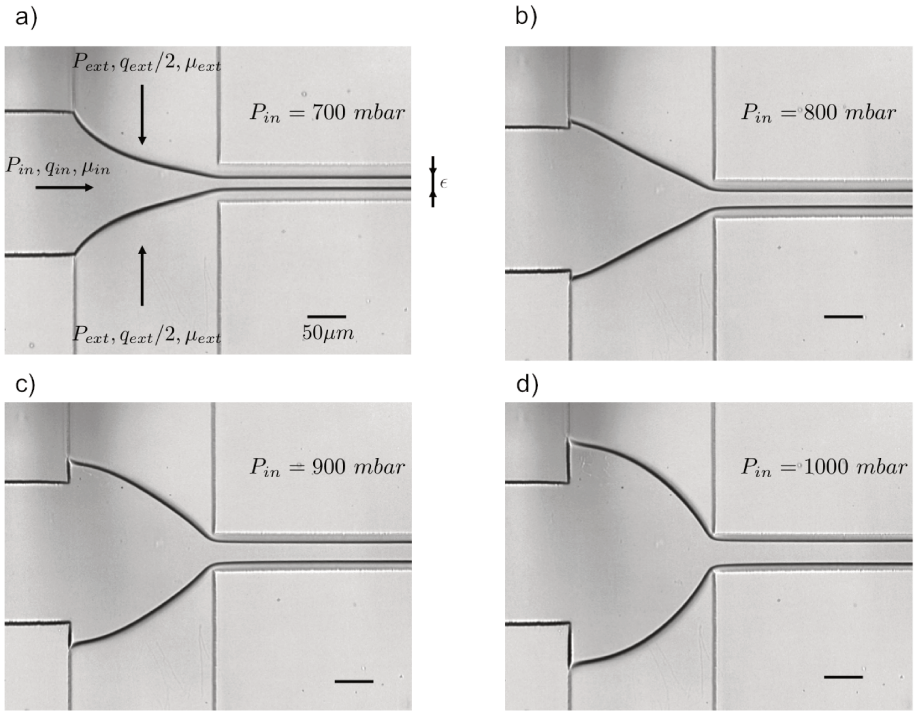

Figure 1.13: **Evolution of the width ϵ with the internal pressure**. Flow moves from left to right. The external pressure P_{ext} is fixed at 1000 mbar. Water is perfused into glycerol 70% (Table 1.1) **(a)** Internal pressure P_{in} = 700mbar, the core width $\epsilon = 15 \pm 3\mu$m. **(b)** P_{in} = 800mbar; $\epsilon = 22 \pm 3\mu$m. **(c)** P_{in} = 900mbar, $\epsilon = 28 \pm 3\mu$m. **(d)** P_{in} = 1000mbar, $\epsilon = 33 \pm 3\mu$m.

same time, keeping the pressure ratio (P_{ext}/P_{in}) constant does not significantly modify the value of the width ϵ (Figure 1.14).

1.3.3 The width of the core flow vary with the aspect ratio

We have just shown that a modification of the pressure ratio influences the width ϵ. We discuss here whether we can predict the width ϵ using the aspect ratio of the channel, the viscosity ratio ϕ and the flow rate ratio χ. In figure 1.15, we plot the width ϵ, non-dimentionalized by three different characteristic lengths α, as a function of the viscosity and the flow rate ratios. The characteristic length α is: the microchannel width w, height h, or the rectangular characteristic length $\sqrt{hw}$. We compare our results with those of Hu et *al.* [52]. They perform their experiments in a square channel ($w = h = \sqrt{hw}$) and found an equation to determine the core width ϵ :

$$\frac{\epsilon}{\alpha} = [1 + (1.5\chi^{1/2}\phi^{2/3})^{-1}]^{-1} \tag{1.1}$$

Because our channel is rectangular, it is not obvious which characteristic length will determine the width ϵ. Thus, we plot several non-dimensioned ϵ as a function of viscosity and flow rate ratios. We superimpose these curves with the theoretical curve determined with equation (1.1) in figure 1.15. The best fit is obtained when ϵ is normalized by the characteristic length $\alpha = \sqrt{hw}$ (green triangles in figure 1.15). The equation of Hu et al. [52] can be adapted to our experiments adapting the characteristic length α to the aspect ratio of the channel.

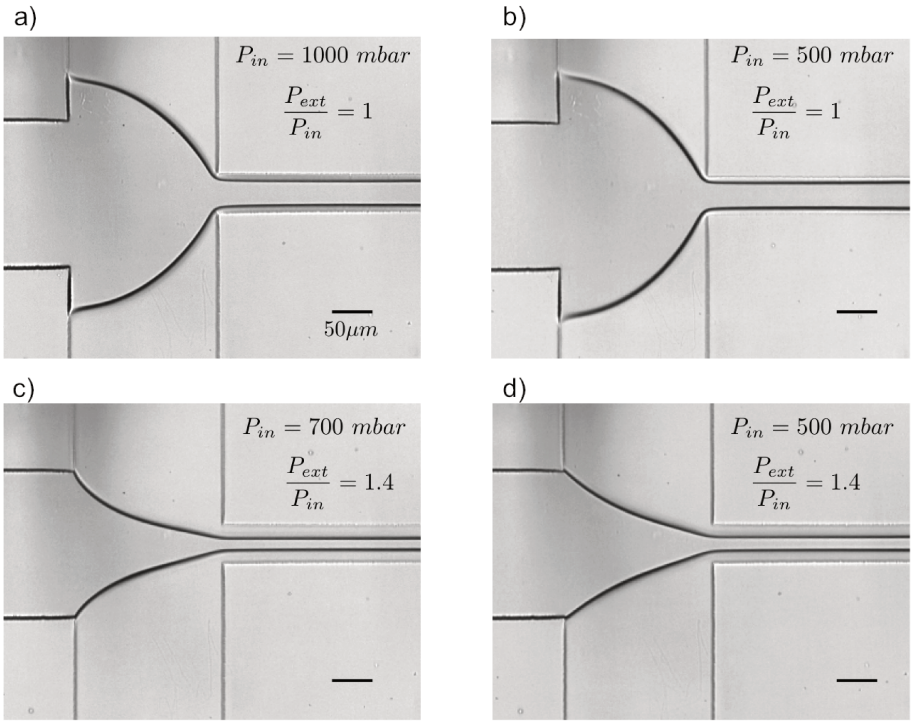

Figure 1.14: **Evolution of the width ϵ with the pressure ratio**. Flow moves from left to right. The pressure ratio is kept constant P_{in}/P_{ext} is 1 (**(a)** and **(b)**) respectively 1.4 (**(c)** and **(d)**). Water is perfused into glycerol 70% (Table 1.1) **(a)** The core width $\epsilon = 15 \pm 3\mu$m. **(b)** $\epsilon = 17 \pm 3\mu$m. **(c)** $\epsilon = 33 \pm 3\mu$m. **(d)** $\epsilon = 34 \pm 3\mu$m.

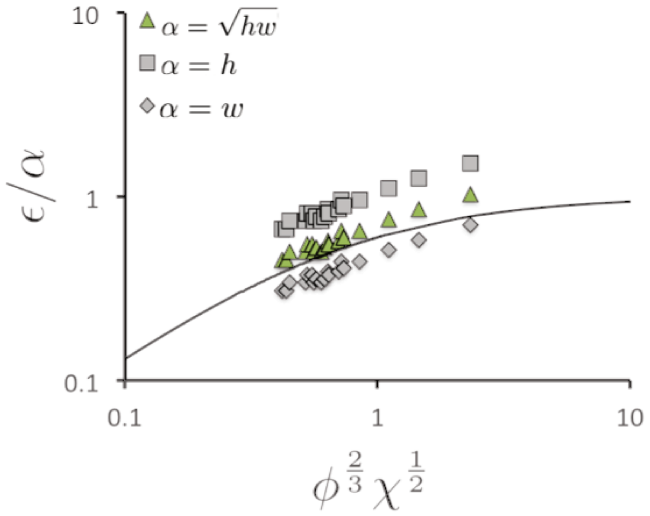

Figure 1.15: **Evolution of the width ϵ with the aspect ratio**. Plot of the non-dimensioned width ϵ with the parameter α, for the fluid pair A (Table 1.1). Solid line represents the equation 1.1. The best fit is with $\alpha = \sqrt{hw}$. Graph adapted from [52, 59].

1.3.4 The width of the core flow variation with the viscosity ratio

We carry out experiments with different fluid pairs in order to change the viscosity ratio. For a given fluid pair, the viscosity ratio is kept constant (Table 1.1). We work at variable pressure ratio

P_{in}/P_{ext} keeping P_{ext} constant in order to modify the core width ϵ. We know the relation between the core width ϵ, the viscosity ratio ϕ, and the flow rate ratio χ thanks to equation (1.1).

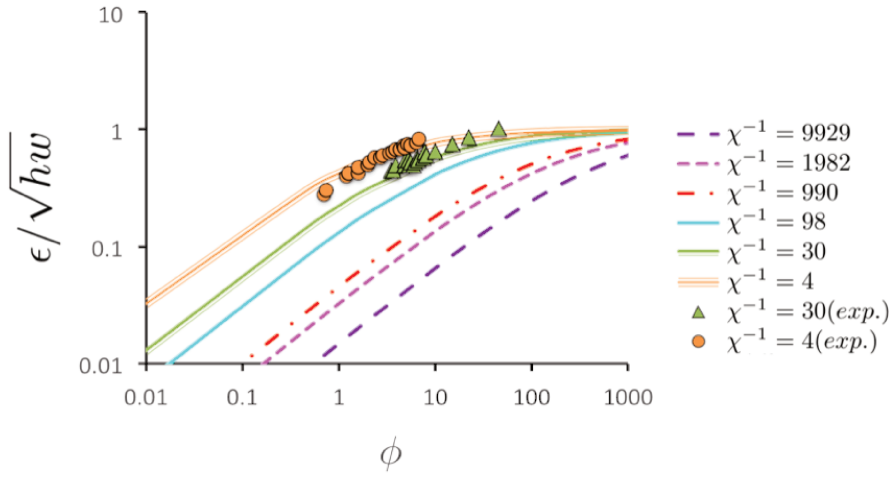

Figure 1.16: **Evolution of the width ϵ with the viscosity ratio**. Plot of $\epsilon/\sqrt{hw}$ as a function of ϕ for the fluid pairs A and B. Green triangles correspond to fluid pair A (water/70% glycerol mixture, χ^{-1} = 30) and orange circles represent experimental data from fluid pair B (alginate/70% glycerol mixture, χ^{-1} = 4.28). Solid lines represent $\epsilon/\alpha = [1 + (K_x\phi^{2/3})^{-1}]^{-1}$ ($K_x = 1.5\chi^{1/2}$) and are adapted from [52, 59]

We extend the curves published in [52] (for viscosity ratios: 9929, 1982, 990 and 98) to lower viscosity ratios. In figure 1.16 the orange and green solid lines respectively correspond to the curve obtained using equation (1.1) for viscosity ratio of 4 and 30. Orange circles and green triangles are respectively the points from experimental data at viscosity ratio of 4 and 30. Experimental data and analytical data are superimposed. That is the proof that even if we are working in deformable PDMS channels, we are able to determine the width ϵ with the knowledge of viscosities. In order to have ϵ constant and in the range of capsule diameter D, we perform capsules flow experiments at constant pressure ratio.

1.3.5 From pressure ratio to flow rate ratio

Originally, microfluidic flow was imposed by controlling the flow-rate ratio by using syringe pump [60]. Syringe-pump is relied on a step by step motor which creates pressure fluctuations into the device and disturb the flow [61]. In order to avoid these fluctuations, pressure controllers have been developed. In a single phase flow, pressure and flow rate are linearly connected at low Reynolds number. As a consequence, we expect that flow-rate and pressure driven flow will lead to similar coflow in a flow focusing. However, Ward et al. [62] have shown differences between droplets formed from flow-rate-driven or pressure-driven pumping. They report differences in the drop formation process and hypothesized that surface tension is involved in these differences. But they were not able to check it.

In their work, Hu et al. [52] are controlling the flow rate in order to accurately control the width

of the core flow ϵ. Because we need a quick response of the flow when modifying the flow strength we are using a setup based on pressure. This modification is not negligible because under a certain internal pressure, the fluid surges backward whereas imposing the flow-rate induces a flow in both parts of the flow focusing. Figure 1.17 shows that the regime of bubble formation is larger by controlling the flow-rate than by controlling pressures [63]. Bubble formation and jet formation work on the same principles. The main difference is the tension of the interface that is larger in the case of the formation of bubbles by perfusing two immiscible fluids. In our case, the stable regime of coflow is larger in a flow-rate-driven coflow than in a pressure-driven one as shown in figure 1.18. In order to compare and implement the experiments made by Hu et al. [52] with our work, we measure the flow strengths with a flow meter. We are then able to make a correlation between the pressures applied, the flow rates, and the width ϵ. We supervised Oriane Chaput during her bachelor thesis to initiate this study. It is the subject of an in progress publication in collaboration with Ilyesse Bihi, Badr Kaoui and Anne Le Goff.

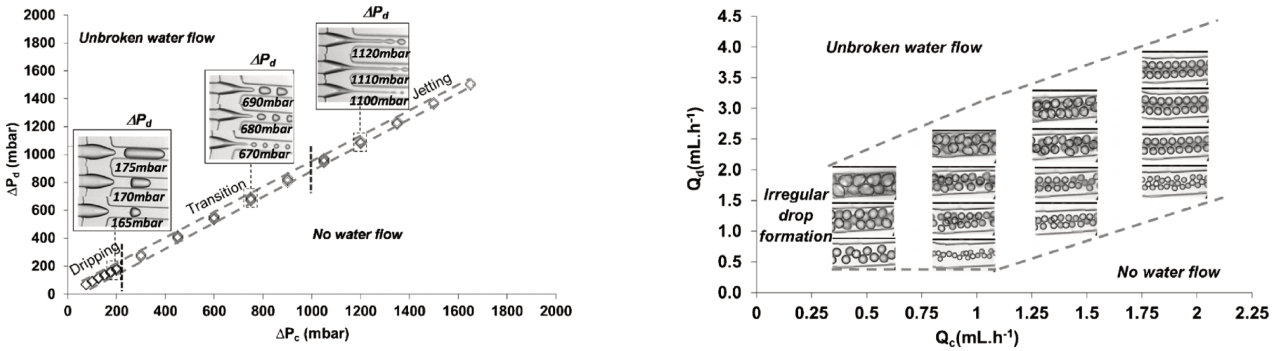

Figure 1.17: **Flow regime diagrams for droplet production**. On the left is a pressure driven flow with water in the centered channel and oil of viscosity 28 mPa.s in the lateral channels, at respectively P_d (i.e. P_{in}) and P_c (i.e. P_{ext}). On the right is a flow-rate driven flow with water flown in the central channel at Q_d (i.e. q_{in}) and oil of viscosity 28 mPa.s flown at a flow rate Q_c (i.e. q_{ext}). Image adapted from [63].

For capsule sorting experiments, we have chosen a unique fluid pair (glycerol, capsule suspension). The applied pressures are selected to have a constant width ϵ, smaller than capsule size. The limit of this method of driving is the critical value under which the internal pressure surges backward. But we expect that this limit is not critical for our experiments. First because we are able to have a width ϵ lower to capsule size. Second because controlling in pressure increases the response time of the coflow when compared to flow-rate-driving systems. Moreover, we have shown in the section 1.3 that the viscosity ratio, the width ϵ and the aspect ratio $\sqrt{hw}$ are related with the flow rate. In conclusion, we are able to know all the perfusion parameters involved in the coflow and understand the processes of capsule flow described in the next section.

1.4 Trajectories in the diffuser

In this section, we seek to determine the condition of perfusion allowing the capsules to deform and inducing a modification of trajectories. Small rigid objects, called lycopods are perfused in the

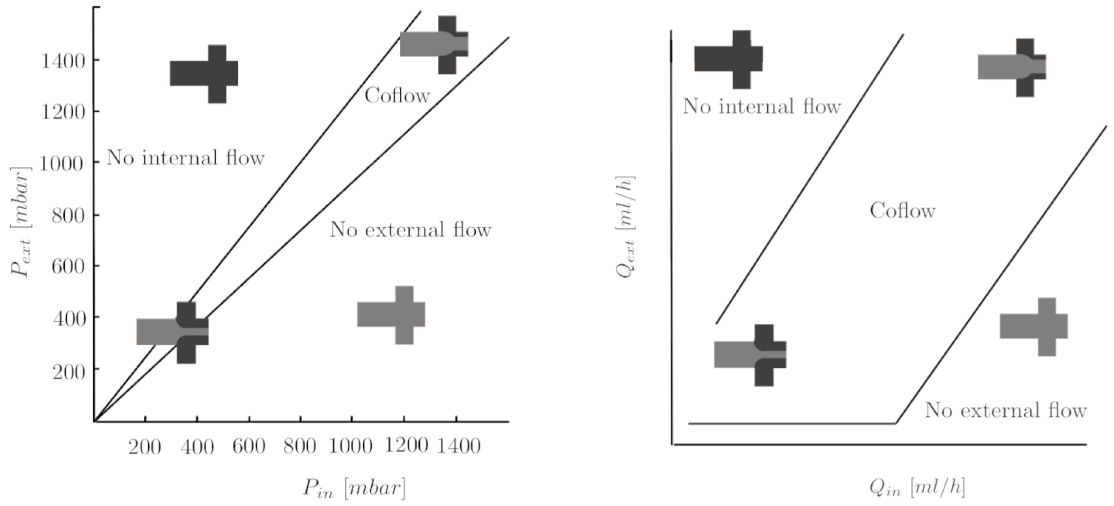

Figure 1.18: **Flow regime diagrams for jet formation**. On the left is a pressure driven flow, the stability regime is small, when internal pressures are low when compared to external pressure. The internal fluid flows backward. On the contrary, on the right plot is a flow rate driven flow which imposes the flow in one direction. Pressures are automatically adapted to allow the flow of both fluids. The regime of stability is larger.

external fluid of the flow focusing. We follow the trajectory of lycopods and determine the velocity field around the obstacle and in the diffuser by considering that a lycopod follows a unique streamline. Then, we perfuse deformable capsules in the inner fluid of the coflow, at low and high flow strength; to understand how micro-objects behave in a diffuser downstream of the obstacle. Their trajectory can be separated in 3 regions. First, capsule is flown into the straight rectangular channel and its trajectory is linear. In spite of the presence of a flow focusing module, the centering of capsules is not perfect. Experimentally, perfect centering does not exist and we call κ the offset. The offset κ is measured as presented in figure 1.19 (a), as the difference between the position of the center of mass of the capsule γ_c and the y-position of the centerline of the channel γ_0: $\kappa = \gamma_c - \gamma_0$. Second, the capsule is squeezed on the obstacle, deforms and passes through the constriction up or down the obstacle. In figure 1.19 (b), we define δ as the distance between the center of the obstacle and the position of the center of mass of the capsule in the constriction. Third, it enters the wide chamber and moves in a straight line until the end of the diffuser. We define β as the angle of deflection between the centerline of the channel and the straight line fitting with the trajectory of the capsule (Figure 1.19 c).

1.4.1 Velocity field in the device

At the opposite than capsules, lycopods are perfused in the external fluid, so they can not be centered into the rectangular channel (Figure 1.20). Lycopods whose diameter is $D_{Lycopod} = 27 \pm 2$ μm are not confined into the constriction. They are thus used as tracers. Figure 1.20 presents a superposition of the trajectories followed by lycopods up and down the obstacle. Lycopods flow around the obstacle and follow a linear trajectory in the diffuser. We use them to determine the positions of external fluid streamlines. For each lycopod, we measure its off-set κ upstream of the obstacle, its distance δ to the obstacle and the angle β between the horizontal axis and its trajectory.

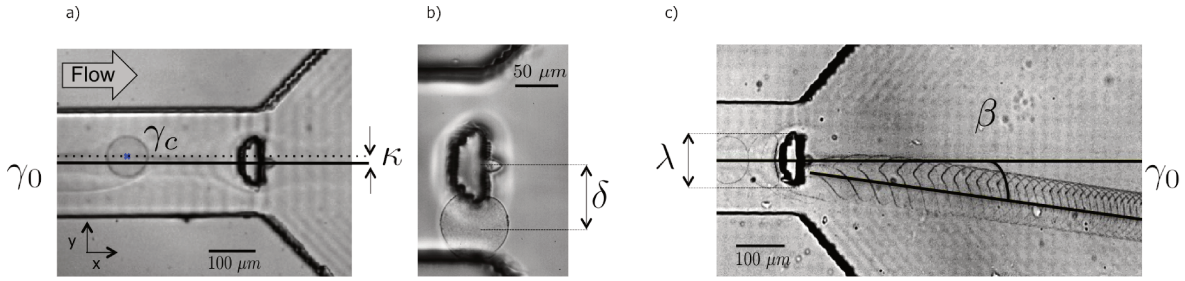

Figure 1.19: **Definitions of the parameters involved in sorting**. Flow is from left to right. **(a)** The position γ_c of the center of mass of the capsule upstream of the obstacle and the position γ_0 of the center of the channel are substracted to measure the off-centering κ. **(b)** In the constriction, the distance between the center of mass of the capsule and the obstacle is defined as δ. **(c)** Superposition of capsule positions during its travel in the microfluidic channel from left to right. β represents the angle of deviation between the linear part of the trajectory and the horizontal axis. λ is the diameter of the obstacle.

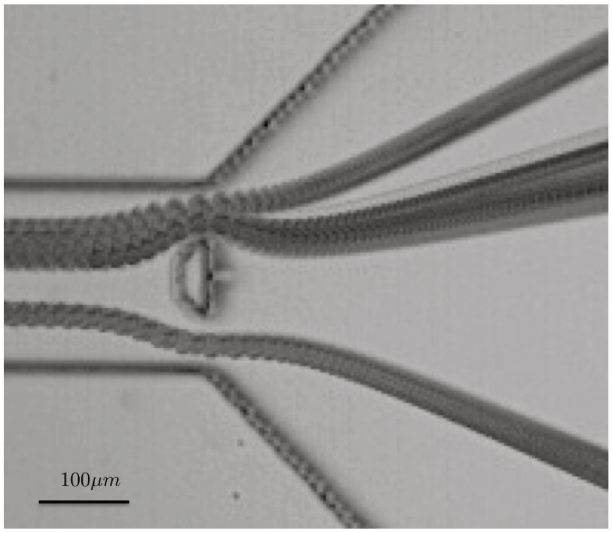

Figure 1.20: **Lycopods trajectory**. Superposition on several images representing lycopods trajectory in the diffuser. We can distinguish the internal fluid in the diffuser where there is no lycopods. Scale bar 100 μm.

Experiments are performed for three different pressure pairs: P_{in} = 267 mbar (resp. 1200 mbar; 2400 mbar) and P_{ext} = 1000 mbar (resp. 4500 mbar; 6000 mbar) including two different ratios (P_{in}/P_{ext} = 0.26 or P_{in}/P_{ext} =0.4). The angle β are plotted as a function of the distance δ in figure 1.21. For the three pressure pairs we obtain a linear scatter plot. When the distance δ increases, the angle β increases. All the curves superimpose, whatever the applied pressures, lycopods trajectory appears to follow the same trend.

As a conclusion, for small rigid micro-objects, the angle of deflection β linearly depends on the distance δ between their center of mass in the constriction and the center of the obstacle. In the next section, we will study the trajectories of larger objects, microcapsules, perfused at low and high pressures.

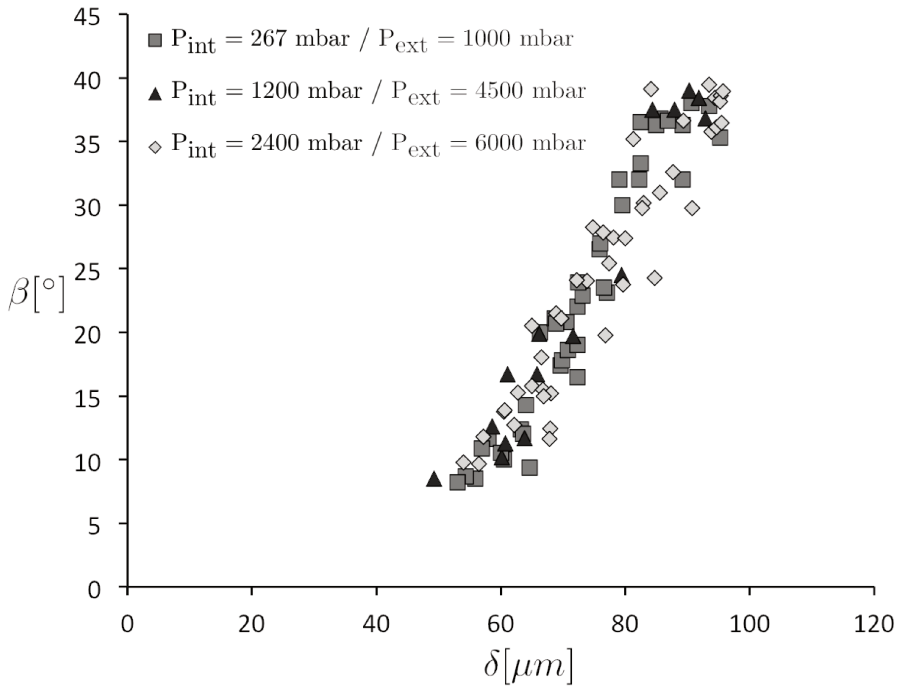

Figure 1.21: **Lycopods angle β as a function of the distance δ.** Plot of the deviation angle β of lycopods as a function of their distance δ from the obstacle in the constriction at different pressure pairs.

1.4.2 Capsules at low pressure

Prior to any flow perfusion experiment, we observe capsules fabricated at pH 5.9 on a glass slide with an inverted microscope. We measure the mean diameter at rest, between slide and coverslip on 174 capsules and find $D_0 = 60 \pm 18$ μm. Capsules are then flowed through a 50 μm gap between the wall and the obstacle, where they are confined. They are then collected at the different outlets (Figure 1.22 b) and their size distribution is determined in each reservoir.

The flow perfusion experiment is exerted in this subsection for the pressure pair : P_{ext} = 1000 mbar the pressure of pure glycerol and $P_{in} = 400$ mbar the pressure of the internal capsule suspension. In order to underline the influence of the diameter D at low pressures, we fulfill the microfluidic device with a capsule suspension produced at pH = 5.9, and analyze the populations collected in each outlet. We find that small capsules (< 50 μm) are located in the centered outlet (outlet 1 in red, Figure 1.22 b). On the contrary, large capsules of diameter larger than the constriction (> 50 μm) are collected in the external outlets 2 and 3. We find an average diameter $D_1 = 39 \pm 10$ μm for outlet 1 (in red), D_2 = 70 ± 8 μm for outlet 2 (in blue) and D_3 = 73 ± 8 μm for outlet 3 (in green). We notice that the capsule colored in blue in figure 1.22 (a) whose diameter D is 80 μm is more deflected in the diffuser than the capsule of diameter 60 μm colored in red. Larger capsules are deflected further from the channel axis than smaller ones.

We then perform the experiment for capsules prepared at different pH (pH 5.9 and pH 8). As mentioned in section 1.2.3 capsules prepared at pH 5.9 are softer than those prepared at pH 8. They

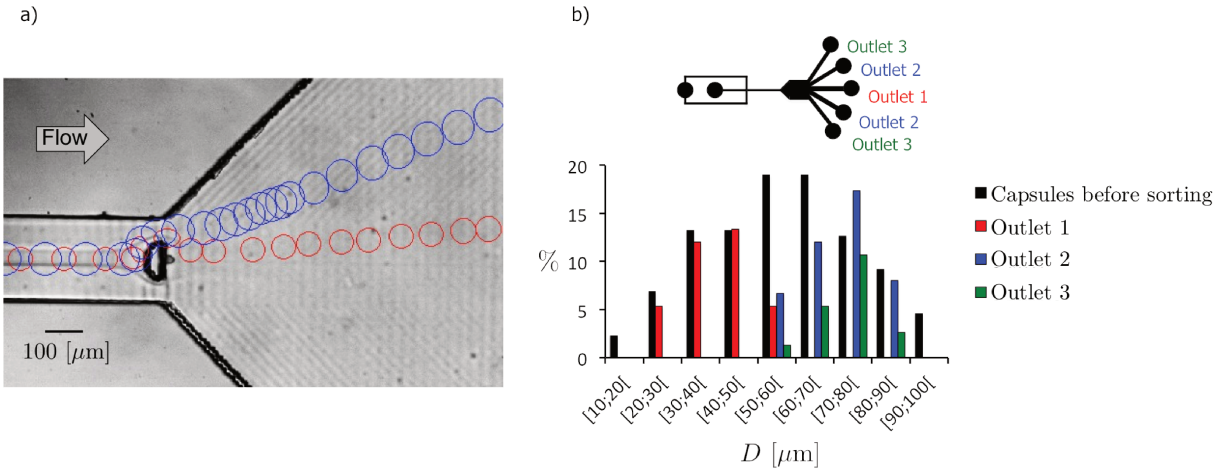

Figure 1.22: **Size-based sorting**. (**a**) Trajectories of a 60 μm capsule (red) and a 80 μm capsule (blue), when they flow in pure glycerol. (**b**) Size distribution of capsules collected at the different outlets. Capsules whose diameter is lower than 50 μm are centered in the diffuser and collected in outlet 1 in red. Capsules whose diameter is higher than 50 μm are collected in the external outlets 2 and 3.

are perfused at low pressures ($P_{in} = 200 - 267$ mbar and $P_{ext} = 1000$ mbar), and we analyzed their trajectories. At low pressures the mean velocity $\pm$ the standard deviation of the capsule is $U_{low} = 0.9 \pm 0.2$ mm.s^{-1} (mean of data for capsules at pH 5.9 and pH 8). We observe, in figure 1.23, the trajectories of soft (in red, Figure 1.23, a) and stiff (in blue, Figure 1.23, a) capsules of diameter 80 μm. Both trajectories coincide. We analyze the trajectory of 39 soft capsules and 23 stiff capsules and we plotted the angle of deviation in the diffuser β as a function of the diameter D. The scatter plots of soft capsules (in red in Figure 1.23) and stiff capsules (in blue in Figure 1.23) can not be distinguished. At low pressures capsules follow the same trajectory whatever their stiffness. We observe that the angle increases with the diameter. That is consistent with the fact that small capsules are collected in the center when large capsules are collected in external outlets 2 and 3. Regardless of their stiffness, capsules flowing at low pressures can be separated according to their diameter.

Capsules are centered in the channel by the flow focusing module. In the constriction, they flow as close to the obstacle as their size allows it. When the capsule touches the obstacle, $\delta = D/2 + \lambda/2$. The trajectory of a capsule of diameter D in the diffuser should then superimpose with the streamline that is located at a distance $\delta = D/2 + \lambda/2$ from the obstacle in the constriction. Since β increases with δ, as shown in section 1.4.1, it is then natural to get a linear increase of β with the capsule diameter D. These results indicate that the system is able to sort micro-objects from their size but not from their mechanical properties at low pressures. It functions as a standard pinched flow fractionation device [23].

1.4.3 Capsules at high pressure

In this section, capsules are perfused at high pressures (P_{in} = 1200 mbar and $P_{ext} = 4500$ mbar). The pressure ratio (P_{in}/P_{ext}) is kept constant when compared to low pressure experiments. An in-

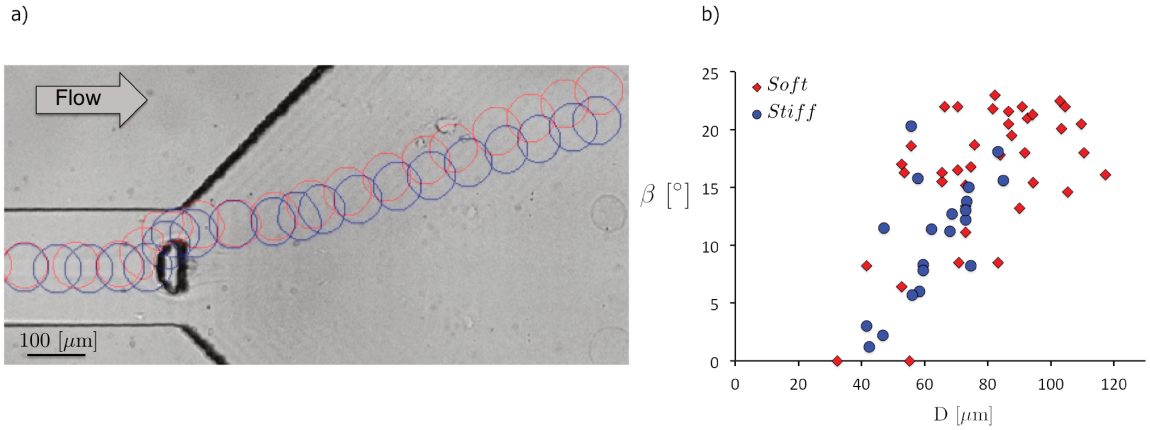

Figure 1.23: **Microcapsule trajectory at low flow strength**. (**a**) Capsule trajectory for capsules of diameter D = 80 μm, and pH 5.9 (resp. pH 8) in red (resp. dark blue) at low pressures ($P_{in} = 200 - 267$ mbar and $P_{ext} = 1000$ mbar). Both trajectories are superimposed. (**b**) Scatter plot of the angle β as a function of the capsule diameter D for soft capsules fabricated at pH 5.9 (red diamonds) or stiff capsules fabricated at pH 8 (dark blue circles).

crease in pressure keeping the P_{in}/P_{ext} ratio constant (constant core width ϵ) induces an increase in the flow rates q_{in} and q_{ext} and consequently in the capsule velocity and forces applied on the capsule when it reaches the obstacle. At high pressures, we found that the capsule velocity is U_{high} = 4.9 $\pm$ 0.4 mm.s^{-1}.

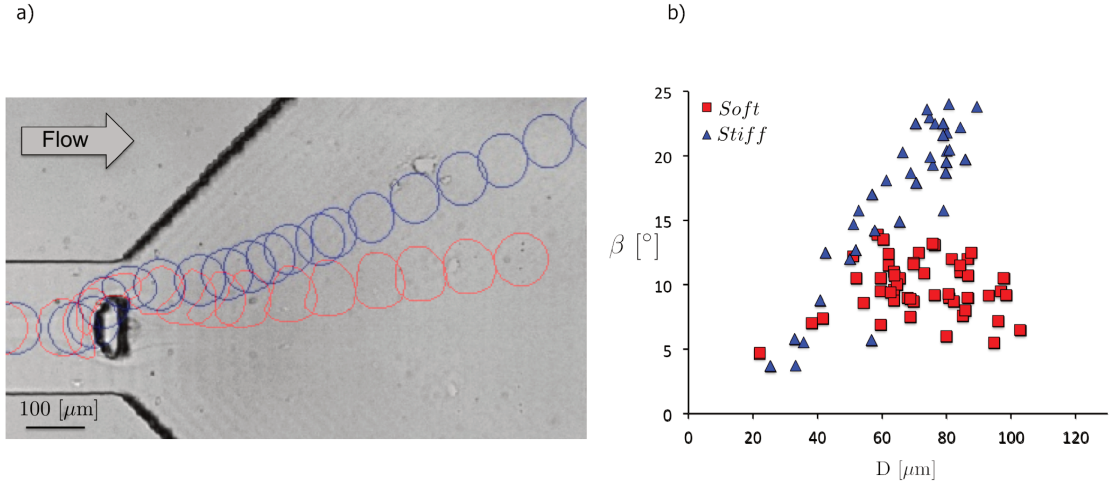

Figure 1.24: **Microcapsule trajectories at high flow strength a**) Capsule trajectory for capsules of diameter D = 80 μm, and pH 5.9 (resp. pH 8) in red (resp. dark blue) at high pressures ($P_{in} = 1200$ mbar and $P_{ext} = 4500$ mbar). (**b**) Scatter plot of the angle β as a function of the capsule diameter D for soft capsules fabricated at pH 5.9 (dark blue triangles) or stiff capsules fabricated at pH 8 (red squares).

We perform the experiments in exactly the same conditions as for low pressure experiments presented previously and we analyze the trajectory of 51 soft capsules fabricated at pH 5.9 and 39 stiff capsules fabricated at pH 8. In figure 1.24 (a), we compare the trajectory of two capsules whose diameter is constant: 80 μm and the stiffness differs. The trajectories of a soft capsule colored in red and a stiff capsule colored in blue, have been drawn. We plot the angle of deflection β as a function of the

diameter D for an entire population of capsules. We can differentiate two behaviors in figure 1.24 (b). Stiff capsule behavior under different pressures is not modified qualitatively neither quantitatively : in figure 1.24 the stiff blue capsule follows a linear trend comparable to low pressures behavior presented before; the slope of this curve is not modified by the increase in pressure. The sorting accuracy is still dependent of the capsule diameter. On the contrary, when pressures are increased, the trajectory of soft capsules is modified: the angle β decreases significantly, and no longer depends on D. When pressures and velocities increase, soft capsules deform more around the obstacle, while it does not impact stiff behavior.

1.5 Sorting principle and parameters

1.5.1 Flow strength and capillary number

Capsules fabricated in two different conditions are flown into the device. We characterize capsule stiffness by the 2D elastic shear modulus of the membrane G_s. G_s is determined with the method of inverse analysis in a previous study [51] (method explained in chapter 3). Capsules fabricated at pH 5.9 have a G_s 2.7 fold lower than those fabricated at pH 8 (Table 1.2). We perform experiments at different pressures to modify capsule velocity and we define the flow strength $\mu_{ext}U$ as the product between the capsule velocity U and the external fluid viscosity μ_{ext}. Low flow strengths do not allow any distinction between soft and stiff capsules (Figure 1.25). But increasing the flow strength enables capsules separation according to their mechanical properties. The angle of soft capsules flatten down around a value of 10° (Figure 1.25).

We then perfuse capsules at fixed G_s and different flow strengths keeping the pressure ratio constant ($P_{in}/P_{ext} = 0.2 \pm 0.03$). For stiff capsules, we notice no difference of behavior whatever the pH (Figure 1.25). On the contrary, for soft capsules, we obtain a decreasing curve with an angle β lower than $24 \pm 4^\circ C$ for each population of capsules whatever their size and velocity. This is consistent with the max angle determined earlier with lycopods. We notice that an increase in flow strength make the angle β decreasing (Figure 1.26). For fixed G_s, capsule deformation only occurs at high flow strength, the trajectory depends on capsule velocity and flow strength. That suggests a competition between elastic and viscous forces. Hydrodynamic forces tend to deform the capsule, while elastic forces of the membrane tend to conserve its initial spherical shape. In a flowing capsule, both effects compete and the elastic non-dimensional capillary number Ca, expresses this competition:

$$Ca = \frac{\mu_{ext}U}{G_s}. \tag{1.2}$$

The capillary number Ca is calculated for each stiffness and each condition of pressure using equation (1.2). An increase in pressure induces an increase in flow strength $\mu_{ext}U$. When the latest becomes comparable to elastic forces, the distance δ between a capsule and the obstacle no longer

Table 1.2: **Perfusion conditions of microcapsules**. Capsules fabricated with different pH are flown with a pressure ratio P_{in}/P_{ext}. The velocity U is measured experimentally, and the surface shear modulus G_s arises from the experiments by Chu et al. [51]. The values of the capillary number Ca are calculated using equation (1.2).

Cond.	**pH**	P_{in} $[mbar]$	P_{ext} $[mbar]$	U $[mm.s^{-1}]$	G_s $[N.m^{-1}]$	Ca
1	5.9	267	1000	1.0 $\pm$0.1	0.030 $\pm$0.007	0.05 $\pm$0.01
2	5.9	1200	4500	5.0 $\pm$0.3	0.030 $\pm$0.007	0.22 $\pm$0.04
3	8	200	1000	0.7 $\pm$0.1	0.081 $\pm$0.026	0.01 $\pm$0.002
4	8	1200	4500	4.8 $\pm$0.6	0.081 $\pm$0.026	0.08 $\pm$0.02

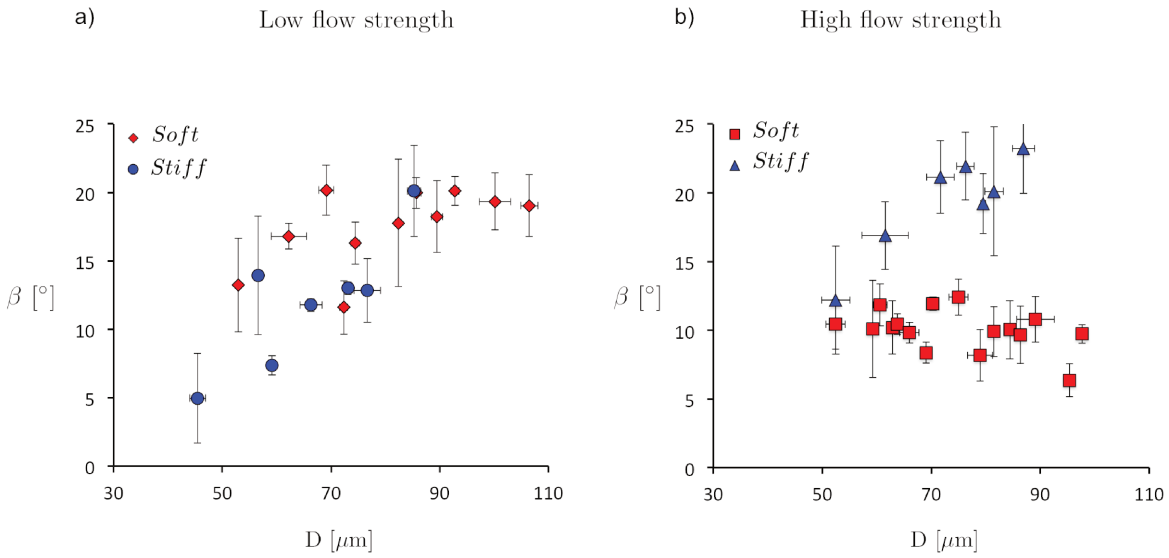

Figure 1.25: **Comparison of soft and stiff trajectories**. The plot represents the angle of deflection β as a function of the diameter, (**a**) at low flow strength, (**b**) at high flow strength. Each point corresponds to a class of 5 μm for capsule diameters between 50 μm and 110 μm. Error bars correspond to the standard deviations.

depends solely on capsule size, but also on capsule stiffness. Deformable capsules are pushed closer towards the obstacle wall (low δ) and end up following the same streamline as smaller objects. Using equation (1.2), we find $Ca < 0.1$ for low flow strength and stiff capsules and $Ca > 0.2$ for soft capsules at high flow strength. It agrees with the literature that reports stiff behavior at $Ca = 0.05$ and soft behavior at $Ca = 0.3$ [44]. Our system allows to sort capsules whose stiffness differs by a factor of 2.7, at high flow strength. But numerical experiments have shown that off-centering modifies capsule behaviors. In the following section we will explain why we can neglect off-centering in our device.

1.5.2 Influence of centering upstream of the obstacle

Increasing the pressures at the entrance of the system increases the flow strength in the channel and the velocity of the capsule upstream of the obstacle. Capsules with different deformability are perfused into the system. When they reach the obstacle, capsules slow down and deform around the obstacle. If the capsule was perfectly centered, it would stay against the obstacle and the deformed shape would result of the equilibrium between the pressure at the rear of the capsule which tend to deform it and the viscoelastic forces of the membrane which tend to keep the spherical shape of the

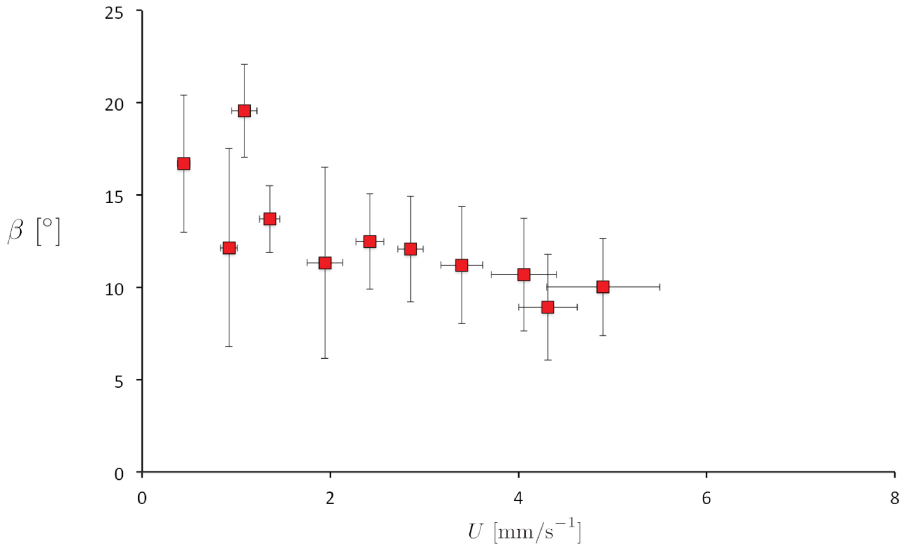

Figure 1.26: **Soft capsule angle as a function of flow strength**. Plot of soft capsule angle of deflection β as a function of capsule velocity in the straight channel upstream of the obstacle. Each point represents a different pressure pair with a pressure ratio P_{in}/P_{ext} of 0.20 ± 0.03.

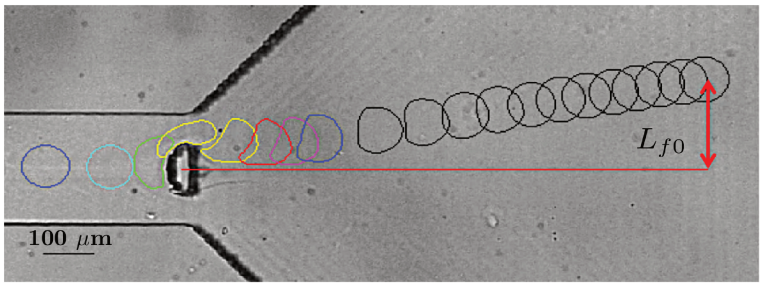

Figure 1.27: **Definition of the distance L_{fo}.** Picture of successive positions of a capsule deforming around the obstacles. Colors help to visualize the shape of the capsule when flowing into the constriction. The distance L_{f0} is the distance between the horizontal axis and the center of mass of the capsule at the end of the diffuser. Scale bar 100 μm.

capsule (equation 1.2). Experimentally, capsules are never perfectly centered on the obstacle and a thin fluid film always remains between the capsule and the obstacle. The parameter of centering is an essential parameter for the trajectory followed by capsules. It plays a role in both deformability- and size-based sorting. We define as off-centering the non dimensional number resulting of the ratio between the distance κ and the capsule diameter D (Figure 1.19 b). The distance κ is defined as the distance between the position of the center of mass γ_c of the capsule in the straight channel and the centerline of the channel γ_0. In this section we will study the influence of the offset on the capsule trajectory.

The trajectory in the diffuser is characterized by two measurements : the angle of deviation β and the final position of the capsule at the end of the linear part of the diffuser. The distance between the center of mass of the capsule at the end of the diffuser and the horizontal axis is called L_{f0} (Figure 1.27). Because it is not possible to have the final position for each capsule, we extrapolate the final

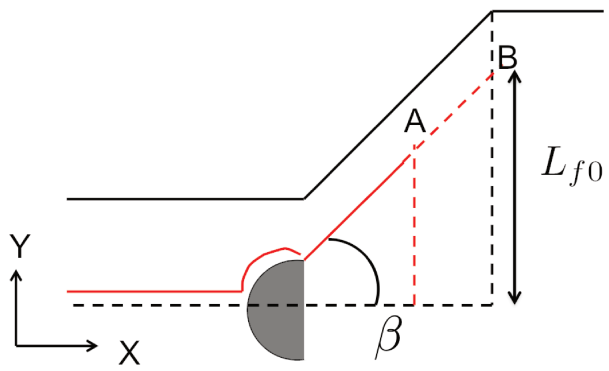

Figure 1.28: **Determination of the distance** L_{f0}. L_{f0} is determined by extrapolating the position B, at the end of the diffuser, of a capsule flowing in the field of view at the position A with an angle β.

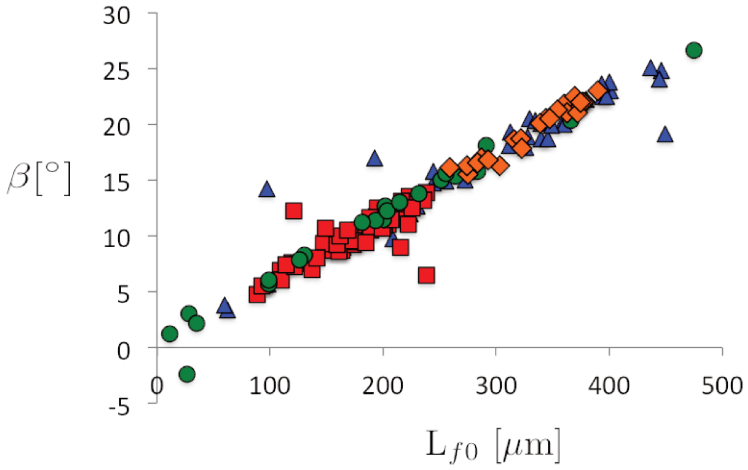

Figure 1.29: **Relationship between the angle β and the distance L_{f0} in the diffuser**. Red squares correspond to experiments performed at high flow strength with soft capsules. Orange diamonds correspond to experiments performed at low flow strength with soft capsules. Green circles correspond to experiments performed at high flow strength with stiff capsules. Blue triangles correspond to experiments performed at low flow strength with stiff capsules.

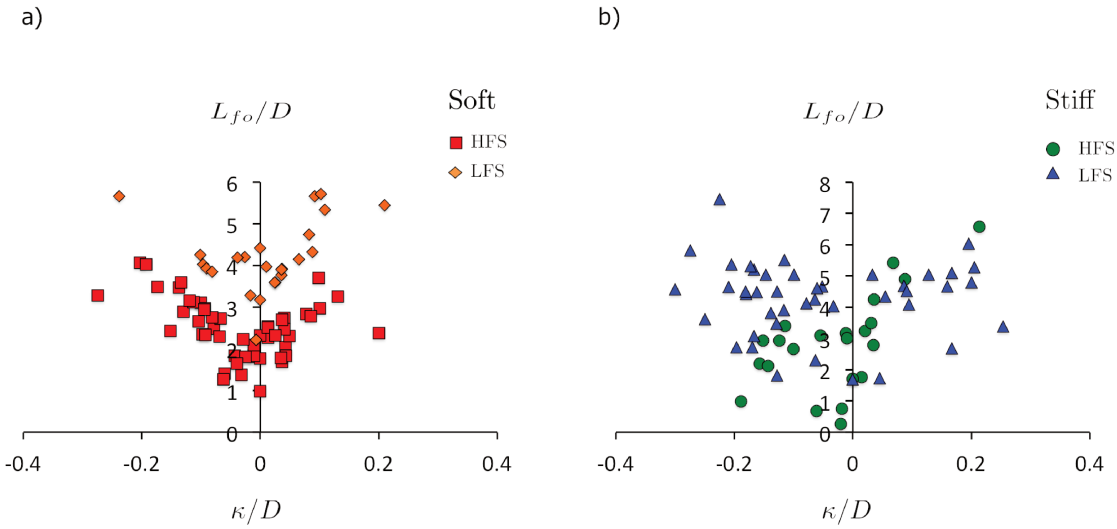

Figure 1.30: **Relationship between the angle β and the offset**. Plot of the distance L_{f0} as a function of the offset κ normalized by capsule diameter D. Negative values of off-centering correspond of capsules flowing down to the obstacle and positive values correspond to capsules flowing up to the obstacle. **(a)** For soft capsules at high flow strength (red squares) and low flow strength (orange diamonds). **(b)** For stiff capsules at high flow strength (green circles) and low flow strength (blue triangles).

coordinates $(x_B\ ;\ y_B)$ thanks to the angle β and a known point coordinates $(x_A\ ;\ y_A)$ (Figure 1.28). The angle β and the distance L_{f0} in the diffuser are related. However the distance L_{f0} gives a complementary information about where begins the linear trajectory. When a soft capsule arrives in the diffuser, it is deformed by the viscous forces and its shape is not round. During relaxation, the capsule gets back to its spherical shape. On figure 1.27 we observe that the linear trajectory of the capsule starts when relaxation is almost completed. The intersection between the linear trajectory of the capsule and the central axis of the channel can either be located before or after the obstacle. With a same angle of deflection a capsule for which the linear trajectory starts further in the diffuser would have a lower distance L_{f0}. Thus the distance L_{f0} takes into account the effects of relaxation of the capsule and the surrounding of the obstacle. We plot in figure 1.29 the angle β of the trajectory as a function of the distance L_{f0} at the end of the diffuser, for soft and stiff capsules, at low and high flow strength. We find that the angle β increases with the distance L_{f0} in a linear manner passing through the origin (Figure 1.29). That means that the modification of the starting point of the linear trajectory does not modify significantly the final position of the capsule in the diffuser. Compared with the total distance of the diffuser (880 μm), the variation of the starting position of the linear trajectory is negligible. Thus relaxation effects do not impact much the trajectory. The characteristic time required for a capsule relaxation is quick and related to the viscosity ratio between the internal of the capsule and the suspending fluid. Measuring the angle of deviation β corresponds to knowing the final position L_{f0}.

In figure 1.30, we plot the final distance L_{f0} as a function of the offset κ, both normalized with the diameter of the capsule D. We can notice that we obtain a "V" shape whatever the condition, resulting of the symmetry of the device. Negative values of κ/D correspond to capsules flowing down to the obstacle while positive values correspond to capsules flowing up to the obstacle. Size effects

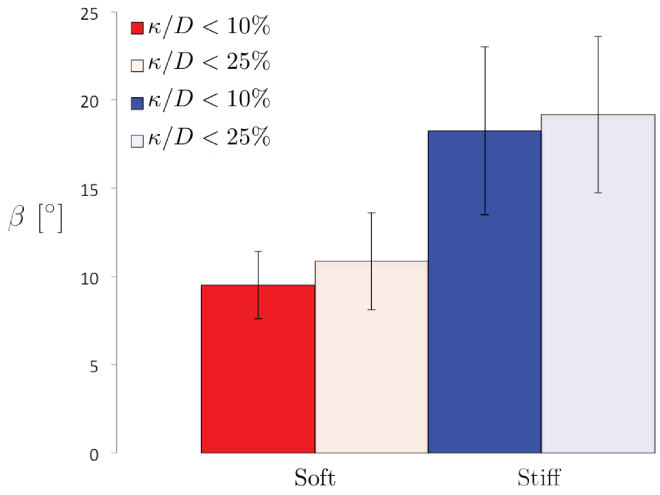

Figure 1.31: **Out-centering effect.** Histogram of the mean angle ± the standard deviation, at high flow strength : for soft capsules with an off-centering lower than 10% (in dark red, n=40), for all soft capsules (in light red, n=51); for stiff capsules with an off-centering lower than 10% (in dark blue, n=12), for all stiff capsules (in light blue, n=33).

are included in the normalization of the axis, which suggests that whatever the size, the trajectory is sensitive to off-centering. A large offset leads to a higher deviation angle whatever the flow strength. For stiff capsules, data from experiments performed at high and low flow strengths are superimposed (Figure 1.30, b). We have seen in section 1.3 that applied pressures control the width ϵ of the core flow. Keeping the external pressure constant and increasing the internal pressure increases the internal flow rate and the jet width. At constant external pressure, the precision of centering is better when the internal pressure is low and the core flow is as thin as possible. But in this case we have a really low throughput and sorting an entire population of capsules is time-consuming. Thus, we have to find a balance between throughput and off-centering. We choose to adapt our pressures to have the width of the core flow ϵ close to the capsule size D.

The flow strength have no influence on the distance δ in the constriction and the distance L_{f0} in the diffuser. That is consistent with the observations we developed in section 1.4. For soft capsules, data obtained at low (orange diamonds, Figure 1.30 a) and high flow strength (red squares, Figure 1.30 a) are distinct but present similar characteristics. In both cases the distance L_{f0} normalized with the capsule diameter D increases with the ratio κ/D, and the symmetry is respected. However, there is no overlap between the two sets of experiments. For a similar out-centering, the distance L_{f0} at low flow strength is always higher than the final distance in the diffuser obtained at high flow strength. This is consistent with the discussion detailed in section 1.4.3. Soft capsules are less deflected at high flow strength, which is traduced by a lower angle β and a smaller distance L_{f0}. The effect of deformability is still present when plotting the distance L_{f0} as a function of the out-centering κ.

In their article, Zhu et al. [44] have numerically noticed the relation between off-centering and the trajectory of the capsule in a diffuser. They have shown that soft capsules were more sensitive to off-centering than stiff capsules. The flow-focusing module at the entrance of the device allows

an off-centering lower than 25% which is enough to sort microcapsules according to their size and deformability, with a good accuracy. We first consider solely capsules with an off-centering of 10% and find an angle $\beta = 10 \pm 2°$ whereas the mean angle for all data is $\beta = 10 \pm 3°$ (Figure 1.31). We obtain comparable values considering the standard deviations. The mean $\pm$ standard deviation of the angle for stiff capsules at high flow strengths is $\beta = 19 \pm 5°$ considering all data (Figure 1.31). Even if the standard deviation is quite large for soft and stiff capsules, there is no overlap. We can consider that with our conditions of pressure, the width of the core flow allows a sufficiently good centering to neglect the effect of off-centering on the angle β.

1.5.3 Influence of capsule position in the constriction

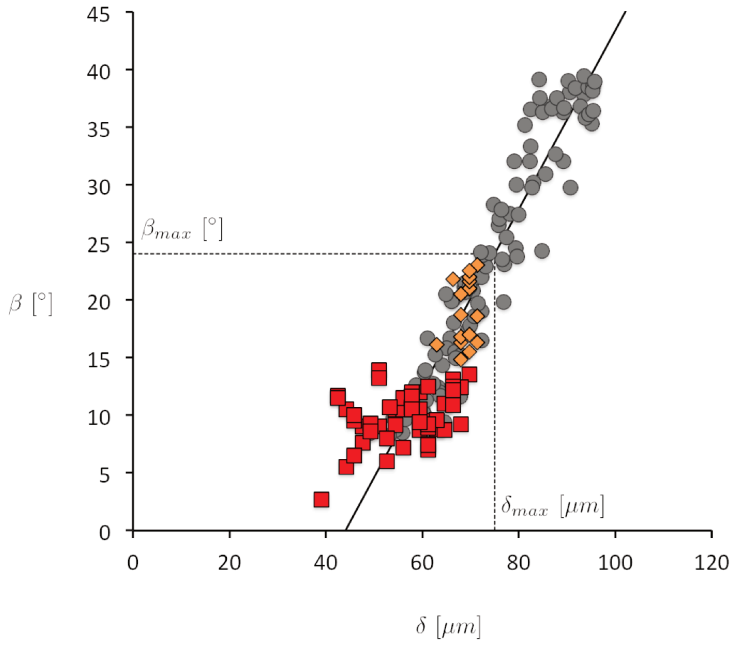

Figure 1.32: **Linear dependency between β and δ for capsules and lycopods and determination of the maximal angle of deviation**. Plot of the deviation angle β of lycopods (grey circles) and soft capsules at low (orange diamonds) and high (red squares) flow strength, as a function of their distance δ from the obstacle in the constriction. For lycopods, data are the same as data already presented in figure 1.21. The solid line represents a linear fit for all the pressure conditions together. The distance δ_{max} is chosen as the distance between the center of mass of a perfectly spherical non deformable micro-object of same diameter as the constriction (50 μm). The angle β_{max} is the corresponding angle for $\delta = \delta_{max}$. δ_{max} = 75 μm, $\beta_{max} = 24 \pm 4$ °. All the capsules have an angle lower than β_{max} and follow the same linear tendency as lycopods.

The capsules used in this chapter have a diameter varying between 50 μm to 110 μm and are thus larger than the 50 μm-wide constriction between the obstacle and the channel wall (Figure 1.19 b). Depending on their size and deformation capsules have different positions in the constriction, and δ vary. We examine here the influence of the distance δ on the angle β (Figure 1.32). The grey circles in figure 1.32 represent the same data as shown in figure 1.21 for lycopods. The fit is realized for all conditions of pressure. Orange diamonds and red squares represent the value for soft capsules perfused respectively at low and high flow strength. We can observe that whatever the flow strength, the angle β as a function of the capsules-to-obstacle distance δ follows the same linear curve for soft

capsules as for lycopods. The only parameter that seems to determine the angle of deflection β is the distance δ. The distance δ only depends on D at low flow strength, when at high flow strength, the effect of mechanical properties is no longer negligible. In order to modify δ we can control the size or the deformation of the capsules.

We already observed that the angle β is linearly dependent of the capsule to obstacle distance δ. The trajectory is limited by a maximal angle β_{max} reached for the largest capsule to obstacle distance δ. We consider a spherical non deformable object of diameter 50 μm. The position of its center of mass is exactly in the middle of the confined zone and we find that the distance between the center of mass and the center of the obstacle is $\delta_{max} = 75$ μm. For a distance δ of 75 μm we find a corresponding angle $\beta_{max} = 24 \pm 4$ °. The precision is given by the standard deviation of the distance of the scatter plot to the linear regression.

We have shown that several parameters influence the position of δ: the capsule size and the deformation of the capsule due to capsule mechanical properties and the flow strength applied. Whatever the flow strength, stiff capsules follow the same trajectory whereas soft capsules are more compressed on the obstacle, deform more and are pushed towards the horizontal axis in the diverging chamber. The angle of deflection β stays the same for rigid capsules and slow soft capsules. When the flow strength increases, capsule velocity U increases, and so does capsule deform around the half-cylinder obstacle, that decreases the distance δ and the angle of deflection β. For an heterogeneous population of capsules whose mechanical properties are unknown, sorting can be realized in two steps. First at low flow strength capsules are separated by size and collected in different outlets. Then the collected populations can be perfused one by one at high flow strength. This time capsules are separated according to their ability to deform around the obstacle. At the end we separate one heterogeneous population of capsules into several populations homogeneous in size and mechanical properties.

Whatever the off-centering stiff large capsules always have the same position δ in the constriction and their angle β tend to β_{max}. But soft off-centered capsules are less deformed on the obstacle than centered capsules because they deform only around a fraction part of the obstacle. Their position in the constriction would then be higher than expected, as well as their angle. We notice that whatever their size, off-centering or deformation, capsules trajectory is controlled by the distance δ. It imposes as the only parameter driving the sorting in our system.

1.5.4 Reproducibility

We perform experiments with populations of capsules with heterogeneous properties of size and stiffness. The objective is to design a sorting device based on deformability capable to sort populations of micro-objects such as capsules and cells. We have shown that we are able to separate microcapsules whose mechanical properties differ by a factor three when the flow strength is high enough to deform the softer population of micro-objects. Capsules used for the determination of the mechanical properties and those perfused into the system are from the same batch but are not the same capsules. We verify the efficiency of our device with several capsules, but never twice with one

capsule.

During his PhD, Edgar Häner used a system with a similar geometry at the millimeter scale [64]. He performed his experiments several times for a single capsule whose mechanical properties and size were highly controlled. In his case, the gap between the obstacle and the wall is 4 mm for a capsule diameter of 4 mm as well. He found that for a single capsule flown in the same conditions, the angle β vary (Figure 1.33). This variability can be explained by the initial off-centering that is the only parameter which vary. For capsules the offset κ is lower than 0.5 mm (i.e. 12.5 %). For gel beads, the initial offset is lower than 1.2 mm (i.e. 30 %). Figure 1.33 shows the results of E. Häner thesis. Individual capsules run into the constriction at a fixed flow rate of $Q = 10$ ml/min. Each symbol corresponds to one capsule. Capsules are ordered in increasing stiffness from left to right. When increasing the force required to deform 50 % of the cell ($F_{50\%}$), the angle β increases and also the variability of the values obtained for the angle β. For capsules of similar deformability (red circles and yellow pentagons), the values of the angle β are similar. That indicates that for an offset lower than 12.5 %, the control of size, and mechanical properties is sufficient to ensure the reproducibility of experiments. However for rigid beads (blue stars), a larger variability in the offset conduces to a larger variability of the angle β. We notice that the green diamonds are three times less deformable than the yellow pentagons and present no overlap of their angles β. It appears that this difference in stiffness is the lower needed for sorting.

The reason why gel beads are less centered than capsules is still unknown. In his thesis E. Häner makes the hypothesis that deformable capsules migrate to the centerline. Due to their deformability, the flow pushes them in the center, which reduces the variability of offset and as a consequence of the deviation angle β. He concludes that for an ideal very well controlled case it is needed to: separate capsules whose stiffness differs at least by a factor three; and have a negligible out-centering effect when compared to the deformation effect. This is consistent with our experiments performed with capsules whose surface shear modulus differs by a factor three and we demonstrate that deformation is much more significant than the off-centering effect.

1.6 Conclusion

We have shown that the trajectory of a capsule flowing in our microfluidic sorter depends on capsule size and deformability. We have demonstrated that capsule sorting based on deformability and size can be achieved experimentally by using the same device at various flow rates. The present device allows us to separate and collect capsules at different outlets after sorting. It is based on the capsule ability to deform around an obstacle and to follow different trajectories depending on capsule size and stiffness.

We have demonstrated that the angle β is only determined by the distance δ between the center of mass of the capsule and the obstacle. The distance δ is influenced by several physical parameters such as: capsule size and mechanical properties, flow strength and off-centering. At low flow strength, the microcapsules are weakly deformed around the obstacle. Thus, the distance δ only depends of the

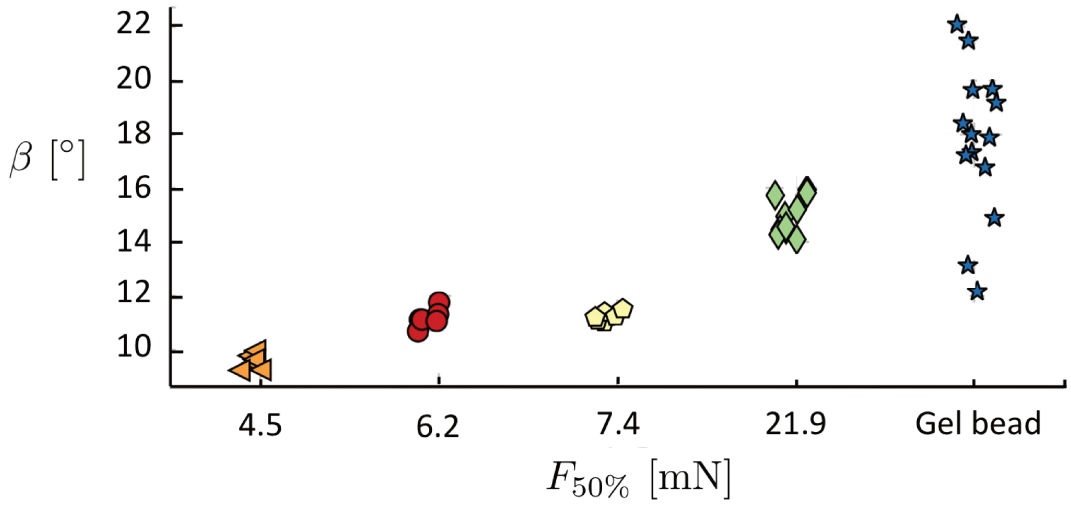

Figure 1.33: **Reproducibility on single millicapsules**. Each symbol corresponds to one single capsule perfused several times in the same conditions of flow strength (Flow rate $Q = 10$ ml/min). The four capsules and the gel bead have a diameter of 4 mm. Capsules initial offset is $\kappa < 0.5$ mm and gel bead initial offset is $\kappa < 1.2$ mm. Image adapted from [64].

size. In the constriction, the center of mass of small capsules is closer to the obstacle than the one of large capsules. At high flow strength it also depends on deformation and off-centering. In order to only sort capsules according to their deformability we need to avoid size and off-centering effects. We demonstrate that thanks to the flow-focusing allowing a core width ϵ on the range of capsule size, off-centering effect is insignificant when compared to size and deformability. In order to prevent size effect, a deformability-based sorting at high flow rate can follow a previous size-based separation at low flow rate, in the desired size range. We are able to separate capsules whose stiffness differs at least by a factor 3.

This is the proof that we have developed a versatile, multipurpose sorting microsystem based on a really simple design. When compared to other existing sorting devices, we demonstrate the sensitivity of our device to sort micro-objects with small size and stiffness contrasts. As these experiments were conduced for rather large capsule dimensions, we developed miniaturized devices adapted to sort heterogeneous population of cells, and help diagnosis of inflammation stage or cancer, and cell differentiation.

Chapter 2

Cell sorting

Contents

2.1 Introduction

2.1.1 Cells: definition and applications

Cells are natural complex capsules. Their membrane is a lipid bilayer enclosing a viscoelastic core, the cytoplasm, made of a liquid environment, the cytosol, and compartments such as the nucleus and organelles. Each component has a specific role in the organization, and the structure of a cell under mechanical stimulations and at rest. The cytoskeleton, mainly composed of intermediate filaments, actin filaments and microtubules (Figure 2.1) is not static. It organizes its structure, shape and motion to adapt to its environment. It is responsible of the mechanical properties of cells and their motion on 3D physical environments such as: bones, vessels, muscles; and performs tasks at the microscale. Characterization of cell mechanical properties is described in chapter 3.

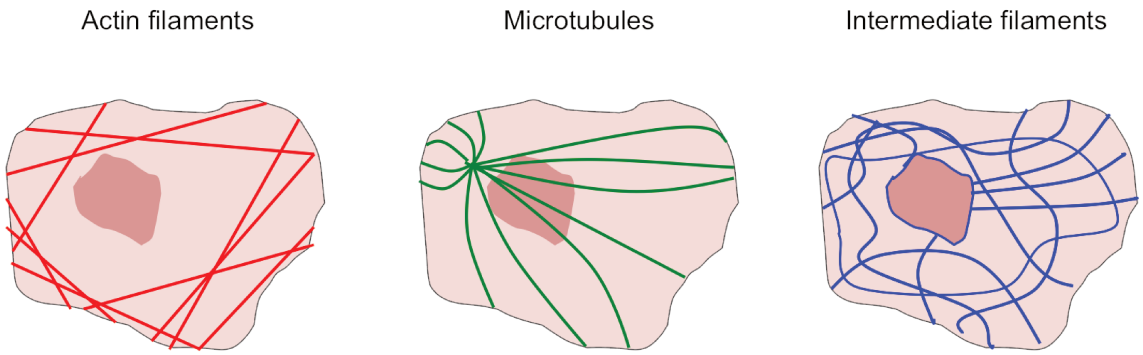

Figure 2.1: **Structure of the cytoskeleton**. Actin filaments (in red) are organized mostly close to the plasma membrane. Microtubules (in green) have an original center called centrosome. They are stiffer than actin and intermediate filaments. Intermediate filaments (in blue) are made of proteins and are located in the cytoplasm. The nucleus is colored in dark pink.

We distinguish two main groups of cells: adherent and circulating cells, whose structure and functions differ. In this study we only focus on circulating cells. Their physicochemical properties depend on their function and their differentiation stage. For example, during their differentiation, MK grow in the bone marrow and become able to extend protrusion in the blood vessels and release platelets (Figure 3). When a vessel is damaged, platelets activate: their shape and structure change to adhere and clog on the lesion [65, 66]. However, an alteration of shape, size and/or mechanical properties can also be the consequence of diseases. That is the case of some invasive cancers [67–69] such as ovarian cancer that softens cells and leads to metastasis formation. Isolating and sorting cells is a powerful tool which enables to study individual cells independently of their heterogeneous initial structure (blood, tissue, bone). Several applications such as: drug treatments, diagnosis and fundamental research on a specific cell type, require cell sorting. In this chapter we review existing sorting devices. Then we present two generations of a microfluidic device aiming at sorting cell suspensions, and inspired from the capsule sorting device presented in chapter 1.

2.1.2 Cell Sorting Methods

Conventional cell separation methods include centrifugation, flow cytometry, fluorescent-activated cell sorting (FACS) and magnetic-activated cell sorting (MACS). Some of them are downscaled in microfluidics in order to reduce costs and volumes. However, microfluidic devices are not always the miniaturization of existing system. The variability of design possible leads to many different devices. We distinguish active methods based on external forces such as electric field, magnetic field, or ultrasounds; and passive methods using the object intrinsic properties such as size, shape and deformability.

Conventional cell sorting devices

Centrifugation

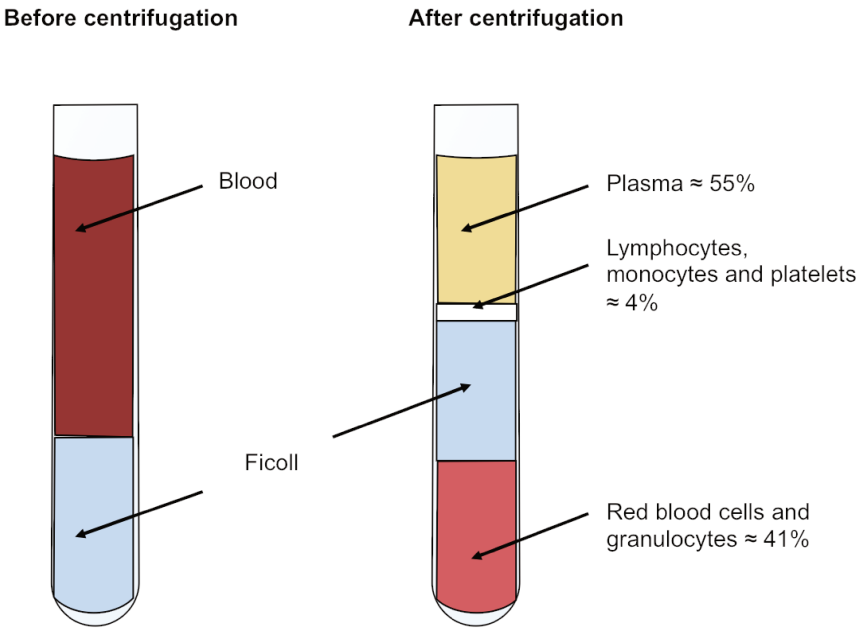

Figure 2.2: **Centrifugation**. Blood is placed on a Ficoll solution. After centrifugation blood cells are separated according to their density. Red blood cells are aggregated by the Ficoll solution and sediment as well as polynuclear cells such as granulocytes. Lymphocytes, monocytes and platelets are at the interface between the Ficoll and the plasma which stays on the top layer and can contain remaining platelets.

Centrifugation principle has been described in 1948 by Lindahl [70] to sort yeast cells. It is a technique of separation based on the difference of density of an heterogeneous population of cells. The method starts to be used extensively in the seventies [71, 72]. Nowadays centrifugation is routinely used in clinic to separate blood cells [73]. For instance, a hydrophilic polysaccharide namely Ficoll is usually used to extract peripheral blood mononuclear cells (PBMC). Several milliliters of whole blood is placed on the top of the Ficoll solution whose density is larger than plasma density. After gradient centrifugation we can distinguish several layers, each corresponding to a category of cells (Figure 2.2). Red blood cells are aggregated by Ficoll and sediment in the bottom of the tube with granulocytes. PBMC are collected just on the top of the Ficoll layer. Plasma that is less dense than cells stays on the top. Depending on centrifugation velocity platelets are located in plasma or in the same layer as PBMC. It is then possible to separate the different layers with a pipette. Isolated PBMC are widely used in research and toxicology as they are involved in the immune system. Centrifugation has already proven its efficiency to separate the different blood cell types, and is used in routine in hospital.

Flow cytometry and fluorescence-activated cell sorting

In flow cytometry, cell suspension run through the cytometer, with an hydrodynamic focusing, in a small nozzle thanks to a faster external sheath fluid (Figure 2.3). Thus cells are flowing one by one in a single line in direction of the laser. The suspension of cells can contain fluorescent cells and non fluorescent cells. As a cell passes through the laser beam, all cells scattered light are measured by two detectors : in front and side respectively called forward scatter detector and side scatter detector. These two detectors respectively determine cell size, and granularity from optical properties of the cell. In fluorescent flow cytometry experiments, additional channels collect and quantify the light

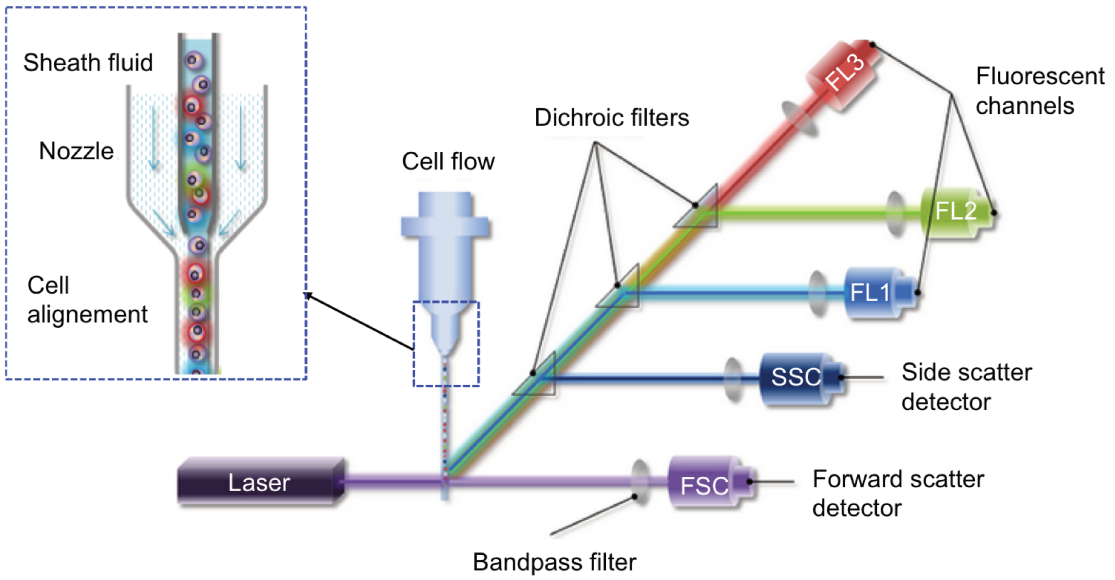

Figure 2.3: **Flow cytometry**. Cells flow through a narrow nozzle which allows them to pass one by one in front of the laser. Front light scatter is detected by the forward scatter detector (FSC) while side scatter light is detected by the side scatter detector (SSC). Several fluorescent channels detect fluorescent signals of different wavelengths. When cells are fluorescent labelled, the fluorescent signal is detected by those channels. Image adapted from Sino Biological website [74].

intensity emitted by cells in different wavelength ranges. It is then possible to analyze the initial sample by the presence or absence of fluorescence corresponding to the positively or negatively protein stained at the surface of the membrane.

Fluorescence-activated cell sorting (FACS) is a special type of flow cytometry. Its specificity is its ability to sort cells in several containers according to their light scattering and the fluorescence emitted. The detection of scattering and fluorescence works exactly the same way as in a flow cytometer. The main difference is that flow cytometer is used to measure the fluorescence signal whereas FACS aims at sorting cells according to their fluorescent properties. It uses the analysis of the fluorescence signal to collect the different populations of cells instead of wasting the sample (Figure 2.4). When the cell passes through the laser, its fluorescence is detected and analyzed by the software. At the exit of the nozzle, vibrations produce droplets containing one cell as a maximum. An electrical charge is applied to the droplet depending on the value of its fluorescence signal and the predetermined threshold. Then the charged droplets flow between two metal plates charged to form a strong electric field which deflects charged droplets into the containers. Finally, droplets of homogeneous populations are collected into several containers.

The main drawback of the flow cytometry is the time needed to sort cells. Also, the limit between positive and negative cells on a scatter plot is determined by the operator which can generate some errors. Nonetheless, it is a great method to separate a large amount of cells and analyze a population qualitatively.

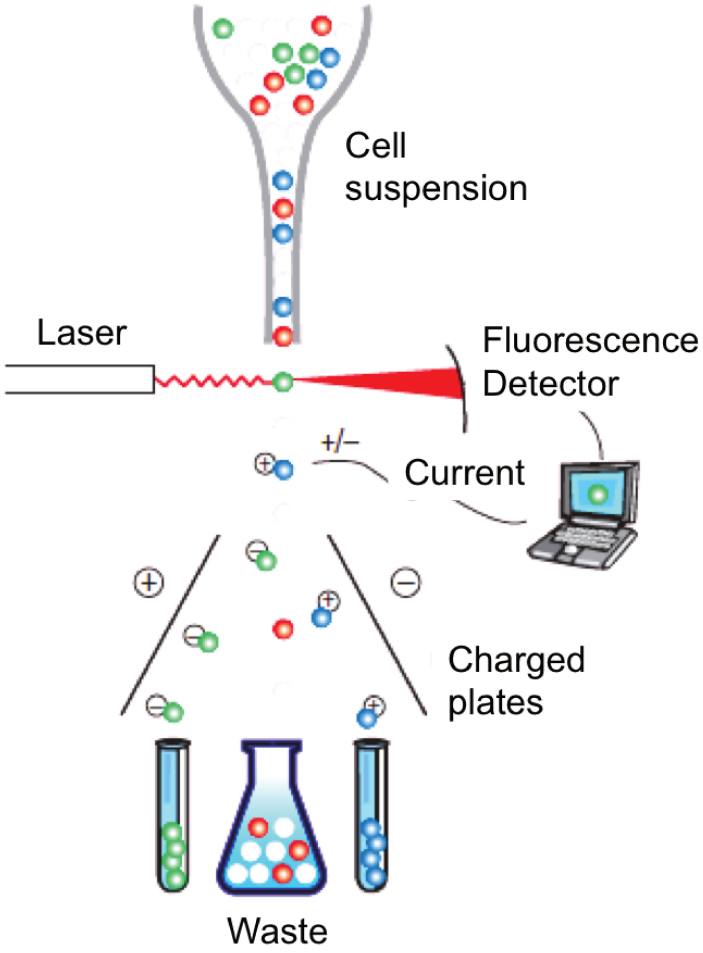

Figure 2.4: **Fluorescence-activated cell sorting**. Stained cells are detected one by one by a laser. At the extremity of the nozzle, droplets containing one cell are formed. The emitted signal is detected by the computer and converted into digital data. A current is applied to the droplet depending on a threshold value. Then the charged droplets flow between a pair of charged metal plates (in opposite signs). Thus droplets are deflected depending on their charge and collected in various containers. Image adapted from [75].

Immunomagnetic cell sorting

Immunomagnetic cell separation is a technique where cells are labelled with magnetic beads instead of fluorescent molecules [77]. Magnetic beads are first coupled with antibodies and mixed with the cell suspension. The targeted population of cells is thus labelled with magnetic beads and can be trapped on the wall of a column placed inside a magnet (Figure 2.5). Unlabelled cells trajectory is not modified by the magnetic field and cells are directly eluted and collected in a reservoir. Targeted cells remained in the column are collected by removing the magnetic field.

Many biomedical applications are using this technique to isolate and purify a sample. For example, $CD34^+$, the progenitors of hematopoietic cells, are first isolated from cord blood using immunomagnetic technique [78]. Other applications are studied for diagnosis [79] and therapy [80].

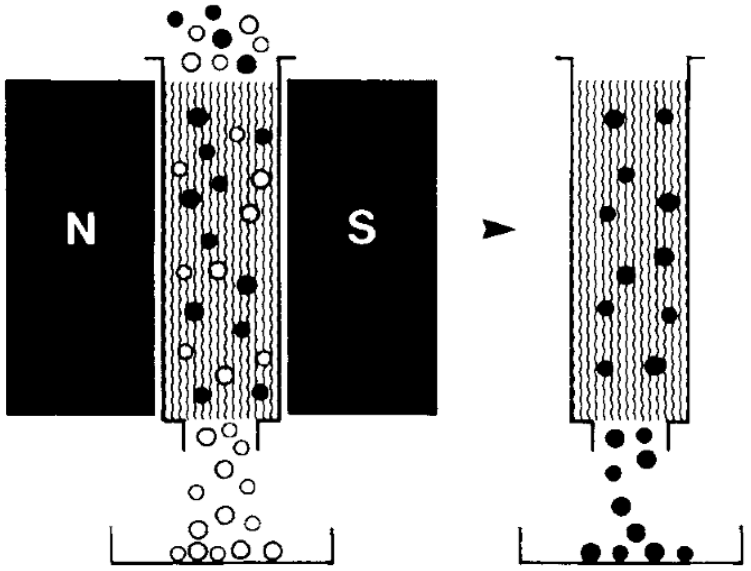

Figure 2.5: **Immunomagnetic cell sorting**. A high magnetic field is applied in a column placed into a magnet. Cells labelled with magnetic beads (in black) will be trapped on the surface of the column while non labelled cells (in white) are flown indifferently through the column and are collected in a container. Removing the magnetic field induces the elution of the cells magnetically labelled, in another container. Image from [76].

Magnetic-activated cell sorting (MACS) is a technique faster than FACS because cells flow through the magnetic column at a larger flow rate than through the cytometry nozzle. However, as FACS, it requires expensive antibodies and a large amount of cells.

Miniaturization of the conventional techniques

For all the techniques presented, the volume of cells required for sorting is about some milliliters. Miniaturization is developed for applications that do not require the manipulation of a large amount of cells. For this reason, FACS and MACS principles have been miniaturized to save volume of cells and antibodies needed. Thus they are specific techniques able to accurately separate single cells with a minimum costs. Miniaturization is an interesting tool for research and clinical applications such as diagnosis.

Fluorescence-activated droplet sorting

In microfluidics, the miniaturization of FACS is often called fluorescence-activated droplet sorting (FADS). Droplet sorting is studied for many applications, not only cell sorting. The aqueous phase can contain DNA [81], molecules, proteins [82], or bacteria [83] in order to encapsulate and sort them. It presents many applications [84] for drug delivery, diagnosis, and chemical reactions including polymerase chain reaction (PCR) [82, 85]. The principle is always based on the detection of a fluorescent signal coupled with the application of a certain electric field.

In FADS, cells are first encapsulated in monodisperse emulsion droplets. Usually, an emulsion of water in oil droplets is produced with a monodisperse range of sizes from 5 μm to 120 μm [86]. Then the fluorescence emitted by the sample is converted by the software on an electric field depending on

the threshold previously determined by the operator [87]. FADS presents both advantages of FACS and microfluidics since it manipulates single cells with a high accuracy (false positive error < 1 in 10^4 droplets), in small volumes (< 1 nL) and is cheaper than FACS as it uses less antibody [88].

Microfluidic MACS

MACS can be used in column as presented earlier or in microfluidic chips. An inhomogeneous magnetic field is applied in the perpendicular direction of the flow. The external field induces a vertical displacement of cells that can then reach a proper outlet. The force decreases with the distance and has to be large enough to manipulate magnetic beads or red blood cells into the system and force them to reach one or the other outlet [89]. The only cells that do not need any label are red blood cells. The presence of hemoglobin make them naturally magnetically sensitive [90, 91]. In the microfluidic device, it is possible to sort more than two populations of cells presenting different magnetic properties. Their position in the diffuser and then the outlet where they are sorted is driven by the magnetic field. In the column it was not the case, the magnetic field trapped the magnetic beads. To sort more than two populations of cells, successive experiments were required.

Other microfluidic techniques

Acoustophoresis cell sorting

Acoustophoresis is a continuous technique where particles migrate with ultrasounds [93]. In an acoustic standing wave field suspended particles or cells are affected by acoustic forces. An ultrasonic transducer is placed underneath the chip (Figure 2.6). The forces applied perpendicularly to the flow direction may lead to particle movement if the acoustic properties of the particle differ from the surrounding medium. Depending on their size, their density, their deformability and the fluid compressibility, cells will not have the same response to frequencies. In a channel, pressure antinodes are on the wall while pressure nodes are in the center of the channel when fundamental mode is applied.

The method is suitable for cells as well as particles [94]. Depending on their density and the frequency modulation, particles are centered in the channel or move following the antinode pressures. Pertersson and coworkers have separated red blood cells from lipids with an efficiency greater than 95 % [95]. Red blood cells (RBC) are centered in the channel in the nodes while the lipids are close to the wall in the anodes pressure. In a microfluidic device the flow is laminar. Thus, the particles remain segregated even after leaving the acoustic field. Then it is possible to collect them in different outlets [96].

For many years, standard acoustophoresis was used to separate cells and particles [96] but cell sorting was limited by a low separation efficiency and a low sensitivity of the system. That was mainly due to short acoustic forces distances. Ding et al. [97] develop a method based on acoustic forces but increasing the separation efficiency by oriented the acoustic waves with an angle. They demonstrate their ability to isolate MCF-7 breast cancer cells from white blood cells. However, acoustic properties of white blood cells and MCF-7 overlap and the system can be improved. Recently,

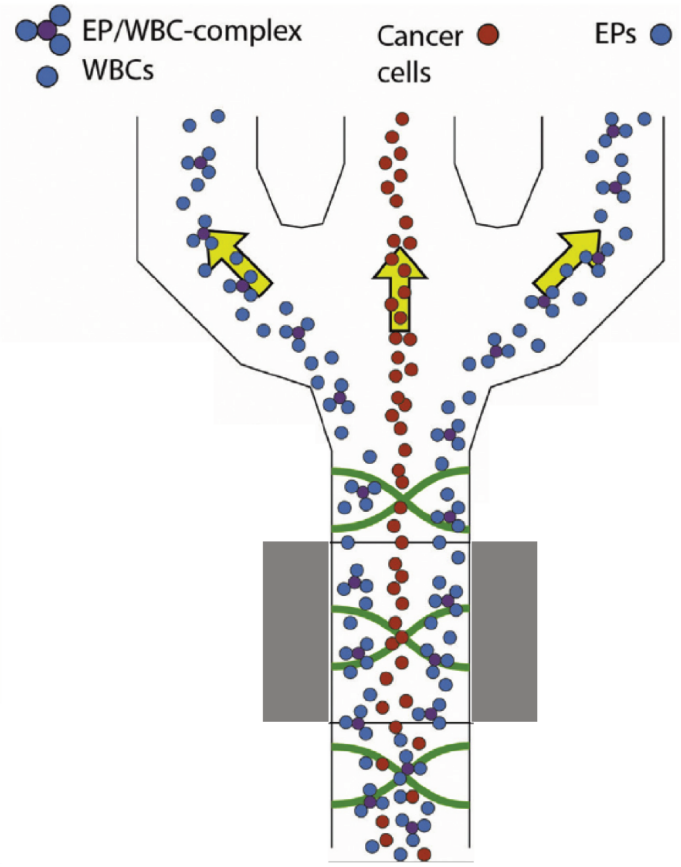

Figure 2.6: **Acoustophoresis**. Continuous acoustic separation according to density. Elastomeric particles coated with CD45-antibody specifically bind to white blood cells to form clusters. Circulating tumor cells flow along the pressure nodes and can be separated from clusters that are flowing in the anti-nodes pressures. Image from [92].

Cushing et al. [92] propose to add elastomeric particles coated with anti-CD45 in order to form white blood cell clusters (Figure 2.6). They reach a separation efficiency of 98.6 % with MCF7 that is promising to reduce the white blood cell environment in further circulating tumor cell sorting.

Passive methods

Passive methods have already been detailed in chapter 1 for microcapsule sorting, and are still applicable to cell sorting. We present here some techniques combining several principles of sorting.

Passive-active methods

In microfluidics, active principle is often coupled with passive methods of sorting in order to optimize the sorting efficiency and use only one device to several steps of sorting. As an example, figure 2.7 presents a device able to isolate circulating tumor cells (CTCs) from whole blood [98]. The device consists of three different regions. First whole blood is mixed with immunomagnetic beads, designed to specifically bind CTCs. Then cells are sorted according to their size in a deterministic lateral dis-

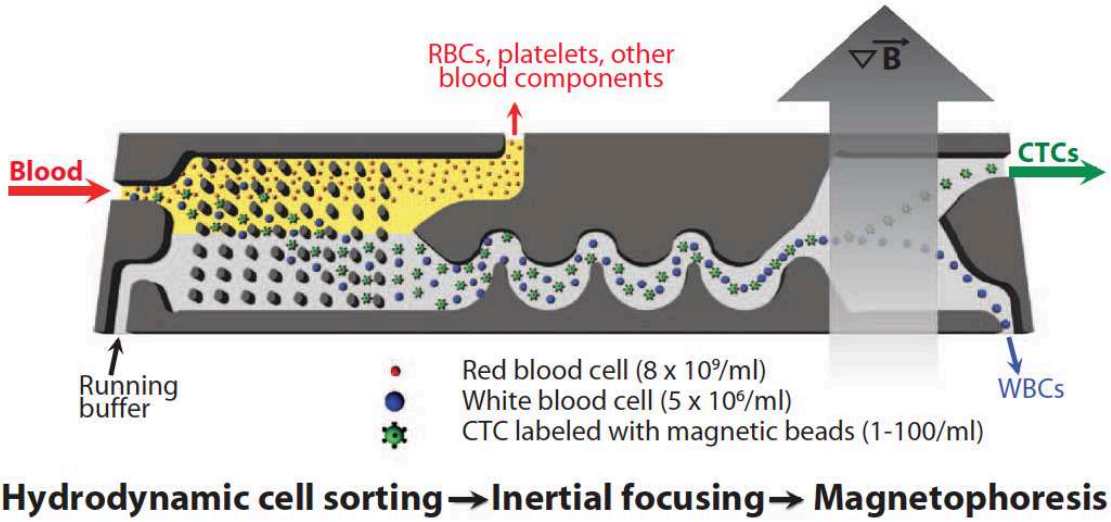

Figure 2.7: **Device coupling deterministic lateral displacement, inertial forces and magnetophoresis**. Principle of experimental sorting to isolate circulating tumor cells. Blood is first mixed with immunomagnetic beads that specifically recognize circulating tumor cells (CTCs). Whole blood is perfused into a lattice which separates cells according to their size. Small cells such as red blood cells and platelets are collected in an outlet while white blood cells and CTCs join a second region of the device. In this region cells are centered thanks to an inertial force in a non-symmetric wavy channel. In the last region, an external magnetic field is applied. CTC trajectory is modified by the field and they reached the more resistive outlet. White blood cells that are not sensitive to the magnetic field are separated from CTCs. Image from [98].

placement region. RBC and platelets that are small in comparison with other cells are collected in an outlet. Only large cells (white blood cells and circulating tumor cells) stay in the system and are centered into the device using inertial forces. Then the channel widens and a magnetic field is applied. The trajectory of CTCs is modified by the magnetic field and they reach an outlet that can not be reached by white blood cells.

2.1.3 Reasons of the miniaturization of our capsule-sorting device

Active methods have demonstrated their efficiency to separate several population of cells. However, the use of antibody can modify cell behavior and prevent the sample to be used again after sorting. It can change cell configuration and modify its initial properties. These drawbacks are not negligible and it appears to be necessary to sort cells with more reliable technologies.

In chapter 1, we presented a review of passive sorting methods based on capsule size or mechanical properties. The advantage of this device is mainly its sensitivity to sort capsules whose mechanical properties only differ by a factor three. Blood cells are a natural example of capsules since they have a core encapsulated by a membrane. They naturally present different sizes and deformability due to their functions. Some diseases alter cell response to mechanical stimulation. In the case of malaria [108, 109], the presence of a parasite inside the cells, called *Plasmodium falciparum*, induces a modification of stiffness. Stiff red blood cells deform less in the capillaries which disturb blood flow. Another disease of red blood cells is sickle cell disease [110]. In this case a mutation of hemoglobin leads to its

Table 2.1: **Summary of sorting techniques**. The table is adapted from [93, 99]

Method	**Separation parameters**	**Method**	**Advantages**	**Drawbacks**	**References**
Centrifugation	Density	Passive	High purity efficiency (99.9 %)	Requires a large volume of cells (some ml)	[71, 73]
DLD	Size Deformability	Passive	High yield efficiency High throughput (350 μl/h)	Fabrication challenge, requirement of many high resolution obstacles	[100, 101]
PFF	Size Deformability	Passive	No clogging	Low throughput (300 μl/h)	[24, 102]
Inertial microfluidics	Size Deformability	Passive	High throughput (10^6 cell/min, 80 10^3 μl/h)	Long channels required	[25, 103]
Flowing through ridges	Size Deformability	Passive	High throughput	Requires a large size or deformability contrast	[104]
Microfluidic filters	Size Deformability	Passive	High throughput (10^9 cells/min)	Frequent clogging	[105, 106]
Acoustophoresis	Size Density	Active	High throughput (10^8 cell/min) High efficiency to sort particles	Limited separation distance to a quarter of the acoustic wavelength	[94, 95, 97]
Magnetophoresis	Magnetic properties	Active	High throughput (200 μl/min) High efficiency for cell enrichment	Expensive Requires magnetic beads coupled with antibody	[78, 80]
FACS	Size, density, fluorescence	Active	Single cell analysis	Expensive Requires fluorescent molecules coupled with antibody Low flow rate (100 cell/s^{-1})	[75, 83, 107]
FADS	Fluorescence	Active	Single cell analysis Low volume	Expensive	[87, 88, 107]

polymerization and conduces to abnormal shapes and a lower deformability. That causes complications of cell circulation, anemia and can provoke the death of the patient. Other examples concerning white blood cells are studied. Sepsis inflammation [111] modifies cell mechanical properties. When they activate, neutrophils become stiffer [112–115] . On the contrary, in case of invasive cancer, cells can become softer and able to pass between endothelial cells and join the blood circulation [67, 68]. That leads to metastasis formation. Also drug treatments can induce a modification of the mechanical properties. Thus, deformability is an interesting biomarker to help diagnosis [116]. To do so microfluidics is an useful tool. Methods of DLD [100], inertial forces in spiral [103], pinch flow fractionation [102, 117] and constrictions [118] are used to separate RBC from white blood cells, detect rare cells, or circulating tumor cells.

The results given in chapter 1 have proven the ability of our system to sort capsules according to their size and deformability by flowing them into a constriction. With this understanding, we design a new sorting device, downscaled from capsule sorting device, and adapted to cell size. We present in this chapter two generations of devices, the experimental challenges in terms of fabrication and perfusion of each system and the results we get. Sorting cells is a very dynamic subject that is interesting also for industries.

2.2 Material and Methods

2.2.1 Microchannel fabrication

The microfluidic device is fabricated in PDMS. The micro fabrication technique is the same as the one explained in chapter 1 section 1.2.1. Several geometries and dimensions have been tested and we will give information about sizes and design when needed in sections 2.3.1 and 2.3.2.

2.2.2 Cell culture

The megakaryocytic cell line DAMI was isolated from the blood of a patient with megakaryoblastic leukemia [119]. The DAMI cell line has a behavior of immature MK. They grow in suspension, with a doubling time around 24 hours. DAMI cells are cultured in MEM medium (Minimum essential medium, Sigma Aldrich; M4526) supplemented with 10 % of fetal bovine serum (FBS) and 1 % penicillin and streptomycin. Each 2 or 3 days, cells are stained with trypan blue (BT), counted on a Malassez glass. Then cells are diluted in a culture cell flask (T25 Greiner) at a concentration of 100 000 cell/ml in 5 ml. They are then stored in an incubator whose temperature is maintained at 37 °C and 5 % CO_2. Their diameter is between 11 μm and 15 μm.

2.2.3 Cell treatments

In this chapter, we use two types of treatments aiming at modifying cell size or cell mechanical properties. In order to change cell diameter we treat the DAMI cell line 3 days with 40 μM of blebbistatin (BBI). In several wells of a $\times$48 wells plate, each with a concentration of 10^5 cells/ml in a volume of 1 ml. In order to change cell mechanical properties, BBI and cytochalasin D (Cyto D) have

been used on the DAMI cell line. Concentration and duration time of incubation are mentioned when needed. Treatment effect is quantified and discussed in chapter 3.

The day before experiment, a solution of neutral red (NR) is prepared in MEM at a ratio of 1/20 volume. Prior to be diluted in MEM, the NR is filtered in 0.2 μm pores. The day of experiment, half of the population is stained 2 hours with NR and the second half is treated with a drug to modify its mechanical properties (see section 2.2.3). Both are then centrifuged 5 minutes at 200 rcf and suspended together in MEM.

2.2.4 Experimental setup

The microfluidic device is placed on the stage of an inverted microscope (DMIL LED, Leica Microsystems GmbH, Germany). The system is filled with two fluids: the cells suspension and an external fluid. The inlets for cells and for external fluids are connected by the means of thin tubes (PTFE, 0.3 mm ID, L_{inlet} = 70 cm, L_{outlet} = 30 cm) to the cell suspension and buffer reservoirs, where a pressure controller (MFCS, Fluigent, France) respectively imposes pressures P_{in} and P_{ext}. Movies are recorded using a high-speed camera (Fastcam SA3, Photron, USA) whose pixel size is 17 μm. Image analysis is performed with the Image J software.

2.3 Adaptation of the microfluidic system to cell size

In this chapter, we present two generations of cell sorting devices. The first one is an exact downscaled replica of the capsule-sorting device. In parallel, we develop an asymmetric version based on the principle of squeezing cells in a constriction and following their trajectory into a diffuser. In this chapter, we present both generations and describe the challenges associated to each design and the results obtained.

2.3.1 First generation: miniaturization of the capsule-sorting device

In chapter 1, we demonstrated that sorting efficiency depends on the capsule to obstacle distance in the constriction δ (Figure 1.19). The optimal constriction size we find is 50 μm close to the capsules size (around 60 μm on average). Cells are smaller than capsules with a diameter between 11 μm and 15 μm. We first design a downscaled system perfectly equivalent in geometry as the one validated for capsules.

Device geometry

The downscaled device has exactly the same design as the capsule sorting device. Only the dimensions vary. The flow focusing is the same as the one for capsule sorting with a width of 200 μm, as reducing its dimensions would only result in an undesired increase of the channel resistivity. The straight channel downstream of the flow focusing is 3000 μm long and 23 μm deep.

We design three versions on the device by varying only the width of the channel and the obstacle diameter. Dimensions are detailed in table 2.2. The desired constriction sizes are 7.5 μm, 12.5 μm and

Table 2.2: **Dimensions of the downscaled devices of first generation**.

Width w [μm]	**Obstacle diameter λ [μm]**	**Constriction width [μm]**
40	25	7.5
50	25	12.5
50	30	10

10 μm, which approaches fabrication limits in terms of resolution. The smallest dimension feasible with paper photomask is 6 μm with a precision of $\pm$15 μm in 750 mm (Selba website). Because the dimensions are so close to the resolution of the lithography technique, we do not expect this device to be efficient at sorting cells, but we use it to perform preliminary experiments and identify the design parameters that need to be tuned in a later version.

We present in figure 2.8 a channel of width 40 μm, and a half-cylinder obstacle of diameter 25 μm. We notice on the picture that, as expected, the size and shape of the constriction is far from the theoretical geometry. The half-cylinder obstacle is not perfectly centered in the channel which will cause asymmetry in the diffuser and erroneous results on collection of cells. Also the half-cylinder shape is not well defined at this scale.

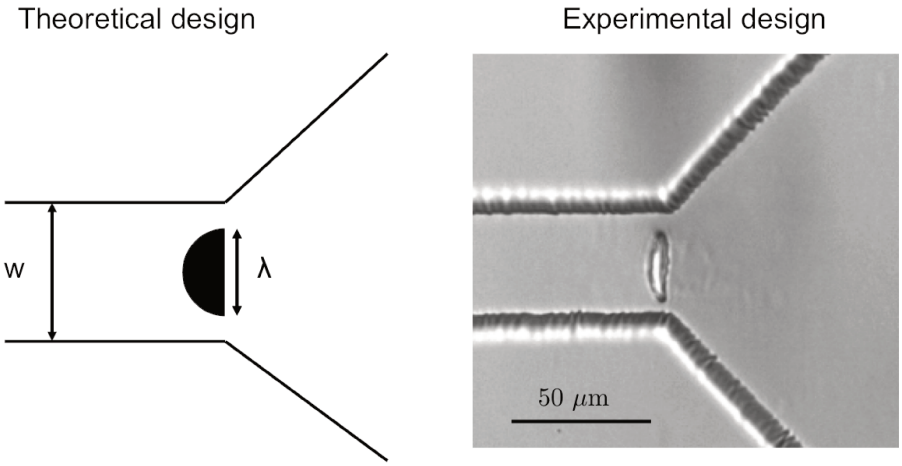

Figure 2.8: **Picture of a downscaled half-cylinder obstacle**. On the left the theoretical design of the channel. Desired dimensions are: width w = 40 μm, and a diameter λ = 25 μm. The constriction size expected is 7.5 μm. On the right, the real geometry. We measure w = 40 μm $\pm$ 2 μm, λ = 20 μm, the upper constriction is 12 μm and the down constriction is 9 μm. The shape and dimensions of the obstacle are far from theory.

Diffusion

Another challenge encountered in the devices from the first generation is the diffusion of the internal fluid into the external one in the straight channel (Figure 2.9). As we work with miscible fluids, diffusion is a non negligible effect. The length of 3000 μm of the straight channel is too long and promotes diffusion. When there is diffusion, the width of the internal fluid is not clearly visible and will lead to off-centering variability. Moreover pressure loss in a long channel is considerable.

In order to reduce both diffusion effect and hydraulic resistivity, we reduce the length of the straight channel.

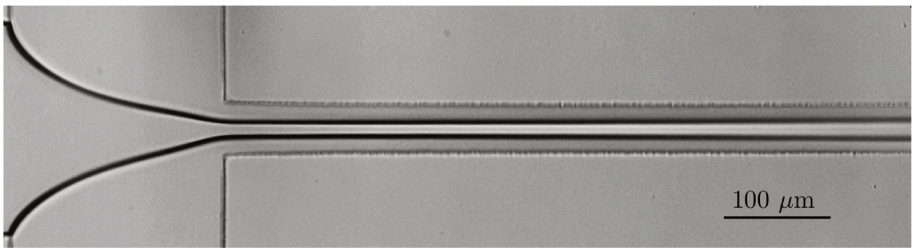

Figure 2.9: **Diffusion**. Culture medium is flowing in an external fluid of 70 % of glycerol. Internal pressure is 600 mbar and external pressure is 700 mbar. The length of the straight channel is 3000 μm. With the length, the two fluids start to diffuse and the interface becomes unclear.

Asymmetry

Figure 2.10 presents the coflow of MEM in a more viscous external fluid. Upstream of the obstacle the internal fluid is centered between the two more viscous layers of fluid, as expected. However, when we observe the flow at the end of the diffuser, we notice an asymmetrical distribution in the outlets (Figure 2.10). The flow is displaced towards the top of the device. Even with a well defined obstacle, the device is not perfectly symmetrical. The asymmetry is small and barely visible close to the obstacle but is amplified in the diffuser. Using the device assuming the distribution is centered around outlet 1 would yield erroneous results. The asymmetry is probably due to fabrication limits. Two reasons are possible: the asymmetry of the mold itself or lack of accuracy during the molding process. Resolution could be improved by using chrome mask for the photolithography; however it is much more expensive than film mask. For preliminary results we were interested to observe cell behavior in such constrictions.

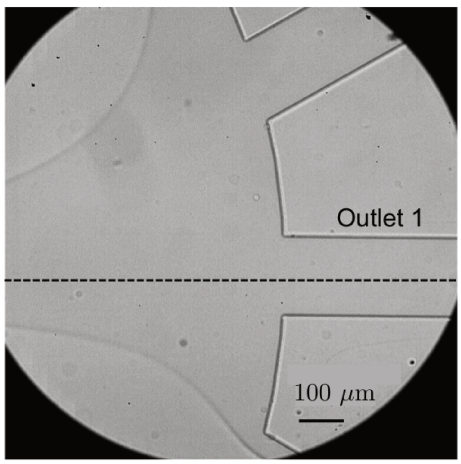

Figure 2.10: **Coflow in a symmetric device**. Picture of the flow shape around an obstacle of diameter 50 μm with a straight channel of width 70 μm. Picture of the same flow at the entrance of the separated outlets. Dashed line corresponds to the center of the channel.

Clogging

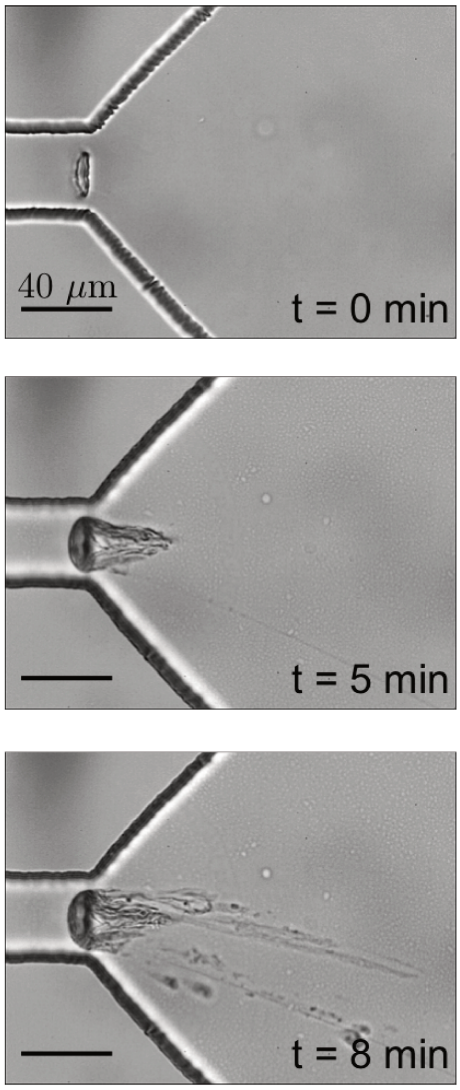

Figure 2.11: **Picture of a constriction clogged by debris**. The obstacle of diameter 25 μm is at the end of a channel of width 40 μm. Cells are suspended in MEM and the external fluid is a solution of PBS. Some debris are surrounding the obstacle and become larger and more numerous over time.

Cells are centrifuged and suspended in MEM not supplemented with serum just before experiment. Figure 2.11 shows a clog formation at a constriction of 7 μm over time. We notice that the downscaled system of first generation is easily blocked during perfusion. At time $t = 0$ min the obstacle is clean, but after 5 minutes some filaments are around the obstacle and after 8 minutes their number increases dramatically. After only few minutes experiments (less than 10 minutes), many debris are surrounding the obstacle. The presence of clogging modifies the flow around the obstacle and will modify cell trajectory and reduce the efficiency of the system. When many debris are surrounding the obstacle they trap other debris and its difficult to clean the device. The flow is disturbed and increasing pressures is not efficient to unblock the constriction since the debris are around the obstacle. Even when the clogging appears only in one constriction, it is difficult to displace it since

increasing pressures increases the flow rate in the bare constriction but increases too slightly forces on the clog. It is often not enough to unblock the constriction. The filaments trapped around the obstacle provide from cell suspension and can be trace of serum remaining after centrifugation and/or the DNA of dead cells.

The symmetric system presents many challenges when using cells. Two of these challenges are directly related to the geometry itself. First, when one of the gap is clogged up or down the obstacle, the streamlines are modified. Increasing the pressure does not increase extensively the forces on the cell clogged in the gap but more fluid goes through the bare gap. This dramatically influences cell trajectories and induces errors in sorting. Second, small imperfections in obstacle centering due to fabrication induces asymmetric distribution of cells in the different outlets. We imagine a device based on the same principle but with an asymmetric profile in order to avoid centering uncertainties.

2.3.2 Second generation: asymmetric device

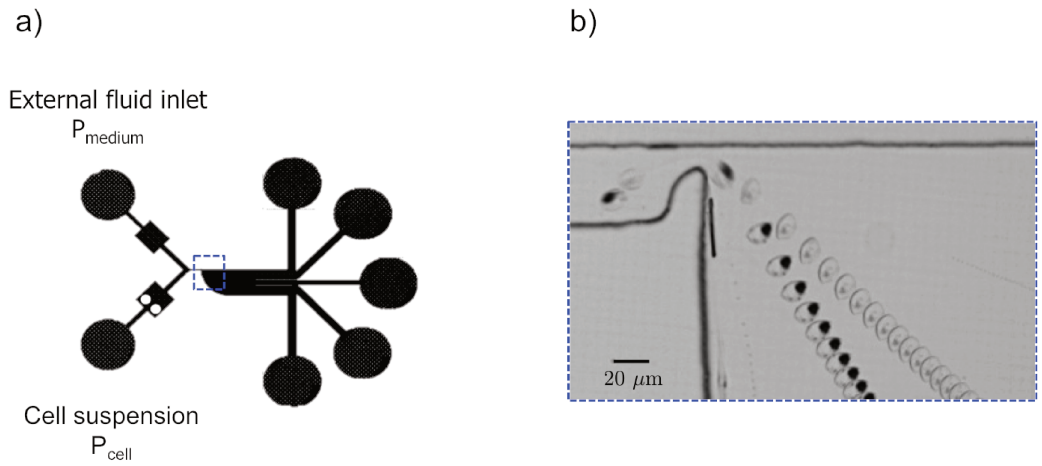

Figure 2.12: **Sketch of the asymmetric device**. The fluids flow from left to right. **(a)** Sketch of the microfluidic device geometry. The system is composed of two entrances one for each fluid in the pinch flow, a diffuser and five outlets to collect cells. The external fluid is perfused at pressure P_{medium}. The cell suspension is perfused in the second inlet at pressure P_{cell}. **(b)** Zoom in the blue delimited area. It is a picture of the constriction at the end of the straight channel. Cells flow into the constriction, and follow streamlines in the diffuser conducing them in the 5 different outlets.

The geometry is presented in figure 2.12. It consists of a pinch flow entrance whose intersection leads to a straight channel of 50 μm width and 27 μm depth. As in the symmetric version, cells are squeezed into a constriction at the end of the channel. Two constriction widths are designed: 13 μm and 20 μm. Cells are flown against a curve which is part of the wall (Figure 2.12 b), instead of the half-cylinder obstacle. An asymmetric geometry presents many advantages. In the absence of an obstacle, we avoid resolution limits we have with symmetric devices. At this scale it is easier to fabricate an obstacle directly on the wall shape than an obstacle inside the channel. Moreover off-centering effects are not limiting the efficiency of the device but asymmetry is used for sorting. The unique constriction prevents problems of off-centering, and unwanted asymmetric flow. Moreover in case of clogging,

increasing the pressures will directly increase the forces applied on the clog and chances to unblock the constriction increase in comparison with symmetric devices.

At the entrance of the system, the flow-focusing is replaced by a pinch flow. The flow is driven in pressure, and we control the width of the fluid containing cells by adjusting P_{cell} and P_{medium} respectively applied to cell suspension and culture medium. Compared with conventional PFF, the narrow constriction allows locally high throughput. Downstream of the obstacle the channel widens and splits into five different outlets to collect cells. In the literature, PFF is known to be a microfluidic technique able to sort micro-objects according to their size, as shown in chapter 1 section 1.1.2. For this reason, we first check the ability of our asymmetric device to sort DAMI cells according to their size.

Cell sorting

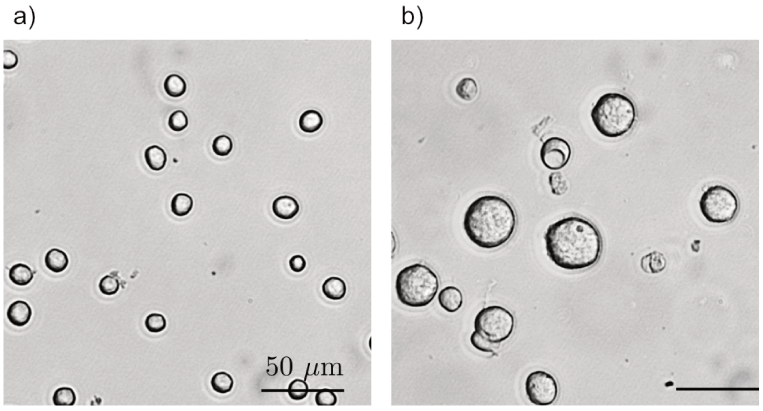

Figure 2.13: **Effect of BBI after 3 days of culture**. **(a)** The DAMI cell line without BBI. **(b)** The DAMI cell line after 3 days treatment with 40 μM BBI.

"

We measure the mean DAMI cell diameter d between slide and coverslip on 102 cells and find $d = 11.2 \pm 1.2$ μm with no cell larger than 16 μm. We use spacers (three layers of tape: final thickness of 0.15 mm) between the slide and the cover slip in order to measure the diameter of non squeezed cells. The cell population is relatively homogeneous in size. In parallel of sorting experiments, Ilyesse Bihi worked on drugs to mimic a mature behavior of the DAMI cell line. He found that treating them 3 days with 40 μM BBI make them become larger (Figure 2.13). Thus we use this treatment for size-based sorting experiments. Prior to perfusion, we measure cell diameter between slide and coverslip on 70 cells and find $d_{BBI} = 23.2 \pm 3.8$ μm with no cell smaller than 16 μm. We centrifuge treated and untreated cells separately, suspend them in MEM culture medium and mix 2 ml of each population at respectively 500 000 cell/ml and 150 000 cell/ml. Prior to perfusion, we measure the size distribution of the cell suspension. We find an average diameter of 16.4 ± 4.9 μm with 75 % of cells larger than 16 μm and 25 % smaller than 16 μm. It corresponds to a composition of 3/4 non treated cells and 1/4 cells treated with BBI, indicating that cell loss induced by centrifugation is negligible. Cells are then flown in the device and collected in the different outlets (Figure 2.14).

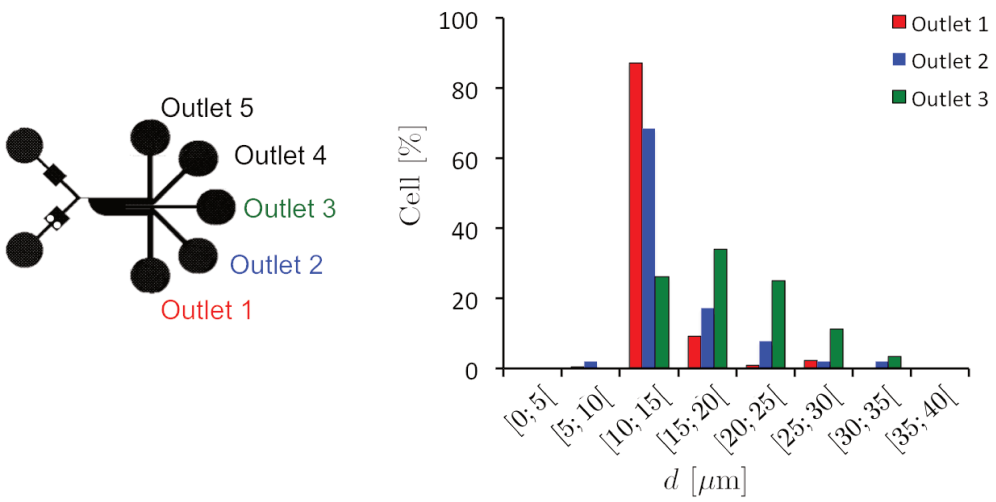

Figure 2.14: **Size-based sorting**. Size distribution of cells collected in the different outlets. Non treated cells (d_{NT} < 16μm) and cells treated 3 days with 40 μM BBI (d_{NT} > 16μm) are perfused into the sorting device. Cells whose diameter is lower than 16 μm are collected in outlets 1 and 2. Cells whose diameter is greater than 16 μm are centered in outlet 3. Outlets 4 and 5 only collect the cell medium.

The perfusions are performed with the following inlet pressures: P_{cell} = 500 mbar the pressure of the cell suspension and P_{medium} = 500 mbar the pressure of the culture medium MEM (corresponding flow rate measured $Q_{cell} = Q_{medium} = 2400$ μl/h). After one hour of perfusion, we scan a droplet of each of the solutions collected in outlets 1, 2 and 3 and measure cell size distribution. Outlets 4 and 5 only collect cell medium. We find an average diameter d_1 = 13.8 $\pm$ 2.6 μm for outlet 1 (in red, Figure 2.14); d_2 = 15.1 $\pm$ 5.3 μm (in blue, Figure 2.14); and d_3 = 19.2 $\pm$ 5.4 μm for outlet 3 (in green, Figure 2.14). We calculate the proportion of cells smaller than 16 μm in each outlet and find 94 % in outlet 1 (n = 227 cells), 81 % in outlet 2 (n = 140 cells) and 37 % in outlet 3 (n = 88 cells) (respectively, cells larger than 16 μm represent 6 % of cells collected in outlet 1; 19 % of cells collected in outlet 2 and 63 % of cells collected in outlet 3).

Size-based sorting principle and efficiency

Cells are maintained as close to the wall as their size allows it by the pinch flow module. DAMI cells used in this part are between 11μm and 35 μm. The constriction is designed to be 13 μm wide and found to be 14.5 $\pm$ 2 μm in practice. Thus depending on their size cells are smaller or larger than the constriction. As detailed in chapter 1, the cell to obstacle distance in the constriction influences the final position of the cell. Smaller cells follow the curved channel wall while larger ones have their center of mass further from the obstacle and follow a trajectory leading to a more centered outlet. We make the hypothesis that the trajectory of cells in the diffuser is the trajectory of the streamline flowing through their center of mass in the constriction. Even if cells flowing in the constriction modify the streamline this hypothesis allows us to predict that small cells, closer to the wall are collected into outlet 1, which is consistent with our experiment (Figure 2.14). Trajectories can no longer be characterized by a single angle measurement since the diffuser has a round shape. The sorting efficiency is now defined as the device's ability to segregate cells in the outlets. We measure a throughput of 60-70

cell/h and calculate the enrichment ratio (ER) as the ratio of DAMI cells (resp. BBI treated DAMI cells) at designated outlets and in the initial mixture: ER = (Cell % in the outlet)/(Cells % in the initial suspension). Cells smaller than 16 μm are enriched by a factors 1.25 in outlet 1 and 1.08 in outlet 2, and cells greater than 16 μm are enriched by a factor 2.52 in outlet 3. This indicates that the system is able to make enrichment. Initial measurements have shown that cells smaller than 16 μm correspond to untreated DAMI cells (resp. cells larger than 16 μm correspond to 3 days BBI treated DAMI cells). Thus, we are able to distinguish two populations of cells whose diameter is different. Large treated cells pass in the centered outlet 3 when small untreated cells are collected in the external outlet 1.

2.4 Conclusion

We have designed and used two generations of devices downscaled from capsule sorting device described in chapter 1. The first generation is symmetric while the second one has an asymmetric geometry. We show that the symmetric device presents many experimental challenges due to fabrication limits and cell clogging during perfusion. In parallel, we design and test an asymmetric version of the system avoiding clogging during one hour experiment. We demonstrate that size-based sorting can be achieved experimentally by using the device.

Sorting cells according to their size is extensively described in the literature. We present here a system of asymmetric pinch flow fractionation easily fabricated with soft lithography technique. It is a passive and cheap system as it does not require any antibody or expensive specific equipment, a pressure controller is enough to carry out sorting. The throughput measured in our device is 60-70 cell/s (i.e. 5 ml/h) which is low for many real applications but high when compared with the literature (300 μl/h, [120]). Also the asymmetry of the device is known to be more efficient than corresponding symmetric geometries [102], and we expect that the obstacle will allow deformation of cells at higher flow strength. In our knowledge PFF is known for size-based sorting but not deformability-based sorting. In comparison with DLD and ridge constricting principles where a lot of pillars or ridges are required for sorting, our design presents a simple geometry easy to fabricate. Also it does not need as high flow rate as systems based on inertia to be efficient.

As these experiment have been conduced with the megakaryocytic cell line DAMI, it will be interesting to test the sorting efficiency with MK from cord blood. Future work is also needed to investigate the ability of the asymmetric device to sort cells according to their deformability, and check if deformability and maturity are correlated. However, we can give some insights based on the knowledge we have with capsule sorting. In chapter 1 we observe that a high flow strength is necessary to deform capsule and induce deformability-based sorting. Experiments on cells have been performed at low flow strength (low viscosity and low cell velocity) and we demonstrated the ability of the system to sort by size. In order to have a chance to sort cells according to their deformability the challenge is to reach high enough flow strength, or modify cell mechanical properties with drugs. Increasing the flow strength can be carried out by increasing fluid viscosity that have to be compatible with cell viability; or increasing pressures applied to make the cell flow faster. Characterization of

cell mechanical properties is required to find a drug able to significantly modify cell deformability. It is discussed in chapter 3.

The cell sorting principle we propose in this chapter to separate mature and immature MK is interesting for many other applications such as improving the diagnosis of sepsis. Sepsis is caused by a bacteria, induces a deficiency of the immune system and can cause the death of the patient. White blood cells are involved in the immune system and activated by infections. During activation, cell organization is modified as well as its deformability. Many studies on neutrophils migration [121] are realized to find sepsis treatments [122, 123] and help diagnosis [124]. The Technology Research Institute (IRT) Bioaster, Paris, seeks to better understand sepsis in order to find new biomarkers [125] and help diagnosis. Our sorting device is a promising tool to respond to their problematic. However, the challenges encountered with our system still need to be solved. Many of the problems mentioned in the chapter have been addressed and are still being addressed in a joined project between UTC and Bioaster called Cellbiom. I contributed together with Bioaster's and UTC's researchers to the supervision of the three students that performed experiments in an improved version cell sorter. As a patent will probably be filed at the end of the Cellbiom project, areas of improvements identified are not presented in this manuscript.

Chapter 3

Mechanical characterization of microcapsules and cells

Contents

3.1 Introduction

Chapters 1 and 2 present a method to sort micro-objects (microcapsules and cells) according to their mechanical properties. In order to know the limits, robustness and efficiency of our device, we want to quantify the mechanical properties of our microcapsules and cells. These properties respectively depend on conditions of fabrication and drug treatments. In this chapter we present a review of existing techniques of characterization in sections 3.1.3 and 3.1.4. Then, we present in section 3.2 the results obtained by inverse analysis for capsules flowing in a narrow straight channel, and the challenges of the method for cell characterization. Finally, we propose in section 3.3 to characterize cells with a tipless AFM adapted to allow global compression of cells.

3.1.1 Mechanical properties characterization

By definition, mechanical properties of an object refer to its resistance to deformation in response to an applied force. When the deformation is small, most materials have a linear response. For elastic materials, the Young's modulus E describes the deformability of a material in simple traction-compression experiments. It is usually defined as the ratio between the stress σ and the strain ϵ ($E = \sigma/\epsilon$). The stress-strain response is directly governed by the force applied to the object. The normal stress applied in this case to the material is called tensile stress (Figure 3.1 a). Another stress namely shear stress occurs by applying a parallel opposite forces on an object (Figure 3.1 b). It is the case of friction for example. We define the shear modulus G as the ratio between the shear stress and the shear strain. For elastic materials the relation between the Young's modulus and the shear modulus is : $G = E/(2(1+\nu))$, where ν is the Poisson's coefficient of the material [126].

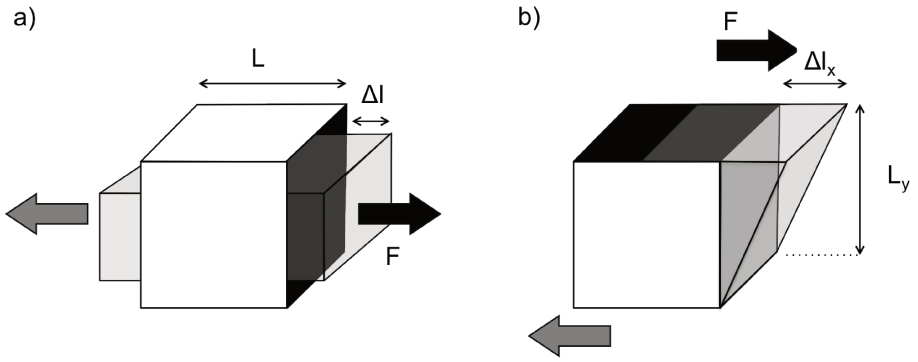

Figure 3.1: **Theoretical deformation of a material submitted to stress. (a)** Determination of the Young's modulus. Normal stress: a force F is applied perpendicularly to the dark surface. The tensile strain is $\epsilon = \Delta l/L$. (b) Determination of the shear modulus. Shear stress: the force F is applied parallel to the dark surface. The shear strain ϵ is the ratio $\Delta l_x/L_y$. Image adapted from [127].

For viscoelastic materials, the stress is no longer proportional to the stain but a notion of temporal dissipation of strain appears. The complex shear modulus is composed of an elastic G' and a viscous G'' modulus: $G = G' + iG''$. Capsules are viscoelastic spherical objects consisting of a core medium enclosed with a thin elastic membrane that protects the internal content from the external environment (chapter 1). The mechanical properties vary as a function of the fabrication principles and the nature of the membrane. Among the most common capsule fabrication processes, there is interfacial polymerization of a liquid droplet, cross-linking layer of proteins and multi-layer of polyelectrolytes. Depending on the function and exchanges with the environment needed, the adapted process is chosen and make the composition and thickness of the membrane vary. In this chapter we present methods of characterization able to determine the Young's modulus E and the shear modulus G.

3.1.2 Cell mechanical properties

Mechanical properties are mainly governed by the cytoskeleton composition of cells. Actin filaments are also called F-actin and result of repeated units of actin proteins called G-actin. They are involved in cell motility and contribute to contraction and adhesion. Microtubules are straight polarized fibers and are used by motor proteins to transport cargos. Intermediate filaments are made of different proteins (keratin, vimentin, and lamins), are present in the whole cell and participate to its integrity. These three components of the cytoskeleton confer their mechanical properties to the cell. However, some researchers are interested in understanding the implication of the nucleus [128] or the membrane [129] in the global mechanical properties of a cell. Thus, they make artificial models to mimic the composition of the membrane or the nucleus and make experiments in the lab trying to reproduce the more effectively as possible the physiological environment. Understanding mechanical properties of single cells is crucial to understand more global mechanical properties as tissue resistance or cells global behavior. Moreover, as presented in chapter 2, some diseases such as malaria [108], sickle cell disease [110], cancer [69] and sepsis [111] induce a modification of cell stiffness.

A lot of tools have already been used to determine cell deformation under stress, but their efficiency depends on the aim of the experiment. Each result in mechanical properties must be associated with the method used. A same cell studied with two different techniques should not have exactly the same Young's modulus value because of the reorganization of the cytoskeleton. In this chapter, we will focus on the characterization of single cell mechanical properties, reviewing the most common techniques. Often, the experiment is combined with a numerical model to define the mechanical properties.

Being able to quantify differences in stiffness is a clue to develop adapted sorting devices. Techniques used to characterize the mechanical properties of capsules and cells can be separated in two groups, leading to global or local deformations [130]. Some techniques such as: compression between two plates, optical stretcher, and microfluidics constriction; give a global knowledge on whole cell mechanical properties. While other techniques such as: microrheology, micropipette aspiration and atomic force microscopy; measure local mechanical properties at the sub-cellular scale. We are discussing limits, advantages and applications of all these techniques. Figure 3.2 summarizes the principle of each technique developed in this chapter.

3.1.3 Global measurements of mechanical properties

Global measurements of the mechanical properties consist in whole cell solicitation. Compression between two plates, optical stretchers and microfluidic constrictions are considered as global techniques because they are constraining the cell in its generality.

Compression between two plates

Compression is a simple way to test mechanical properties of an object. A sensitive force transducer which measures the forces applied as a function of the plate separation is connected to the

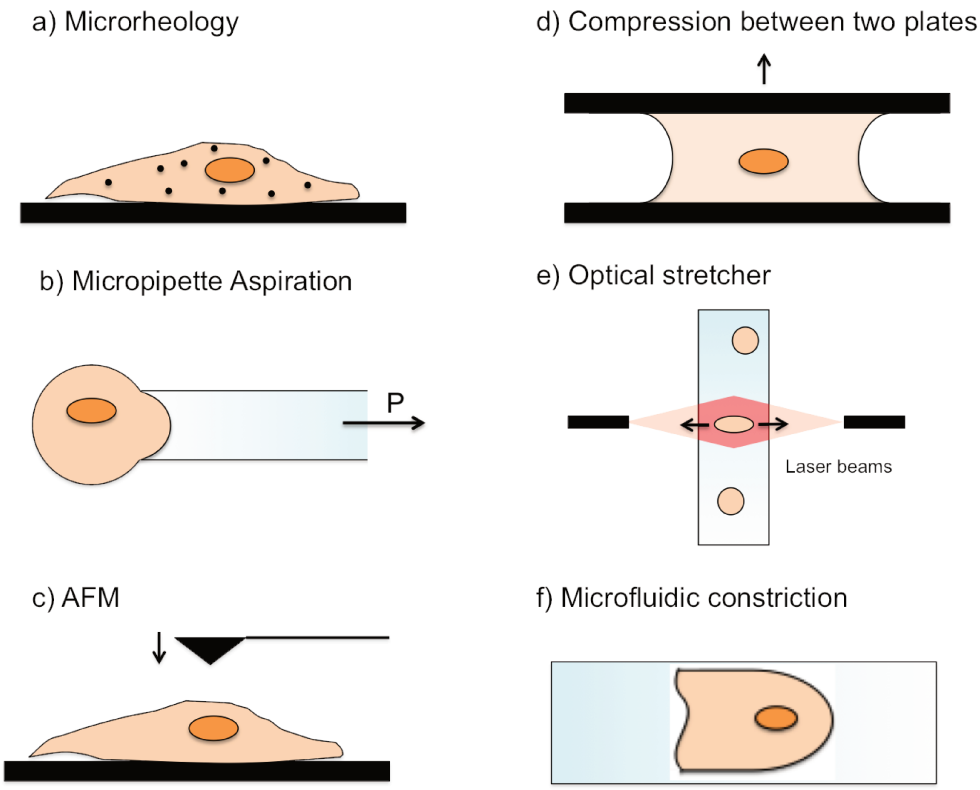

Figure 3.2: **Techniques of mechanical properties characterization.** Techniques commonly used to determine mechanical properties of cells. **(a-c)** Local techniques, **(d-f)** Global techniques. **(a)** Microrheology is based on the displacement of particles tracked in cells by thermal agitation. The viscous properties of the membrane can then be determined. **(b)** Micropipette aspiration consists in measuring cell deformation when it is aspired by the micropipette whose diameter is smaller than the cell. The deformation profile depends on pressures applied and is relied on cell stiffness. **(c)** Atomic force microscopy (AFM) is a technique of indentation. The cantilever deflection depends on cell stiffness. **(d)** Compression between two plates is the first tool we imagine when thinking of mechanical properties. Micro-objects deform between the two plates depending on the forces applied and the deformability of the objet. **(e)** Optical stretcher traps the cell thanks to two laser beams, at high intensity the forces are able to deform the cell. **(f)** Microflow deformation is a passive non invasive technique which consists in flowing micro-objects in a narrow constriction. The shape of the object depends on the ratio between the diameter of the channel and the diameter of the object; the pressures and the viscosity of the fluid.

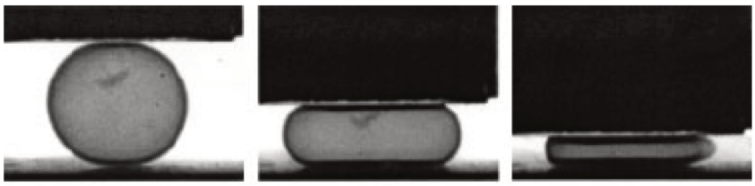

Figure 3.3: **Compression between two plates**. Capsule is compressed between two parallel plates. The deformation to an applied force gives the stiffness of the capsule. Image adapted from [131].

compression setup. It consists of placing the object to characterize on a fixed plate and approach another plate in contact. Squeezing the object with a certain force leads to a certain deformation. Respectively imposing a certain deformation allows to measure the required applied forces. The apparent elastic modulus is related to the deformation, the relaxation time and the forces applied. Thus compression has often been used to study capsule stiffness and rupture [131]. Using the method with

cells in suspension is challenging because they are not immobilized on the surface and can move away from the two plates. Thoumine and coworkers, in 1997, performed cell compression between two plates on fibroblasts [132]. In order to avoid cell to escape, one of the plate needs to be adhesive. That induces cell spreading and induces perturbation on the measurements of mechanical properties and small relaxation time can not be detected. The measurements are sensitive to the microplates surface. Depending on the coating cells response will be different and relied on cell adhesion forces. The responses detected by the sensors will give information on cell mechanics far from its physiological configuration. The conception of devices mimicking the physiological environment of cells is challenging.

Optical stretchers

Optical stretching is a method combining cell trapping with optical tweezers and deformation with a high intensity laser. Optical tweezers is a light-based method to trap and manipulate single cells. In 1986, Ashkin proposed an optical trapping method for dielectric particles by a single-beam gradient force [133]. He trapped dielectric microparticles plunged into water due to the negative pressure of light. This method was promising to allow trapping of small particles, colloids, aerosols and open perspectives on biological trapping. In 1994, Perkins et al. have measured DNA elongation thanks to optical tweezers [134]. They fixed a latex microbead to one end of the DNA string and trapped it with a laser. DNA was immersed into an aqueous solution and elongates into its full extension under a fluid flow. They measured the extension and the relaxation of a single DNA molecule. With this technique, there is no need of chemical or biological molecules to deform the target molecule. Nonetheless, to visualize DNA they used a fluorescent marker. Light and fluorescence could modify the mechanical properties of a molecule or a cell. Also, in this case, optical tweezers are only used on immobile molecules or cells and need an external force to determine the mechanical properties (in the case of DNA the fluid flow gave the force needed to elongation). To deform cells only thanks to light, researchers have developed optical stretchers.

Optical stretcher is a non invasive light based method used to quantify the deformation of cells. It has been developed for the first time in 2001 by Guck et al [135]. The principle is inspired by optical tweezers. The main difference is the use of two lasers unfocused which permit to stretch the cell instead of only trapping it. The two lasers are in the opposite site of the cell and exert forces on the cell in the laser beam axis. The forces arising from the momentum transfer of light to the surface of the cell deform it due to the modification of the refractive index. It gives quantitative results about cell elasticity. Deformability is an intrinsic biophysical marker allowing a label free characterization. Cells do not need any prior treatment before stretching and are deformed with no physical contact. For these reasons it has been used in sorting devices [136], to separate leukocytes from malignant cells. However, an intense light exposure causes cell heating and intensity needed to deform the cells are quite high. Moreover, the relation between deformation, and the forces applied is not direct and needs a lot of mathematical models [137]. The method has proven its efficiency to measure cell mechanical properties and is the only method in our knowledge where the deformation is realized with no physical contact [138], but the throughput is still low on the order of 100 cells/hour. Also, the

method needs a complex experimental fabrication with the presence of optical fibers and the forces applied are weak.

Microfluidic constrictions

Another microfluidic method is based on the use of narrow channels. Cells, capsules or bubbles are deformed by the flow in a constriction where there is friction against the wall. Several parameters are measured such as: the deformation profile of the micro-object, the time spent in the channel, the time necessary to enter in the channel, the difference of pressure between the entrance and the exit of the channel, the hydrodynamic forces, the object velocity and the fluid viscosity. All these parameters are relied on mechanical properties of the fluid, and the object.

Figure 3.4 presents a leukocyte flowing into a rectangular channel. It flows successively through two rectangular constrictions. Analysis of the time to enter and staying into the constriction gives indication on cell stiffness [139]. Stiffer cells stay longer in the constriction than softer ones. And usually, softer cells have a larger elongated index calculated as the ratio between the elongated length of the cell in the channel and the initial diameter of the cell [140]. When the channel widens at the exit of the constriction, relaxation times are measured [118, 141]. The technique allows to easily have quantitative data about speed, time of penetration, relaxation and shape of the squeezed cell in the channel. Based on this principle, Preira et al. [106] develop a gradual filter method with gaps becoming smaller and smaller. The method presents other advantages such as its ability to characterize mechanical properties of a population and not only single cells, in the small volume used during experiments. This is very interesting for cancer diagnosis or other pathologies modifying the mechanical properties of cells such as the acute respiratory distress syndrome [142]. Experiments can give a fast idea about the presence of abnormal cells. In order to improve the technique and being able to quantify cell stiffness, inverse analysis method has been developed with capsules in the laboratory.

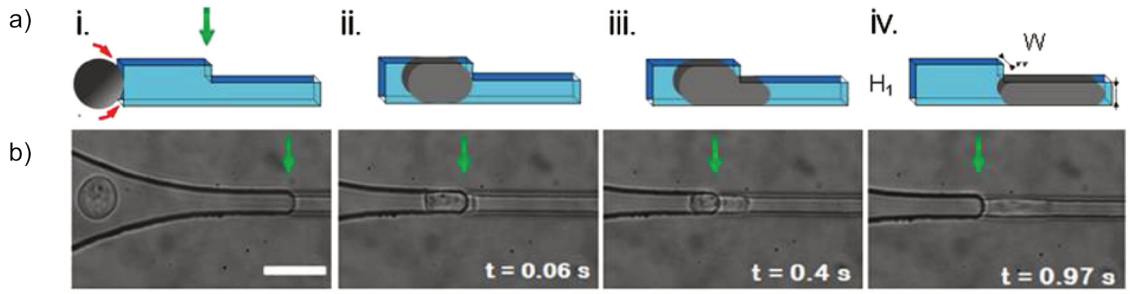

Figure 3.4: **Leukocyte cell passing through a rectangular section**. **(a)** Sketch of the microfluidic device consisting of two rectangular section channels where the second one is narrower than the first one. The green arrow indicates the interface between the two channels. (i) The cell at the entrance of the first constriction; (ii) at the entrance of the second constriction; (iii) The cell starts flowing in the narrow constriction. (iv) Complete entry of the cell into the narrower constriction. (b) Optical images of a cell entering the constrictions. The cell deforms in order to pass through the constrictions. Physical parameters such as entry time, transit velocity and elongation profile are then analyzed. Scale bare 20 μm. Image from [142].

Lefebvre et al. have proposed a method to quantify mechanical properties of micron-sized liquid core microcapsules. The method consists in flowing capsules into a narrow channel of cylindrical or square sections. Capsules are confined into the channel and their shape depends on: the size ratio between the capsule diameter and the section, the velocity of the capsule and the viscosity of the internal and external fluids. The advantage of this method is its efficiency to measure several capsules elastic moduli [143] and among them the surface shear modulus G_s. Simulations are performed to predict capsule behavior in several conditions of confinement and perfusion. The analysis of the shape obtained in square and cylindrical channels have been done by inverse analysis. To characterize the membrane mechanical behavior, the deformed shape of the capsule into the micro-tube is when compared to numerical predictions saved in a database for the same flow conditions as for the experiment. Knowing capsule speed, shape, size ratio, and fluid viscosity, we are able to obtain the capillary number Ca, and the best fit gives the unknown surface shear modulus G_s by the relation: $G_s = \mu U/Ca$. In 2011, Chu et al. have applied this method to the characterization of batches of capsules produced with different conditions of pH [51].

In conclusion, mechanical properties of micro objects as capsules and cells need an inter disciplinary approach. Several techniques exist with their own advantages and drawbacks. The most adapted technique depends on which parameter we are looking for.

3.1.4 Local measurements of mechanical properties

In this section, probes used for local measurements are much smaller than microcapsules or cells. Thus it is possible to make several measurements on the same sample. That can help to demonstrate and understand heterogeneities in a single object.

Atomic force microscopy

Atomic force microscopy (AFM) is a scanning probe microscopy (SPM) as several other methods such as: scanning tunneling microscopy, and scanning electron microscopy. G. Binning et al. [144] have exposed in 1986 the principle of the AFM which is a combination between scanning tunneling microscopy and stylus profilometer. AFM imaging is different from conventional microscopy. A tiny tip of less than 15 nm radius and 20 μm height (Nano World website) is attached to a resilient cantilever. AFM consists of measuring interaction forces between a force-sensitive lever and the surface of a sample. The system scans the sample surface thanks to a piezoelectric platform which moves in 3D, scanning in horizontal directions and adapting the vertical position of the probe as a function of the sample profile to keep constant the distance between the probe and the sample. Interaction between the tip and the sample induces a deflection of the cantilever. This bending is usually detected by the deflection of a laser beam focused on the extremity of the cantilever. The forces applied to the sample are calculated by measuring the deflection of the lever knowing the cantilever stiffness. They are determined by Hooke's law :

$$F = -kz \tag{3.1}$$

where F is the force, k the stiffness of the lever and z the vertical displacement of the bended cantilever. Typically forces are in the range of pico-Newton or nano-Newton for an indentation of order nano-meter to micro-meter. AFM can be used in three different modes : contact, tapping and non contact modes. The result of an AFM experiment is a force-distance curve. The distance is given by the position of the piezo motor and the forces by the deflection of the cantilever.

Tapping mode microscopy and non contact mode microscopy are used to scan a surface and determine its roughness. Tapping mode consists in cantilever vibration with a high amplitude in order to touch the sample during vibration. Non contact mode consists in vibration of the cantilever at low amplitude close to the sample (in the attractive domain). Contact mode allows both the scanning of the surface to define the roughness and the determination of the mechanical properties of a sample. Contact between the tip and the sample induces the deformation of smooth samples.

The microscope is placed in an acoustic isolated box on a vibration-damping air table. The lever is mounted on a solid support called cantilever. Sample and cantilever are mounted on a piezo-electric system allowing to displace them with a nano-metric precision. At the end of the cantilever, there is a dedicated place for a tip. Tips are usually in silicon or silicon nitride, but the size and shape vary with the applications. Most common shapes are the sphere, the cone and the quadratic pyramid as shown in figure 3.5. These shapes do not deform the materials the same way and its crucial to check the shape of the tip before experiments to avoid errors due to a deformed tip. The sphere and the cone are axisymmetric while the quadratic pyramid is not. For an elastic problem considering an elastic axisymmetric probe, the force applied to the elastic surface is given by Hertz approximation. The Herz model is valid for homogeneous, elastic, isotropic materials of thin membrane, with no adhesion between the sample and the tip (of spherical shape) [145]. In 1971, Johnson adapted Hertz model in order to correlate the force of indentation and the Young's modulus [146]. The formula called "Hertz approximation" is:

$$F = \frac{4}{3} \cdot \frac{E}{1-\nu^2} \cdot \sqrt{R_T} \cdot \delta^{\frac{3}{2}} \tag{3.2}$$

where F is the force applied by the cantilever, E is the Young's modulus, ν the Poisson ratio, R_T the tip radius and δ the indentation depth.

For a non-elastic cone, the force leading to the penetration in the elastic body can be resolved with the Sneddon approximation [147]. To find the force applied by a non axisymmetric pyramid on an elastic surface, Bilodeau proposed an approximation assuming no friction and a half-space contact with the surface [148]. The geometry of the tip and the rigidity of the cantilever are chosen based on the expected mechanical properties of the sample to be tested.

At the beginning, AFM was used to determine the surface profile of materials such as metals. It allows to determine smooth surface profiles and non conductive sample profiles. Instead of a diamond needle that was used earlier, the probe is in metal and the sensitivity of the measure is directly linked with its size. The advantage of AFM is the possibility to have a non-contact mode and a tapping mode which avoid the deterioration of the sample. Moreover, AFM is adapted to non-conductive samples

which is not the case of scanning tunneling microscopy.

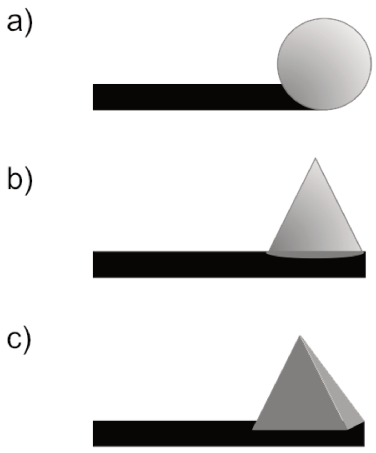

Figure 3.5: **Tip geometries.** AFM cantilever often present a tip which can have different shapes depending of the applications. **(a)** Colloidal probe is used for elastic axisymmetric problems. **(b)** Conic probe is non-deformable and axisymmetric. **(c)** Square-base pyramidal probe allows a non-axisymmetric deformation.

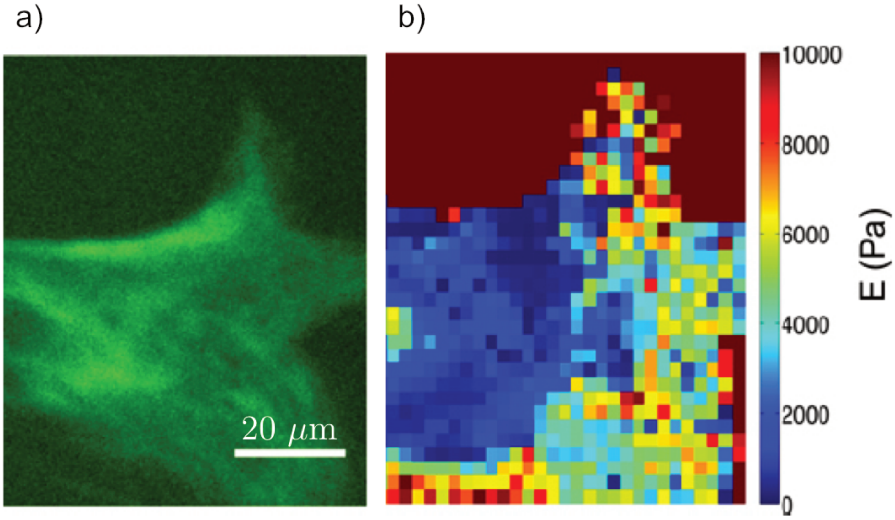

Figure 3.6: **AFM stiffness cartography. (a)** Fluorescent picture of a transfected fibroblast with a GFP vimentin. (b) Stiffness map of the same area of the cell, reconstructed from AFM scan force in a defined area. The stiffness varies inside the cell. Image adapted from [149].

AFM is also used for biological applications [150]. It allows to image biological samples with molecular resolution in buffer solution. AFM enables research on different sample types such as: proteins [151], membranes [152], single living cells [153, 154], cell adhesion [155, 156], nucleus [157], and tissue [158]. It is a sensitive method to study isotropic objects, allowing the detection of small perturbation responses and reconstruct a map of the different stiffness measured inside a cell spreading on a surface (Figure 3.6). However, the necessity to work with attached objects, and the local response of the sample, limit the use of AFM for cells in suspension.

One of the method developed for cells in suspension has been tested with microcapsules commonly used as cell models. In 1991 Ducker et al. [159] proposed a method based on a colloidal probe. It consists in attaching a silica sphere of diameter several micron, namely colloid to a tipless cantilever. It allows a sphere/sphere contact with a surface contact increased (compared with sharp tip) between the probe and the spherical object, reducing the local stress applied [160]. As the surface contact is larger than with sharp tip, the cell moves less between the sphere and the substrate even if not attached. This method has been used to study hydrogel microcapsule stiffness varying the pH [161] or thin-wall biomimetic microcapsules [162]. As well experiments have been performed on chondrocytes, adipocytes and osteoblasts cells in their spherical and spread shapes using a borosilicate glass sphere [163]. However it is still a local measurement and for cells in suspension it is tricky to construct a stiffness map as the cell will probably move between two measurements. Thus other tipless AFM method using a wedge have been developed to measure global deformation of cells and will be described in section 3.3.

Microrheology

Particle tracking microrheology is a quantitative method which can be used in flow in physiological conditions. The method consists in injecting beads into the cytoplasm of living cells [164, 165]. Following the brownian motion of beads inside the cell can be relied on viscous properties of the cell. It consists in measuring the ability of particles to flow, and displace into the cytoplasm as shown in figure 3.7. Here, beads are injected in a wounded fibroblast. In blue beads exhibit a more confined motion than in red. That suggests that their motion is reduced by external forces. The viscosity of the cytoplasm is probably increased in the blue area in comparison with the red one. It is a completely passive method where no forces are aded, allowing local measurements of the shear modulus G. A cartography of the cell viscosity can then be drawn. Bead displacement around 1 nm is tracked in fluorescence and analyzed in terms or viscosity and elasticity in the cytoplasm. That requires a high spatial resolution of the microscope. At this scale following the displacement of single beads is quite difficult. In order to decrease the uncertainty due to interpretation of the bead motion, researchers have developed the two-points microrheology which consists of an algorithm that correlates the motion of bead pairs [166]. To visualize the motion of beads in the cell it is required to immobilize cells. For this reason, blood cells that are in suspension are poorly studied with this method. However some experiments have been performed with neutrophils by immobilizing them in micropipettes [167] to study their viscoelasticity when they are squeezed.

Magnetic twisting cytometry is a variant of microrheology. Instead of using thermal forces to displace particles in the cytoskeleton, magnetic microbeads are attached to the membrane and move by magnetic torques [169]. Displacements are relied on the magnetic field applied [170]. Particle tracking microrheology measures local viscoelastic properties of the cytoplasm while magnetic twisting cytometry is more connected to membrane and cytoskeleton stiffness. Both are adapted to living cells but their applications are limited to soft tissue characterization.

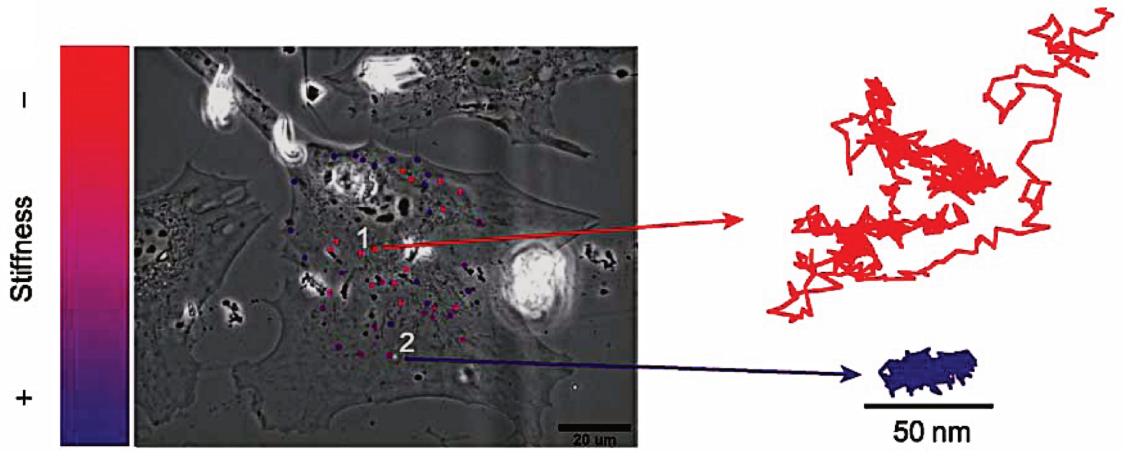

Figure 3.7: **Particle tracking microrheology.** Application of intracellular microrheology in a fibroblast. Microbeads are tracked in fluorescence. The colors points are larger than microbeads diameter to help the visualization. Beads have a Brownian motion depending on the stiffness in the area their are located. In the softer part the beads easily move and the motion is more extended (in red) than in stiffer areas where the motion area is restricted (in blue). Image adapted from [168].

Micropipette aspiration

Micropipette aspiration is a method that has been widely used to measure mechanical properties on living cells. It consists of a partial aspiration of cells into the hole of the pipette, smaller than the size of the cell. A negative pressure gradient is imposed at the end of the pipette. Into the tube the aspired cell part takes a round shape. The length of the cell inside the micropipette is recorded as a function of time [171]. There are different techniques to determine cell or capsule mechanical properties. Using two micropipettes to stretch the capsule in both sides, or using a micropipette on suspended or attached cells. As an example we present in figure 3.8 a neutrophil flowing in a micropipette towards a bead. Depending on the adhesive contact we observe different distances run in the micropipette before cell motion stops. The method is adapted to characterize visco-elastic properties of different object types such as capsules [11] and cells. Neutrophils are found to have a viscous behavior whose surface tension is about 30 pN/μm and a cytoplasm viscosity around 100 Pa.s. Other cell types such as chondrocytes and endothelial cells have a solid like behavior due to their function and an elastic modulus of 0.5 kPa has been measured [171].

The volume of the cell protrusion in the tube, is related with the aspirating pressures applied and allows the access to cell mechanical properties. This method has been largely used to study amoeboid migration [130], and neutrophil stiffness after treatment with cytochalasin B (CytoB). Non treated neutrophils have been found to have a cortical (surface) tension of 268 $\pm$ 12 mN/m, while CytoB 30 μM treated cells have a cortical tension of 135 $\pm$ 7 mN/m. CytoB 30 μM also decreases cell cytoplasm viscosity by almost 65 % [173]. Another application consists in quantifying the single-cell forces of pushing and pulling forces of T-lymphocytes during activation and determining the variation of Young's modulus over time [174]. The Young's modulus is measured by indentation each 10 seconds with a small bead while the cell is in contact with another bead. At rest the cell Young's mod-

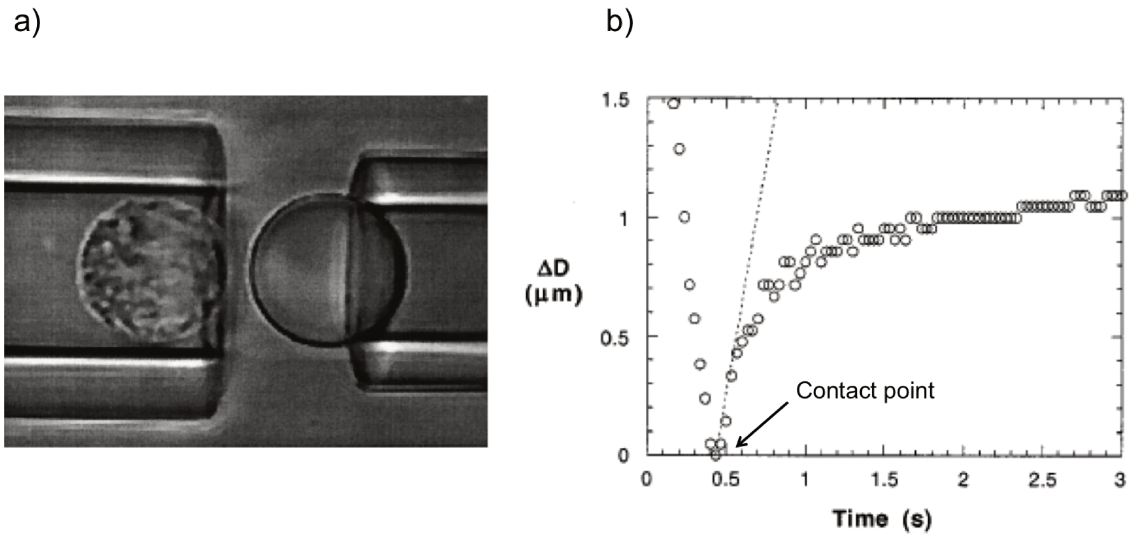

Figure 3.8: **Micropipette aspiration**. **(a)** On the right a bead is fixed on a micropipette. On the left a neutrophil is flowing through another micropipette. **(b)** During the first 0.5 s the cell approaches the bead. The cell flow towards the bead until contact (the distance ΔD between the bead and the cell is 0 μm. Here, either the cell freely moves back in the micropipette (dashed line) or adheres to the bead. Adhesion makes the motion cease after a while around an asymptotic value. Image adapted from [172].

ulus is measured at 128 $\pm$ 16 Pa. After contact the T-cell activates and its Young's modulus reaches 292 $\pm$44 Pa. Many models exist to analyze cell deformation and determine mechanical properties. Historically, linear viscoelastic half-space analytical model were used [175]. However, analytical methods assume that the cell is infinitely large and undergoes slight deformation, which is not the case in micropipette aspiration where the cell deformation is large. Using the finite element method [176], take into account the real geometry of cell, boundary conditions and lead to more accurate predictions of cell deformation than those of analytical methods [177].

The advantages of the method are its high versatility, the possibility to be in liquid and the ability to apply low forces on suspended or attached cells. However, it requires expert operator as the experiment preparation and realization takes time and formation to place all the micropipette aligned in a petri dish [178].

Atomic force microscopy as well as micropipette aspiration are limited by the size of the probe. The number of cells analyzed by time unit is quite short because of the time needed for indentation (resp. deforming capsules under pressure).

3.1.5 Methods used for our application

We need to characterize the mechanical properties of capsules and cells in order to separate them according to their mechanical properties. Chapter 1 and chapter 2 present a sorting method based on the ability of objects to deform in a constriction. Capsules flowing in our sorting systems undergo large, global deformation over very short time scales (a few milliseconds). That is the reason why

Table 3.1: **Summary of techniques for mechanical properties characterization**. All methods presented are compatible with living cells. We summarize here advantages, and drawbacks of each method. The parameters measured are the Young's modulus E, the shear modulus G, the surface shear modulus G_s and the viscoelasticity μ.

Method	Measured parameter	Advantages	Drawbacks	References
Microrheology	E [Pa] G′ [Pa] G″ [Pa]	High frequency (up to 100 kHz) Passive method	Only for soft materials (G « 100 Pa) Not adapted for suspended cells	[165][166]
Micropipette aspiration	E [Pa] μ [Pa.s]	Adapted for non linear deformation measurement Adapted to adherent and suspended cells High forces range (10 pN to 10^4 nN)	Limited by the pipette diameter Low throughput Modeliazation needed to access force profiles	[171]
AFM	E [Pa] μ [Pa.s]	Quantification of the elastic modulus High spatial resolution (depending on the tip geometry) Large range of forces (100 nN to 1 μN)	Low scanning speed Low throughput	[144][150] [153][179]
Compression	E [Pa] μ [Pa.s]	Large range of forces (around 100 nN), Uniaxial deformation	Low throughput	[131][132] [180]
Optical stretcher	E [Pa] μ [Pa.s]	No physical contact with the sample Non destructive Adapted to suspended cells	Low throughput (100 cell/h), High power of the lasers (500 mW) Limited choice of wavelength, Local heating of the cell Modeling needed to access force profiles	[181][135]
Microfluidic constrictions	G_s [Pa]	Quantification of the shear modulus, Global deformation, High throughput (10 000 cell/h)	Limited by the high speed camera frequency Limited by numerical models	[143][182]

global measurements are really interesting in our case.

Among all the existing techniques described earlier and summarized in table 3.1, local deformation techniques will give completely different information than global techniques. The deformation we get in our sorting devices is a fast global deformation. We want to characterize capsule mechanical properties in the closest configuration as the one in the sorting device. Among global techniques, optical stretching is well adapted to understand intrinsic mechanical properties of the micro-object with no contact. In our case, the contact with the wall and the obstacle can modify capsule and cell

mechanical properties. In order to quantify the properties of our micro-objects, the two methods that seem the most appropriate are the flow in microfluidic constrictions available in Compiègne, and the micro-plate compression.

In the following sections, we present two methods to characterize microcapsules and cells. In section 3.2 we describe the characterization for microcapsules using inverse analysis for capsules flowing in straight cylindrical constrictions. We measure the velocity of cells in rectangular straight channels. Quantitative measurements are more challenging for cells than for capsules. In section 3.3 we characterize cell mechanical properties using a tipless AFM method, for several drug treatments.

3.2 Microfluidic constrictions

3.2.1 Material and methods

Device geometry and fabrication

Capsule device

The microfluidic device consists of a glass tube of internal diameter 75 μm (Beckman Coulter). The tube is inserted in another glass tube of internal diameter of 400 μm in order to be connected with silicon tubes (Figure 3.9). Silicon tubes are then connected to the perfusion setup. In order to fix the position of the glass tube, the whole system is placed in a small Petri dish of 12 cm of diameter. Then it is embedded into cross-linked PDMS.

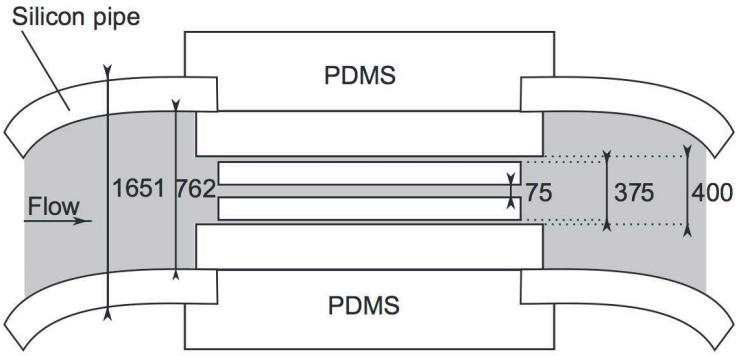

Figure 3.9: **Microfluidic channel with a circular constriction**. Schematic of the cylindrical microchannel setup to be connected to the perfusion system. Image from [51].

Cell device

The microfluidic device consists of two chambers of height 30 μm connected to each other by a rectangular straight channel in PDMS of width w = 10 μm, length L = 3000 μm and height h = 14 μm as shown in figure 3.10. The diameter of inlet and outlet holes drilled in the chambers is 0.75 mm. The PDMS fabrication technique is described in chapter 1.

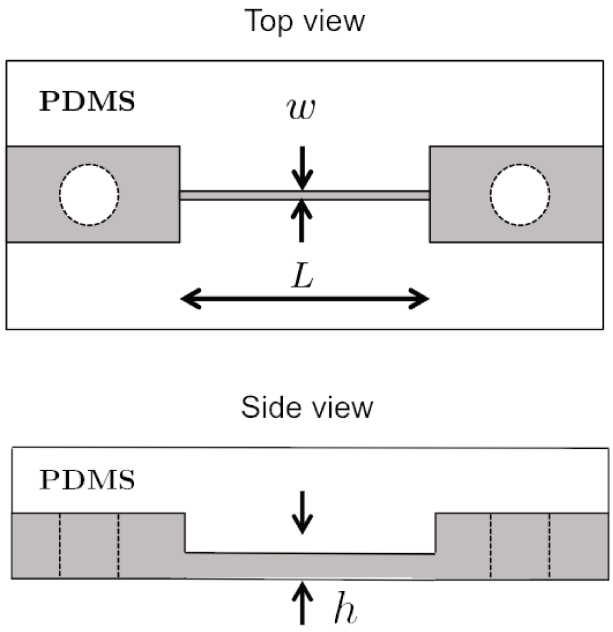

Figure 3.10: **Microfluidic channel with a rectangular constriction**. The channel consists of a channel of width w = 10 μm, height h = 14 μm and length L = 3000 μm.

Capsule preparation

Liquid-core ovalbumin microcapsules are prepared at the University of Reims Champagne-Ardenne, in France, by Florence Edwards-Lévy following the protocol detailed in chapter 1 section 1.2.2. Two batches of capsules are prepared. The pH of the albumin solution is 5.9 for the first one and 8 for the second one. Capsules are stored in water at 4°C. Before experiment, 20 μl of microcapsules are suspended in pure glycerol. The suspending fluid viscosity is much lower (800 cP) than the one of pure glycerol (1300 cP) due to the presence of water in the capsule solution. To control the viscosity during the experiment as much as possible, we perform at 20 °C and measure the viscosity of the suspending fluid after each set of experiments with a Couette viscometer (Thermo Haake).

Cell preparation

DAMI cells are cultured following the protocol detailed in chapter 2 section 2.2.2. Between 30 000 and 150 000 cells are suspended in 2 ml of medium (MEM, medium) in a tube agitated at 200 rcf to avoid sedimentation.

To modify cell mechanical properties, we use cytoskeleton drugs: blebbistatin (BBI) (Sigma Aldrich, Munich, Germany, final concentration 40 μM or 10 μM), cytochalasin D (CytoD) (Sigma Aldrich, Munich, Germany, final concentration 2 μM or 10 μM). BBI is known to inhibit myosin II [183] that is involved in cortical tension. Cyto D is a drug inhibiting actin polymerization [184].

Set-up for capsule and cell perfusion

The microsystem is placed on the stage of an inverted microscope (DMIL LED, Leica Microsystems GmbH, Germany) with a dry $\times$ 63 objective. The flow is driven in pressure with a pressure pump (MFCS, Fluigent, France). The system is connected to the reservoirs with PTFE tubes of internal diameter of 0.3 mm. The inlet and outlet tube lengths are respectively fixed at 60 cm and 30 cm. The reservoir containing cells is placed at the entrance and an empty reservoir placed at the outlet collects cells or capsules flowing out of the microsystem. A high speed camera (Fastcam SA3, Photron, USA) whose pixel size is 17 μm is mounted on the inverted microscope.

We observe the capsules in the center of the rectangular channel. Images are acquired with a frequency of 10 000 images per seconds, then analyzed using the Image J software. We simultaneously measure the shape and velocity of the flowing cell or capsule.

3.2.2 Capsule inverse analysis

The numerical model used to describe the flow of a capsule in a cylindrical channel has initially been proposed by Quéguiner and Dominique Barthès-Biesel [185]. Then it has been improved by Diaz et al. [186] in the sense that they introduce different viscosity for the internal and the external fluids and take into account the entrance of the capsule in the constriction. Later Lefebvre et al. [143] proposed to use the model to determine the elastic properties of a membrane in a cylindrical or a square microchannel. Then it has been used by Chu et al. in order to measure the surface shear modulus G_s of albumin capsules prepared with different conditions of pH [51].

The numerical profiles database available at the laboratory has been calculated by Thi-Xuan Chu during her PhD [187], considering a Neo-Hookean behavior of the membrane. The model is accurate for small strains and hyperelastic materials. Only two non dimensioned numerical parameters are necessary to describe the capsule profile: the confinement ratio a/R between the capsule radius a and the channel radius R; and the capillary number Ca determined by the fluid viscosity μ and, the capsule velocity U and mechanical properties. Profiles are characterized by their lengths L_x the total length of the elongated capsule, and L_{fr} between the apex of the capsule and the curvature (Figure 3.11).

Experimentally, spherical microcapsules are flown in a cylindrical channel by imposing pressures. We measure capsule velocity U, and the lengths L_x and L_{fr} of the deformed capsules. We then explore the database in order to find the corresponding capillary number Ca. When more than one capillary number is possible, we average the value. We check the validity of the obtained Ca by superimposing the experimental profile with the numerical profile corresponding to the Ca. We validate the value of Ca only if both profiles superimpose. Knowing the viscosity and capsule velocity, we are able to determine the surface shear modulus of the capsule G_s given by the relation $G_s = \mu U/Ca$.

The profile obtained in the constriction is compared with the numerical profiles of the database for the same condition of confinement. Then we identify the capillary number Ca which leads to a

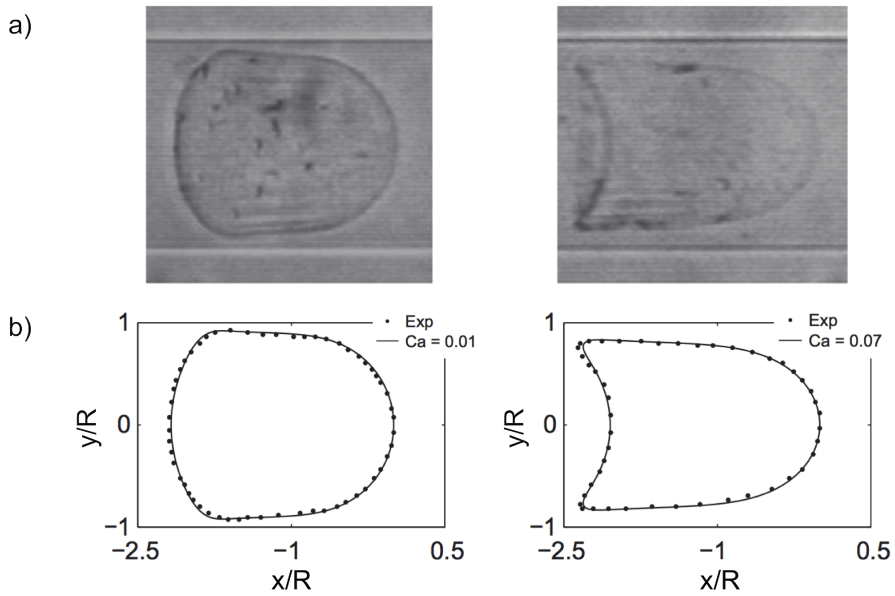

Figure 3.11: **Inverse analysis**. Two capsules fabricated at same pH 5 are flowed into a cylindrical microchannel at two different speeds. Their size is almost the size of the tube. a) Pictures of the experimental shapes. b) Fitting between experimental profiles and numerical simulations at two different capillary numbers. L_x is the total length of the capsule in the flow direction, L_{fr} is the length between the apex and the curvature of the capsule. Figure adapted from [51].

superposition of the numerical and experimental profiles. Figure 3.11 presents in (a), experimental profiles at two different conditions of flow. They have similar initial size but different velocities in the channel and thus different capillary number Ca. In (b), the figure 3.11 shows how we superimpose the experimental (dashed line) and numerical (plain line) profiles.

The aim of this work is to determine the surface shear modulus for the membrane of capsules fabricated with two different conditions of pH. We have chosen to use capsules fabricated in the same conditions as those used by Chu et al. [187] in order to calculate the modulus G_s with their numerical database. First we perform experiments with 20 stiff capsules. With undeformed capsules (pH 8), the numerical model does not work, the capillary number Ca is too low to be detected. In the literature, Chu et al. [187] have found $G_s = 0.081 \pm 0.026$ N/m, which is the value used in chapter 1. In order to better characterize our stiff capsules, we should perform experiments in more confined channels (between 50 μm and 75 μm), that are not available at the laboratory. Another possibility is to perform at higher flow strength, increasing the viscosity or the pressures applied but we are limited by the capacity of the condenser and the pressure resistance of our device.

Then, we perform the same experiment with 32 soft capsules. Among them only height are considered to determine the G_s modulus. Others are too large (confinement ratio greater than 1.2) to be considered, form train of capsules in the channel, do not present a parachute shape or present parameters in a gap of the database. We present in figure 3.12 (a) and (b) respectively the capsule with the lowest and the highest confinement ratios among the 8 capsules measured. Experiments have been carried out in the same conditions of flow and we determine a capillary number of $Ca = 0.02$ which

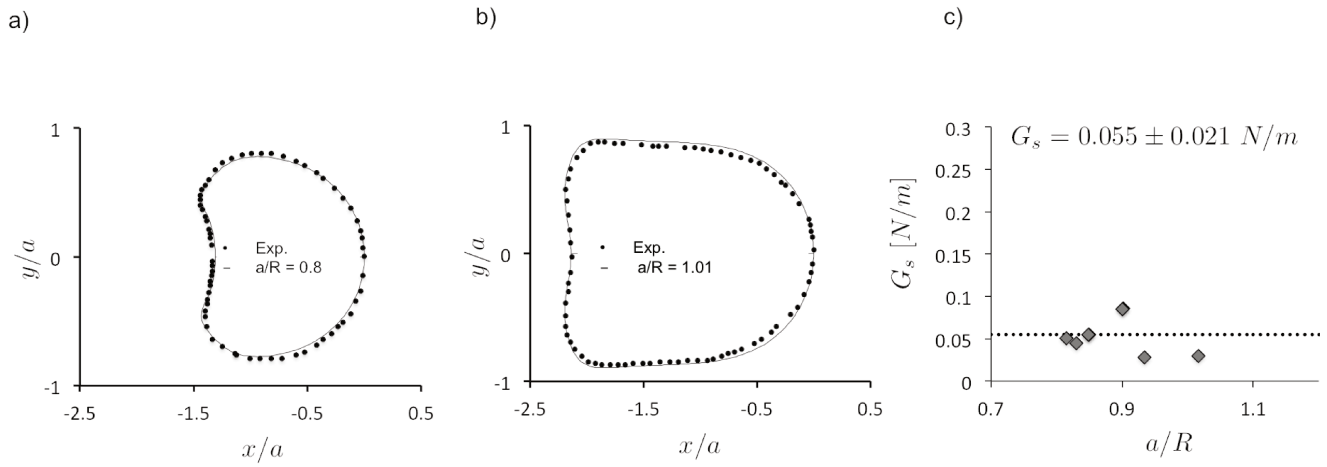

Figure 3.12: **Determination of the experimental value of G_s for soft capsules**. Capsules performed at pH 5.9 flowing with a capillary number of Ca = 0.02 in a cylindrical channel of 75 μm. **(a)** Correlation of the experimental profile (black dots) and the numerical profile (plain line) with a confinement ratio of a/R = 0.8. **(b)** Correlation of the experimental profile (black dots) and the numerical profile (plain line) with a confinement ratio of a/R = 1.01. **(c)** Plot of the surface shear modulus G_s as a function of the confinement ratio a/R. The dashed line represents the average value obtained.

leads to an average value of the surface shear modulus of $G_s = 0.054 \pm 0.021$ N/m. Compared with Chu et al. [187] value for soft capsules, $G_s = 0.030 \pm 0.007$ N/m, our capsules are stiffer. However we are in the range of capsules prepared 5 minutes at pH 5 ($G_s = 0.042 \pm 0.016$) and capsules of pH 5.9 with a reticulation time of 15 minutes ($G_s = 0.048 \pm 0.022$ N/m). As our capsules are prepared at pH 5.9 with 5 minutes reticulation time but from a different batch of capsules than the one used for the article, mechanical properties can vary. Because of the heterogeneity of the capsule suspension, we have large variability of standard deviation. We consider as reasonable the error we make by considering the already published values for soft and stiff capsules. We are conscious that the value of the modulus G_s are not perfectly exact but respect the correct tendency to be used in chapter 1.

3.2.3 Cell characterization

Other similar studies have been performed in square section channels [188]. The advantage of a square section is the ease of fabrication with common soft lithography methods. It is possible to easily fabricate channels of different size (up to 5 μm) in PDMS. We have no cylindrical channel small enough available at the laboratory to characterize cells with the same technique as for capsules (section 3.2.2). We design a channel in PDMS to confine the cells and study their profile in a straight rectangular channel. Figure 3.13 shows the profile of a cell traveling at the end of the constriction. The shape of the cell is similar as the one of capsules in cylindrical channels. However, here, we are not using inverse analysis to characterize cell mechanical behavior. At the laboratory, it exists a database for capsules flowing in a cylindrical [51] or square channels [188] but not yet in a rectangular channel. Some simulations have been tested in channels of section 3/2 but after a while the profile becomes asymmetric [189]. It can be the consequence of the aspect ratio. In cylindrical channel we assume the capsule profile is axisymmetric. A square channel probably slightly deform the axisym-

metric profile [188]. In a rectangular channel, the capsule profile is not axisymmetric and can not be described from single view observation [190]. For these reason a numerical database is not yet available at the laboratory for the rectangular geometry. The determination of the surface shear modulus of cells whose membrane is thin by inverse analysis could be interesting. But in order to have reliable measurements, the numerical data base should take into account the internal composition of a cell. By inserting inclusion to mimic the presence of a nucleus or at least considering a viscoelastic model instead of a purely elastic one. The creation of the data base adapted for cells requires deep investigation. Moreover, when they mature, MK membrane invaginates into the cytoplasm to form a membrane reservoir (Introduction, Figure 3). Thus the determination of the surface shear modulus is not the best elastic modulus to characterize MK deformability.

A variation in stiffness may modify cell velocity. Chu et al. [51] have shown that the velocity ratio between capsule and mean fluid velocities increases monotonically with the capillary number Ca ($Ca = \mu U / G_s$), for a same confinement ratio. It means that considering the fluid velocity U and the fluid viscosity μ constant, an increase in Ca results in an increase in cell velocity v. To increase Ca, the shear modulus G_s has to be low. Soft capsules should thus flow faster than stiff capsules considering the mean velocity constant. A possible explanation is that stiff cells deform less in the constriction and their friction along the wall is larger than in the case of soft cells flow. We fix the pressure at 300 mbar and measure cell lengths and velocity into the constriction at the end of the channel where imperfections of the channel due to fabrication limits are always the same. We assume that cells are flowing one by one in the channel and that the mean velocity of the fluid is constant. To really control this parameter, we should control the flow rate.

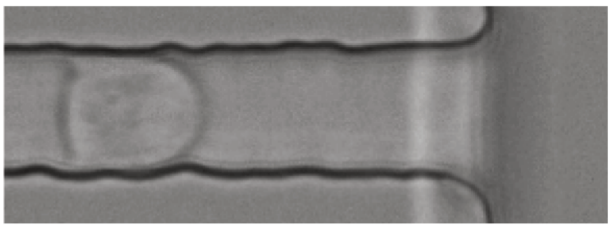

Figure 3.13: **Untreated cell flowing into a straight rectangular channel**. Picture of a cell flowing from left to right at the end of a straight rectangular channel in PDMS. The shape is similar to the shape obtained for microcapsules in the cylindrical channel.

Table 3.2 presents the velocities obtained for different cell treatments but same condition of perfusion. We notice no significant differences in lengths in the flow direction ($p > 0.05$ with the ANOVA test calculation) for all the treatments tested. However, the velocity of cells treated with BBI 10 μM for 30 minutes is significantly lower than untreated cells ($p < 0.001$). That appears to correlate with the literature that expect a stiffening of cells in suspension when inhibiting myosin II [191]. Increasing BBI concentration seems to inhibit its effect on cell length and velocity. There is probably other effect of BBI at high concentration that inhibit its effect on deformability.

Several hypotheses can explain this lack of difference between the control and all the treatments

Table 3.2: **Velocity in the constriction for diverse cell treatments**. Cells are perfused at 300 mbar in a rectangular channel of 10 μm wide, 3 mm long and 14 μm deep. N represents the number of cells characterized. Cell velocity is presented as the average $\pm$ the standard deviation.

Treatment	**Concentration [μM]**	**Duration [min]**	L_x**[μm]**	**Cell velocity [mm/s]**	N
Control	/	60	15.4 ± 2.2	92.2 ± 5.9	25
DMSO	4	60	15.7 ± 2.0	82.5 ± 5.4	14
BBI	40	60	15.5 ± 3.0	94.5 ± 6.4	25
BBI	10	60	15.1 ± 1.9	72.5 ± 6.7	46
CytoD	2	30	17.2 ± 3.1	93.5 ± 8.4	20
CytoD	2	10	15.2 ± 2.3	86.5 ± 7.1	10
CytoD	10	30	15.6 ± 2.8	97.7 ± 6.1	11

(except BBI 10 μM). First, the treatment may not impact cell mechanical properties. Second, the channel is not confining enough the cells to underline different profiles. Third, the hydrodynamic forces μU are too low to distinguish different stiffness. Increasing the hydrodynamic forces is possible by increasing the viscosity μ or the velocity U. Increasing the velocity is limited by the frequency of acquisition available for the camera (10 000 images per second). Increasing the viscosity without reducing the velocity requires an increase in the driving pressure. That can be achieved at the laboratory since our pressure controller limit is 7 bars. A possible way to increase the viscosity of the medium is the addition of Dextran (average molecular weight 500 kg/mol) at a concentration of 10 % (w:v) compatible with cell viability. Due to the lack of quantitative data to compare with experimental results, we decided to use another technique and perform AFM experiments.

3.3 Tip-less AFM

As mentioned in previous section 3.2, there is no significant difference in cell length and velocity in rectangular micro-channels for non-treated cells and cells treated with blebbistatin (BBI) and cytochalasin D (CytoD). We wonder if the absence of difference is due to the method of characterization or the lack of effect of the drug treatments. We present in this section results obtained in Saarbrücken with a technique using an AFM wedged cantilever instead of a tip. For the sake of simplicity we will design as tipless, AFM experiments performed with the wedge cantilever. This technique allows compression tests with a high sensitivity on forces applied. We measure the resistance to compression of single cells to quantify cell mechanical properties. In order to globally deform the cells, the cantilever is wedged with a polymer to perform compression between two plates. We fix the applied force or the deformability percentage in order to calculate the Young's modulus of cells treated with different drugs.

3.3.1 Material and methods

Cell preparation

Around 40 000 cells in 2 ml are initially placed in a 35-mm diameter tissue culture dish (glass bottom FluoroDish FD35-100; World Precision Instruments, Sarasota, FL). Then cytoskeleton drugs

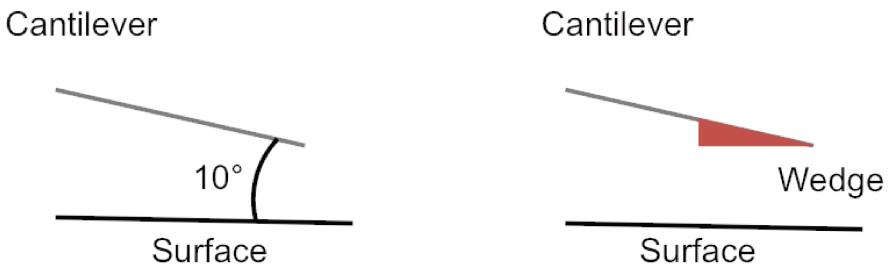

Figure 3.14: **Wedging cantilever**. Picture of a tilted cantilever before (on the left) and after wedging (on the right). The wedge allows a plate to plate contact between the surface and the cantilever while the bare cantilever is used for local contact.

are added to the dish with concentration and duration mentioned in table 3.3. The role of each drug is detailed in section 3.3.2. After treatment, the FluoroDish is directly placed on the stage of the microscope. DAMI cells are in suspension and do not adhere to glass surface during the experiment.

Table 3.3: **Summary of cell treatments for tipless AFM experiments**. Cells are treated with several drugs in order to modify their mechanical properties.

Drug Treatment	Abbreviation	Concentration [μM]	Treatment duration	Supplier
Blebbistatin	BBI	40 μM	40 min - 3 days	Sigma Aldrich
Latrunculin A	Lat A	0.5 - 1 μM	10 min	Sigma Aldrich
Cytochalasin D	Cyto D	5 μM	30 min - 2 h	Sigma Aldrich
Calyculin A	Cal A	2.6 - 5 nM	30 min	Sigma Aldrich
ROCK inhibitor	Y-27632	10 μM	30 min	Tocris Bioscience, Lille, France
Neutral Red	NR	1/40 - 1/30 v:v	1 h 30 min	Sigma Aldrich

Wedged cantilever

In order to have compression between two parallel plates of living cells, an AFM-cantilever is wedged with the method described in [192]. A tipless cantilever in nitride is used, whose thickness is 600 nm, back side coated with a 45 nm Ti /Au layer (Model: MLCT-O10, Brucker), whose frequency is between 90 to 160 kHz and with a spring constant of 0.6 N/m. The wedge is made of an epoxy polymer reticulated at the end of the cantilever. Figure 3.14 illustrates the correction of the tilted angle of 10° by the wedge. The UV-curing polymer (NOA 63, Norland Optical Adhesive, Cranbury, USA) is first placed in a FluoroDish, on a glass bottom. With a pipette tip, we form non-polymerized NOA droplets of different sizes on a glass surface. The glass slide is placed on the stage of the microscope and the bare cantilever is approached to a droplet whose size matches that of the cantilever's end, until contact. It is important to have no bending of the cantilever during this process in order to have a flat non-tilted wedge surface. The wedge is cured by UV at the maximum power for 5 minutes. Because NOA does not adhere to glass, the solid wedge remains attached to the cantilever as it is retracted from the dish. Each wedged cantilever is observed by electron microscopy to check top (Figure 3.15, (a)) and lateral (Figure 3.15, (b)) topographies. When the surface is smooth and the angle corrected to have a non- tilted surface, the cantilever is ready to be mounted on the AFM head.

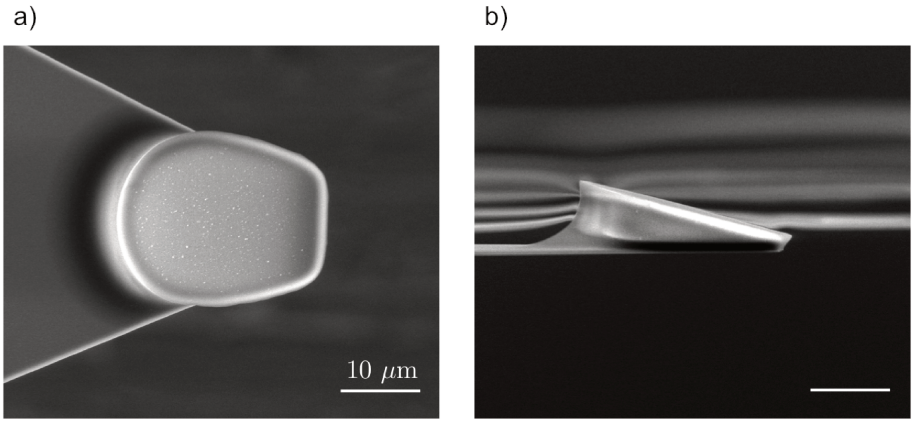

Figure 3.15: **Wedged cantilever**. Scanning electron microscopy images. **(a)** Top view of the epoxy wedge. **(b)** Side view of the epoxy wedge. Images acquired by Daniel Flormann, at INM in Saarbrücken.

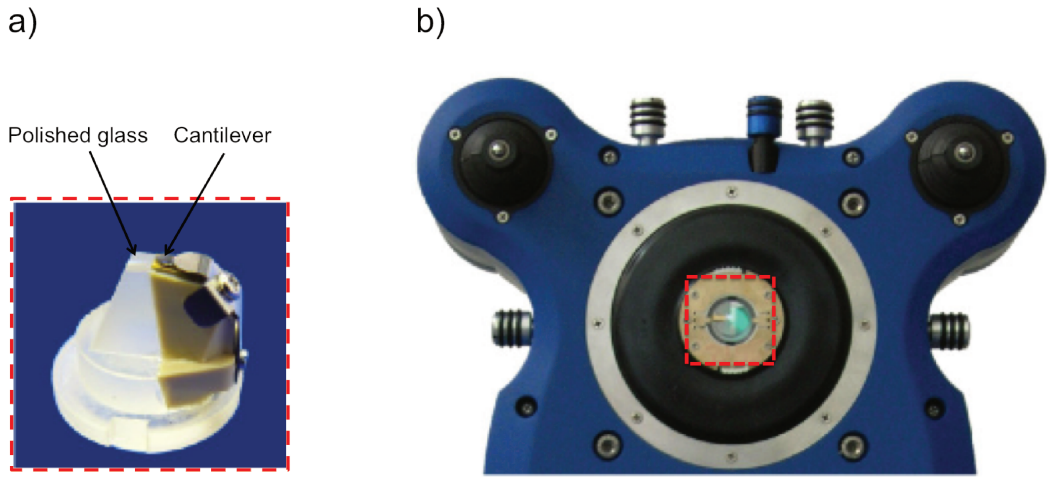

Figure 3.16: **Mount the cantilever**. **(a)** The cantilever is clamped to the glass block. **(b)** Then the glass block is placed on the top of the AFM head. Bottom view.

Experimental set up

The wedged cantilever is placed and fixed on a standard JPK glass block (Figure 3.16 a) on the top of a polished glass area. The glass block is then mounted on an atomic force microscope head (CellHesion; JPK Instruments) (Figure 3.16 b). A rubber seal ring is placed around the glass block, on the AFM head to avoid evaporation. A drop of liquid (MEM medium) is put on the top of the cantilever to avoid air trapping between the lever and the liquid medium where cells are in suspension. Then the dish containing cells is mounted on the stage of the microscope. The AFM head is placed on the top of the dish. AFM head and the dish are mounted on a piezoelectric scanner which can move in three directions. The laser beam is focused on the metal part of the lever (in the opposite side of the wedging). The normal forces exerted on the cell induce a vertical deflection of the cantilever which results in the deflection of the reflected laser beam detected on the photodiode (Figure 3.17 b). That allows us to compare different cell treatment effects on cell mechanical properties. Before each measurement, we scan the sample, choose the cell we will characterize and take a picture in order to later

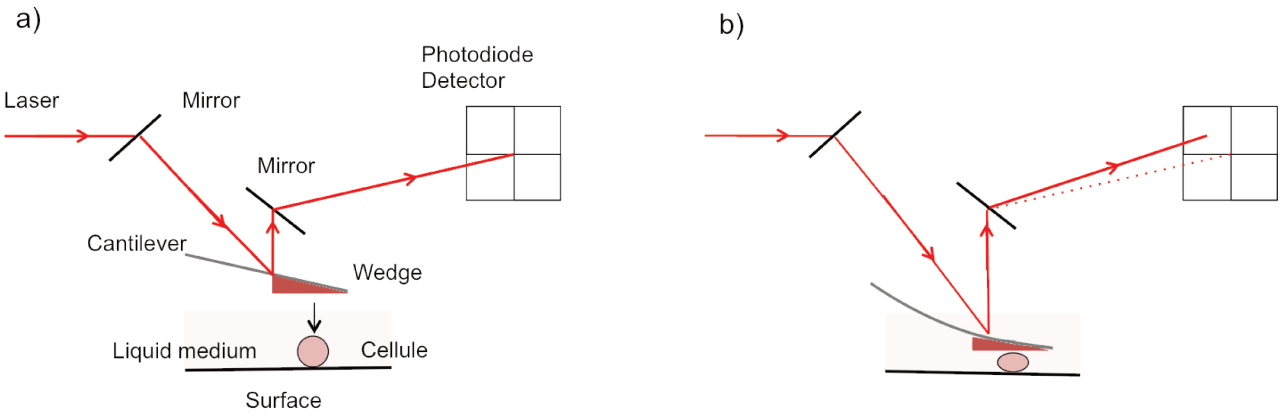

Figure 3.17: **Sketch of the principal components of an AFM**. **(a)** A laser is aligned with the cantilever and the center of the detector, by modifying the inclination of the mirror. This step is realized with no contact with the surface to avoid any bending of the cantilever. **(b)** When the cantilever is in contact with the surface or with the sample, it deforms. The laser is then deflected and the variation observed in the detector is relied on stiffness with the Hooke's law.

measure its diameter. We measure the mechanical properties of at least 10 cells for each treatment, with one measurement per cell. For each cell, we measure cell deformation at load of 2 nN or 5 nN with none or 2 minutes contact time and plot the force-distance curves. Between two measurements, we pull up the cantilever in the liquid, and displace the sample with the piezo stage to find another cell in the dish.

Calibration

Each time a cantilever is mounted onto the microscope calibration is required. Calibration depends on the position of the cantilever and the fluid used (air, or liquids). AFM calibration is performed in a culture dish containing culture medium which has the same viscosity and reflection index as the medium suspending cells. The aim of calibration is to correlate the laser signal with the piezo motors in order to measure the forces exerted at the cantilever. The calibration consists in aligning the laser with the cantilever and the photodiode detector by adjusting the position of the mirror, as shown in figure 3.18. The laser is well aligned and ready for operation when the sum signal is maximum (around 3 Volts). The photodiode screen is the sensor that collects the light reflected on the cantilever. When the cantilever is at rest, the laser beam should hit the middle of the screen. The position in the photodiode is measured by the voltage difference between the different quadrants of the photo-diode [193]. The calibration is realized in two steps: i) the adjustment of the sensitivity (Figure 3.19) and ii) the spring constant calibration (Figure 3.20).

The sensitivity calibration allows to relate the voltage signal, measured by a capacitive sensor, with a displacement of the piezo motor. In order to obtain the sensitivity value, the cantilever approaches the stiff glass surface of the bottom of the dish. When touching the glass surface, the cantilever deforms and the laser beam detected by the photodiode differs to the original position. In figure 3.19, the black curve represents the approach and the red curve the retraction. The horizontal part of the curves correspond to the vertical distance run by the head of the AFM when the lever is not in contact

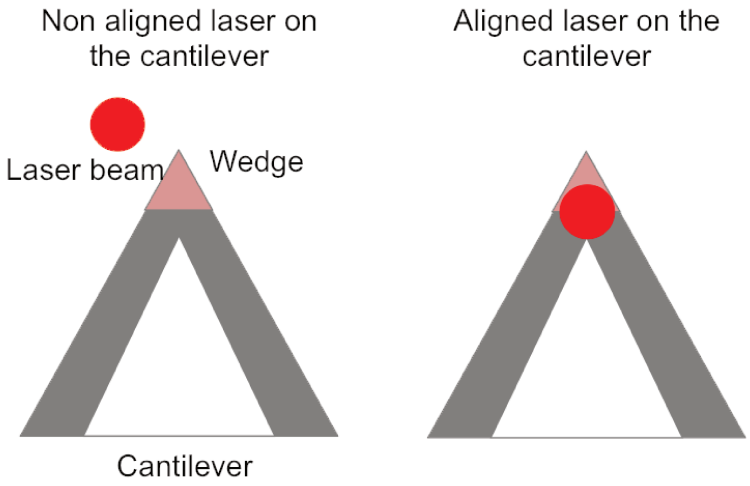

Figure 3.18: **Alignment of the laser beam on the cantilever**. Sketch of the alignment of the laser to the cantilever. On the left, the laser beam is off the cantilever and the sum laser signal detected by the photodiode detector is low. On the right, the laser is aligned with the cantilever which is the correct position for measurements. The laser signal is maximum.

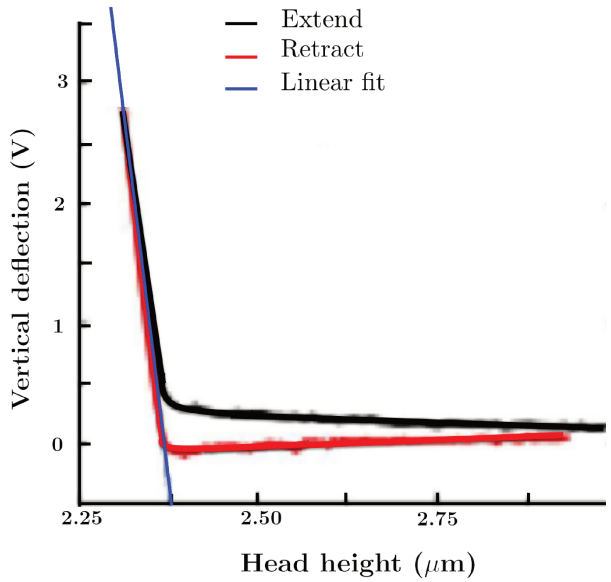

Figure 3.19: **Sensitivity calibration curve**. Vertical deflection as a function of the displacement of the cantilever. The linear part of black curve is the approach of the cantilever from the surface until the inflection point which corresponds to the contact point. The linear fit (in blue) corresponds to the approximation of retract slope. Image adapted from [193].

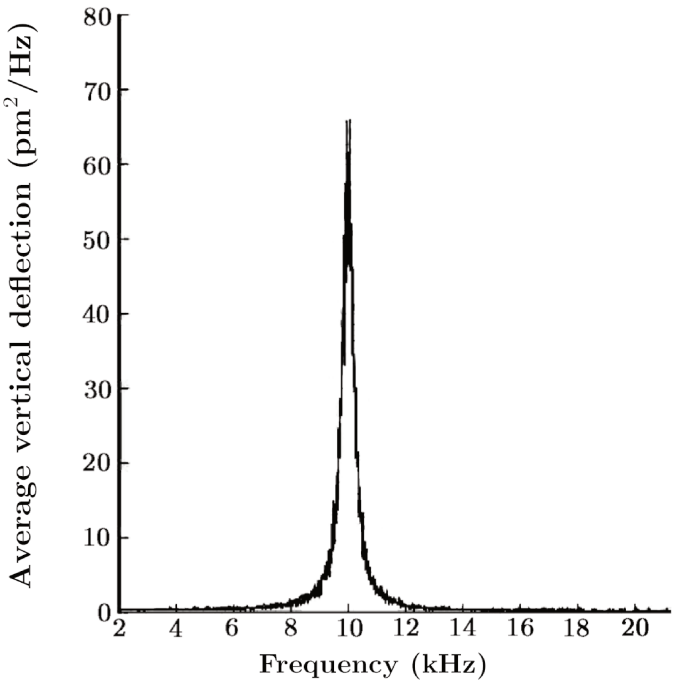

Figure 3.20: **Spring value calibration curve**. With no contact between the cantilever and the substrate, the cantilever oscillates at some frequencies. The fit of the fundamental mode allows the measurement of the spring value. Image adapted from JPK instruments User Manual.

with the cell. After the contact point, the cantilever pushes against the material. The deflection of the cantilever increases with the distance after contact and shift the detected voltage (here at rest 3 volts). The cantilever retracts and the deflection decreases until it reaches its initial position. The slope of the approaching curve gives the sensitivity value which correlates the change in voltage with the piezo movement.

Experimentally, the spring value is determined by the cantilever deflection when it oscillates far from the surface. The resonant modes of the cantilever are obtained due to thermal fluctuations stimulation [194]. We fit the fundamental mode and estimate the cantilever spring constant with a correction factor depending on the cantilever geometry. The resolution of the equipartition theorem allows to determine the value of the correction factor [195], and is not detailed here.

Analysis

Cell diameter is determined using a circular fit with the software image J. Force-distance curves are analyzed using JPK software. It consists to analyze the approach or retraction curve. The retraction curve is usually used to measure cell adhesion. For the determination of the Young's modulus, we are using the approach curve. The contact point between the wedge and the cell is determined as the inflection point of the curve (Figure 3.21). Then the deflection of the cantilever increases with the indentation and is directly related to the force applied on the cell. Prior the experiment we fix the force the cantilever has to apply on the cell before retracting. Since the final force applied on cells is always the same, their deformation depends on their stiffness. We define the Young's modulus as the

tangential slope of the force-displacement curve for an indentation of 15 % of the cell diameter which is the limit of small deformation regime avoiding nucleus response [154]. The best fit to determine the Young's modulus uses the Hertz model.

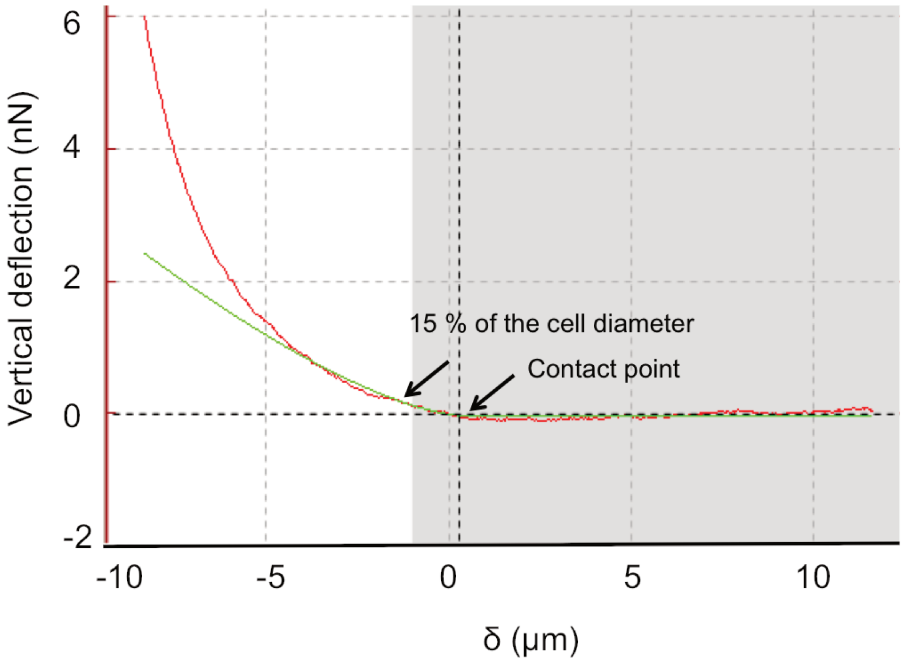

Figure 3.21: **Determination of the Young's modulus**. Approach curve. Plot of the vertical deflection of the cantilever as a function of the indentation depth δ. The distance 0 μm corresponds to the contact point. Then the cantilever compresses the cell until a certain force whose value is determined prior to experiment. The Young's modulus is the slope of the green curve which fit the part of the red curve in the grey box until a max indentation of 15 % of the cell diameter.

Our cantilever is tipless but wedged. We assume that compressing a round cell with a plate is equivalent than having a round tip characterizing a flat surface. Thus we consider the cell diameter is the tip diameter. The deformation of 15 % of the cell diameter is not small enough to only consider membrane deformation response but include the cytoplasm response. Thus the Hertz model is too simple to accurately characterize quantitatively the cell Young's modulus E. However it is a currently used model to analyze force-displacement curves and give an approximation of the elastic modulus enough to qualitatively compare experiments realized in the same conditions of cantilever, operator, and loading forces.

3.3.2 Cell characterization

Determination of size and mechanical properties of non treated cells

We measure the diameter of each cell before the experiment. For each population of cells we perform compression at least on 10 cells. The size and the Young's modulus are expressed as the mean $\pm$ the standard deviation. We call control experiments, experiments performed on non treated cells.

Table 3.4: **Results of tipless AFM experiments**. *N* represents the number of cells characterized. Cell diameter and stiffness are presented as the mean ± the standard deviation for an indentation of 15 % of the cell diameter.

Treatment	**Concentration [μM]**	**Duration**	**Cell diameter D [μm]**	**Cell Young's modulus [Pa]**	N
Control	/	1 h	15.16 ± 1.66	27 ± 21	82
BBI	40	3 days	24.63 ± 3.65	20 ± 18	15
S-nitro BBI	40	40 min	15.13 ± 1.13	28 ± 19	15
Cyto D	5	2 h	16.12 ± 2.48	8 ± 7	10
Cyto D	5	30 min	15.21 ± 1.45	33 ± 22	13
Lat A	0.5	10 min	15.12 ± 1.99	13 ± 8	10
Lat A	1	10 min	15.00 ± 1.71	10 ± 4	13
Cal A	0.0026	30 min	15.72 ± 2.08	91 ± 88	25
Cal A	0.05	30 min	15.98 ± 1.85	105 ± 94	18
Y-27632	10	30 min	15.27 ± 1.97	79 ± 82	18

We realize a set of control experiments before each set of measurements in order to validate the robustness of the cantilever and be able to compare results not realized the same day. We only compare experiments whose control results do not present differences neither in size or stiffness. If the value of the control vary it can result of defects on the cantilever, errors in cell culture or cell aging. In case of doubt on control measurements, we do not present the results of experiments performed at this date. Regrouping all the comparable controls of 5 days of experiments on 82 cells, we obtain a non treated cell average diameter of 15.16 μm $\pm$ 1.66 μm and a mean Young's modulus of 27 $\pm$ 21 Pa (Table 3.4).

The dispersion is large and we assume that in a population of cells, it exists a high variability of stiffness that can be related to the heterogeneity of the population and the operator error during analysis. The comparison with value obtained in the literature is tricky as it is difficult to know the detail of the performance and analysis. With AFM it is always better only to compare value obtained in the same conditions, with a same cantilever and one operator. Also there is few AFM experiment on cells in suspension and none to our knowledge about the characterization of the DAMI cell line. In order to measure the effect of a treatment on cell mechanical properties, we compare the control and the treatment by pair and evaluate their statistical differences with an ANOVA test, Instat3.

Size effect of drug treatments

We measure cell size of cells treated with different drugs. We find no significant size effect of drugs, the diameter of cells is still around 15 μm except for cells treated 3 days with BBI whose diameter is larger : 24.63 ± 3.65 (Table 3.4). That is consistent with observations we already discussed in chapter 2 where we noticed an increase in diameter after 3 days treatment of BBI and used this treatment for size-based sorting.

Mechanical properties of treated cells

Actin polymerization effect on cell mechanical properties

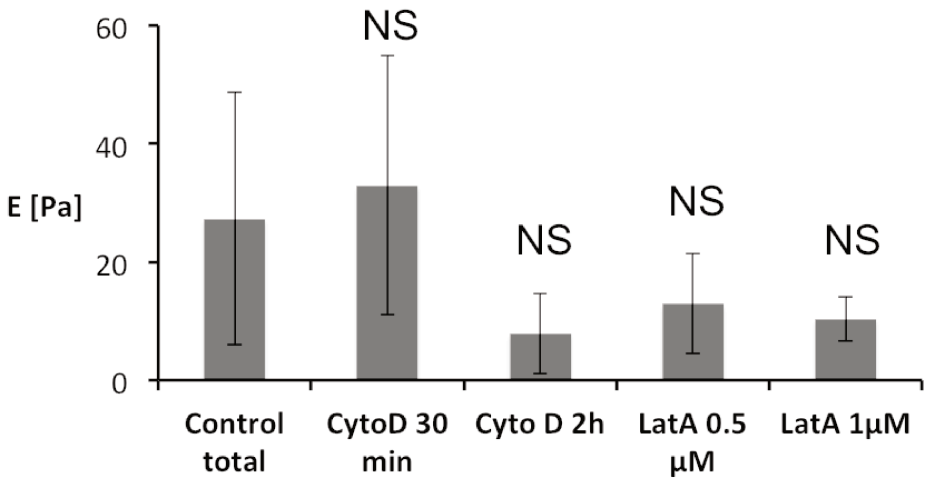

Figure 3.22: **Stiffness of cells treated with actin polymerization drugs**. Histogram presenting cell Young's modulus for different treatments : 5 μM CytoD at different duration (2 h and 30 min), and LatA at 0.5 μM and 1 μM. NS corresponds to not significant differences to the control $p > 0.05$, * corresponds to $p < 0.05$, ** corresponds to $p < 0.01$, and *** corresponds to $p < 0.001$ in the ANOVA test, Instat3, compared with control.

Cytochalasin D is known to inhibit actin polymerization which is supposed to conduct to cell softening [184]. We carry out 13 measurements for cells treated 30 minutes with 5 μM CytoD. We find no significant differences between the control and the CytoD-treated cells, as shown in figure (3.22). Increasing the duration time of treatment from 30 minutes to 2 hours in the incubator at 37°C, we perform on 10 cells and find a Young's modulus of 8 ± 7 Pa. The lower value of the average Young's modulus indicates a decrease of cell stiffness. That might results of a larger CytoD effect due to the increase of treatment duration, however the difference is not significant.

Latrunculin A is a drug inhibiting actin polymerization as well as CytoD but is known to have a short therm effect to disrupt actin filaments organization which is stable over time whereas CytoD effect evolve with time [196]. Measurements with the AFM are thus performed just after treatment, we count 10 minutes in order to have a stabilization in temperature in the AFM cabinet. We find a Young's modulus of 10 ± 4 Pa for cells treated with 1 μM and 13 ± 8 Pa for cells treated with 0.5 μM. It appears that LatA does not significantly soften cells neither in comparison with the control (Figure 3.22).

Myosin activity effect on cell mechanical properties

Blebbistatin directly inhibits myosin II activity [183]. BBI 40 μM does not modify cell mechanical properties in agreement with observations made in section 3.2.3 in constrictions. We perform tipless AFM measurements on 16 cells treated 3 days with 40 μM BBI and find an average Young's modulus of 20 ± 18 Pa (Table 3.4). Figure 3.23 shows that this value is equivalent to the one of the control. The lack of effect of BBI is potentially due to its inactivation caused by its sensitivity to light. Thus we perform tipless AFM measurements on 16 cells treated 40 minutes with 40 μM of S-nitro BBI which is the same molecule as BBI but non sensitive to light. We find an average Young's modulus of 28 ± 19

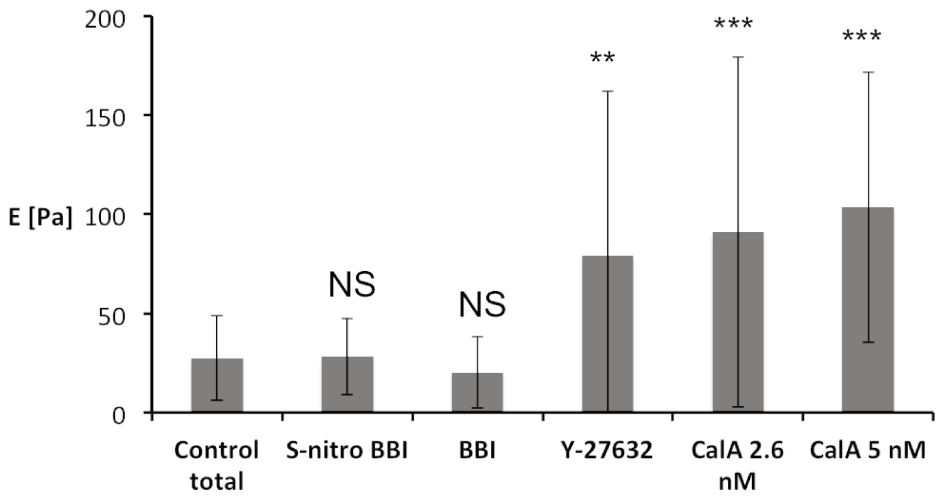

Figure 3.23: **Stiffness of cells treated with myosin inhibitors and enhancers.** Histogram representing cell Young's modulus for different treatments inhibiting myosin activity such as: BBI, S-nitro BBI and Y-27632; and two concentrations of CalA enhancing myosin activity (2.6 nM and 5 nM). NS corresponds to not significant differences to the control $p > 0.05$, * corresponds to $p < 0.05$, ** corresponds to $p < 0.01$ and *** corresponds to $p < 0.001$ in the ANOVA test, Instat3, compared with control.

Pa (Table 3.4), which is not significantly different from the control or the treatment with BBI. The light sensitivity of BBI does not seem to affect the effect of the drug on cell stiffness. In order to validate this observation, tipless AFM measurements have to be done on cells treated 40 minutes with BBI and compared with results obtained with S-nitro BBI. Since there is no significant difference with the control, we estimate BBI is not modifying cell stiffness. In the literature it has already been shown that BBI has no effect on the Young's modulus of HL-60 cell line (human leukemia cells) [197]. BBI effect seems to depend on cell type and adhesion.

Y-27632 inhibits ROCK whose role is the phosphorylation of myosin phosphatase [198]. As a consequence it inhibits actomyosin activation [199]. That should have different effects on adherent cells or cells in suspension since they have different cytoskeletal structure. We measure the Young's modulus on 18 cells and find 79 ± 82 Pa on average (Table 3.4). That is significantly larger than the Young's modulus of the control. The drug seems to stiffen cells that are in suspension. It is consistent with the literature where myosin II has been shown to soften cells in suspension [191]. BBI and Y-27632 inhibit myosin but using different channels that can explain the difference of effect of the two drugs.

Calyculin A is an enhancer of myosin. It inhibits myosin-light-chain phosphatase [200, 201] and increases the contractility of the cell. We first perform on cells treated 30 min with 50 nN of CalA. However, the contractility became so high that it was impossible to do the measurement. The cells became so rigid that it was impossible to squeeze them between the wedge and the glass plate. Any pressure exerted by the cantilever pushed the cell away from the probe. Thus we decrease the drug concentration. Results obtained with 5 nM and 2.6 nM are shown in table 3.4. We respectively find a Young's modulus of 91 ± 88 Pa and 105 ± 94 Pa for each concentration. The two concentrations are not significantly different when compared to each other but are larger than the control Young's

modulus. It seems that it corresponds to the highest stiffness measurable for DAMI cells treated with this drug.

Discussion

In the constrictions presented in chapter 2, whole cells are quickly deformed. The deformation of cells in the constriction is not enough to deform the nucleus. We consider a deformation of 15 % of the cell diameter in order to determine the cell Young's modulus as it is the limit to avoid the nucleus response.

The mechanical characterization of the DAMI cell line is poorly studied in the literature. However, Young's modulus have been published for other cell types. With a pyramidal tip of 3 μm height AFM, Rosenbluth et al. [179] gives a Young's modulus for blood cells: 156 $\pm$ 87 Pa for neutrophils, 855 $\pm$ 670 Pa for myeloblast and 48 $\pm$ 35 Pa for the Jurkat lymphoblast cell line. When compared to these values DAMI cells seem to already have a soft behavior, with a Young's modulus of $E = 27 \pm 21$ Pa.

Tipless AFM measurements bring some light on the effect of several drugs that are compared with the untreated cell mechanical properties. We show that BBI does not modify significantly cell mechanical properties. It is not possible to use it for deformability based sorting; however, it increases cell diameter. Which presents many advantages for our applications. First, we already demonstrate the ability of our asymmetric device to sort a mixed population of untreated cells and 3 days BBI treated cells according to their diameters (Chapter 2). Second, since DAMI cells behave as immature MK we want to modify their organization in order to be close to their mature structure. It is known that MK became larger when they mature [202] and cells treated 3 days with BBI will be used as a model for mature MK in the next two chapters 4 and 5.

Among other drugs tested, CytoD and LatA has shown no significant softening of DAMI cells that already present a soft behaviour. In contrast, Y-27632 and CalA stiffen cells approximately by a factor 3, respectively by inhibiting ROCK and phosphatase. As cells are in suspension Y-27632 stiffen cells while it should soften adherent cells [203]. In the chapter 1 we demonstrated the ability of our device to sort microcapsules whose surface shear modulus G_s is separated by a factor 3 ($E = 2(1+\nu)G$, where ν is the Poisson coefficient). The dispersion in stiffness was lower than the one we get with cells. Considering the high standard deviation, we expect that a difference of factor 3 will not be enough to separate cells into the diffuser. We advice to test the efficiency of the device with a double treatment of cells.

Future work have to be carried out to evaluate the ability of the device to sort a mix population. In first investigation we recommend to choose a pair allowing a balance between treatment duration and stiffness contrast. For example the pair of treatments 5 nM of CalA and 1 μM of LatA whose size is homogeneous and whose stiffness shows a difference of factor 6, could be interesting to test. However, when two populations are treated with different drugs we need to rinse the extra amount of

each drug before mixing in order to have no competition between the two drugs. Thus it is necessary to verify the irreversibility of the drugs effect over time. Then we will need to find a staining which will not modify cell mechanical properties but help visualization of the two populations.

3.4 Conclusion

In the sorting device presented in chapter 1 and 2, capsules and cells are confined in the constriction. Time spent in the constriction is short (less than 1 ms) and the object deforms globally. In order to characterize the mechanical properties of populations to be separated, a technique whose principle is close to the squeezing is required. For this reason, we chose a microfluidic method that had been developed at the laboratory, flowing capsules and cells in microfluidic constrictions. The inverse analysis method used by Thi-Xuan Chu during her PhD to create a database for capsules flowing in a cylindrical channel, has been used here to characterize our microcapsules. We compare the results obtained by Chu and ours using capsules prepared in the same conditions but not from the same batch. We find a good correlation of the results and admit that capsules fabricated at pH 8 are 3 times stiffer than capsules prepared at pH 5.9. However, the method is less robust for the characterization of cells.

The characterization of cell mechanical properties has first been realized in rectangular microchannels. We measure cell velocity and lengths at fix pressure of 300 mbar for untreated cells, cells treated with BBI and cells treated with CytoD. We find no significant differences in both profiles and velocity for one of the treatments. Many hypothesis could explain these results. The rectangular constriction is too large to squeeze the cell efficiently. The hydrodynamic forces are maybe not enough to distinguish two populations. Increasing the velocity is not an option because we are limited by the speed camera frequency. However keeping the velocity in the same range by increasing the viscosity and the pressures increases the hydrodynamic forces and thus the deformation. However the design of new constrictions fall behind schedule and the numerical data base available at the laboratory yet only exists for square and cylindrical channels. Thus we decided to use another method.

Complementary results performed at the INM, in Saarbrücken in Germany, with the AFM put in light the lack of differences in mechanical properties of cells we want to characterize. It partly explains the difficulties we find to sort cells according to their mechanical properties. Also, we carry out many experiments to find treatments that modify enough cell mechanics to plan to sort them. We find that among the drugs tested only those modifying myosin activity significantly have an effect on our cells. In particular, CalA 5 nM stiffens them by a factor 3. We are planning new experiments with the new information we get in order to better know the limits and perspectives of our sorting device.

Chapter 4

Time-lapse observation of the elongation of megakaryocytes

Contents

4.1 Introduction to megakaryocyte elongations

Platelet transfusion has been used for therapy since the seventies [204, 205]. However, donation is the only method to collect platelets for transfusion and is not sufficient to transfuse all the patients who need it. Many patients are transfused with platelets from five whole blood donations while the same amount of platelets would be given during one platelet donation [206]. As an alternative to

platelet donation, *in vitro* platelet production is studied. The idea is shown in figure 4.1. Stem cells are amplified and differentiated into megakaryocytes (MK). Then MK are cultured until maturation, and placed into bioreactors to produce *in vitro* platelets by fragmentation (Figure 3). The latest are finally transfused to a patient. Differentiated stem cells can be the ones of the patient himself. Thus, it reduces the risk of incompatibility and insure stem cells availability. *In vitro* platelet production is a dynamic field with many challenges. The main consists in finding the stem cells source and defining protocols for MK differentiation. In the manuscript, we only focus on one step of the process: the fragmentation of MK into platelets. We develop microfluidic tools to study *in vitro* MK elongation and fragmentation in flow. This biomechanical approach interests many groups all around the world and our group is one of them. The field is dynamic and several companies are involved in the projects. It is the case of Platelets Biogenesis in the US, Megakaryon in Japan and PlatOD in France.

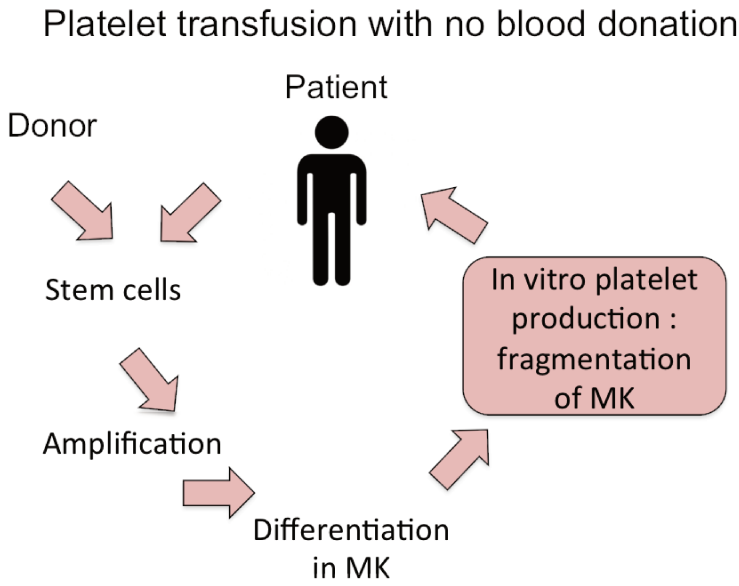

Figure 4.1: **Platelet transfusion without blood donation**. Stem cells are differentiated into megakaryocytes. They are cultured and they produce platelets into bioreactors. Platelets produced are transfused to a patient. An overview of *in vitro* platelet production techniques is detailed later in this section.

4.1.1 Production in static conditions

We review here various methods developed to mimic and study *in vitro* platelet production. In early studies, MK were cultured in liquid medium in static conditions. In the past 10 years, more sophisticated models based on microfluidics and tissue engineering techniques were developed for dynamic MK culture and/or platelet harvesting. As platelet formation is a multisite process involving the bone marrow, bone marrow sinusoids and lung capillaries, these biomimetic models are very diverse.

Mouse MK cultured in liquid conditions in a well have been shown to produce platelets when they arrive at maturation (Figure 4.2). When the MK is mature, it extends cytoplasm filaments called proplatelets. They elongate and form small fragments of cytoplasm called preplatelets and platelets

[207]. The release of platelets in static conditions requires hours [208]. Moreover platelets obtained in these conditions adhere at the bottom of the plate and are probably already activated. They cannot be easily collected and used for transfusion.

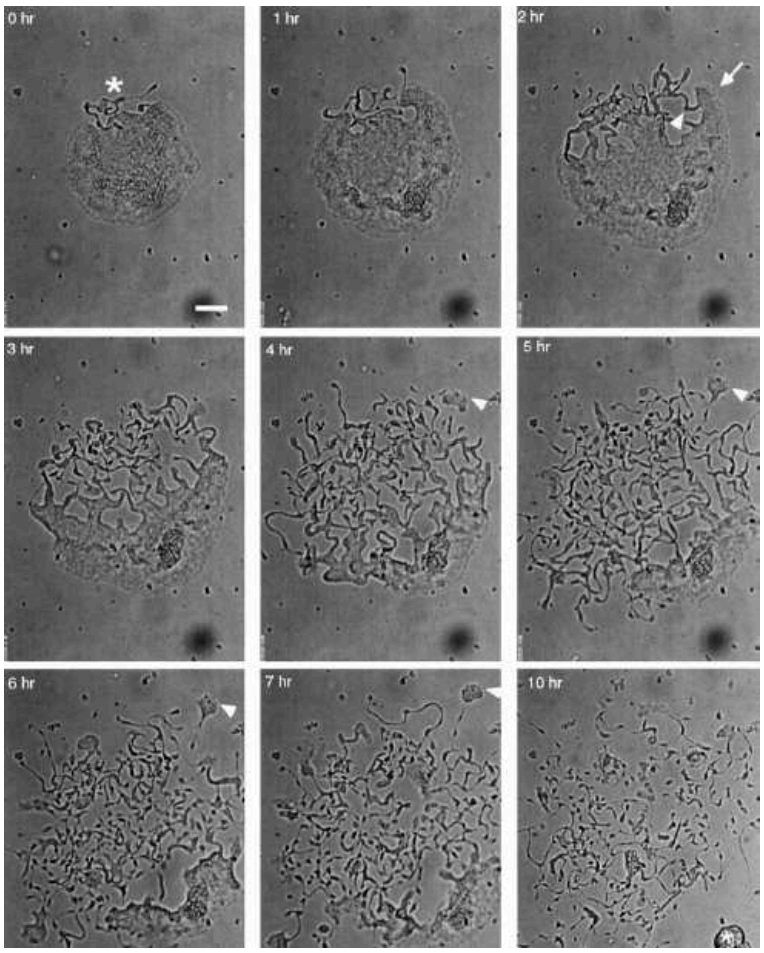

Figure 4.2: **Platelet production in static conditions**. Mouse megakaryocyte forming *in vitro* proplatelets. The formation starts on one side (asterisk symbol). The proplatelets become thinner and thinner, elongate and some platelets detach (arrow heads 4 h to 7 h). Image from [207].

4.1.2 Production in dynamic conditions

In 2003, Li et al. [209] presented a bioreactor to culture and differentiate murine embryonic stem cells into a wanted cell type. The first bioreactors proposed for *in vitro* platelet production has been described in 2009. Dunois-Lardé et al. [7] showed that MKs perfused at high flow rate in a microfluidic channel coated with VWF release platelets at a much faster pace than in static conditions. The second one described by Sullenbarger et al. [210] uses a 3D scaffold coated with fibronectin and thrombopoietin to support the cells and facilitate stem cell differentiation into MK and the production of platelets. Later, taking into account the oxygen gradient present in the bone marrow, they improve their system by controlling the oxygen content [211]. However, the system does not allow accurate control of pressures and shear stress, the production runs continuously for one day for a yield of

platelets produced of one per cultured MK.

Systems mimicking the vascular niche

In vivo MK differentiation takes place in the bone marrow. In order to mimic the migration of MK from the bone marrow to the blood vessels, Nakagawa et al. [212] developed a device in which the chambers are separated by a wall pierced with oblique micro slits. This porous wall mimics the endothelium of a sinusoid irrigating the bone marrow. Figure 4.3 shows the design of the channel. MK are trapped between the slits and generate platelets. The top flow applies pressures onto MK whereas the bottom flow applies shear forces loading to cytoplasm pieces that have the same size as *in vivo* platelets. The number of platelets produced with this manner is 3 to 6 fold higher than in static conditions. That is a promising result, but they do not present the membrane biomarkers CD41 and CD42b that are necessary for platelet activation.

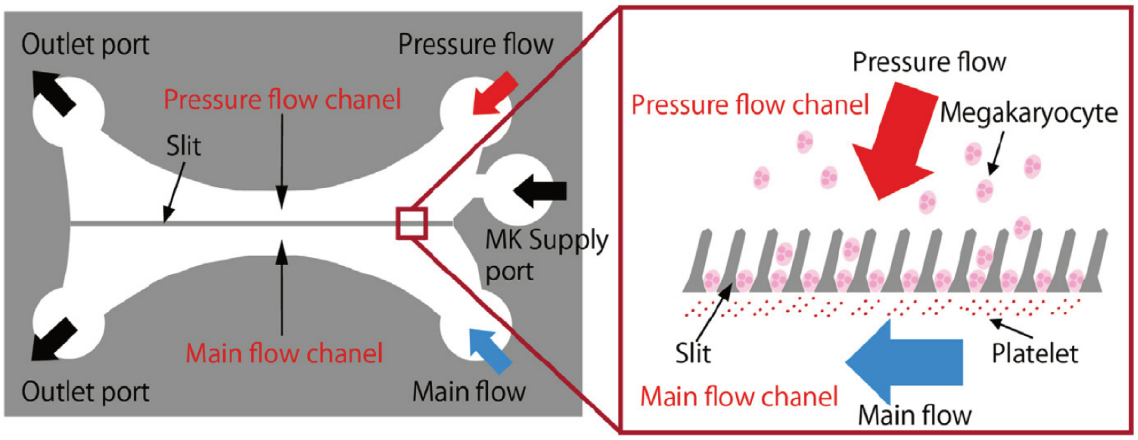

Figure 4.3: **Platelet bioreactor, slit design**. The pressure flow and the main flow directions form an angle of 60°. MK are perfused in the top part of the channel. They are trapped between slits of width 16 μm separated by 4 μm. The shear rate exerted by the main flow helps the production of platelets. Each part of the system is connected to one outlet. Platelets are collected in the bottom outlet. Figure from [212].

Later, Thon et al. [213] proposed a microfluidic device based on the same principle as the one presented by Nakagawa et al. [212]. The main difference is the shear rate imposed on the MK trapped between the slits (100 to 1000 s^{-1}) and the geometry of the gaps. Instead of tilted slits with a gap of 4 μm, this system propose slits more shallow than in the previous model (Figure 4.4). The system improves the time of platelet release, instead of 18 hours needed in static conditions, this device allows a production in two hours, and increases platelet production yield by 50 % in comparison with static conditions. However, only few MK can be trapped in the gaps. In order to capture more cells it is needed to modify the geometry of the system.

Systems mimicking the bone marrow

Pietrzyk-Nivau et al.[202] propose a method of culture in 3D using hydrogels. The porous 3D

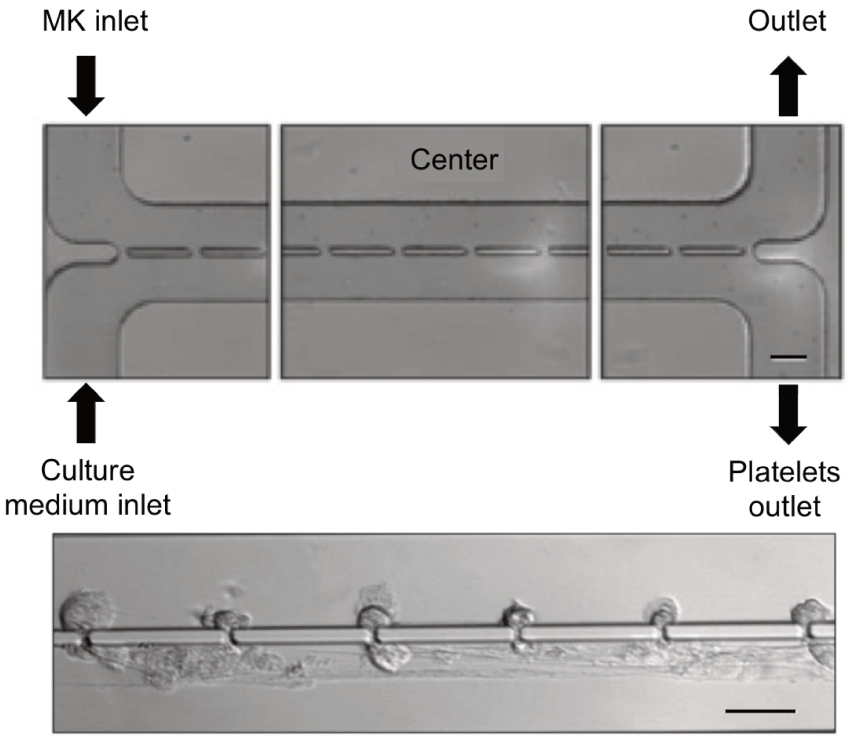

Figure 4.4: **Platelet bioreactor, 2 μm gap design**. Sketch of the microfluidic device with successive columns of 10 μm per 90 μm separated by 2 μm. Bottom picture shows the production of proplatelets from a primary mouse MK perfused at a shear rate of 60 s^{-1}. Scale bare 50 μm. Figure from [213].

architecture of the hydrogel provides an environment close to the one of the bone marrow and mimics the bone marrow stiffness. Culture of hematopoietic stem cells in hydrogel have been shown to differentiate into MK [214] and produce platelets. Platelets have been tested in flow cytometry and present CD41 an CD42b membrane receptors. Mimicking bone marrow environment in 3D architecture seems to help MK differentiation and production of platelets.

Di Buduo et al. propose an hybrid system for studying both the differentiation of MK in the bone marrow and the production of platelets in the vessel. It consists of a cylindrical microchannel in a mixture of silk, fibronectin and collagen, mimicking the bone marrow vasculature, and embedded in a hydrogel seeded with MK [215] (Figure 4.5). Mature MK seeded into the hydrogel travel through the silk sponge and finally adhere to the silk microtube. There, proplatelets are extruded from the MK through the silk vessel and the endothelial cells. The platelets produced flow freely through the microtube. Here, culture medium optionally supplemented with RBC is perfused at a shear rate of 60 s^{-1}. In order to control the microtube stiffness, several mixtures have been tested. The advantage of this system is its great similarity with the physiological conditions.

Platelet formation in the capillaries: importance of shear rate

The effect of shear rate on platelet production has been studied *in vitro* in the group of D. Baruch [7]. In order to submit MK to the physiological shear rate reached in blood capillaries, pressures are

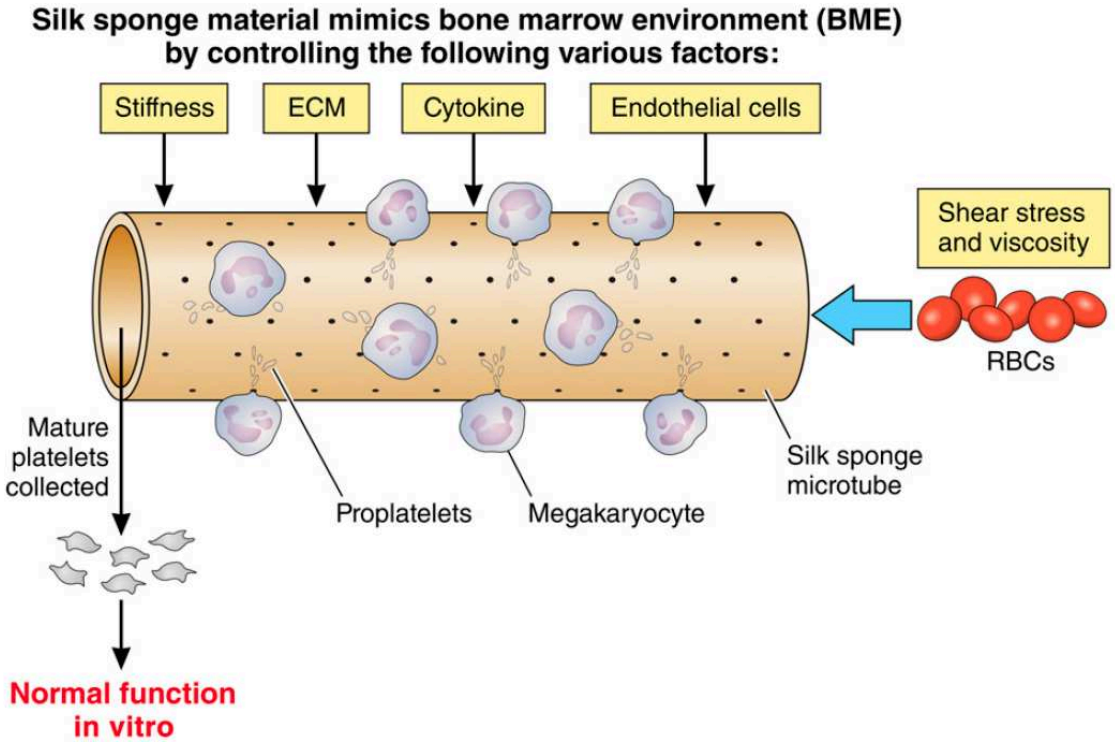

Figure 4.5: **MK differentiation and platelet production in a biomimetic channel**. Sketch of an *in vitro* megakaryopoiesis principle. MK are seeded on the silk sponge, mature and migrate in the microtube. There they start to extend proplatelets through the silk membrane mimicking the bone marrow sinusoid vessel. In the bottom part of the microtube, endothelial cells are cultured and release cytokines that help MK maturation. Into the microtube, RBCs in culture medium or culture medium alone is perfused with a shear rate of 60 s^{-1}. Platelets produced join the internal flow and are collected at the end of the microtube. Figure from [216].

adapted to reach a shear rate of 1800 s^{-1} on the wall. A rectangular bioreactor is coated with VWF in order to interact with MK. Among MK interacting with VWF they distinguish MK immobilized at the surface that will probably elongate, from MK that translocate on VWF in a temporary rolling motion. The high shear rate allows the MK to break and release platelets after only 20 minutes perfusion. However, platelets are generated close to the wall in the microfluidic chamber. There is a risk of activation in case of prolongated contact with VWF [217]. Also most MK flow through the chamber at high velocity and do not interact with the VWF. Thus they do not elongate neither they produce platelets. Even among MK interacting with the VWF, some are just translocating at the surface and stop.

A second bioreactor has been designed with a forest of pillars in the chamber in order to increase the surfaces coated with VWF and optimize the MK capture yield. Each of the sixteen channels is 500 μm wide, 52 μm deep and 17.3 cm long. Into the straight part of the serpentine shape is a forest of pillars coated with VWF [8]. The interaction between the VWF and the MK allows to trap advected MK behind the pillars (Figure 4.6). Each pillar is able to trap one MK. The number of pillars is calculated in order to trap enough MK to produce a large amount of platelets. Anchored MK elongate in the bulk until they break into pre-platelets and platelets. The pillars have the advantage to make MK release platelets in the bulk, which avoids platelet activation. The bioreactor aims at producing

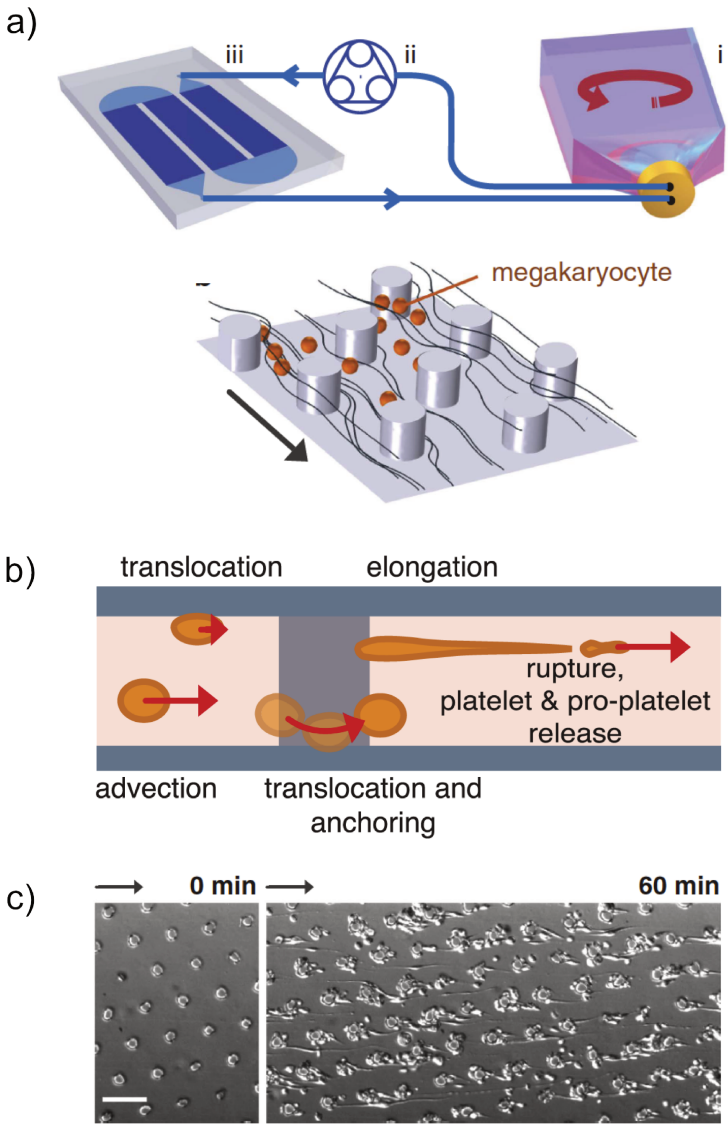

Figure 4.6: **Platelet production in high shear rate**. **(a)** Sketch of the experimental device. Cell suspension, located in the culture flask (i) is perfused thanks to a peristaltic pump (ii), into the bioreactor (iii). It forms a loop, cells that are not captured at the end of the bioreactor return to the flask and are perfused again and again. The dark blue region corresponds to the forest of pillars coated with the specific VWF protein. Pillars are arranged in a tilted hexagonal lattice. This configuration make each MK (orange spheres) streamline (black lines) to encounter at least one pillar. **(b)** Side view of the channel representing only one pillar. The MK roll (translocate) on the surface or is advected in the flow. When it encounters the pillar, it translocates at its surface and anchors behind the pillar. Then it elongates and breaks into preplatelets and platelets. **(c)** Top view of the forest of pillars before cell perfusion and after one hour perfusion. Scale bar is 100 μm. Figure from [8].

a lot of platelets to collect and characterize them. The number of platelets produced after 2 hours of perfusion is enough to test their functionality with standard experiments in microscopy, cytometry and aggregometry. These tests have shown that platelets produced are non activated when collected and able to activate. Almost 4 platelets / MK are collected which is quite low in comparison with the physiological yield (10^2 - 10^3 platelets / MK) [218]. An explanation of the low platelet per MK obtained is that some of them are not mature enough to produce platelets. Among anchored MK some

are not elongated and do not produce platelets. Platelets produced *in vitro* in these devices could benefit from a better understanding of the biomechanics of cell elongation and rupture.

4.1.3 Focus on a microfluidic device to understand platelet formation from isolated cells

Platelet formation principles are multiple and we do not completely understand which parameters conduce to platelet release from MK. High shear rates are necessary to accelerate platelet production and the MK perfused in the microfluidic device containing VWF-coated pillars produce functional platelets. In the forest of pillars the lack of visualization of the phenomenon is a limit to understand platelet production process since pillars modify cell elongation trajectory (Figure 4.7). We design a new microfluidic device in order to visualize cell anchoring, elongation and rupture for single cells. In this chapter we use time lapse microscopy to study elongation and rupture at the individual cell scale, as well as an attempt to monitor oxidative stress in an elongating cell. We perform experiments in parallel with cord blood MK in Paris at INSERM U1140, and with the DAMI cell line in Compiègne at UTC. We propose methods to analyze cell elongation kinetics, and characterize their spatiotemporal evolution. Also we attempt preliminary experiments to predict cell rupture.

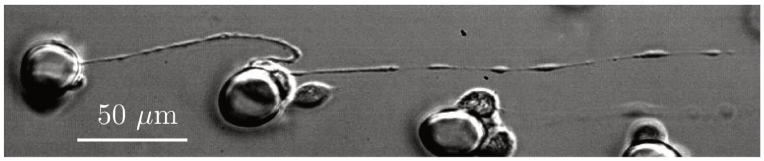

Figure 4.7: **Elongation of a MK on a pillar**. Top view of a MK whose elongation trajectory is modified by the other close pillars in the chamber. Figure from [8].

4.2 Material and Methods

4.2.1 Microfluidic device and fabrication

The microfluidic device geometry is represented in figure 4.8. In comparison with the bioreactor, the number of obstacles (pillar (Figure 4.8) or beam (Figure 4.9)) is reduced in the chamber. More space (1 mm) between two obstacles is dedicated to the observation of the elongation that occurs in the flow direction. The device consists of a straight channel of thickness 34 μm, width 2 mm and length 17 mm with twenty columns of thirty-three suspended pillars (or thirteen suspended beams), attached to the roof but not to the glass slide. Pillars have a diameter of 30 μm and thickness 20 μm. Beams are 100 μm wide, 20 μm thick and 2 mm long, and separated from each other by 900 μm. The system is produced in PDMS using the protocol described in chapter 1, section 1.2.1. In the chapter, the system with pillars is used for experiments on cord blood MK and the system with beams is used with the cell line.

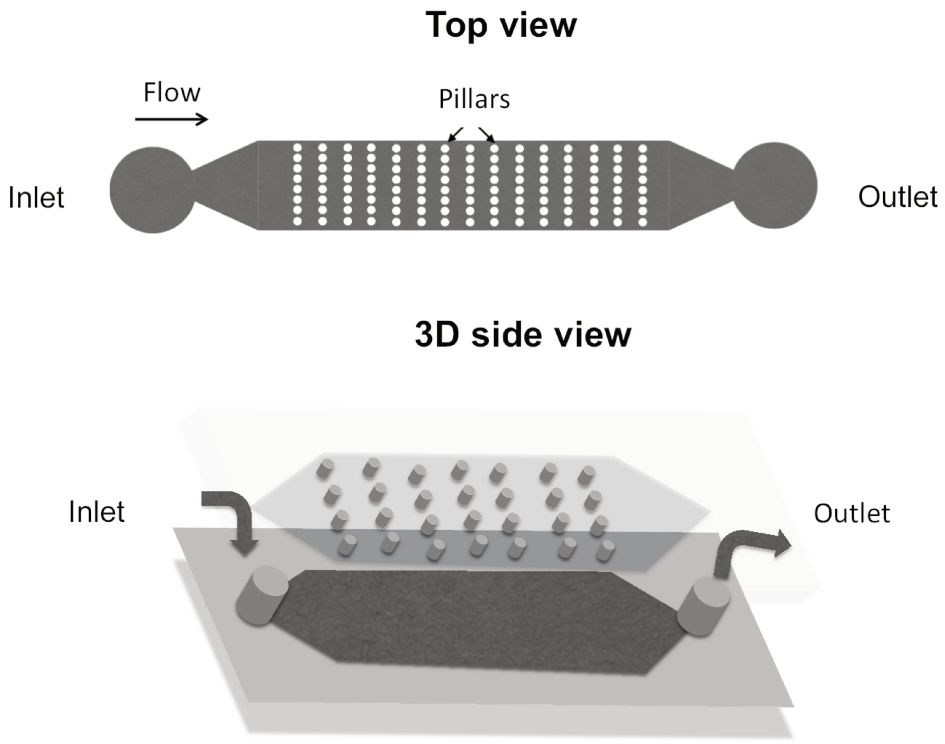

Figure 4.8: **Design of the microfluidic channel used for single MK elongation study**. Sketch of the top view of the channel of width 2 mm. It consists of twenty columns of thirty-three suspended pillars of diameter 30 μm each and 20 μm thick. The distance between the wall and pillars is 14 μm.

In order to trap cells on the surface of the pillars we coat microsystems with VWF. VWF is dissolved in PBS (phosphate-buffered solution; pH 7.4, Gibco, ref : 10010-031) at a concentration of 40 μM. The microsystems are filled the day before experiment with 15 μl of this solution and stored overnight at 4°C in a humid atmosphere.

4.2.2 Cell preparation

First experiments have been performed at INSERM U1140 on primary MK. However, during these experiments, several technical problems appear such as the visualization of cell filaments in both bright field and fluorescence. In order to address these experimental challenges, we perform experiments at the UTC with the stimulated DAMI cell line that presents less heterogeneities than primary cells, and is more repeatable. Also it is easier to culture, is less expensive, requires less chemical drugs and can be manipulated in laboratory of biosafety level L1.

MK from cord blood: INSERM experiments

Megakaryocytes are differentiated from cord blood provided by the Saint Louis Hospital cell therapy unit. $CD34^+$ hematopoietic stem cells isolated from cord blood by an immunomagnetic technique are cultured by S. Poirault-Chassac , at INSERM U1140, in Paris. Culture is performed in medium IMDM-BIT 15% (Iscove modified Dulbecco medium, and BSA Insulin Transferrin, Stem cell Technology), supplemented with α-monothioglycerol (Sigma-Aldrich) and liposomes. The first 5 days of

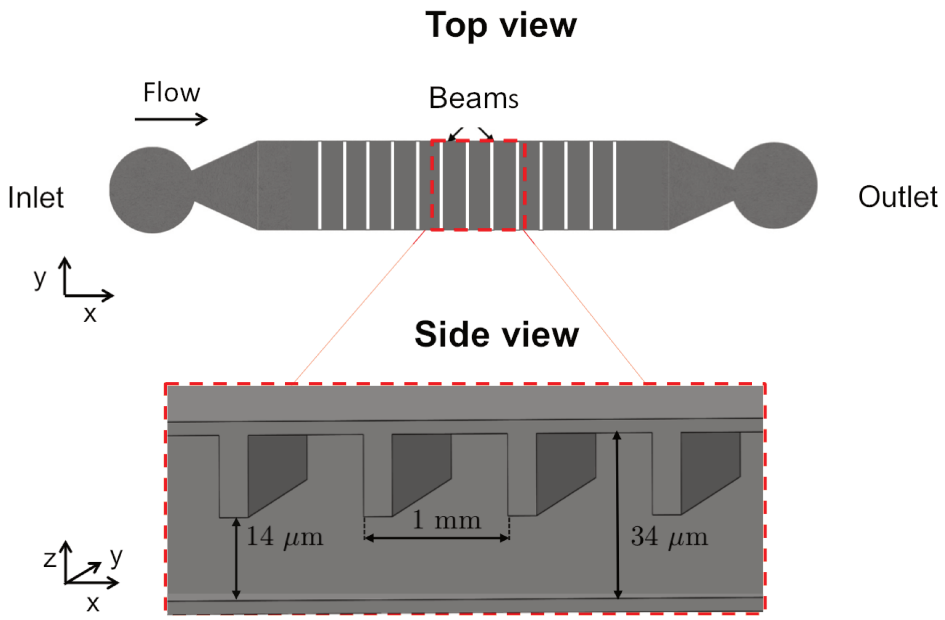

Figure 4.9: **Design of the microfluidic channel used for single DAMI cell elongation study and laser ablation**. Sketch of the top and side views of the channel. It consists of thirteen suspended beams of 100 μm wide, 20 μm thick and spaced by 900 μm. We call suspended beam the thickest part of the PDMS that forms upper beam in the channel. The channel width is 2 mm, which corresponds to beam length.

culture, 3.2 10^5 cell/mL are cultured in the medium supplemented with 50 nM of thrombopoietin (TPO), a hormone involved in MK differentiation, and 20 ng/mL of stem cell factor to help differentiation. From day 6, the medium is only supplemented with 20 nM of TPO. Until maturation (at day 12 or 13), cells are maintained at 7 10^5 cells/mL.

After 12 or 13 days of culture MK are centrifuged at 163 rcf for 10 minutes and the pellet is diluted in 1.5 mL of IMDM medium. Cells are placed on the top of a BSA gradient of 5 layers respectively at 2%, 5%, 7%, 10% and 12%. The tube is centrifuged 15 minutes at 80 rcf. Mature MK are separated from progenitors, and platelets already formed in statics. They are suspended in IMDM medium at a concentration of 2 10^5 cell/mL.

Then they are exposed 20 minutes at 37°C to 10 μM of MitoSOX (Invitrogen, Grand Island, NY, USA). MitoSOX is an indicator of the presence of superoxide ion in mitochondria. Its fluorescent properties are presented in figure 4.10. Its absorption wavelength is 510 nm and the emission wavelength is 580 nm. Finally cells are diluted in IMDM medium at a concentration of 2 10^5 cell/mL in 5 mL to 10 mL.

DAMI cell line: UTC experiments

DAMI cell culture is detailed in chapter 2 section 2.2.2. Cells are treated with blebbistatin (BBI) 40 μM for 1 day in a 48 wells cell culture plate. Each well is filled with 10^5 cells in 1 ml of medium MEM supplemented with 10 % FBS and 1 % penicillin and streptomycin. We fill as many plates as required for perfusion. Prior to staining, cells are centrifuged 5 minutes at 290 rcf and suspended in 1 ml PBS.

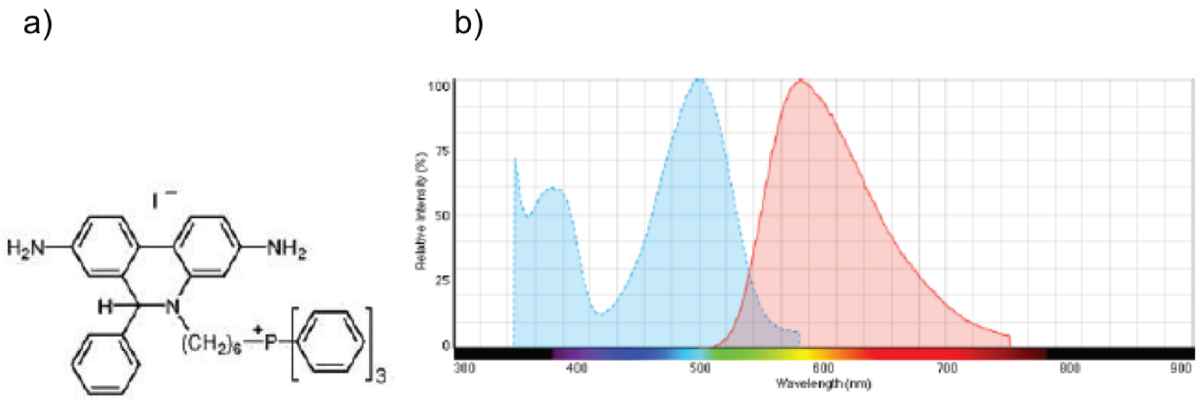

Figure 4.10: **MitoSOX fluorescent properities**. Product information by Thermo-Fisher. **(**a) MitoSOX chemical structure. (b) Absorption (blue line) and emission (red line) spectra for the fluorochrome.

Then they are exposed 10 minutes at 37°C to 1 mM of MitoSOX. In order to avoid centrifugation-induced cell damage, we do not rinse the probe with PBS but dilute it with 4 ml of MEM without antibiotics and FBS. Experiments are performed in the dark in order to avoid bleaching.

4.2.3 Experimental setup for perfusion

MK from cord blood

Experiments with the cord blood MK are performed at the INSERM U1140. The microfluidic device is placed onto the stage of an inverted microscope (Zeiss Axiovert) on which is mounted a high sensitivity numerical camera (Rolera MGi+). The channel is connected to a syringe pump with silicon tubes. The system is rinsed with PBS at a shear rate of 1800 s^{-1} (i.e. a flow rate of 41 μL/min) to remove unbound VWF. Then cells are perfused 1 h 30 min to 3 h and are observed in bright field or in fluorescence.

DAMI cell line

Experiments with the DAMI cell line are performed at the Université de Technologie de Compiègne. The microfluidic device is placed on the stage of an inverted microscope (Leica DMI 6000B, Leica Microsystems, Germany) on which is mounted a fluorescent camera (Leica DFC300 FX, Leica Microsystems, Germany)). The channel is connected to a pressure pump (MFCS 2 bar, Fluigent) with PEEK tubes of internal diameter 0.25 mm. Prior to cell perfusion the system coated with VWF is rinsed with PBS at 20 mbar for at least 15 min. Then we replace the PBS solution by the cell suspension. We fixe the pressure at the entrance at 104 mbar to generate a shear rate of 1800 s^{-1} on the wall. A gentle agitation of the cell reservoir allows the suspension to remain homogeneous. Part of the cells adhere on VWF and we follow the behavior of single cell elongation. We want to avoid having too many cells in the system. The cell suspension is infused in the system for 20 minutes. Then, the cell reservoir is disconnected and replaced by a reservoir containing pure medium. Adherent cells are thus exposed to a constant shear stress, but their number remains low so that they do not interfere with one another.

4.2.4 Image acquisition

Acquisition starts 20 minutes after MEM perfusion, i.e. 40 minutes after cells enter in the channel, in order to let them elongate. To follow cell elongation over time, we acquire images in time lapse which is an acquisition mode allowing to take images at a regular frequency allowing to follow the elongation over a period of time. We choose the frequency of the time lapse and the illumination parameters in order to avoid bleaching of the fluorescent probe.

MK from cord blood

Images are acquired in bright field and then in fluorescence on different cells. Bright field acquisitions are performed simultaneously on 5 cells during 40 minutes at the magnification of $\times 20$ or $\times 40$ with a time lapse of one image per second. Images are acquired in fluorescence with an excitation wavelength of 510 nm, for 5 minutes, on cells stained with MitoSOX. Images are post treated using the Image J software. The physical length of one pixel is 16 μm. The superposition of bright field and fluorescent images on one cell is not possible with this set-up because when the microscope switch between fluorescence and bright field filters the microscope stage moves.

DAMI cell line

The microscope presents the advantage to acquire fluorescent and bright field images on the same field with a delay of 2 seconds corresponding to the time required to switch filters. Images are acquired in bright field and in fluorescence with an excitation wavelength of 580 nm at a $\times 20$ magnification. The exposure time is set to 70 ms in bright field and between 800 and 1000 ms with the filter N21 in fluorescence. The light intensity is set respectively to 18 % in bright field and 5 % in fluorescence. Images are post treated using the Image J software. The physical length of one pixel is 17 μm.

4.3 Elongation characterization

4.3.1 Shape of the elongated filament

We observe the elongation of MK in the microfluidic device coated with VWF. All MK behave differently under flow and their shape vary over time. We can distinguish four steps illustrated in figure 4.11. First, the MK is captured at the surface of the pillar. It interacts with VWF factor and is always anchored behind the pillar where it is submitted to hydrodynamic forces. Second, it elongates in the direction of the flow. The filament is thick and become thinner with elongation. Third, we can notice heterogeneities in the filament that looks like undulations. Finally, the filament condenses in some areas and form beads. The MK has a shape of necklace with several beads corresponding to future preplatelets or platelets, we call this shape beads on a thread. It is known that elongation is an heterogeneous process over time [219]. In the present work, we seek to quantify these heterogeneities and focus on the elongation velocity.

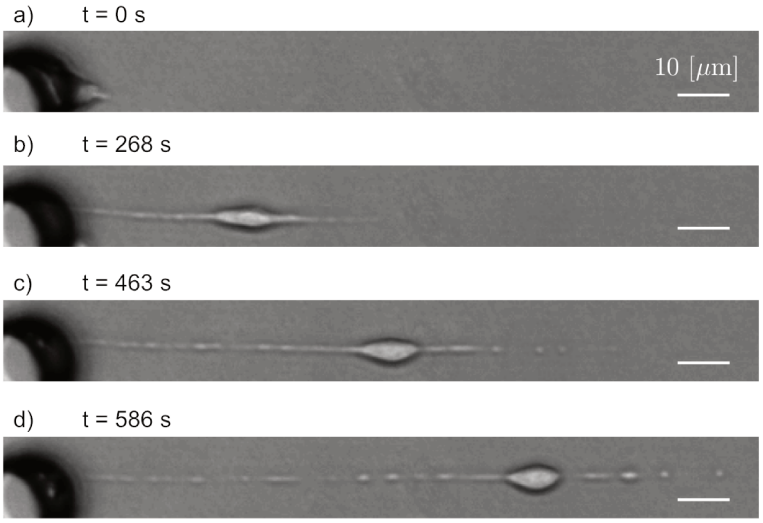

Figure 4.11: **The different steps of MK elongation**. Images of the elongation of a MK from cord blood after 14 days of culture (by Ilyesse Bihi). **(a)** First the MK is captured onto the pillar coated with VWF. **(b)** Second, the cell elongates in the flow. The cytoplasmic filament is thick and elongates in both side of the cell body. **(c)** Then condensation areas appear and form an undulation shape. **(d)** Finally the filament forms a chain of pearls as a necklace.

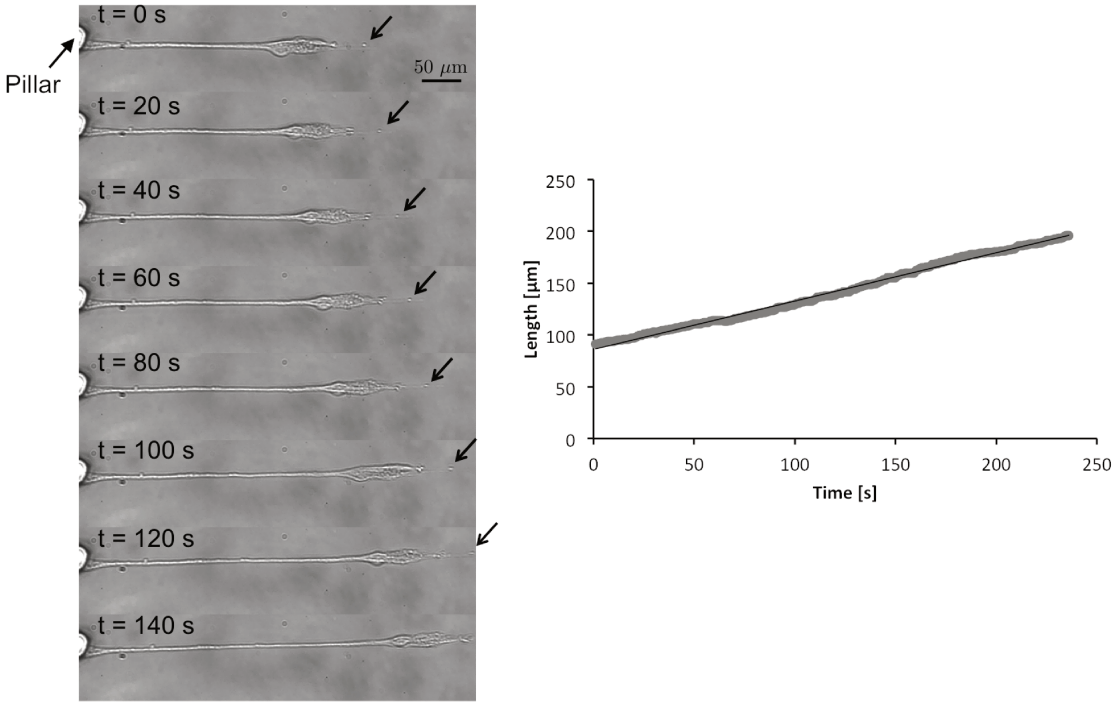

Figure 4.12: **Elongation of a MK**. The flow is from left to right. Scale bar 50 μm. A cord blood MK is observed in bright field. **(a)** Acquisition of images by Meriem Lebsir. Pictures of successive images of the elongation. Black arrows point the evolution of the position of a bead over time. **(b)** Plot of the total length of the cell over time. Experimental points are plotted in grey. The black line is the linear fit. We find an average velocity of 0.446 $\pm$ 0.006 μm/s.

4.3.2 Elongation velocity over time

We characterize cell elongation by measuring the distance between the pillar where the MK is captured and the end of the elongated filament over time. Images are acquired with a frequency of

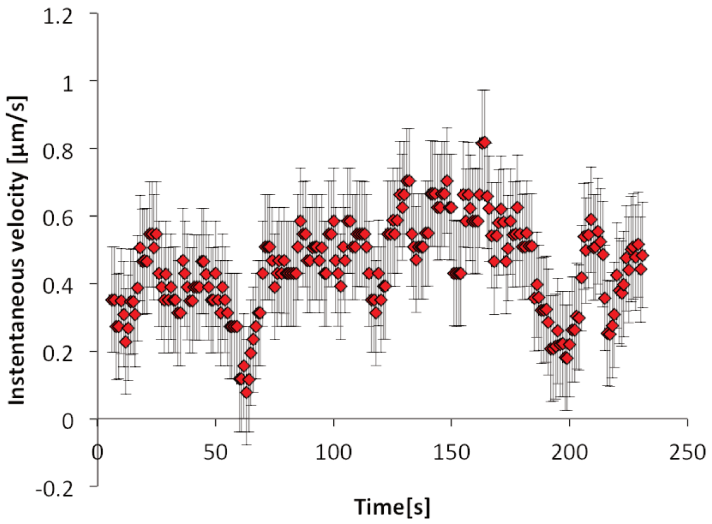

Figure 4.13: **Plot of instantaneous velocity over time**. The instantaneous velocity values of the distance run by the end of the filament over 10 s are the red diamonds.

one image per second. Figure 4.12 shows a MK in elongation and a plot of the total distance of the MK as a function of time. We fit the experimental value with a linear regression. We find an average velocity of 0.446 μm/s. In order to better visualize the evolution of the velocity, we plot in figure 4.13 the instantaneous velocities as a function of time. Each point corresponds to the instantaneous velocity calculated over 10 seconds. In this example, we notice that the velocity remains positive, which suggests the filament does not retract during the acquisition period. However, the velocity is not constant over time. The filament does not elongate with a constant velocity, we observe acceleration phases (0 s to 15 s ; 60 s to 90 s; 200 s to 215 s), deceleration phases (15 s to 60 s; 160 s to 200 s) and constant phase (90 s to 160 s).

The instantaneous velocity is defined as $U = L/t$ where U is the velocity, L the length and t the time (t=10 s). Assuming an error of 2 pixels when measuring the filament length, we get a precision ΔL = 0.8 μm. Error bars correspond to the uncertainty on U calculated as $\Delta U = U\frac{\Delta L}{L}$, and are smaller than data points in figure 4.12. We plot the instantaneous velocity as a function of time for 11 MK and find an average elongation speed between 0.29 $\pm$ 0.10 μm/s and 0.98 $\pm$ 0.14 μm/s. It exists a large variability between two cells that can be due to their intrinsic properties.

4.3.3 Spatial distribution of elongation velocity

We plot the spatiotemporal diagram in figure 4.14 of the filament elongation namely kymograph. It corresponds to the modification of grey intensity over time along the filament. The pillar is on the left of the image, it is recognizable by the vertical straight line corresponding indicating that it does not move over time. The MK followed has a beads-on a thread shape and elongates. The variation of intensity along the horizontal axis is due to the presence of beads. Thus we can follow the position of remarkable beads over time. The filament does not linearly elongates. If elongation was linear,

each bead would follow straight lines on the kymograph which is not the case. Sometimes a segment between two beads slows down and sometimes it goes faster. We can notice, on figure 4.14 that the elongation is heterogeneous inside the cell. Even if on average the cell elongates (the position of the free extremity moves towards the right side of the image while the other is anchored to the pillar), some segments between two beads stretch (segment (ii)) while others contract (segment (iii)). Also we notice the apparition of beads over time (blue arrows in segment (i)) corresponding to condensation zones in high elongation rate areas.

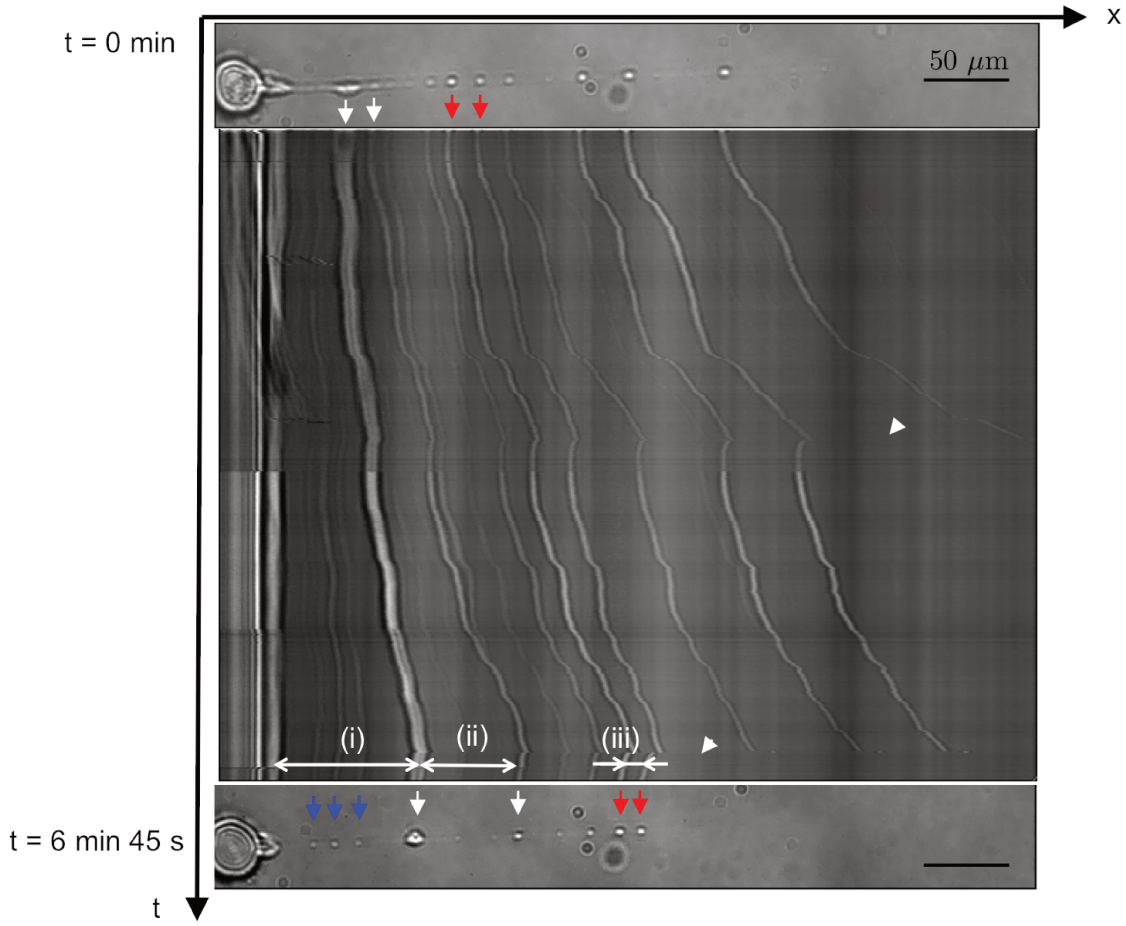

Figure 4.14: **Spatiotemporal diagram of cell elongation**. Acquisition of images by Meriem Lebsir. Cord blood MK elongation under flow. At $t = 0$ min acquisition starts. We stop it after 6 min 45 s. The spatiotemporal diagram allows to follow the behavior of the filament over time. Red arrows show the initial and the final positions of two single beads. (i) The apparition of beads (blue arrows), visualized in the spatiotemporal diagram as new lines. (ii) Elongation of the segment between the two beads pointed with the white arrows. (iii) Local retraction of a segment between the two beads pointed with the red arrows. Write arrow heads point times of ruptures. After rupture we observe a global contraction of the filament. Scale bare 50 μm.

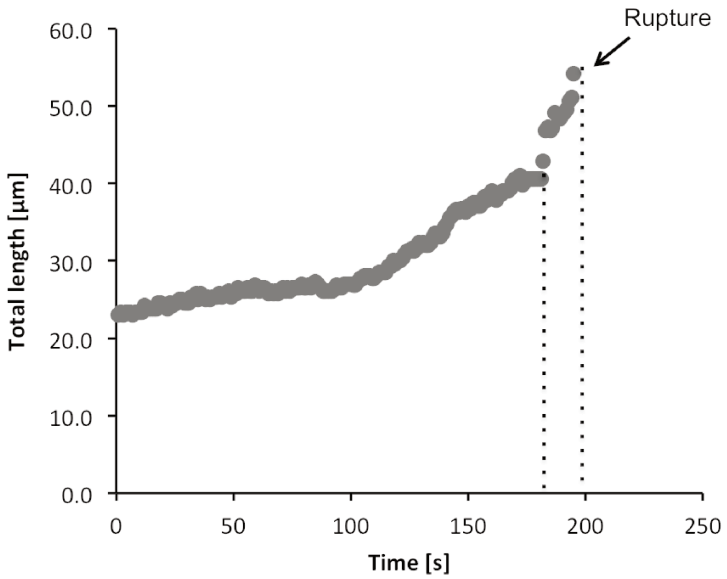

Figure 4.15: **Acceleration between rupture**. Acquisition of images by Meriem Lebsir. Plot of the distance as a function of time for a MK which breaks after 195 s elongation. During the 10 s prior the rupture elongation accelerates.

4.3.4 Study of ruptures

In order to visualize the beads, we perform with a $\times 40$ magnification. Thus the spatial resolution is 205×205 μm. MK can grow much longer. For this reason we are not able to visualize the whole filament in the same field and we probably miss ruptures occurring out of field. Thus, rupture is a phenomenon rarely observed in our device. However, on the 25 MK followed during one of the experiments performed, five ruptures have been observed. In figure 4.15, we show the velocity of one of them. We observe an acceleration of elongation during the 10 seconds preceding rupture.

In this section, we focus on the last 10 s preceding each rupture event, and we seek to quantify the heterogeneity in elongation velocity described in section 4.3.3. On five cells we distinguish 52 segments that do not break and 9 segments that break (several ruptures can occur on the same cell). A segment is the distance between two beads detected when there is a modification of intensity in the filament. We call non-rupture the events between two beads that do not break, and rupture the events where ruptures occur. We measure the length of each segment juste before rupture, their elongation velocity during the 10 seconds before rupture and the elongation rate. The elongation rate is calculated as the elongation velocity as a function of the segment length. In table 4.1, we present the average value of length (l), velocity (V) and elongation rate.

We observe that on average segments that break have an elongation velocity greater than the one of segments that do not break. Segments where ruptures occur are longer than non rupture segments (Figure 4.16).

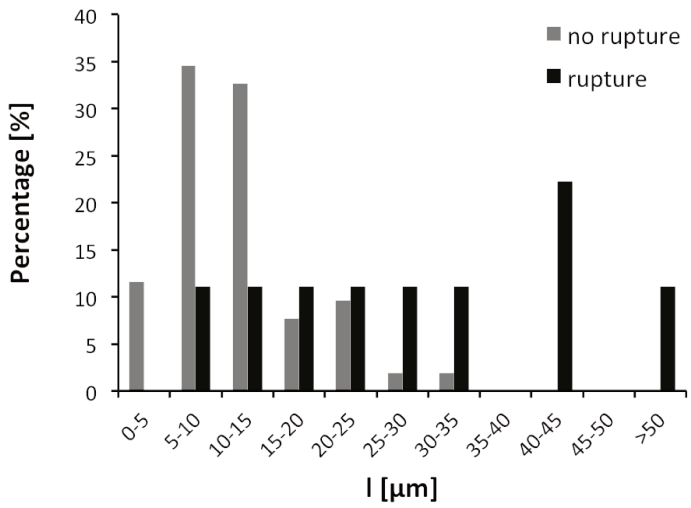

Figure 4.16: **Histogram of the distribution of length for rupture and non rupture segments**. 52 non rupture segments and 9 rupture segments on 5 MK have been measured.

Table 4.1: **Summary of rupture and non rupture measurements**. Measurements of the average length (l), average elongation velocity (V) and average elongation rate for rupture and non rupture segments. Results are expressed as the mean $\pm$ the standard deviation.

	l [μm]	V [μm/min]	Elongation rate (min^{-1})	Number of segments
Non rupture	11.6 ± 6.2	3.2 ± 15.8	0.2 ± 1.0	52
Rupture	30.9 ± 18.7	17.2 ± 18.7	0.6 ± 0.5	9

At the scale of the whole cell, it is already known that the elongation velocity is inhomogeneous. We demonstrate here that elongation rate inside the cell is also highly heterogeneous. In the next section we try to simultaneously monitor cell metabolism and elongation.

4.3.5 Role of the reactive oxygen species

MK elongation is a very dynamic process involving fast and local cytoskeleton reorganizations. To better understand which regions of the cell are actively involved in this process, we use fluorescent microscopy to map the metabolic activity in elongating MK. Many cellular reactions are fueled by oxygen [220], in particular during MK differentiation [221] and platelet production [222], we choose to target ROS and in particular mitochondrial superoxide anion. We use the fluorescent probe MitoSOX (Red mitochondrial superoxide indicator for live-cell imaging) which is specific to the mitochondrial superoxide anion ($O_2{}^{\cdot -}$). In this section we study the effect of elongation on the production of the superoxide anion in fluorescence by staining cells with MitoSOX.

On cord blood isolated MK: INSERM experiments

In this section, we present results obtained by Meriem Lebsir [223] during her master thesis. The fluorescence intensity is averaged in a delimitated area kept constant in all images and containing the

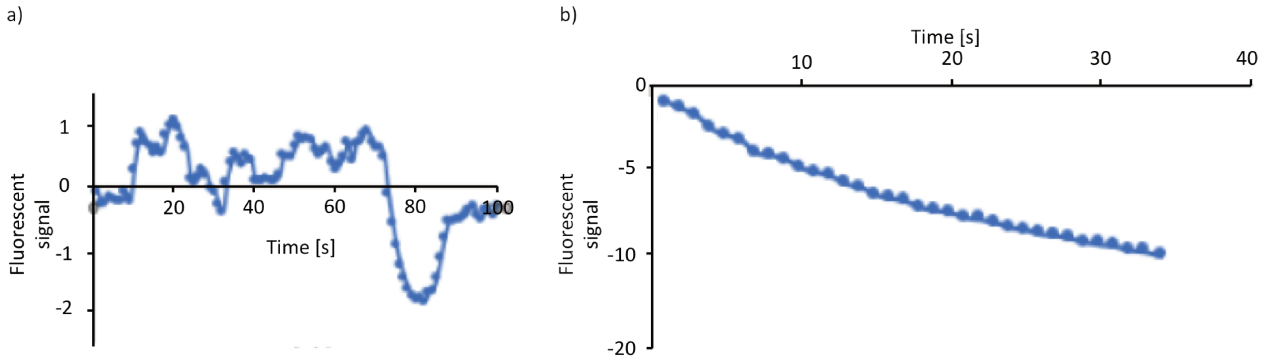

Figure 4.17: **Plot of the fluorescent signal as a function of time for cord blood MK**. Adapted from [223]. **(a)** Fluorescence acquisition starts after 37 minutes perfusion. The fluorescence intensity vary over time resulting on the presence of superoxide anion. **(b)** Fluorescence acquisition stats after 2 hours perfusion. The fluorescent signal decreases over time, probably resulting on photobleaching.

cell filament in each image. In order to avoid noise due to background signal and the signal of cells in flow, the region of interest is chosen as close to the filament as possible. We call fluorescent signal the difference $(F_t - F_0)$ between the mean fluorescence intensity at time t (F_t) and the mean fluorescence intensity in the first image of the acquisition at time $t = 0$ s (F_0). In figure 4.17 (a), we measure the fluorescent signal of one cell as a function of time. Acquisition is performed for 100 seconds after 37 minutes of perfusion. We observe fluorescence signal variations. Since MitoSOX stains the super oxide ion produced by mitochondrial activity, fluorescence traduces its presence. At high fluorescent signal we assume an extensive mitochondrial activity. On the contrary, figure 4.17 (b), acquisition is performed for 34 seconds after 2 hours of perfusion. We observe a decreasing profile of the fluorescent signal as a function of time. We observe no pic of fluorescence, the signal only decreases over time probably resulting of photobleaching.

We seek to understand if the production of ROS occurs in specific elongation sites: beads, high elongation rate, or close to the extremity of the filament. We have to distinguish real variation in the fluorescent signal (indicating ROS activity) to photobleaching which is the degradation of the fluorescent molecule by light. Fluorescence acquisition should be performed before 40 minutes to observe mitochondrial activity and avoid bleaching of the fluorescent probe MitoSOX. However, the inability of the microscope to switch between fluorescence and bright field without moving the microscope stage, does not allow us to make correlation between elongation rate and the production of ROS neither their position into the filament. Moreover, to study the influence of elongation on the production of superoxide anion, we have to wait the MK elongates enough which requires some time.

Improvement of the protocol with the DAMI cell line: UTC experiments

In this section, we seek to develop a protocol to superimpose bright field and fluorescent observations, and avoid photobleaching. We perform these experiments at the UTC where the fluorescent microscope allows to switch filters between bright field and fluorescence. We use the DAMI cell line

to establish the protocol because their culture is easier than the one of MK, more reproducible and requires less chemical agents. Since the cell line behaves as immature MK we decide to treat it with 40 μM BBI that have been shown to mimic the behavior of mature MK in chapter 2. Images are successively acquired in bright field and in fluorescence. For a same period of time and a same field, we follow the cell elongation in bright field and the production of superoxide anion in fluorescence.

Both images are not acquired simultaneously since the microscope has to switch filter between the two images. Time to change filter between bright field and fluorescence is 2 seconds. During one cycle the microscope acquires images and changes filters twice. Thus to acquire one image with the superposition of bright field and fluorescence it takes almost 5 seconds. It corresponds to the highest step time we can impose during the time lapse. Figure 4.18 presents one cell which elongates for almost 10 minutes. We measure the elongation velocity on seven cells and on average, we find 0.055 $\pm$ 0.001 μm/s which is much lower (by a factor 10) than cord blood elongation velocity find in previous section (0.50 $\pm$ 0.17 μm/s). Two of the consequences are that we observe the whole elongation of the filament as its length is smaller for DAMI cells than for cord blood MK but ruptures and high elongation rates are rare. Moreover, for these experiments, cells are treated with BBI only for one day as at this time the role of BBI on the cell line was not well known. However we show in chapter 2 that after 3 days of treatment with BBI they become larger and mimic mature MK behavior. Increasing the treatment duration should increase the ability of cells to elongate.

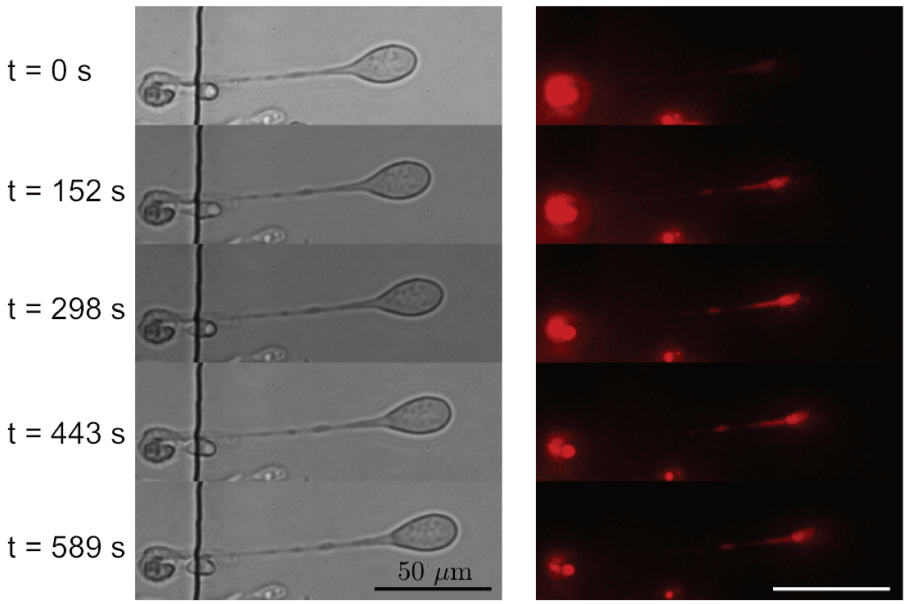

Figure 4.18: **Pictures of DAMI in elongation in fluorescence and bright field**. Images acquired by O. Chaput and G. Aldebert. On the left succession of images in bright field of the elongation of a cell treated 1 day with BBI and stained with MitoSOX. On the right, corresponding images in fluorescence.

We observe in the previous section that the elongation is faster during the 10 seconds preceding rupture. However, the temporal limit imposed by the switch between filters does not allow to precisely study rupture phenomenon. The technique only allows us to detect the superoxyde anion in

the condensed zone of the cell (beads, body)(Figure 4.18). Into the filament the signal is lower. Even if the concentration in superoxyde ion is the same than in the beads and body, the reduction of the width of the filament can be sufficient to explain the decrease in fluorescent signal. The filament is so thin in non condensed zones that the fluorescent signal will maybe be too low to be detected with our camera, whatever the concentration in superoxyde ion. Also the results suggest that the observation of fluorescence variation, traducing mitochondrial activity, should be performed before 40 minutes experiment. In order to detect if the mitochondrial activity is related with cell elongation and/or rupture, we should in future work analyze small regions of interest in different parts of the filament in order to correlate the evolution of the fluorescent signal and the elongation velocity or the probability of rupture.

4.4 Conclusion

We studied single cell elongation behavior in microfluidic chambers and we observe that the elongation speed is not homogeneous during a period of time as it has already been demonstrated in the literature [219]. We also noticed spacial heterogeneities along the filament: some segments elongate while others contract. The reason of these heterogeneities is unknown but we remark acceleration during the 10 seconds prior each rupture. Spontaneous ruptures are rarely observed because elongated filament of cord blood MK is longer than the view field of the camera and we do not know yet how to predict rupture. In next chapter we develop a method to initiate artificial ruptures to be studied.

It is known that ROS are involved in megakaryocyte maturation and platelet production thus, we suppose that ROS may have a role in MK elongation and rupture mechanisms. We stained cord blood MK with MitoSOX to follow the production of the mitochondrial superoxide anion during elongation at the INSERM U1140. We find a variation in fluorescence only for cells observed before 40 minutes perfusion. Beyond 40 minutes, we observed a decrease of the fluorescent signal due to photobleaching.

In order to superimpose images acquired both in fluorescence and in bright field, we carry out experiments at the UTC on the DAMI cell line. We manage to perform time lapse observations alternating between BF and fluorescence during 40 minutes without photobleaching. We show that the fluorescent signal is present in beads and the cell body proving the mitochondrial activity. However the length of the filaments is not long enough to quantify the implication of elongation in the production of the superoxide anion.

The superposition of fluorescence and bright field is essential for this study. In future work experiments on cord blood have to be performed at the UTC in order to quantify the influence of elongation on superoxide anion production. However we are now able to follow the elongation of a cell in fluorescence and bright field. It is a promising tool to understand elongation and rupture mechanisms that will be performed in the frame of the TRIMEP project.

Chapter 5

Laser ablation

Contents

5.1 Introduction

5.1.1 Cytoskeleton remodeling during PLT formation

During the formation of platelets, mature MK extend long cytoplasmic protrusions called proplatelets in the blood circulation [224]. These dramatic morphological changes involve fast reorgani-

zation of the cytoskeleton. Observations in diverse *in vitro* models of platelet formation indicate that elongating MK shrink if exposed to a massive dose (10 μM) of microtubule-targeting drug nocodazole [7], but not if the drug concentration is lowered to 100 nM [219]. Nocodazole triggers microtubule disassembly at high concentrations, but only prevents polymerization of the free ends at lower doses. These results seem to indicate that microtubules, but not microtubule growth, is necessary for MK elongation. Elongation is also reversed upon addition of a dynein inhibitor, that prevents microtubules from sliding along one another [219]. In this study, MK were genetically modified to express a GFP-labeled EB3 protein, so that the extremity of microtubules was fluorescently stained. This is to our knowledge the only work where cytoskeletal dynamics are observed in elongating MK. Sliding-induced elongation rates as high as 3 μm/min are measured, and hydrodynamic forces can further accelerate elongation in dynamic bioreactors as high as 30 μm/min. Viscous forces applied on the filament are on the range of nano Newtons, while a bounding between MK and VWF is only some pico Newton order of magnitude [225]. Thus, MK cytoskeleton is involved in cell elongation and at the same time balance hydrodynamic forces together with anchoring forces due to VWF-MK interactions.

At the end of this process, platelets have a discoid shape due to the presence of a bundle of coiled microtubules, called marginal band, under their membrane [226]. Because microtubules are extremely rigid, with a persistence length of about 1 mm, the energetic cost of assembling them to form the marginal band is high and this structure has to be the result of an active, regulated process [227]. The very late stages of platelet formation, when the elongating MK breaks to release proplatelets, have not yet been studied in detail.

Spontaneous ruptures of MK from cord blood as well as from cell line is rarely observed in our bioreactors. All the cells perfused do not elongate, and all elongated cells do not break. Moreover, the total length of an elongated MK is often longer than the field view of the camera. So the likelihood of a rupture occurring in a random field of view is very low. In the previous chapter, we identified high segment length and elongation rate as signatures of an imminent rupture. Although this will help selecting appropriate field of views for capturing rupture events, another strategy is developed in this chapter.

We aim here at studying rupture by controlling when and where it occurs in the filament. We propose to severe microtubules and study the variation in elongation velocity. To do so we adapt the method of laser ablation, usually used in static conditions [228], in flow. Laser ablation technique is not available at Université de Technologie de Compiègne but is a complementary tool to understand the filament elongation behavior. For this reason, we initiate a collaboration with the INM (Institute of New Materials), in Saarbrücken, in Germany, in the lab of Jun. Prof. Dr. Franziska Lautenschläger who is specialist in cell biophysics.

5.1.2 History and applications of laser ablation

Electrons present in the external layer of the atom can absorb or emit energy as photons. Energy of a photon is given by the equation of Planck-Einstein [229]: $\Delta E = h\nu$, where h is the Planck constant, ν the light frequency in hertz (Hz) and ΔE the energy of absorption or emission. Figure 5.1 illustrates the principle of atom absorption and emission of photons. When an atom receives a photon with a specific wavelength, it adsorbs the energy and is in an excited state. Spontaneously, the atom can go into ground state by emitting a photon. In the case an excited atom receives a photon, it induces the way to go back into the original state of the atom and emit a second photon with exactly the same wavelength, frequency, phase and direction that the photon received. That is the principle of stimulated emission.

In 1960, Maiman [230] invented a principle stimulating optical beam using a ruby. A laser (Light Amplified Stimulated Emission Radiation) is a source of monochromatic, unidirectional, coherent light, of high intensity, based on the principle of simulated emission. A laser consists of many atoms placed in a chamber between two mirrors. Some photons excite the atoms which will at some point be almost all activated. When one of these atoms spontaneously go back to its ground state it emits a photon able to initiate a cascade of stimulated emissions from the excited atoms. The mirrors reflect the photons and create a laser beam.

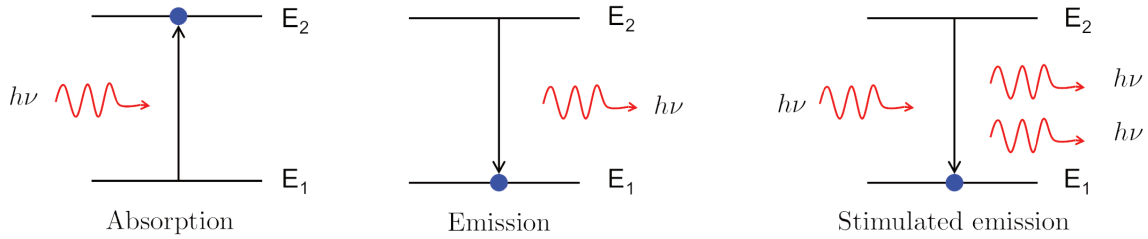

Figure 5.1: **Absorption and emission of photons**. Spontaneous absorption of a photon consists of a gain of energy $h\nu$ for an electron. When an electron loses energy the atom spontaneously emits a photon. In the case an electron is already in the upper layer of energy and receives external excitation as a photon, it emits two photons. This phenomenon is called stimulated emission.

When a high intensity laser is focused on a small area, the exposed material is damaged: this is the principe of laser cutting, welding, and ablation. Laser ablation can be used on metals for example for the formation of colloids [231] or the control of crystalline nanowires formation [232]. The experiment is performed in a solvent to trap the colloids. Soon after the invention of laser ablation on materials, it was clear for researchers that the method will have many applications to manipulate and damage biological samples [228]. One of the first experiment on biological tissue has been realized in 1965 where Amy et al. [233] damaged a mitochondria with a ruby laser beam. But it is in the 80's that the microsurgery using laser really starts to be used on biological structures [234]. Even if the method is not recent it has been improved a lot and the use of lasers on biological samples presents many advantages due to the precision and specificity of the technique. It is now possible to ablate either part of a cell or a part of a whole organism.

The study of laser ablation on metals has been coupled with biological applications. In biolog-

ical tissues, it is known that metallic ions are not homogeneously distributed. In order to help the diagnosis of some diseases, laser ablation can be used to quantify the presence of ions in a slice of tissue, for example in brain [235]. Other complex structures such as : zebrafish kidney [236], veins [237] or axon repair [238, 239]; have been studied. The main objective is to understand how biological structure repairs and what is the role of specific components in complex cellular functions such as: migration, differentiation, growth and apoptosis. Usually these functions were studied by disturbing the cell. Microneedles were commonly used to dissect a cell [240, 241]. However, the study of cell behavior and reparation is limited by the alteration of the membrane. To study the different organites of a cell with microneedles, we need to isolate them [242]. On the contrary, laser ablation allows sub-micrometric accuracy and is a non invasive method. Organites do not have to be isolated to be studied. Due to its ability to dissect and ablate many different structures and its non-contact interaction with the sample, laser ablation is used at several scales in laser surgery: single cell, tissue, and internal cell structure.

At the cellular scale, the principle is to focus a laser on the region of interest in a cell and disturb it without killing it with a sub-micrometer precision [243]. Many studies have been accomplished on mitochondria [244] and cell cortex in order to understand the role of microtubules [245, 246] and actin stress fibers [247–249]. They can be visualized with fluorescent probes and are ablated to understand their biophysical properties. Severing cytoskeletal elements such as actin and microtubules allows to measure tension forces [250–252] in the filaments, and repair after ablation [253, 254]. Several studies have taken advantage of laser ablation to study the forces involved in different stages of cell life. For example, studies have been performed on the junction between two epithelial cells to determine the tension involved in cell aggregation [255–257]. Because ablation does not kill the cell, other applications consist to study how cells repair after damage. Cell cytoskeleton ablation induces the apparition of blebs [258] which is the consequence of the cytoplasmic pressure release. After a while, the cell gets back to its initial position. Many studies are also conducted on cell differentiation to understand which phenomenons are involved in mitosis [259], or the separation of the two daughter cells.

The last step in cell differentiation is called abscission. The mechanisms leading to cell division and how the microtubules are reorganizing into the daughter cells have been described thanks to a combination between traction force microscopy and laser ablation [260]. The laser damage the filament between the two daughter cells (Figure 5.2, a) and the traction forces of the cell before and after ablation are studied. However, ablation does not necessarily leads to breakage. In figure 5.2 (b), we present a partial ablation. Only the microtubules are damaged but the membrane persists keeping the link between the two daughter cells. The microtubules are able to grow again in the membrane tube. Later spontaneous abscission will occur. This work inspired us to study tensions in elongating cells. The production of platelets from megakaryocytes is similar to abscission. Both mechanisms are governed by the reorganization of microtubules and the final result is the rupture of a filament. The main difference is that abscission is studied in static conditions on adherent cell while megakaryocyte rupture is studied in flow. Thus the use of traction force microscopy can be used to know forces in the case of abscission. However, for elongated MK in flow it becomes more challenging. The flow

induces adding forces and the measurement of tension is not direct. So we will only focus on characteristic velocities of elongation and contraction before and after ablation.

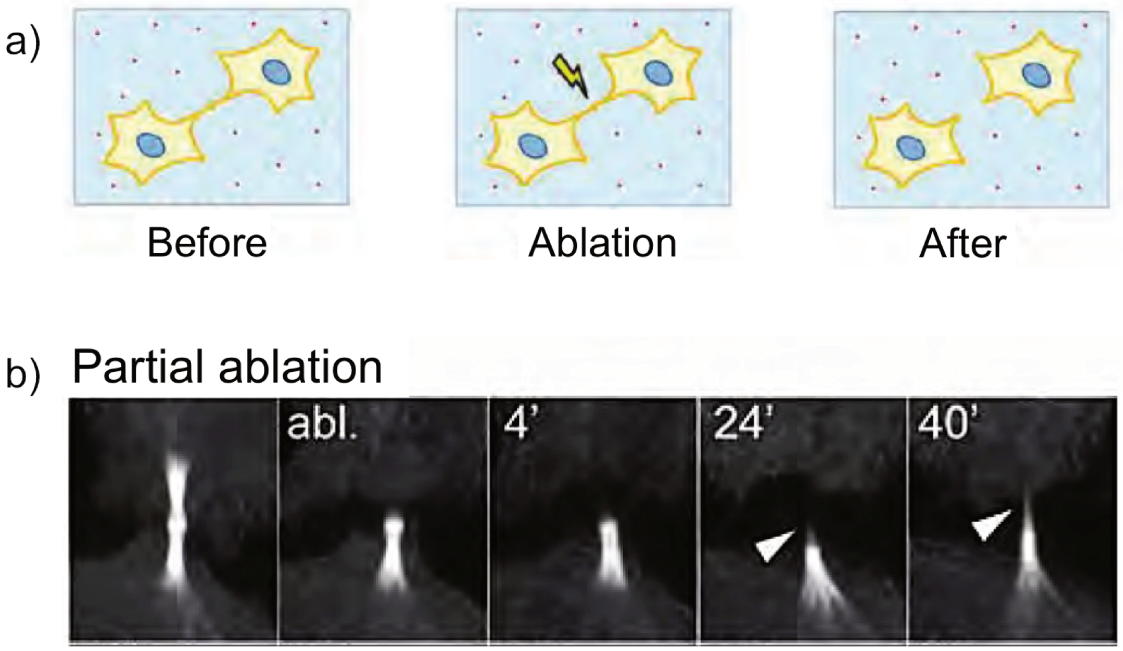

Figure 5.2: **Sketch of laser ablation on cells before abscission**. Abscission is the last step of cell division when the two daughter cells are separated. **(a)** Laser ablation on the bridge between the two cells permits to mimic abscission and measure traction forces of the cells by measuring the displacement of the cells in the substrate. **(b)** With a lower power intensity of the laser, partial ablation of the bridge is possible. Microtubules are cut but the membrane is not damaged. Microtubules regrow in the membrane tube and reform the bridge. abl. is for ablation and the time is seconds after ablation. Arrow heads show the regrowth of the microtubules. Image adapted from [260].

5.1.3 Principle of the laser ablation technique

Laser ablation is based on the highly focus beam which induces enough energy to damage a material. The confocal microscope on which is mounted the MicroPoint laser allows to visualize the cell in bright field to have an overview of the cell, and in fluorescence to focus the laser on the zone of interest. There are two lasers involved in the optical path. First, the CSU 647 (Confocal Scanning Unit) is used to visualize the microtubules in fluorescence with a wavelength corresponding to deep red. Second, the MicroPoint allows laser ablation experiments by focusing the laser onto the sample (Figure 5.3). The first pathway corresponds to common fluorescence microscopy (in blue in figure 5.3). The exciting light is emitted by a lamp. A filter selects the wavelength needed to excite the fluorescent probe. Then the beam is reflected on a dichroic mirror to be directed on the sample direction. It passes through the objective and illuminates the sample. The fluorescent probe is excited and emits light with an increased wavelength (in green in figure 5.3). The emitted light passes the objective and the dichroic mirror. Finally it passes through the emission filter before reaching the camera. The second pathway permits laser ablation. The MicroPoint laser is inserted into the pathway of the confocal microscope (in red in figure 5.3). The laser is reflected by the dichroic mirror. A tube length allows to

focus the laser on the sample with a high accuracy. Cells can also be illuminated in bright field as in all inverted microscope.

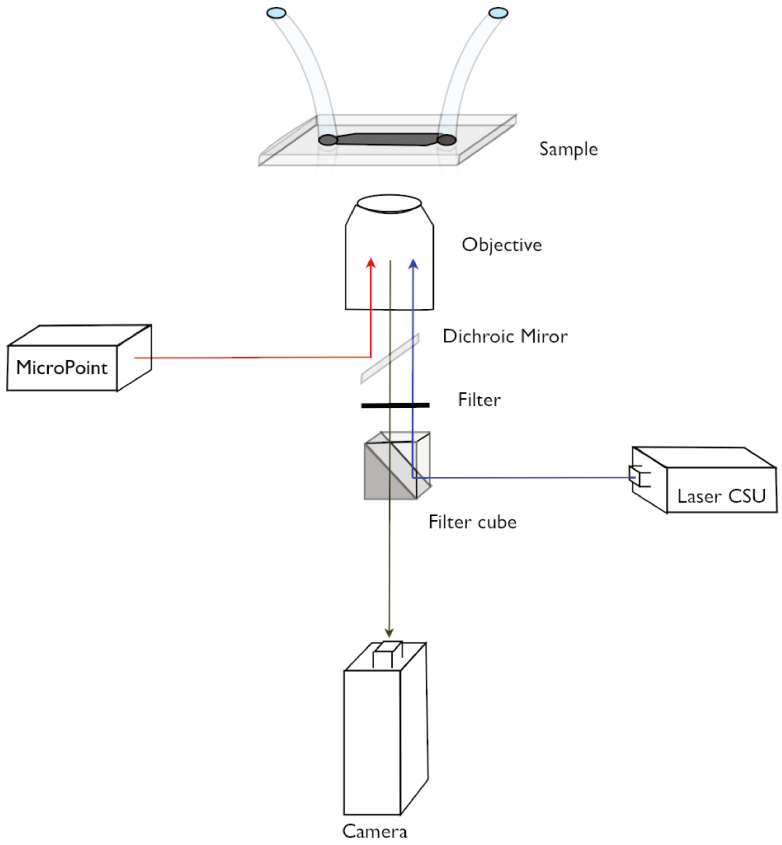

Figure 5.3: **Sketch of laser ablation principle**. Confocal microscopy and laser ablation (MicroPoint) are added on an inverted microscope. The sample is placed on the microscope platform and illuminated with a monochromatic lamp. One laser is used for the confocal microscopy, the visualization in fluorescence (Laser CSU) in blue. The laser beam has a specific excitation wavelength reflected on a filter cube. The path crosses the objective and illuminates the sample. The wavelength emitted by the fluorochrome is directed on the camera. The second laser is used for ablation (MicroPoint). It works the same way but is focused on a small specific area of the sample. It is used only few seconds and its high intensity saturates the camera.

5.1.4 Organization of the chapter

We propose in this chapter to study cell rupture with the method of laser ablation. The method is usually used in static conditions. In our case, it consists in severing microtubules by focusing a high intensity laser, without killing the cell. During ablation, we are not able to acquire images because the intensity of the laser saturates the camera. Nonetheless, we are able to switch between bright field images and fluorescent images in order to superimpose both responses. The objectives are (i) to adapt the principle of laser ablation, well known in static conditions, in flow; (ii) to understand the role of microtubules in rupture; (iii) to measure retraction times of the filament after rupture. This chapter is organized as follow. A first section (5.2) presents the geometry of the system, the preparation of cells and the experimental set-up. A second section (5.3) presents the elaboration of the laser ablation

experiment from static conditions to in flow conditions. A third section (5.4) presents where to ablate in an elongating cell. A forth section (5.5) shows the preliminary results obtained on elongation velocity, rupture and contraction velocity.

5.2 Material and methods

5.2.1 Microchannel design and fabrication

The microfluidic system geometry is presented in chapter 4 on figure 4.9. It consists of a straight channel of thickness 34 μm, width 2 mm and length 17 mm, with thirteen beams (also called ridges [104]) of width 100 μm, thickness 20 μm, and length 2 mm, separated by 900 μm. The system is produced in PDMS using the protocol described in section 1.2.1. The silicon mould was replicated in epoxy resin in order to be easily transported.

The resin (type R123 Soloplast, Vosschemie) is mixed with the hardener (type R614, Soloplast, Vosschemie) at a ratio of 1:3. Then the mixture is poured in a Petri dish (30 g epoxy for a dish of diameter 3.5 cm). It is placed next to the PDMS sample under vacuum. Air trapped during mixing escapes easily because the solution is not too viscous. The PDMS stamp is dropped on the epoxy surface. The air between the two surfaces diffuses through the porous degassed PDMS. After 2 days at room temperature the stamp of PDMS is peeled off the epoxy mold. The epoxy replica is ready to be used. The protocol is modified: PDMS poured in the replica is not placed at 70°C but reticulates at room temperature for at least 24 hours. This avoids the creation of chemical bonds between epoxy and PDMS. The PDMS chip is then punched and sealed onto a microscope cover glass.

Microsystems are coated with VWF in order to trap cells on the surface of the beams. VWF is dissolved in PBS (phosphate-buffered solution; pH 7.4, Gibco, ref : 10010-031) at a concentration of 40 μM. The microsystems are filled the day before experiment with 15 μl of this solution and stored overnight at 4°C in a humid atmosphere.

5.2.2 Cell culture and treatment

DAMI cells are cultured as described in section 2.2.2. We have shown in chapter 4 that after 72 hours of BBI treatment, the cells become larger and that the re-organization of the cell induces an ability to elongate. BBI inhibits myosin II A which is involved in the cytoskeleton cortex structure [183]. In the literature, Shin et al. have shown that a treatment of megakaryocytes (MK) with 20 μM BBI for 3 days increases the number of *in vitro* platelets produced [261].

Non treated cells tend to flow in the device without being trapped at the surface of the pillars. We observe that the yield of DAMI captured on VWF is optimized for a 3 days exposition to 40 μM of BBI.

5.2.3 Staining of cell cortex

We want to stain cell cytoskeleton and particularly actin filaments and microtubules in living cells and look for probes that have a minimal impact on the viability of cells and on their ability to elongate. We noticed during preliminary experiments at INSERM US-1140 that megakaryocyte activity is disturbed by intense illumination with blue wavelengths. The elongation is stopped and the platelets production inhibited (not tested with the DAMI). Thus we decided to avoid short wavelength and stain actin filaments and microtubules in separate experiments, using red probes.

At the INM the SiR-tubulin and the SiR-actin were available (Figure 5.4 a, b). Both are based on the silicon rhodamine fluorochrome whose absorption wavelength is 652 nm and the emission wavelength is 674 nm. That corresponds to far red wavelengths. Absorption-emission spectra are drawn on figure 5.4 (c).

SiR-actin is coupled with the drug jasplakinolide which binds to F-actin and allows its labeling in living cells. Jasplakinolide is known to have a role in the polymerization of actin [262]. A depolymerization of actin should not affect cell ability to elongate.

On the other hand, SiR-tubulin is based on docetaxel which is a microtubule-stabilizing drug close to paclitaxel (Taxol). Taxol is known to prevent microtubules depolymerization and has been used for more than 15 years as a chemotherapeutic agent [263]. As MK elongations are not governed by microtubule (de)polymerization but sliding, we expect little effect of paclitaxel on elongation.

We test both probes on DAMI cells treated 3 days with 40 μM of BBI, in static and in dynamic conditions, and on non-treated cells in statics.

Staining of actin

We stain F-actin in DAMI cells in suspension. Figure 5.5 shows images acquired in bright field and fluorescence mode after 1 hour incubation at 37°C with 1 μM of SiR-actin. The fluorescence intensity is low on average, and cells that appear bright are no longer round and likely to be damaged. In order to increase the fluorescent response, verapamil is often added to SiR at a concentration of 10 μM. This drug inhibits efflux pumps and calcium channels. We assume that the weakly staining is due to an active process in the cell leading to fluorescence release. Blocking the calcium channel has been shown in the literature to help SiR probe to stay into certain cell types [264]. The addition of verapamil could alter cell viability blocking the pumps but in our case it does not seem to modify the shape and viability of the cells (Figure 5.5, c). We notice that, in static conditions, the staining with SiR-actin is stronger with verapamil. As expected for suspended cells, the actin filaments form a ring on the boundary of the cell. The staining with SiR-actin + verapamil in figure 5.5 (d) shows a better efficiency than without verapamil in figures 5.5 (b).

We repeated the experiment with blebbistatin-treated cells. In Figure 5.6 we see that although

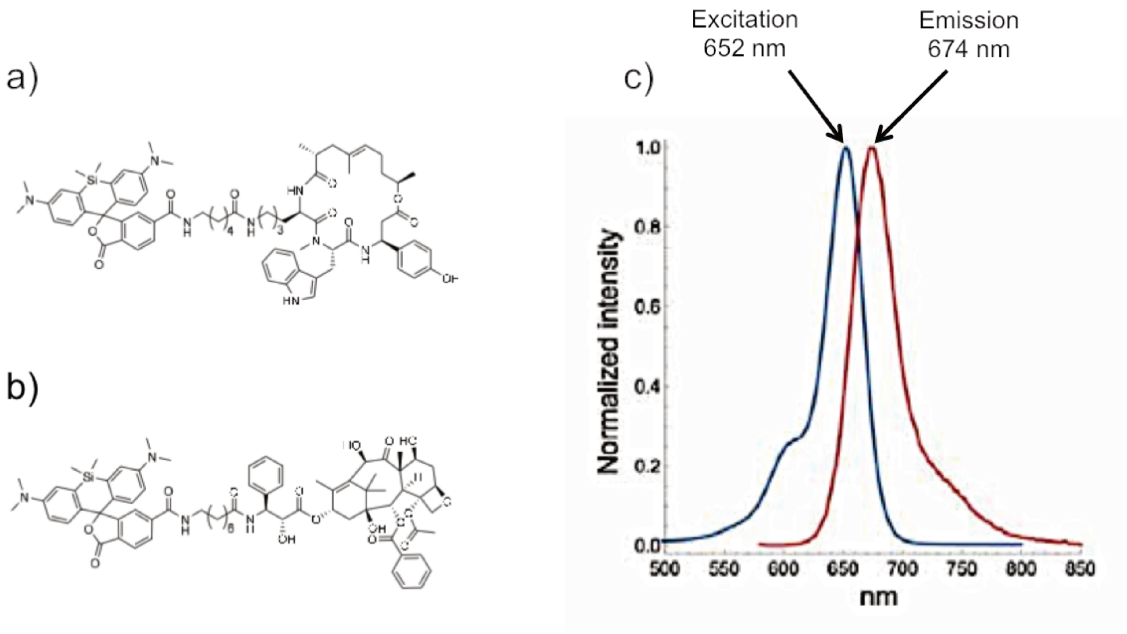

Figure 5.4: **SiR-actin and SiR-tubulin properties**. Product information by Spirochrome **(a)** SiR-actin chemical structure: $C_{71}H_{88}N_8O_{10}Si$, molecular weight 1241.6 g/mol. SiR-actin consists of jasplakinolide and rhodamine fluorochrome. **(b)** SiR-tubulin chemical structure: $C_{73}H_{86}N_4O_{16}Si$, molecular weight 1303.6 g/mol. SiR-tubulin consists of docetaxel and rhodamine **(c)** Absorption (blue line) and emission (red line) spectra for both fluorochromes.

BBI-treated cells are larger, they behave in a similar manner in response to SiR-actin staining: the fluorescence signal is low on average, and increases in deformed cells and upon addition of verapamil.

We use the protocol of perfusion detailed in chapter 4 section 4.2.3 with BBI-treated DAMI cells stained with SiR-actin and verapamil. We acquire images as soon as cells adhere to the surface. Soon after capture, we can visualize the ring of actin (Figure 5.7, b) in the cell body. But as soon as the cell elongates, the intensity becomes weaker and the filament is never fluorescent. The use of SiR-actin does not seem to be adapted to visualize the filament in fluorescence in order to ablate it.

Staining of microtubules

We stain microtubules (Figure 5.8) in DAMI cells which are in suspension, with (Figure 5.8 c and d) and without verapamil (Figure 5.8 a and b). We make same experiments on DAMI cells treated 3 days with BBI (Figure 5.9). We notice that, as SiR-actin, SiR-tubulin requires verapamil to enter the cell (Figures 5.8 d, and 5.9 d). Moreover, SiR-tubulin + verapamil seems to stain a large majority of cells and its efficiency is not modified with the presence of BBI.

In bright field, cells do not appear perfectly round but their cortex structure, visualized in fluorescence microscopy, is organized as expected [265]: a halo of actin superimposed with a coil of

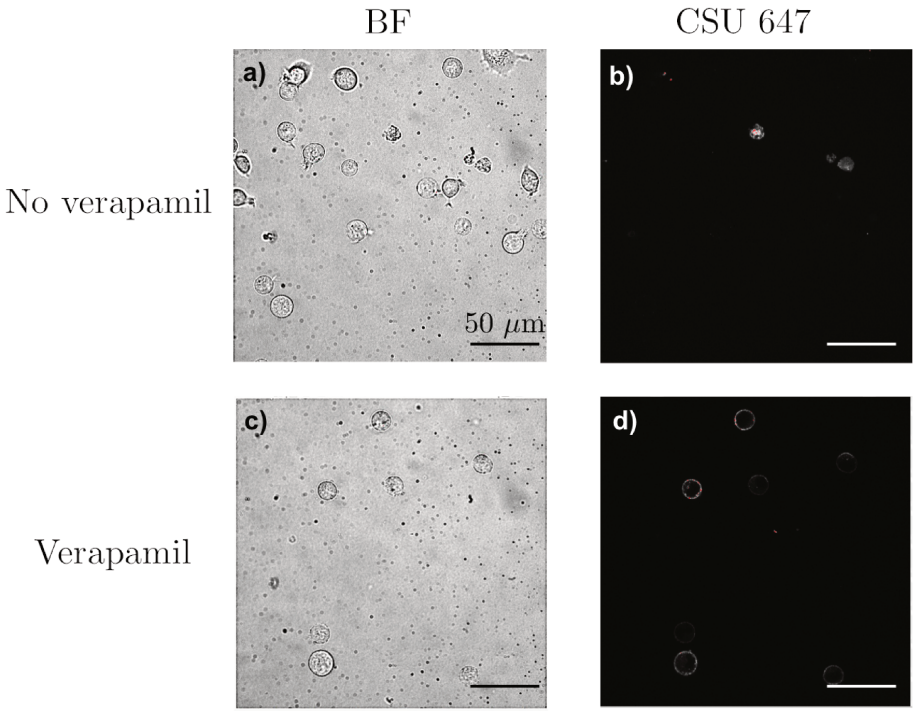

Figure 5.5: **DAMI stained with 1 μM SiR-actin**. **(a)** without verapamil, in bright field. **(b)** without verapamil, in fluorescence with emission wavelength of 647 nm. **(c)** with 10 μM verapamil, in bright field (BF). **(d)** with 10 μM of verapamil, in fluorescence with excitation wavelength of 647 nm. Scale bar 50 μm.

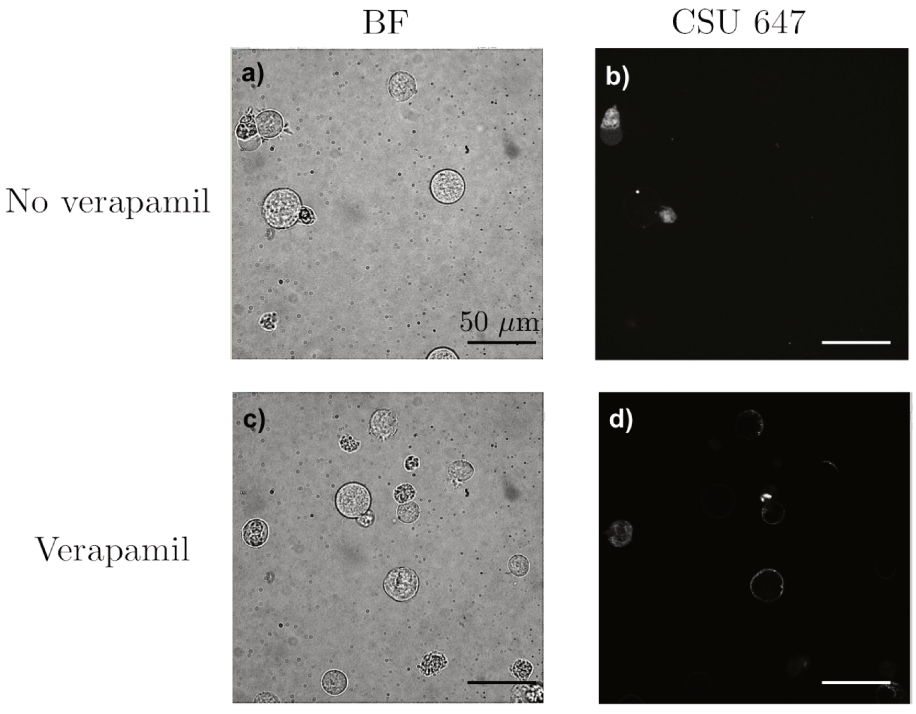

Figure 5.6: **DAMI treated 3 days with blebbistatin 40 μM, stained with 1 μM SiR-actin**. **(a)** without verapamil, in bright field. **(b)** without verapamil, in fluorescence with emission wavelength of 647 nm. **(c)** with 10 μM verapamil, in bright field. **(d)** with 10 μM of verapamil, in fluorescence with excitation wavelength of 647 nm. Scale bar 50 μm.

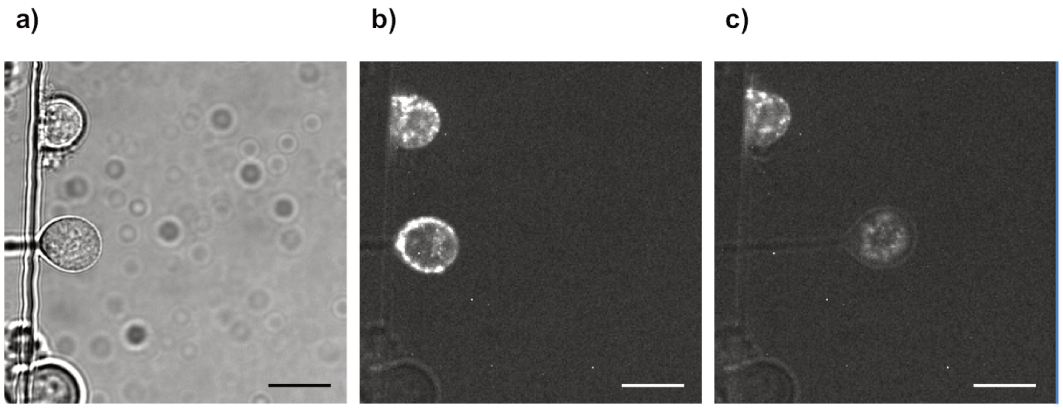

Figure 5.7: **Images of a DAMI in elongation stained with SiR-actin, supplemented with verapamil**. Flow is from left to right. Scale bar 25 μm. **(a)** Bright field picture, the cell elongates and form a thin filament. **(b)** Visualization of actin filaments in fluorescence, the intensity is lower in the filament than in the cell body.

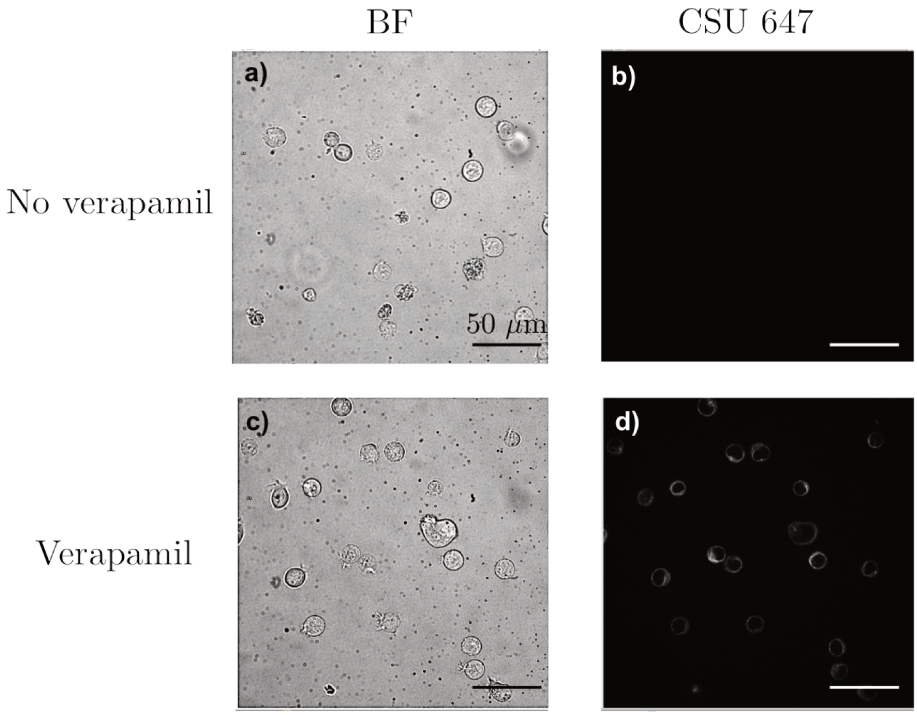

Figure 5.8: **DAMI stained with 1 μM SiR-tubulin**. **(a)** without verapamil, in bright field. **(b)** without verapamil, in fluorescence with emission wavelength of 647 nm. **(c)** with 10 μM verapamil, in bright field. **(d)** with 10 μM of verapamil, in fluorescence with emission wavelength of 647 nm. Scale bar 50 μm.

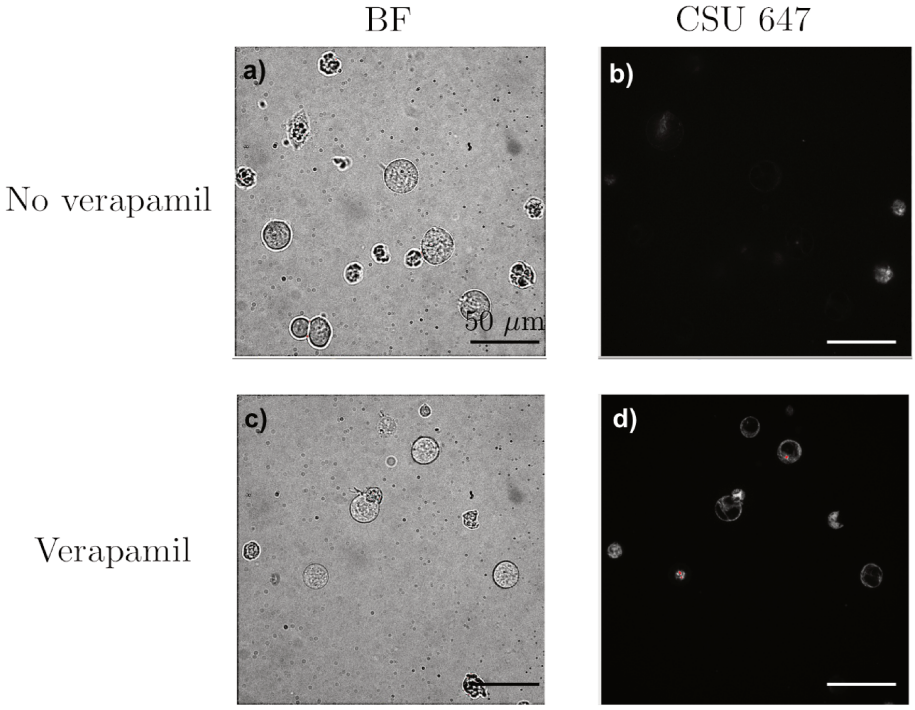

Figure 5.9: **DAMI treated 3 days with blebbistatin 40 μM, stained with 1 μM SiR-tubulin**. **(a)** without verapamil, in bright field. **(b)** without verapamil, in fluorescence with emission wavelength of 647 nm. **(c)** with 10 μM verapamil, in bright field. **(d)** with 10 μM of verapamil, in fluorescence with emission wavelength of 647 nm. Scale bar 50 μm.

microtubules and some microtubules in the cytosol connected to a centrosome to the external ring. We have seen that microtubules are more fluorescent than actin filaments.

In dynamic conditions in a flow chamber, we can visualize the microtubules in the filament (Figure 5.10), whereas actin was only visible in the cell body. Close to its anchorage point at the surface of the ridge, the filament appears dark. This is due to the fact that the flow is not plane in the vicinity of the obstacle, and the filament is therefore not perfectly horizontal. Only the second half is in the focal plane of the microscope. Nevertheless, we can precisely focus the laser on the bright part of the filament. Thus we will stain microtubules using the protocol detailed in section 5.2.4.

5.2.4 Cell preparation

For laser ablation experiments, DAMI cell line is treated 3 days with 40 μM of BBI in a volume of 2 ml at a concentration of 10^5 cells/ml in one well of a 6 wells cell culture plate (Cat. No. 657 160, Greiner BioOne). In order to visualize microtubules, in the DAMI cell line, 5.10^4 cells/ml in 1ml are treated 1hour with 10 μM verapamil and 1μM SiR-tubulin (Spirochrome), in a fluoroDish (World precision instruments), at 37°C, before the experiments. Then they are centrifuged (HERMLE Z326K, GmbH, Germany) 5min at 200 rcf and the pellet is resuspended in 4ml of MEM (Minimal Essential Medium Eagle) (M4526-500ML, Sigma Aldrich). The cells are around 10^4 cells/ml and ready for the perfusion.

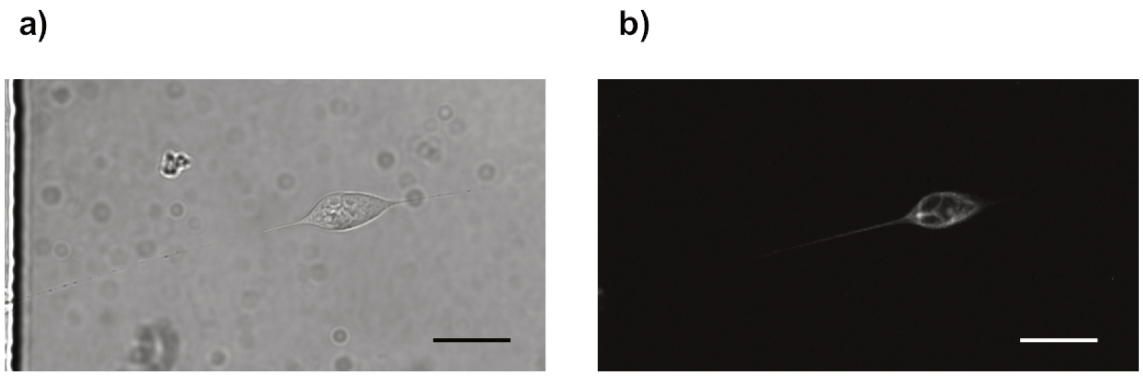

Figure 5.10: **Images of a DAMI in elongation stained with SiR-tubulin, supplemented with verapamil**. Flow is from left to right. Scale bar 25 μm. **(a)** Bright field picture, the cell elongates and forms a thin filament. **(b)** Visualization of microtubules in fluorescence, the intensity is lower in the filament than in the cell body.

5.2.5 Experimental setup

The microfluidic chip is placed on an inverted confocal microscope (Nikon Eclipse Ti-E GmbH, Düsseldorf, Germany) with a $\times$60 oil-immersion objective, 1.4 NA. The system is connected to an autonomous pressure pump (Fluigent, France) with PTFE tubes of internal diameter of 0.3 mm. The inlet and outlet tube lengths are respectively fixed at 70 cm and 30 cm. Reservoirs, at the entrance with the cell suspension and at the exit to collect the solution, are placed at the same height in order to have no adding pressure. When no pressure is imposed at the entrance, the fluid is at rest. Prior to the experiment, the VWF is rinsed with PBS at least 10 minutes at 100 mbar before perfusing the cells. During the experiment, condition of perfusion and shear stress are the same as described in section 4.2.3.

As mentioned in section 5.2.4 microtubules are stained with the probe SiR-tubulin. A laser of wavelength 647 nm illuminates the cells. Fluorescent images of the microtubules are recorded using an ORCA-Flash 4.0 V2 sCMOS camera (Hamamatsu Photonics Europe GmbH). The camera has a small pixel size of 6.5 μm and a total resolution of 2048$\times$2048 pixels, providing a large spatial resolution. Image acquisition is realized with the NIS-elements software. Images are acquired in bright field and in fluorescence in order to have a superposition between the whole cell and the position of microtubules. Exposure time is respectively 30 ms and 400 ms for bright field and fluorescence images. The intensity of the laser is fixed at 15 % in order to limit bleaching effect during the 20 minutes duration of each acquisition.

Ablation of the DAMI microtubules is conduced with a second laser: the MicroPoint (Andor Technology) ultraviolet nitrogen-pumped dye laser, also mounted on the microscope. The zone that can be reached by the laser is smaller than the field of view of the camera. Thus we have to place the target cell in this zone and select the region of interest (ROI). It is the region where we will fire and so damage the selected zone. The MicroPoint is an additional module mounted on a confocal microscope already equipped in FRAP, and spinning disc modules. This laser is thus not yet implemented in the software, it is instead controlled by a macro which has to be run before each set of measure-

ments. We fix the MicroPoint settings: the delay between laser pulses is 60 ms and the laser shoots every two points in the selected ROI. The MicroPoint power is given in the following sections.

Time-lapse images are acquired before and after ablation to follow the cell elongation. A first phase acquisition is performed successively in BF and fluorescence as fast as possible (one image every 1.5 seconds which corresponds to one image every 3 seconds for each channel) for 20 loops (20 images in BF and fluorescence are acquired). Then 1 loop is dedicated to ablation, and finally BF and fluorescence images are again successively acquired as fast as possible for 10 to 15 minutes. For a given cell, the whole cycle lasts a little more than 15 minutes. Experiments are successively performed on different cells from the same sample. Although the laser is focused, the white light used for bright field time lapse observations is not and causes bleaching. After two hours of experiment, the fluorescent signal becomes too weak to be detected. Images are analyzed using the Image J software (Fiji).

5.3 Development of laser ablation protocol

Laser ablation equipment is available in Saarbrücken. With Emmanuel Terriac, we realized the calibration of the laser using a highlighter-drawn pattern on a glass slide in order to precisely locate the region of interest. First we reproduced an existing experiment and practice on adherent cells in static conditions. Then we developed a protocol for cells elongating in flow.

5.3.1 Calibration

To perform laser ablation on a specific sub-cellular structure, the position of the laser has to be precisely controlled, especially when the region to ablate is thin. Thus, it is necessary to correlate the position of the laser with the field of the camera. We use a glass bottom fluorodish (World Precision Instruments, Tissue Culture Dish with cover glass bottom, FD35) with a highlighter-drawn pattern to calibrate the laser. The thickness of the glass is 170 μm. We fire 16 calibration points in the x-direction and 16 points in the y-direction in order to form a cross which is the automatic figure for calibration (Figure 5.11). The accuracy of the calibration depends on the fire point size, which depends on laser intensity. For each point, we manually checked its position (x, y). Selecting all the points one by one creates a link between the camera and the laser.

As shown in figure 5.12 (a), as written in the calibration manual, the region accessible for the MicroPoint is smaller than the full field captured by the camera. This zone appears in red on the screen. In order to check the efficiency of the calibration, we select a region of interest (ROI) in the MicroPoint range. The ROI corresponds to the zone we want to ablate. When the ROI is selected in the captured image, we can start the acquisition and the laser ablation. We then verify the shape of the ablated region as shown in figure 5.12 (b). If the calibration is perfectly realized, the shape ablated corresponds to the shape of the ROI and is located exactly at the place we defined for the ROI. The calibration depends on the refraction index (oil or air objectives). When modifying the objective magnification, the calibration has to be done again.

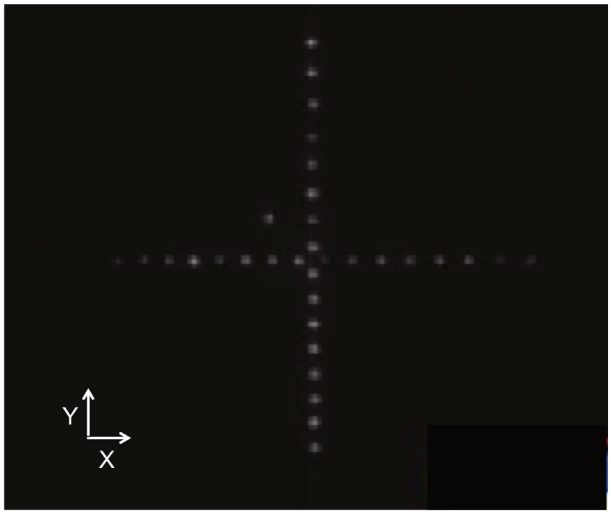

Figure 5.11: **Calibration points**. The calibration motif: 16 points in the x-axis and 16 points in the y-axis, crossed in the middle. The size of the fire points depends on the laser intensity. Checking manually the position of each point permits the correlation between the laser and the camera.

5.3.2 Ablation in static conditions on adherent cells

We first perform laser ablation on transfected fibroblasts expressing fluorescent microtubules. It is easier to start with adherent cells close to the dish surface to be sure the depth of field is enough to focus the laser on microtubules. Figure 5.13 shows that just after ablation, at 14 seconds of acquisition, there is a black line corresponding to the position of the ROI. After two minutes, this darkened region becomes brighter again. But, before this, we can notice in figure 5.13 that at 29 seconds of acquisition, the dark zone has grown larger. This indicates that, shortly after ablation, microtubules retract on both sides of the ROI. It means that the laser severs microtubules without killing the cell. The reorganization of microtubules lets us assume that the cell is repairing itself after ablation. Because fibroblasts are adherent cells, their microtubules are close to the glass surface. In order to avoid breaking the glass, we need to use a low intensity power of 65 % for laser ablation. Cells in suspension are further from the glass surface. The distance the laser has to travel is longer to submit the microtubules at the same energy to sever them, we need a higher intensity. The maximum intensity the MicroPoint can reach is 85 %.

5.3.3 Ablation in static conditions on cells in suspension

DAMI cells are grown in suspension, and are placed in a microfluidic chamber for experiments. Thus the power of the MicroPoint has to be adapted. First we visualize the microtubules in statics, to show the ability of the laser to damage microtubules without killing the cell (Figure 5.14). In figure 5.14 we can see a DAMI cell whose microtubule ring is severed. Ablation of cells in suspension seems to create a motion of the cell in the opposite direction (data not shown). In bright field, we observe that laser ablation initiates the apparition of a bleb : a growth at the point where occurs ablation (Figure

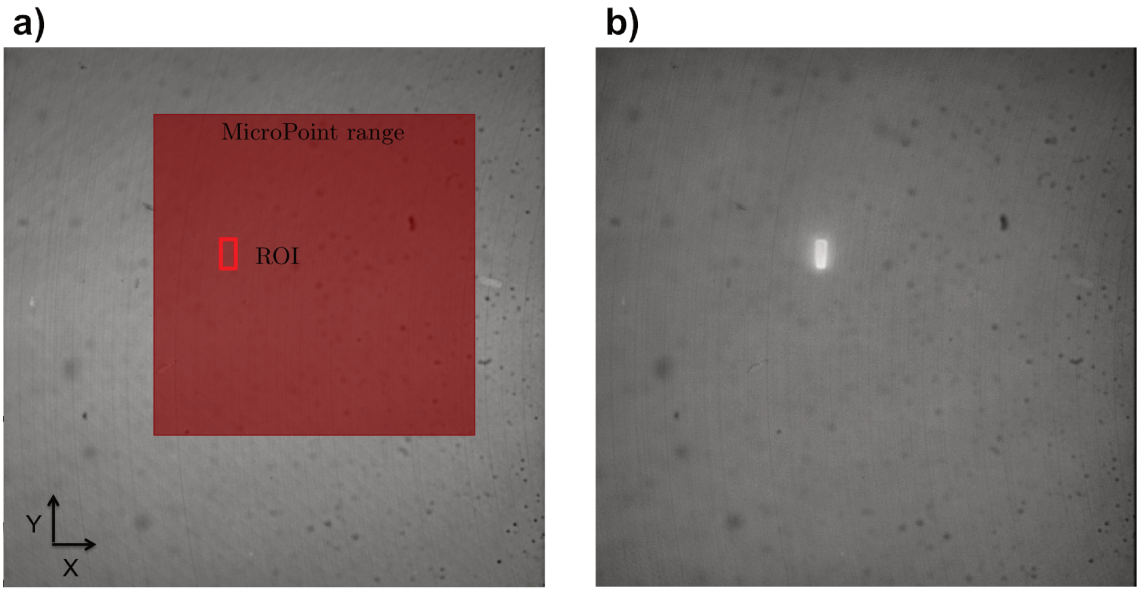

Figure 5.12: **Selection of a ROI**. The field of the camera is 2048 $\times$ 2044. Here we illuminate the highlighter in a glass bottom fluorodish. **(a)** Before ablation, the red square shows where the MicroPoint laser can physically fire. In the capture of the live image we need to select a ROI which corresponds to the area where the laser will fire from the top left-hand corner to the bottom right-hand corner of the ROI. **(b)** Live image after ablation. The bright shape corresponds to the ROI shape where the laser fired. When the ROI shape corresponds to the shape after ablation, the calibration is finished and the laser is ready for experiments.

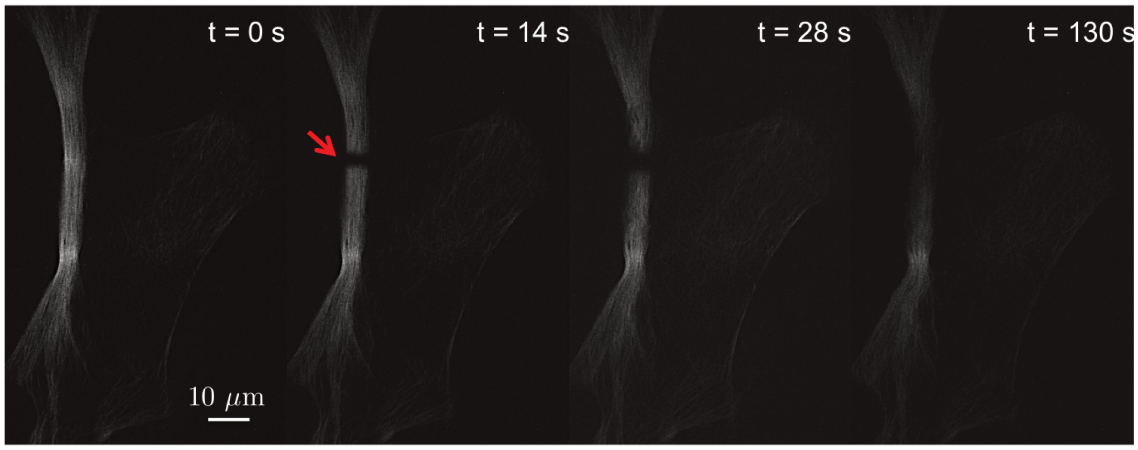

Figure 5.13: **Ablation of microtubules in static conditions on adherent fibroblast**. Ablation of a transfected fibroblast adhering on glass surface. MicroPoint power : 65%. The red arrow points the position of ablation. Two minutes after ablation, their is recovery of the fluorescence that can be the consequence of microtubules repair after bleaching. Scale bar 10 μm.

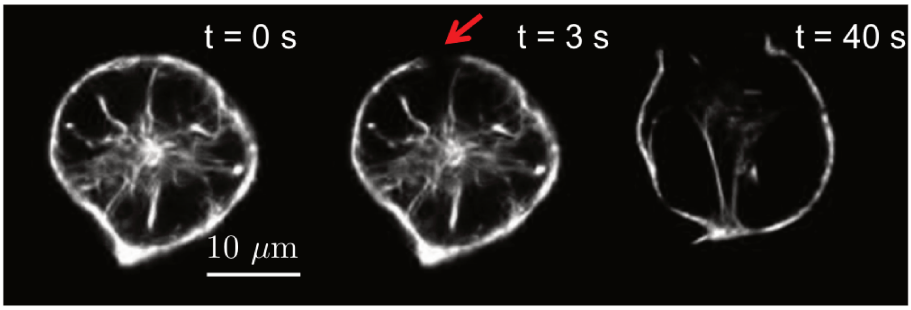

Figure 5.14: **Ablation of microtubules in static conditions on cell in suspension**. Ablation of a DAMI previously treated 3 days with 40 μM BBI and stained 1 h with 1 μM SiR-tubulin + 10 μM verapamil. MicroPoint power : 85%. The red arrow points the position of ablation.

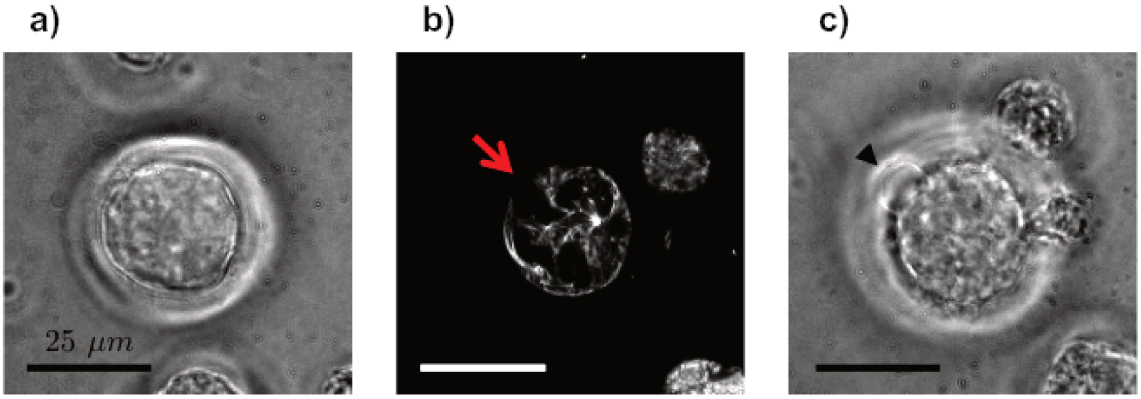

Figure 5.15: **Ablation of microtubules induces the apparition of bleb**. DAMI treated 3 days with 40 μM BBI and stained with 1 μM SiR-tubulin and 10 μM verapamil. Scale bar 25 μm. **(a)** Visualization in bright field before ablation. **(b)** Visualization in fluorescence just after ablation at MicroPoint power of 85 %. Red arrow points the ROI ablated. **(c)** Visualization in bright field after ablation. Black arrow head points the bleb.

5.15). However, after few minutes the bleb disappears. It has already been studied in the literature and after blebbing, the cell reorganizes and recovers its initial shape [258]. As for adherent cells, cells in suspension repair after ablation. We proved our ability to disturb microtubules organization in statics for cells in suspension. That is promising for experiments realized in flow on thin filaments of microtubules. The protocol used is static conditions has been adapted in dynamic conditions and is described in section 5.3.4.

5.3.4 Ablation in dynamics

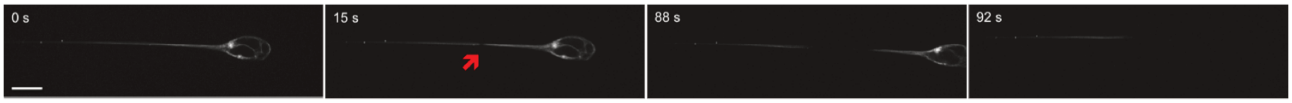

Figure 5.16: **Ablation of microtubules in dynamic conditions**. Successive images of a DAMI treated 3 days with 40 μM BBI and stained with 1 μM SiR-tubulin and 10 μM verapamil, perfused in a microfluidic device. The cell is trapped at the surface of the beam and elongates. The flow is from left to right. At 0 seconds, the acquisition starts, laser ablation occurs after 14 seconds acquisition. The red arrow points the ROI area ablated. The filament elongates during almost one minute and breaks between 88 seconds and 92 seconds. Scale bar is 20 μm.

We performe laser ablation on cells elongating at the surface of a ridge coated with VWF. In figure 5.16, we can see a DAMI elongating from left to right. Conditions of perfusion and acquisition are detailed in section 5.2.5. We call $t = 0$ s the time at which we start the acquisition. The elongation of the cell is followed until the ablation time at 15 seconds. We observe on this example that after laser ablation, the ROI area bleaches as in static conditions. The cell continues to elongate during almost 1 minute until a rupture occurs. That suggests that the filament is not entirely damaged, but only the microtubules. If the power of the laser is too high, we can severe the membrane with the microtubules which will lead to an immediate breakage of the cell. But if the power of the laser is too low, it only induces bleaching and does not damage the microtubules. The aim of the ablation in dynamics is to study the rupture phenomenon. Thus, we have to find the minimum power of the laser able to severe microtubules and lead to rupture. The power of the MicroPoint varies between 65 and 75 % of the laser depending on the z-position of the filament in the microfluidic device.

5.4 Choosing the ablation position

First, we reproduce experiments already performed at UTC and at the INSERM U1140, in order to be sure the DAMI cell line behavior was the same after a long travel between Compiègne and Saarbrücken. We carry out experiments in the same conditions of perfusion as detailed in section 4.2.3. In brief, we fix the inlet pressure at 104 mbar in order to have a shear stress of 1800 s^{-1} close to the wall in the microfluidic device. We perfuse DAMI treated 3 days with 40 μM BBI and stained 1 hour with SiR-tubulin. Cells can have several shapes and elongation velocities. In order to characterize elongation velocity, we follow the extremity of the filament over time. When the extremity is out of view, the easiest way to measure the elongation is to follow the cell body. Elongation velocities presented in this section are all measured between the beam and the extremity of the filament. Thus we do not consider very long filaments that are not entirely in the field view. We then calculate instantaneous

speeds as the distance travelled by the extremity over 10 seconds. The results are presented as the average of instantaneous speeds $\pm$ uncertainties. The initial length of the filament when starting the acquisition is scaled as distance $= 0$ μm.

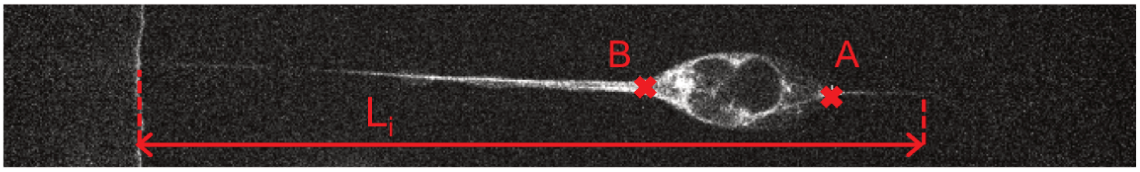

Figure 5.17: **Definition of the parameters to measure elongation velocity**. Picture of a cell elongating in the microfluidic device. L_i is the distance between the beam and the extremity of the filament when we start the acquisition. Two recognizable points A and B are followed in order to measure elongation velocity over time. A is the point prior the cell body and B the point following the cell body.

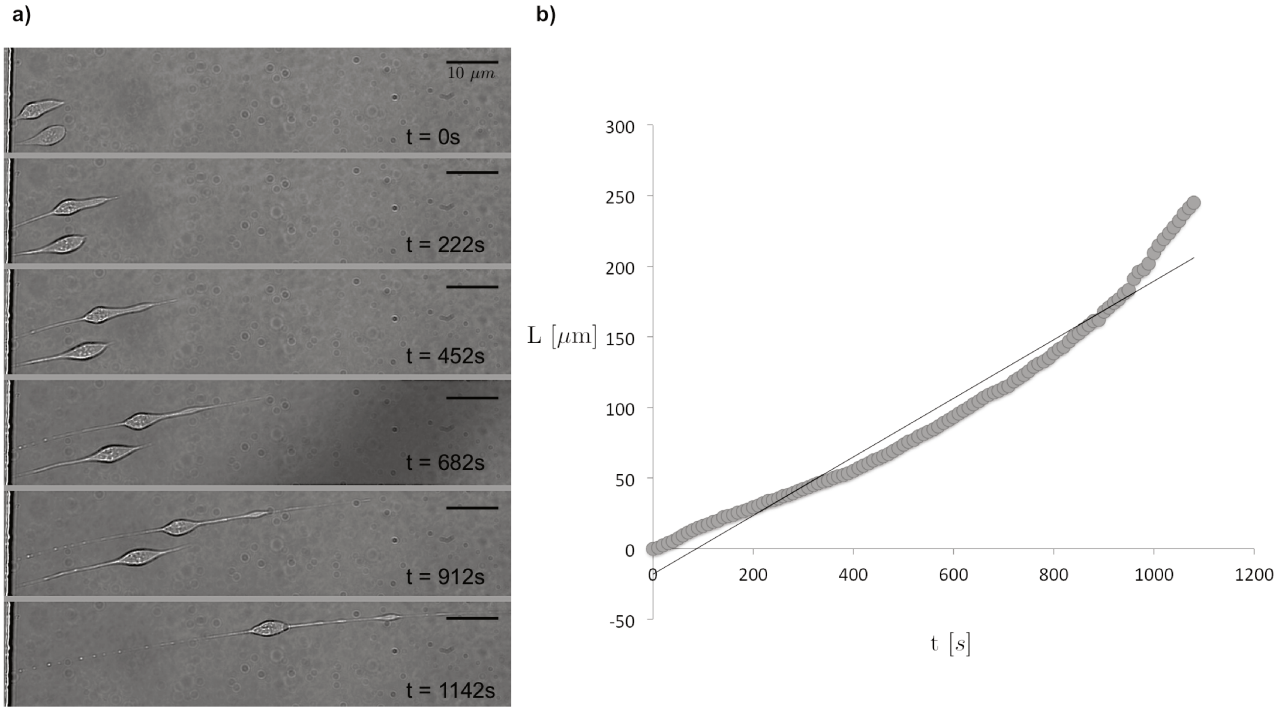

Figure 5.18: **Elongation of SiR-tubulin stained DAMI cells**. The flow is from left to right. Scale bar 10 μm. DAMI were previously treated 3 days with 40 μM BBI and stained with SiR-tubublin supplemented with verapamil. **(a)** Picture of two cells exposed to a same flow elongate. On the top the cell body separates and the filament presents a shape of necklace with several beads. In the bottom, the cell filament elongates until the cell detaches from the beam after almost 15 minutes. **(b)** Plot of the total length of the cell on the top of the image in **(a)** over time. Experimental points are plotted in grey. The dashed line is a linear fit. We find an average velocity of 0.2268 ± 0.0006 μm/s.

In chapter 4 we discussed spatial heterogeneities present in the filament, when it elongates. In order to be insensitive to these variations, we measure the total length L of the filament over time. We acquire images for 20 minutes, or until the cell detaches from the beam. Figure 5.18 (a), presents two cells elongating in a channel. The cell in the bottom of the image elongates from the beam to the cell body. However, prior the cell body, in point A, figure 5.17, there is weak elongation, the body

becomes to be sharp. After 15 minutes observation, the cell detaches from the beam. No formation of beads have been detected, the bond between VWF and the cell is weak. On the contrary, the cell on the top elongates in both parts of the cell body, and there is formation of beads. Figure 5.18 (b), represents the evolution of its total length over time. The dashed line corresponds to a linear fit. We can observe that the experimental curve is up or down the fit.

We use these data to compute elongation velocities, averaged over the whole duration of the experiment. The positions of the extremity of the filament and the beam are measured with $\pm$ 2 pixels of accuracy. The physical size of a pixel with the camera we are using (Hamamatsu) is 6.45 μm. The magnification is $\times$20 so one pixel size is 0.32 μm. The uncertainty generated by measuring the total length of the filament is $\pm$ 2 pixels (i.e. $\pm$ 0.645 μm) which is small when compared to the measured lengths.

We measure the elongation velocity for six cells, in bright field. We start the acquisition just after the cells adhere to the ridge. We find an average elongation velocity of 0.1025 μm/s with a standard deviation of 0.059 μm/s. In chapter 4 we studied elongation in bright field for cells treated with BBI with no staining. We found an average velocity around 0.054 μm/s with a standard deviation of 0.035 μm/s. It seems that SiR-tubulin slightly increases elongation velocity but not in a significant manner. This variation of velocity can be explained by many other factors. First experiments on unstained cells and SiR-tubulin treated cells are realized with two different batches of cells. Unstained cells are cultured at the UTC, while stained cells are cultured at physics laboratory in the Saarland University in Germany. For each batch, we average the velocity of only seven cells. Moreover we already explained in chapter 4 that it exists a large variability in elongation velocities among cells from the same batch. We assume that the effect of Sir-tubulin on elongation is not significant to study cell rupture.

Table 5.1: **Elongation experiments.** N corresponds to the number of experiments. U is the average velocity considering the total length of the filament. U_A is the average velocity considering the point A on the cell body (Figure 5.17). U_B is the average velocity considering the point B on the cell body (Figure 5.17).

N	U **[μm/s]**	U_A **[μm/s]**	U_B **[μm/s]**
1	0.0449 ± 0.0021	/	/
2	0.1115 ± 0.0013	0.1172 ± 0.0001	0.1001 ± 0.0001
3	0.0796 ± 0.0008	0.1285 ± 0.0001	0.1247 ± 0.0001
4	0.0781 ± 0.0034	0.0570 ± 0.0011	/
5	0.2268 ± 0.0006	0.1853 ± 0.0001	0.1293 ± 0.0001
6	0.0804 ± 0.0006	0.0617 ± 0.0002	/
Average	0.1025 ± 0.0015	0.1100 ± 0.0003	0.1180 ± 0.0001

As the entire cell is not always wholly visible in the field of view, either because it is too long or because its extremity is not in the focal plane, we seek to estimate elongation velocity based on the displacement of the points A and B defined in Figure 5.17, respectively preceding and following the cell body. The initial length of the filament when the acquisition starts is called L_i. Table 5.1 shows that U_B always accounts for 70% to 97% of the total cell velocity U. This suggests that the portion between B and the free end of the cell moves as a solid body and that elongation is more concentrated

in the filament between the ridge and the point B. For a study of elongations, this is likely to be the zone of interest.

We showed in the previous chapter that ruptures occur in the regions of maximal local elongation, often close to the end of the filament. In order to reproduce this phenomenon, we first choose an area of ablation located between the anchorage point and the cell body where we visualize the filament. For ablation experiments we will increase the magnification to $\times 60$ in order to precisely cut the microtubules. Well, at this magnification the field of view is reduced and the extremity of the filament is often out of the field view. That is the reason why in next part we follow the points A and B to calculate elongation speed instead of the extremity of the filament.

5.5 Preliminary results

We just followed cell elongations without ablation and determined the position of ablation in the filament between the beam and the cell body. In this section, we present the preliminary results of ablation of microtubules in elongated cells. We perform experiments varying the MicroPoint laser power. Whatever power is used, we notice that ablation induces rupture, as is illustrated in Figure 5.19. After ablation, three stages are observed and depicted in Figure 5.20 : fast elongation (i), ruptures (ii) and contraction (iii). In a first section, we describe the choice of the laser power. We finally study the contraction following ruptures.

5.6 Choosing the ablation power

Our objective is to sever microtubules without damaging the cell membrane. To find the most appropriate illumination conditions, we carry out experiments with a variable power of the MicroPoint laser. When the power of the MicroPoint laser is less than 65%, the ROI is bleached but no damage to the microtubules is observed (the darkened zone does not expand before fluorescence recovery). Beyond a power of 75 %, ablation triggers immediate ruptures, which suggest the simultaneous severing of both microtubules and membrane. The table 5.2 summarizes the conditions of experiments performed with a power between 65% and 75 %. For each laser shot, we measure the elongation velocity before and after ablation and the delay between ablation and rupture.

The six experiments presented here have a delay higher than 30 seconds between ablation and rupture (Table 5.2). Figure 5.21 presents a scatter plot of the delay of rupture after ablation as a function of the MicroPoint power. The power of the laser does not seem to have any impact on time between ablation and rupture. However some experiments realized at power 65% have shown no rupture of the filament (not shown). The difficulty in this case is to know if the laser damaged the microtubules. The focalization of the laser is probably the most important factor. However, as the filament is exposed to the flow, its position can be modified between the moment we chose the ROI on the image capture and the moment we make ablation. If the microtubules are out of focus during

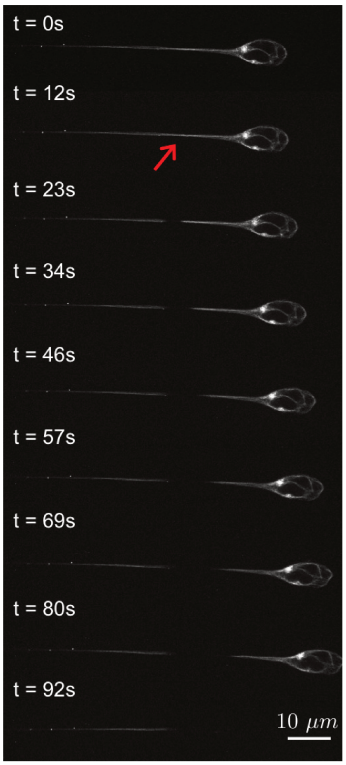

Figure 5.19: **Ablation of the filament**. Flow is from left to right at pressure 65 mbar. Scale bar 10 μm. Red arrow represents the ablation point. Ablation occurs at t = 13 s. **(a)** Montage of successive images of a DAMI cell in elongation in flow. After ablation, the dark hole expends, the microtubules are severed. The filament breaks at t = 92 s which is 1min 20 s after ablation.

ablation we will see bleaching at the localization of the ROI but no rupture.

At low power it is difficult to be sure of damaging microtubules. However if the power is too high (greater than 75%) the filament breaks instantaneously. The reason is probably that we damage all the cell and the flow carry the non attached part of the filament. Thus we have to find the best compromise allowing to only severe microtubules. After several experiments we expect 72% to be the best choice in our configuration. In all our experiments rupture occurs between 10 seconds and 1.5 minutes after ablation. Because the rupture is not immediate, we can conclude that the ablation of microtubules (Figure 5.19 (a)) does not damage completely the membrane. However, rupture is often followed by contraction and sometimes other ruptures.

We characterize elongation velocity before and after ablation with the method detailed in section 5.4. We first measure elongation velocity of the cell during 45 seconds before ablation. Then we measure elongation velocity of the cell until rupture. We can notice an increase of velocity after ablation. On average the velocity after ablation U_{ALA} is 0.84 $\pm$ 0.33 μm/s, that is threefold higher than the velocity before ablation U_{BLA}, for the six experiments presented. It is much faster than when compared to spontaneous ruptures we get in chapter 4 at an average velocity of 0.28 $\pm$ 0.30 μm/s.

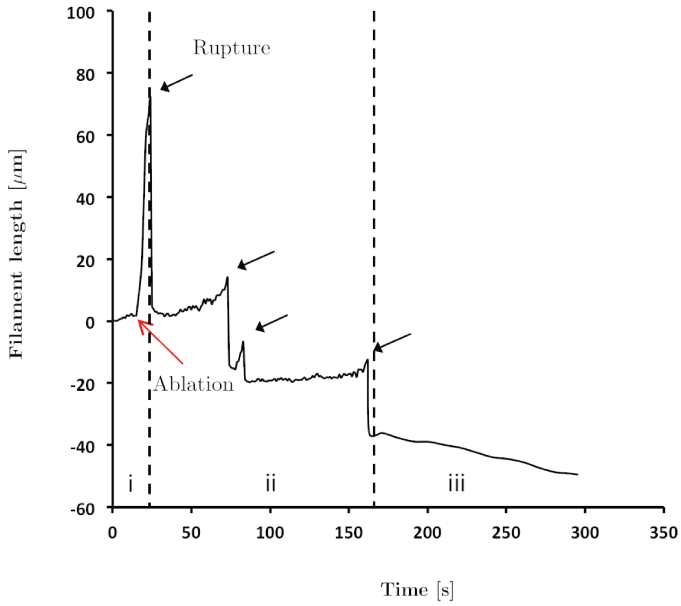

Figure 5.20: **Ablation is followed by ruptures and contraction**. Plot of the total length of the filament as a function of time. Red arrow shows the point of ablation. Black arrows point the ruptures. (i) In the first phase of 20 seconds, the cell elongates. After ablation, the elongation velocity increases extensively. (ii) Successive ruptures are also preceded by 3 to 5 seconds elongation phases. (iii) After the last rupture, the remaining part of the filament contracts with a velocity of 0.10 μm/s (in the literature, the retraction velocity of a MK after platelets release is around 0.06 μm/s [8]).

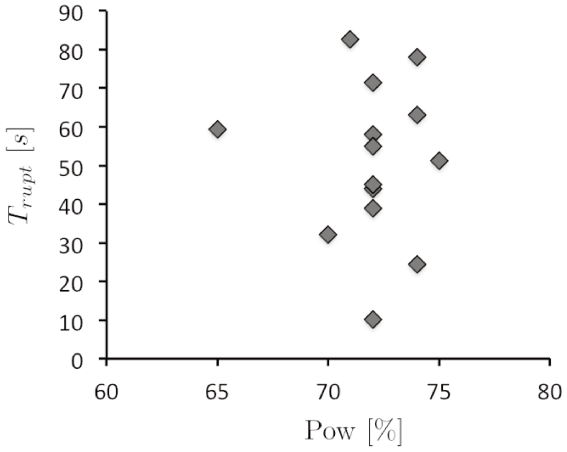

Figure 5.21: **Rupture delay as a function of laser power**. Scatter plot of the rupture delay as a function of the power of the laser applied. We notice no correlation between the power and the delay of rupture after ablation.

5.6.1 Contraction velocity after ablation

In this section we describe the behavior of the cell after ablation and in particular the retraction following ruptures. Figure 5.22 presents a cell for which ablation occurs after 13.5 seconds observation, at the right tip of the cell body. As a consequence, the right part of the cell is released in the flow. We observe the evolution of the remaining part of the cell simultaneously in bright field and fluorescence

Table 5.2: **Laser ablation experiments.** N represents the number of experiments analyzed. Pow is the power of the MicroPoint used for the ablation, in %. T_{rupt} represents the time between ablation and rupture, in seconds. L_i is the initial distance between the cell body and the beam (or the extremity on the left if the beam is not in the field view). U_{BLA} is the elongation velocity before laser ablation. U_{ALA} is the elongation velocity after laser ablation but before rupture. The A point corresponds to the point preceding the cell body and B is the point following the cell body (Figure 5.17). Images are acquired in bright field (BF) and/or fluorescence (CSU647).

N	**Pow**[%]	T_{rupt} **[s]**	L_i **[μm]**	U_{BLA} **[μm/s]**		U_{ALA} **[μm/s]**		BF or CSU647
				A	B	A	B	
1	71	83	221	0.314	0.246	/	1.047	CSU647
2	72	45	220	0.554	0.495	1.044	1.085	BF
3	72	58	122	0.174	0.164	0.242	0.219	BF
4	72	39	186	0.146	0.120	1.000	0.931	BF
5	65	59	160	0.179	0.134	1.117	1.053	BF
6	72	55	198	0.210	0.210	0.786	0.718	BF

for 5 minutes. During the three first minutes after ablation, we can see in bright field the formation and the retraction of a bleb (Figure 5.22, t = 42 s to t = 231 s). A similar phenomenon has already been observed in statics (Figure 5.15). In fluorescence, we can observe how microtubules reorganize in the cell recovering from ablation. We observe on both bright field and fluorescent images that the length of the cell remains constant for a few minutes. Elongation starts again at $t = 231$ seconds with a velocity of 0.11 μm/s. At this date, bright field images illustrate the resorption of the bleb and the fluorescence is recovered in the ablated region. An explanation could be that microtubules priority after damage is to reorganize in order to repair cell cortex.

As already explained, we want to induce rupture in order to mimic spontaneous platelet formation. However, in our experiment, we make laser ablation in a part of the filament that is selected among the regions of highest elongation rate in the cell, but not necessarily in a region that is ready for spontaneous rupture. Thus the place where occurs rupture is not a place where spontaneous ruptures would occur. With DAMI cells, spontaneous ruptures are extremely rare. They are more frequent in experiments with primary cells. They usually occur in regions that have a necklace structure, between two beads growing away from one another with a high velocity. This is more frequently observed on the right side of the cell body, in the freely floating filament. In our cell line model, necklace structures are more difficult to obtain, and the region with the highest elongation rate seemed to be the one between the ridge and the cell body. Moreover, in fluorescence, it is easier to visualize the filament between the pillar and the cell body. We are aware that the induction of rupture is probably not in an area for spontaneous rupture. However, we expect to observe similar consequences between spontaneous and artificial ruptures even if causes are different.

We also notice that the first rupture is often followed with several spontaneous ruptures when we damage the filament. Figure 5.23 shows a cell attached to the beam coated with VWF. Some beads at the extremity of the filament accelerate and detach in the flow (Figure 5.23 b). After five ruptures the filament shrinks with a velocity close to elongation velocity prior ablation (0.17 μm/s). Because we do not have the equivalent images in fluorescence, we do not know whether the remaining filament still contains microtubules (and dynein). It is unclear what triggers the retraction: is there a maximum

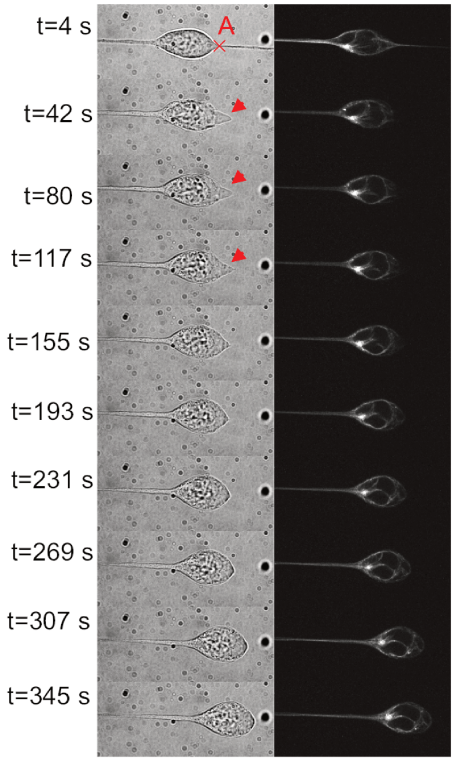

Figure 5.22: **Repair of the cell**. Pictures of successive positions of a cell perfused at 65 mbar in the microfluidic channel. Ablation occurs at the right tip of the cell body at time t = 13.5 s. Ablation seems to inhibits elongation. On the left images in bright field. On the right corresponding images in fluorescence. Microtubules are stained with the probe SiR-tubulin. In bright field, a bleb appears (red arrow head) in the position of ablation. In fluorescence we observe microtubules reorganization. After time t = 231 s, the cell re-grows.

number of ruptures per cell ? Also, we can wonder whether the remaining filament still has the potential to further elongate in the future, and if so, under which conditions.

5.7 Conclusions and perspectives

In this chapter we described the elaboration of a protocol for laser ablation on suspended cells elongating in a microfluidic device. First, we have chosen to stain the cell cortex. The staining of actin was not efficient to visualize the elongated filament so we decided to stain only the microtubules with the SiR-tubulin probe. Although this probe can be toxic for cells, we chose the maximum amount recommended in the data sheet (1 μM) in order to visualize the staining as long as possible. Even then, the intensity was weak. For a better staining efficiency we added 10 μM verapamil. Even if that drug stresses the cell, we observed that most of them were stained and alive after treatment. However, during the perfusion, several cells adhere to the beam and do not elongate, these cells seem dead. In order to reduce the stress of the cell just before perfusion, it would be a good idea to not centrifugate cells after staining but just dilute the cells in medium in order to have 10^4 cells/ml in 5 ml.

Then, we developed the ablation of microtubules in static and in dynamic conditions. In static conditions, ablation is quite simple. The microtubule ring is severed and a bleb appears. That signifies

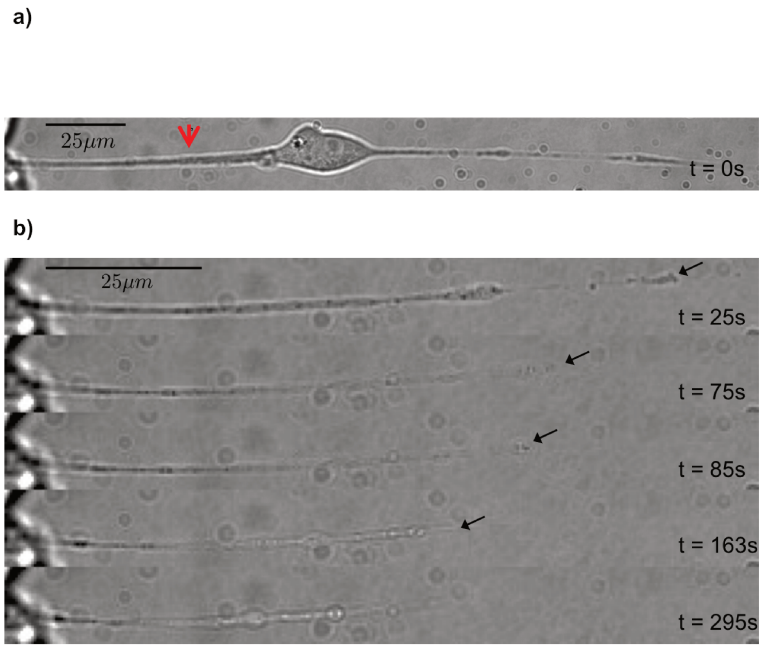

Figure 5.23: **Retraction of the filament**. Fluid flows from left to right. The cell is attached on VWF at the surface of a beam. **(a)** Picture of the cell in flow before ablation, the cell elongates with a velocity of 0.17 μm/s **(b)** We follow the total length of the filament and noticed several ruptures of the filament. The red arrow in picture (a) shows the point of ablation. Black arrows in picture (b) indicate the points of successive ruptures. Ablation occurs after 15 seconds acquisition.

that the rupture of the cortex creates a zone where the internal pressure is released [258]. Preliminary results in dynamic conditions on filament ablation in elongated DAMI cells are promising. We have shown that the ablation of microtubules conducts to the rupture after less than 2 minutes. We have demonstrated that the elongation velocity increases much more after ablation than for spontaneous ruptures. Damages caused by the laser appear to have an additional effect on cell elongation velocity. The main rupture of the filament is often followed by several ruptures of the extremity of the filament. After each rupture, there is a retraction of the filament followed by an acceleration before next rupture.

The quality of results is limited by some of the technical features of the equipment. The switch between bright field and fluorescence took at least 1.5 seconds. This long period is partly due to the time the halogen lamp needs to switch on and off. In order to be faster, we have 3 possibilities. 1) Change the halogen lamp for a LED which reaches the maximal illumination instantaneously. 2) Insert a shutter on the illumination path in order to always have the lamp on. 3) Stop using bright field and stain the membrane to visualize the shape of the cell. We have to choose a fluorochrome whose adsorption wavelength is larger than 500 nm in order to avoid blue light that stops MK elongation. Typically a fluorochrome emitting in the orange wavelengths should be interesting for double staining. The advantage of a double staining microtubules/membrane is the rapidity of the acquisition. Otherwise, the laser ablation can occur of both filters. Until now, laser ablation was done in several time because of the switch for the acquisition of images. Also, during ablation no image is taken because of the saturation of the camera. Having both information of the position of the membrane

and the microtubules in fluorescence should help to have ablation in only one loop.

Finally, with the acquisition of more images, we expect to characterize elongation and contraction velocity during rupture. It would also be interesting to develop a method to calculate the tension forces in the filament. It would help to understand why in a bioreactor, some cells elongate and never break spontaneously. If it exists a minimal tension necessary to induce rupture and at the same time the formation of platelets, it would help us to design more adapted microfluidics bioreactors, to increase the tension in the filament.

Conclusions

In vitro platelet production is a dynamic field of research mainly limited by the low yield of platelets produced. One hypothesis to this limit is the heterogeneity in size and elasticity of the initial suspension of MK. In this thesis, we develop microfluidic tools aiming at sorting MK and understanding elongation and rupture processes of MK.

In a first part, we have demonstrated that our passive microfluidic device is able to sort microcapsules according to their size and/or deformability. Size is the main parameter of sorting thus, in order to only sort microcapsules according to their deformability a previous size-based sorting is required. It can be performed in the same microfluidic device by adjusting the flow strength applied. We downscaled the device to adapt cell diameter which is experimentally challenging and induces technical problems such as: clogging, fabrication and the determination of fluids; which are now resolved. We obtained satisfying results for cell size-based sorting and promising results for cell deformability-based sorting. Another difficulty encountered in this project is the characterization of cell mechanical properties. Even if many methods of characterization are described in the literature as well as many drug treatments able to modify cell mechanical properties, most of them are adapted to adherent cells whose behavior is completely different to the one of cells in suspension. Even among cells in suspension, it exists a large variability due to the cellular types. Thus, blebbistatin, a drug known in the literature to impact cell mechanical properties for a large number of cell type, only has an effect on cell size after three days but not on our cell mechanical properties. We identified tipless AFM as an efficient tool to estimate the Young's modulus at the cell scale. Also we find that calyculin A respectively stiffens DAMI cells significantly. In future work it is planned to test the efficiency of the sorting device using cells treated with this drug. Another perspective is to characterize primary megakaryocytes mechanical properties and sort the DAMI cell line whose behavior correspond to immature MK, from mature primary cord blood MK.

In a second part, we study MK elongation and rupture by controlling flow conditions. We point in light that MK elongation rate vary over time, as already observed *in vivo*. These fluctuations of elongation velocities are not resulting of flow perturbations but are the consequence of the balance between microtubules sliding responsible of elongation and the actomyosin cytoskeleton which tend to resist against elongation. Biological activities leads to fluctuations of the elongation rate. We have shown that fluctuations are not only present at the cellular scale but also at local scale between two beads. Locally some segments between two future platelets stretch while others contract in an other-

wise elongating cell. We have analyzed instantaneous ruptures and shown that platelet release occurs in long segments whose elongation velocity is fast. In future work we expect it will help us to identify cell that will potentially break in order to observe and analyze many MK ruptures. Finally, we have demonstrated that damaging microtubules during laser ablation experiments provoke artificial ruptures.

In the long term, we can expect these results to contribute to better understanding of mechanisms involved in *in vitro* platelet production to help the conception of a new platelet bioreactor more efficient than the existing ones; and develop tools for sepsis diagnosis using cell deformability as a biomarker.

Publications

Published :

D. Vesperini, O. Chaput, N. Munier, P. Maire, F. Edwards-Lévy, A.-V. Salsac, and A. Le Goff, "Deformability- and size-based microcapsule sorting", *Medical Engineering and Physics*, 2017.

Medical Engineering and Physics 48 (2017) 68–74

Contents lists available at ScienceDirect

Medical Engineering and Physics

journal homepage: www.elsevier.com/locate/medengphy

Deformability- and size-based microcapsule sorting

Doriane Vesperini[a], Oriane Chaput[a], Nadège Munier[a], Pauline Maire[a], Florence Edwards-Lévy[b], Anne-Virginie Salsac[a], Anne Le Goff[a,*]

[a] Biomécanique et Bioingénierie (UMR CNRS 7338), Université de Technologie de Compiègne - Sorbonne Universités, France
[b] Institut de Chimie Moléculaire de Reims (UMR CNRS 7312), Faculté de Pharmacie, Université de Reims Champagne-Ardenne, France

ARTICLE INFO

Article history:
Received 19 January 2017
Revised 20 June 2017
Accepted 25 June 2017

MSC:
00-01
99-00

Keywords:
Microfluidics
Capsule
Deformability
Separation

ABSTRACT

Biomedical applications often require to sort cells according to their physical properties, such as size, density or deformability. In recent years, microfluidics has provided a variety of tools to sort micro-objects. We present here a simple microfluidic device consisting of a channel containing a semi-cylindrical obstacle against which capsules are squeezed by the flow, followed by a diverging chamber where streamlines separate. We demonstrate that this basic system is capable of sorting elastic microcapsules according to their size at low flow strength, and according to the stiffness of their membrane at high flow strength. Contrary to most existing sorting devices, we show that the present one is very sensitive and capable of discriminating between capsules with differences in membrane elasticity of order unity.

1. Introduction

The shape and mechanical properties of blood cells govern many important phenomena, such as margination [1], adhesion [2], and extravasation [3]. Pathologies such as cancer [4] or infections [5] may alter cell size and stiffness. Abnormal stiffness can be used as a sorting parameter in the detection and isolation of pathological cells [6].

Microfluidics presents many advantages for cancer diagnosis applications, such as small reaction volumes, high sensitivity, and ability to sort micro-objects (particles, capsules, and cells) as described in [7]. Among label-free separation techniques, the most studied are size-based sorting devices: deterministic lateral displacement [8,9], dielectrophoresis [10], hydrophoresis [11], acoustic waves [12,13], and inertia [14]. Other methods, such as immunocapture [15] or fluorescence-activated sorting [16] involve labels, i.e. specific markers located at the surface of the micro-objects. Finally, other techniques such as optical stretchers [17] and stiffness-dependent separation [18] can sort heterogeneous populations based on their mechanical properties. While size-based microfluidic sorting has already been studied extensively [19], the concept of sorting based on deformability has emerged more recently and proves very promising [18,20].

In bioengineering, particles, capsules and vesicles are considered as simplified models for cells [21–23]. Capsules are biomimetic micro-objects consisting of a thin elastic membrane reticulated around a liquid core. The membrane can be made of natural components such as proteins: human serum albumin (HSA) [24], or ovalbumin [25]. The behavior of capsules is studied under conditions mimicking physiological situations, such as flowing through a constriction [26], and in the context of drug encapsulation and delivery [27].

The influence of confinement has been extensively studied for millimetric and micrometric capsules flowing through cylindrical [25], square [28], or rectangular channels [29].

In a recent numerical study, Zhu et al. [30] proposed to sort elastic capsules based on their deformability by flowing them around an obstacle through a straight channel followed by a diverging chamber. The experimental validation of deformability-based sorting techniques is not trivial because of the lack of homogeneous populations of micro-objects with well-controlled stiffness. We have created a microfluidic device with such a geometry. We use spherical albumin microcapsules whose mechanical properties depend on the production conditions.

In this article, we evaluate the feasibility of experimentally sorting heterogeneous populations of microcapsules depending on their stiffness.

* Corresponding author.
E-mail address: anne.le-goff@utc.fr (A. Le Goff).

http://dx.doi.org/10.1016/j.medengphy.2017.06.040
1350-4533/

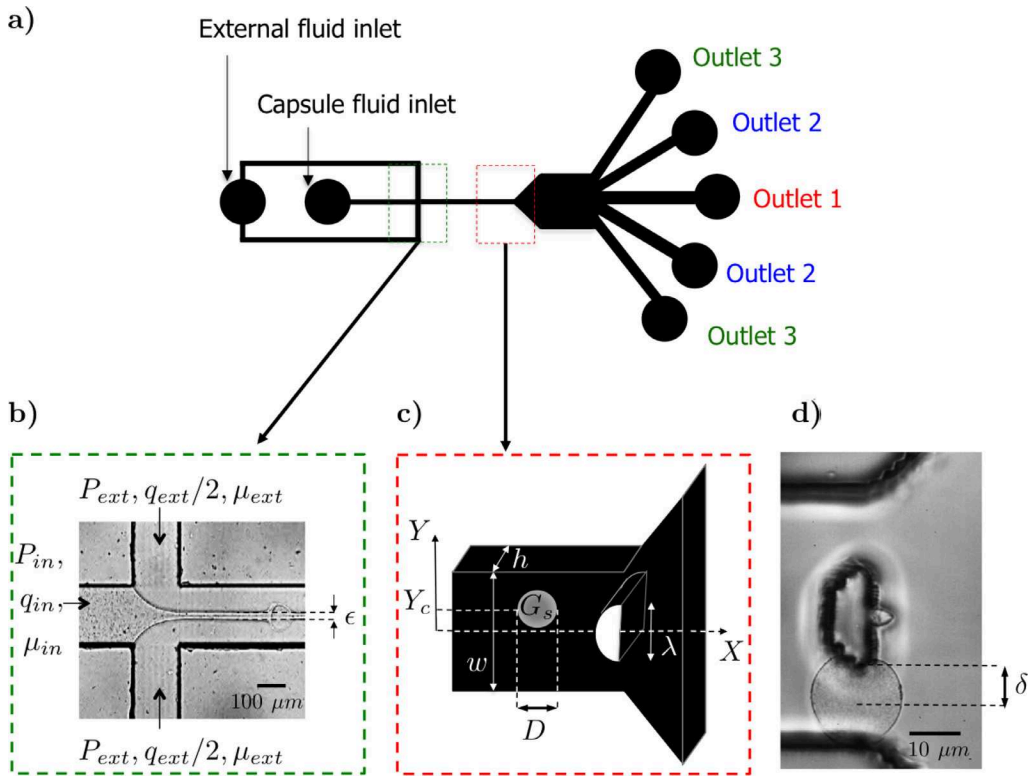

Fig. 1. Sketch of the experimental device. The fluids flow from left to right. (a) General view of our sorting device. (b) Photograph of the flow-focusing at the entrance of the straight channel. The capsule suspension is pinched by an external viscous fluid of viscosity μ_{ext}, and forms a fluid thread of viscosity μ_{in} and thickness ϵ. (c) Dimensions of the obstacle and of the rectangular straight channel. (d) The distance between the center of mass of the capsule and the obstacle is defined as δ.

2. Materials and methods

2.1. Capsule suspensions

Capsules are prepared by interfacial cross-linking as described elsewhere [31]. Briefly, a water-in-oil emulsion is formed using a 10% ovalbumin solution in a phosphate buffer pH 5.9 or pH 8, dispersed in cyclohexane added with 2% (w/v) sorbitan trioleate. Adding 2.5% (w/v) terephtaloyl chloride to the organic phase induces ovalbumin cross-linking at the interface and the formation of the membrane. This chemical reaction is stopped by dilution with chloroform:cyclohexane (1:4, v/v) after 5 min. Capsules are then rinsed with an aqueous solution of polysorbate, then with pure water, resuspended in water and stored at 4 °C. We obtain a polydisperse population of capsules of diameter D, determined with the Image J software using a circular fit, and expressed as the mean ± the standard deviation. The deformability of capsules obtained by this protocol has been shown to depend on the pH of the buffer solution containing ovalbumin. Capsules prepared at higher pH are more rigid than those prepared in more acidic conditions [25]. Capsule stiffness is characterized by the 2D elastic shear modulus of the membrane G_s.

2.2. Microfluidic device

The sorting device (Fig. 1) consists of a straight rectangular channel of width w and depth h that contains a semi-cylindrical obstacle of diameter λ at its end (Fig. 1c). Upstream of the main channel, a flow-focusing module is added to focus the capsules onto the center of the obstacle (Fig. 1). Downstream of the obstacle, the channel widens (Fig. 1a), then splits into several exits. The width of the confined zone between the side wall and the obstacle was chosen to be smaller than the capsule size (Fig. 1d). We define as δ the distance between the center of mass of the capsule and the pillar.

2.3. Production of the microfluidic device

Microfluidic chips are produced in PDMS using standard soft lithography techniques [32]. PDMS and curing agent (Sylgard) are mixed in a 10:1 ratio and cast onto the master, which consists of a silicon wafer with SU8-photoresist microstructures (Microfactory, Paris). After baking for 2 h at 70 °C, the PDMS is cross-linked and can be peeled off from the SU8 master. It is then plasma-bounded together with a glass slide using air plasma generated by a plasma-oxidizer (HARRICK, NY 14850, USA). After 2 h in a stove at 70 °C, the device is ready to be used.

2.4. Experimental setup

The sketch of our experimental setup is shown in Fig. 1. A pressure controller (MFCS, Fluigent, France) is used to impose a pressure P_{in} to the core fluid and a pressure P_{ext} to the external fluid. The chip is placed on the stage of an inverted microscope (DMIL LED, Leica Microsystems GmbH, Germany). Videos are recorded using a high-speed camera (Fastcam SA3, Photron, USA).

2.5. Coflow experiments

We carry out coflow experiments with miscible fluids. The reservoirs containing the external and internal fluids are connected to the pressure controller using PEEK tubes with an internal diameter of 0.25 mm. A fluid of viscosity μ_{in} is perfused at pressure P_{in} into another fluid of viscosity μ_{ext} moved at pressure P_{ext} ($\mu_{in} < \mu_{ext}$). The pressures applied to each entrance are adjusted, varying P_{in}/P_{ext} in order to control the core flow width ϵ

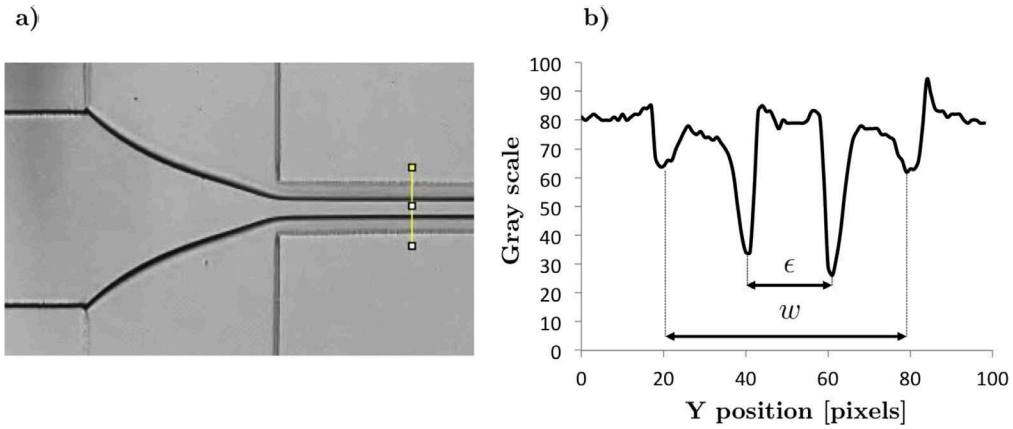

Fig. 2. (a) Photograph of a coflow of an internal flow of pure water injected into a solution of 70% of glycerol (Fluid pair A, Table 1). (b) Gray scale profile along the line (Fig. 2a) used to measure the inner flow width ϵ, and the width of the channel w.

Table 1
Fluid properties for different coflows with μ_{in} (resp. μ_{ext}) as the viscosity of the inner fluid (resp. external fluid), and the viscosity contrast $\chi^{-1} = \mu_{ext}/\mu_{in}$.

Fluid pair	Internal fluid	External fluid	μ_{in}[cP]	μ_{ext}[cP]	χ^{-1}
A	Pure water	Glycerol 70%	1	30	30
B	Alginate solution	Glycerol 70%	7	30	4
C	Capsule suspension	Pure glycerol	800	1300	2

(Fig. 1b). Different fluid pairs (Table 1) are used for calibrating the flow and establishing the relationship between the flow rate ratio $\phi = q_{in}/q_{ext}$ and the width ϵ.

Coflow experiments are performed with different fluids, whose properties are summarized in Table 1. We prepare a 70% glycerol/water mixture (24397-365, VWR, France) and a 1% (w/w) low viscosity alginate (A1112, Sigma-Aldrich, St Louis, MO, USA) solution in water containing 0.9% NaCl and 0.2% Hepes. The alginate solution is agitated at least 2 days at 4 °C.

For variable values of the internal and external pressures, we measure the external and internal flow rates, q_{ext} and q_{in}, in the two inlets of the flow-focusing module thanks to a flowmeter (Flowell, Fluigent, France). The value of the flow rate ratio ϕ is deduced.

Images are post-processed with the software Image J. A ROI (Region of Interest) line is drawn, containing the channel edges of the straight part (Fig. 2a). The core flow width ϵ is defined as the distance between the two minima of the gray curve plot (Fig. 2b).

2.6. Capsule flow

We prepare the capsule suspension with 20 µL of capsules in 1 g of pure glycerol. The reservoirs containing the external and internal fluids (Fluid pair C, Table 1) are connected to the pressure controller using PTFE tubes with an internal diameter of 0.3 mm. In order to accurately capture capsule trajectories in the diverging chamber, we operated at 250 frames per second with a resolution of 1024 × 768 pixels, with a 10 × magnification for all the videos and images. We measure the capsule speed U in the straight channel upstream of the obstacle, before any deformation, and the trajectory followed by the capsule in the divergent chamber (Fig. 4a), at different flow strengths. We define the flow strength as the product $\mu_{ext}U$. Varying the pressures P_{in} and P_{ext} modifies U, and in consequence the flow strength.

The position Y_c of the center of mass upstream of the obstacle is compared to the position of the middle of the channel $Y_0 = 0$. The off-centering κ is defined as the difference between the two values and non-dimensionalized by the capsule diameter D, $\kappa = \frac{Y_c - Y_0}{D}$.

3. Results

3.1. Coflow at the channel entrance

Before flowing microcapsules in our device, we flowed two miscible viscous fluids to characterize the coflow in the flow-focusing module. The aim of the flow-focusing module is to center the core flow in the straight rectangular channel upstream of the obstacle. In the experiments presented in the following section, we flow capsules in the core flow and expect them to be centered onto the obstacle. But, beforehand, we carry out coflow experiments without microcapsules to understand the coflow behavior when varying the viscosity ratio $\chi = \mu_{in}/\mu_{ext}$ (Table 1).

For a given fluid pair, the viscosity ratio is fixed Table 1), and only the inlet pressures are modified. We modify the internal pressure P_{in} keeping the external pressure P_{ext} constant, adjusting the range of variation to avoid backward surge in one or the other inlet and measure the width ϵ. We worked at variable P_{in}/P_{ext} in order to characterize the behavior of coflows and determine the relation between the width ϵ, the viscosity and flow rate ratios χ and ϕ (Fig. 3a).

The values of the internal thread width ϵ are plotted in Fig. 3 as a function of the viscosity ratio ϕ and flow rate ratio χ. It is non-dimensionalized by three different lengths α: the rectangular microchannel width w, height h and characteristic length $\sqrt{hw}$. The experimental results are plotted along with the ones published by Hu and Cubaud [33]. In their study conducted in a square cross-section channel ($w = h = \alpha$), they showed that the core thread width scales as:

$$\frac{\epsilon}{\alpha} = [1 + (1.5\chi^{1/2}\phi^{2/3})^{-1}]^{-1}. \quad (1)$$

We prove that the depth h, which is the smallest length in our device, does not limit the core flow width ϵ. In a square channel the three characteristic lengths are equal, and it was not obvious to know which characteristic length constrained the width ϵ. When ϵ is rescaled by $\alpha = \sqrt{hw}$, the data collapse onto the master curve defined by Eq. (1) (Fig. 3a). We then plot $\epsilon/\sqrt{hw}$ as a function of the flow rate ratio ϕ for different viscosity ratios χ and show that our experimental values agree with Hu and Cubaud [33] predictions (Fig. 3b). $\epsilon/\sqrt{hw}$ increases when the viscosity ratio χ^{-1} decreases. That means that the width ϵ can be easily deduced when we vary the pressures and flow strengths in the case when the optical contrast between the 2 fluids is low or absent. In the following experiments with capsules, we apply pressures in order to

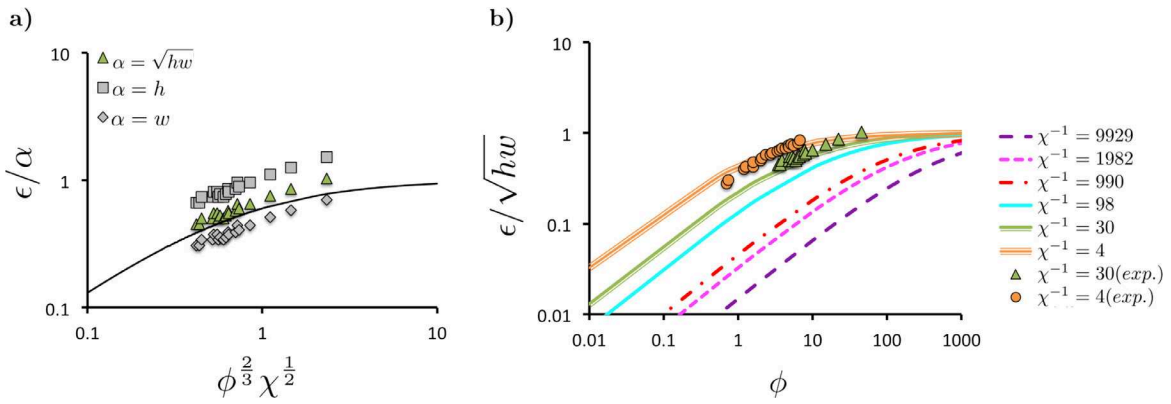

Fig. 3. The width ϵ of the core flow is expressed as a function of the flow rate ratio ϕ and the viscosity ratio χ. (a) Plot of ϵ/α for the different dimension parameters α, for the fluid pair A. Solid line represents $\epsilon/\alpha = [1 + (1.5\chi^{1/2}\phi^{2/3})^{-1}]^{-1}$. Best fit for $\alpha = \sqrt{hw}$. (b) Plot of $\epsilon/\sqrt{hw}$ as a function of ϕ for the fluid pairs A and B. Triangles correspond to fluid pair A (water/70% glycerol mixture, $\chi^{-1} = 30$) and circles represent experimental data from fluid pair B (alginate/70% glycerol mixture, $\chi^{-1} = 4.28$). Solid lines represent $\epsilon/\alpha = [1 + (K_x\phi^{2/3})^{-1}]^{-1}$ ($K_x = 1.5\chi^{1/2}$) and are adapted from [33].

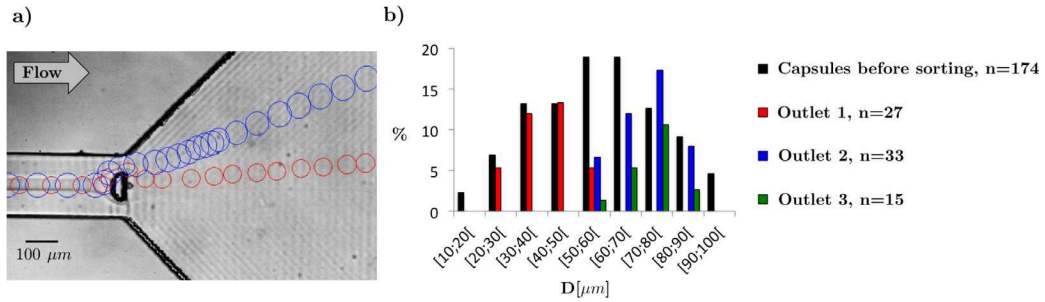

Fig. 4. (a) Trajectories of a 60 µm capsule (red) and a 80 µm capsule (blue), at various instants of time when they flow in pure glycerol (Fluid pair C, Table 1). (b) Size distribution of capsules collected at the different outlets. (For interpretation of the references to color in this figure legend, the reader is referred to the web version of this article).

have values of the internal thread size ϵ smaller than the capsule diameter D.

3.2. Influence of size on the capsule trajectory

Prior to any flow perfusion experiment, we observe capsules on a glass slide with an inverted microscope. We measure the mean diameter $D_0 = 60 \pm 18$ µm in statics, between slide and cover, on 174 capsules. Capsules are then flowed through a 50 µm gap between the wall and the obstacle, where they are confined. They are then collected at the different outlets Fig. 1a) and their size distribution is determined. The external fluid is pure glycerol (Fluid pair C, Table 1) with an external pressure $P_{ext} = 1000$ mbar. The internal fluid is the capsule suspension (Fluid pair C, Table 1) with an internal pressure $P_{in} = 400$ mbar.

We notice that larger capsules are deflected further from the channel axis than smaller ones (Fig. 4a). This is confirmed by the capsule size measurements at the three outlets (Fig. 4b). We found an average diameter $D_1 = 39 \pm 10$ µm for outlet 1 (in red, Fig. 1a), $D_2 = 70 \pm 8$ µm for outlet 2 (in blue, Fig. 1a) and $D_3 = 73 \pm 8$ µm for outlet 3 (in green, Fig. 1a). These results indicate that the system is able to sort micro-objects from their size. It functions as a standard pinched flow fractionation device [34]. The position of the center of mass of the capsule in the confined zone seems to influence the trajectory followed by the capsules. The smaller the capsule, the closer its center of mass from the obstacle, and the smaller δ. For an identical initial position, the larger capsules pass further from the obstacle and are more deflected than smaller ones in the divergent chamber. The trajectory of capsules seems to be sensitive to the capsule-to-obstacle distance δ, which is the only modified parameter in size-based sorting.

3.3. Influence of flow strength on the capsule trajectory

The experiment is now repeated, with the same fluids (Fluid pair C, Table 1), for different pressures: $P_{in} = 200$ mbar and $P_{ext} = 1000$ mbar (low flow strength), and $P_{in} = 1200$ mbar and $P_{ext} = 4500$ mbar (high flow strength). An increase in pressure keeping the P_{in}/P_{ext} ratio constant (constant core width ϵ) induces an increase in the flow rates q_{in} and q_{ext} and consequently in the capsule speed and forces applied to the capsule when it reaches the obstacle. Depending on the capsule mechanical properties, the capsule deforms more around the obstacle and its trajectory may vary. The capsules produced at pH 5.9 are softer than those produced at pH 8 (Table 2) [25]. We can notice that the stiffness of the two batches of capsules, defined as the ratio of G_s, differs only by a factor of 3 ± 1.5. Nonetheless, at constant flow strength, the viscous forces push softer capsules towards the obstacle wall as they flow around it, rather than stiffer capsules. This is due to the fact that viscous forces are balanced with elastic forces and that the more the capsule deforms, the closer the center of mass of the capsule and the obstacle (small δ). We show in Fig. 5 that the flow strength may have an influence on the trajectory of some capsules, depending on their stiffness. Capsules prepared at pH = 5.9 are less deflected at high flow strength (yellow capsule, Fig. 5a) than at low flow strength (pink capsule, Fig. 5a). On the contrary, capsules prepared at pH = 8 follow roughly the same trajectory whatever the applied viscous force (Fig. 5b). For the stiffest capsules (pH = 8), the trajectory is not affected by an increase in

Table 2
Capsules produced with different pH are flowed under a pressure ratio P_{in}/P_{ext}. The velocity U is measured experimentally, and the surface shear modulus G_s arises from the experiments by Chu et al. [25]. The values of the capillary number Ca are calculated using Eq. (2).

Cond.	pH	P_{in} [mbar]	P_{ext} [mbar]	U [$mm.s^{-1}$]	G_s [$N.m^{-1}$]	Ca
1	5.9	267	1000	1.1 ± 0.1	0.030 ± 0.007	0.05 ± 0.01
2	5.9	1200	4500	5.0 ± 0.3	0.030 ± 0.007	0.22 ± 0.04
3	8	200	1000	0.7 ± 0.1	0.081 ± 0.026	0.01 ± 0.002
4	8	1200	4500	4.9 ± 0.6	0.081 ± 0.026	0.08 ± 0.02

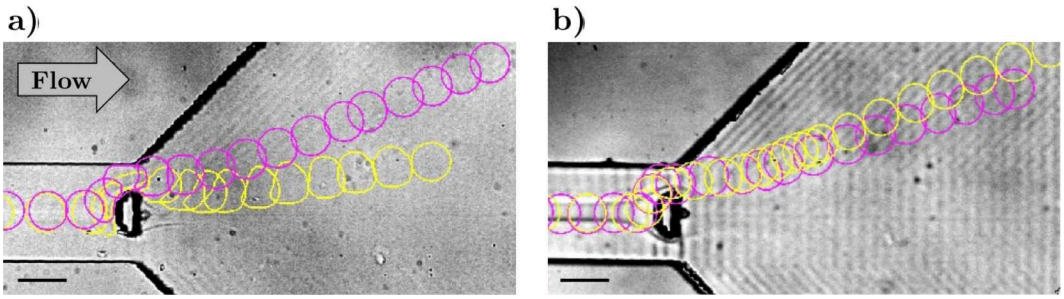

Fig. 5. Trajectory of capsules in the diverging flow chamber. Capsules were flowed at low (pink) and high (yellow) flow strengths. (a) Capsules prepared at pH 5.9. (b) Capsules prepared at pH 8. The scale bars correspond to 100 µm. (For interpretation of the references to color in this figure legend, the reader is referred to the web version of this article).

flow rates. This means that even at high pressure, the flow strength $\mu_{ext}U$ remains too small to overcome the elastic forces characterized by the 2D elastic shear modulus G_s.

4. Discussion

In the flow-focusing module at the entrance of our system, the capsule suspension forms a jet surrounded by a more viscous glycerol. The results presented in this paper show that we are able to control the width ϵ of the core flow, for a given viscosity ratio χ, by modifying the pressures applied at the entrances of our system. In the literature, the flow through flow-focusing microsystems has been abundantly studied but involves mostly the coflow of immiscible fluids, mainly for bubble [35] and droplet formation [36]. The velocity profile in the coflowing fluids differs significantly depending on whether the most viscous fluid is the internal [37] or the external one [33]. Although there are considerably fewer studies in the literature on the latter case, recent works have explored the geometry of fluid jets [33]. But no study had been conducted in rectangular channels. We show that the universal equation $\epsilon/\alpha = [1 + (1.5\chi^{1/2}\phi^{3/2})^{-1}]^{-1}$ established by Hu and Cubaud [33] in a rigid square channel for a viscosity ratio χ^{-1} between 100 and 10,000 remains valid for smaller viscosity contrasts ($\chi^{-1} = 30$ and $\chi^{-1} = 4$ in our experiments). More interestingly, the current results extend this law to soft PDMS channels with rectangular cross-section, provided the effective length scale $\alpha = \sqrt{hw}$ is used. We can imagine that for a rectangle with a larger w/h ratio, the length h would limit more effectively the width ϵ and modify the previous equation. It would be interesting to perform experiments in wider channels in order to find the limit of validity of this scaling law.

By flowing microcapsules of various sizes and mechanical properties in our device, we showed that a heterogeneous population of capsules can be sorted by size, at low flow strength. The sorting principle is similar to Pinch Flow Fractionation (PFF). In PFF systems, particles or bubbles are squeezed against a wall by an external flow. Small and large micro-objects take up distinct streamlines that can be later separated in a diverging chamber [34,38]. Unlike systems described in the literature, our device has a symmetrical design, with a constriction on each side of the obstacle. The streamline towards which smaller objects are pushed is the centerline of the channel, not located along a wall not located along a wall. This could allow a faster collection of small objects.

As in PFF devices, the trajectory of a capsule in the sorting device is governed by the distance δ between the obstacle and the center of mass of the capsule in the confined zone. At low flow strength, δ only depends on the size of particles to be sorted and increases with capsule diameter. Viscous forces are too small to deform capsules as they flow around the obstacle. Whatever their stiffness, δ is the capsule radius ($D/2$) and δ is maximal for capsules whose diameter is equal to the constriction width. At larger flow strength $\mu_{ext}U$, hydrodynamic forces increase and become comparable to elastic forces. In this case, the distance δ between a capsule and the obstacle no longer depends solely on capsule size, but also on capsule stiffness. Capsule sorting then depends on the capillary number:

$$Ca = \frac{\mu_{ext}U}{G_s}. \quad (2)$$

The capillary number compares viscous and elastic forces. Deformable capsules are pushed closer towards the obstacle wall (low δ) and end up following the same streamline as smaller objects. We can therefore imagine sorting microcapsules by deformability using our device. This has to be done at high capillary number Ca.

For fixed G_s, capsule deformation will only occur at large capillary number, i.e. at high flow strength $\mu_{ext}U$. We seek to determine the critical capillary number Ca_c beyond which capsule trajectory starts to depend on the mechanical properties. In earlier experiments, the shear modulus G_s has been measured for several conditions of pH and reticulation time [25]. At low flow strength, pH 5.9 and 8 capsules follow the same streamline: no deformability-based sorting occurs. At high flow strength, on the other hand, soft capsules deform around the obstacle while stiff capsules do not. Using Eq. (2), we find $Ca < 0.1$ for stiff capsules and/or low flow strength (Table 2). For soft capsules, at high flow strength we find $Ca > 0.2$. This yields two different values for the distance δ between the obstacle wall and the capsule center of mass, and the two populations can be separated. Our experimental results suggest that Ca_c lies between 0.1 and 0.2. This is consistent with the numerical results found in the literature, which report on a stiff behavior at $Ca = 0.05$ and soft behavior at $Ca = 0.3$ [30]. In conclusion, a moderate increase in the shear modulus G_s results in a significant mod-

ification of the trajectory when we impose high pressures in order to have $Ca < 0.1$ for a population of capsules and $Ca > 0.2$ for the other one.

The populations of rigid and soft capsules used in our experiments are polydisperse, with diameters between 55 µm and 85 µm. Many size-based separation techniques require a large size contrast between objects to be sorted, and a frankly bimodal distribution [18,34]. It is quite the opposite here: when microbeads much smaller than capsules are added to the suspension, not all of them are collected in the central outlet. This is due to the fact that they are not properly centered by the flow focusing. The distance $Y_c - Y_0$ between their center of mass and the channel axis can be as large as $\epsilon - D$. Small objects are therefore much more likely to be off-centered than objects of size $D \simeq \epsilon$, which are more efficiently confined in the jet. Similarly, capsules that are much larger than the constriction have to deform to pass through the obstacle. Whatever the flow strength, they take up the whole space available and $\delta = \frac{w-\lambda}{4}$. In our system, optimal separation is thus achieved with narrow size distributions, when all objects to be sorted have a size comparable to that of the fluid thread generated by the flow focusing. In the literature, techniques based on deterministic lateral displacement or inertia have demonstrated their ability to sort bimodal populations of micro-objects. Devices relying on inertial forces to separate particles usually operate at Reynolds number (Re) between 1 and 50 [14]. In our system Re computed with particle velocity and the smallest of the 2 viscosities always remain smaller than 10^{-3}, indicating that inertial forces are negligible. We propose in this article a more sensitive device, which can sort micro-objects exhibiting moderate variability in size or deformability.

5. Conclusion

We have demonstrated that capsule sorting based on deformability and size can be achieved experimentally by using the same device at various flow rates. The present device allows us to separate and collect capsules at different outlets after sorting. It is based on the capsule ability to deform around an obstacle and to follow different trajectories depending on capsule size and stiffness. Rigid capsules follow the same trajectory, whatever the flow strength, while soft capsules are pushed towards the channel axis when the viscous forces increase. The trajectory followed by a capsule in the diffusing chamber is governed by the distance δ between the center of mass of the capsule and the obstacle in the constriction. In a polydisperse suspension, where both size and mechanical properties vary, the system can be used in two steps. A deformability-based sorting at high flow rate can follow a previous size-based separation at low flow rate, in the desired size range. This is the proof that we have developed a versatile multipurpose sorting microsystem based on a really simple design. Compared to other existing sorting devices, we demonstrate the sensitivity of our device to sort micro-objects with small size and stiffness contrasts. Further developments are expected to minimize our device dimensions and will open new perspectives to sort heterogeneous populations of cells, and help cancer diagnosis or cell differentiation.

6. Author contributions

A.L.G. conceived the experiments; D.V., O.C., P.M. and N.M. performed experiments; F.E.-L. made the capsules; D.V., A.-V.S. and A.L.G. analyzed the data; D.V., A.-V.S. and A.L.G. wrote the paper.

7. Conflict of interests

The authors declare no conflict of interests. The founding sponsors had no role in the design of the study, in the collection, analyses, or interpretation of data, in the writing of the manuscript, or in the decision to publish the results.

Acknowledgments

D.V. acknowledges financial support from the French Ministry of Research. This project has been funded by Picardy Region (FORPLAQ project).

References

[1] Zhao H, Shaqfeh ES, Narsimhan V. Shear-induced particle migration and margination in a cellular suspension. Phys Fluids 2012;24:011902. doi:10.1063/1.3677935.
[2] Dong C, Lei XX. Biomechanics of cell rolling: shear flow, cell-surface adhesion, and cell deformability. J Biomech 2000;33:35–43. doi:10.1016/S0021-9290(99)00174-8.
[3] Woodward J. Crossing the endothelium. Cell Adhes Migr 2008;2:151–2.
[4] Condeelis J, Segall JE. Intravital imaging of cell movement in tumours. Nat Rev Cancer 2003;3:921–30. doi:10.1038/nrc1231.
[5] Mills JP, Diez-Silva M, Quinn DJ, Dao M, Lang MJ, Tan KSW, et al. Effect of plasmodial RESA protein on deformability of human red blood cells harboring Plasmodium falciparum. PNAS 2007;104:9213–17. doi:10.1073/pnas.0703433104.
[6] Suresh S. Biomechanics and biophysics of cancer cells. Acta Mater 2007;55:3989–4014. doi:10.1016/j.actamat.2007.04.022.
[7] Gossett DR, Weaver WM, Mach AJ, Hur SC, Tse HTK, Lee W, et al. Label-free cell separation and sorting in microfluidic systems. Anal Bioanal Chem 2010;397:3249–67. doi:10.1007/s00216-010-3721-9.
[8] Inglis DW. Efficient microfluidic particle separation arrays. Appl Phys Lett 2009;94:013510. doi:10.1063/1.3068750.
[9] Huang LR, Cox EC, Austin RH, Sturm JC. Continuous particle separation through deterministic lateral displacement. Science 2004;304:987–90. doi:10.1126/science.1094567.
[10] Guo F, Ji X-H, Liu K, He R-X, Zhao L-B, Guo Z-X, et al. Droplet electric separator microfluidic device for cell sorting. Appl Phys Lett 2010;96:193701. doi:10.1063/1.3360812.
[11] Choi S, Song S, Choi C, Park J-K. Microfluidic self-sorting of mammalian cells to achieve cell cycle synchrony by hydrophoresis. Anal Chem 2009;81:1964–8. doi:10.1021/ac8024575.
[12] Shields CW, Johnson LM, Gao L, López GP. Elastomeric negative acoustic contrast particles for capture, acoustophoretic transport, and confinement of cells in microfluidic systems. Langmuir 2014;30:3923–7. doi:10.1021/la404677w.
[13] Petersson F, Aberg L, Sward-Nilsson A-M, Laurell T. Free flow acoustophoresis: Microfluidic-based mode of particle and cell separation. Anal Chem 2007;79:5117–23. doi:10.1021/ac070444e.
[14] Kuntaegowdanahalli SS, Bhagat AAS, Kumar G, Papautsky I. Inertial microfluidics for continuous particle separation in spiral microchannels. Lab Chip 2009;9:2973–80. doi:10.1039/b908271a.
[15] Nagrath S, Sequist LV, Maheswaran S, Bell DW, Irimia D, Ulkus L, et al. Isolation of rare circulating tumour cells in cancer patients by microchip technology. Nature 2007;450:1235–9. doi:10.1038/nature06385.
[16] Baret J-C, Miller OJ, Taly V, Ryckelynck M, El-Harrak A, Frenz L, et al. Fluorescence-activated droplet sorting (FADS): efficient microfluidic cell sorting based on enzymatic activity. Lab Chip 2009;9:1850–8. doi:10.1039/b902504a.
[17] Guck J, Ananthakrishnan R, Mahmood H, Moon TJ, Cunningham CC, Käs J. The optical stretcher: a novel laser tool to micromanipulate cells. Biophys J 2001;81:767–84. doi:10.1016/S0006-3495(01)75740-2.
[18] Wang G, Mao W, Byler R, Patel K, Henegar C, Alexeev A, et al. Stiffness dependent separation of cells in a microfluidic device. Plos One 2013;8:e75901. doi:10.1371/journal.pone.0075901.
[19] Shields CW, Reyes CD, López GP. Microfluidic cell sorting: a review of the advances in the separation of cells from debulking to rare cell isolation. Lab Chip 2015;15:1230–49. doi:10.1039/c4lc01246a.
[20] Gossett DR, Tse HTK, Lee SA, Ying Y, Lindgren AG, Yang OO, et al. Hydrodynamic stretching of single cells for large population mechanical phenotyping. PNAS 2012;109:7630–5. doi:10.1073/pnas.1200107109.
[21] Walter J, Salsac A-V, Barthès-Biesel D, Le Tallec P. Coupling of finite element and boundary integral methods for a capsule in a Stokes flow. Int J Numer Methods Eng 2010;83:829–50. doi:10.1002/nme.2859.
[22] Kaoui B, Krüger T, Harting J. Complex dynamics of a bilamellar vesicle as a simple model for leukocytes. Soft Matter 2013;9:8057–61. doi:10.1039/c3sm51032h.
[23] Dupin MM, Halliday I, Care CM, Alboul L, Munn LL. Modeling the flow of dense suspensions of deformable particles in three dimensions. Phys Rev E 2007;75:066707. doi:10.1103/PhysRevE.75.066707.
[24] Gubspun J, Gires P-Y, de Loubens C, Barthès-Biesel D, Deschamps J, Georgelin M, et al. Characterization of the mechanical properties of cross-

linked serum albumin microcapsules: effect of size and protein concentration. Colloid Polym Sci 2016;294:1381–9. doi:10.1007/s00396-016-3885-8.
[25] Chu TX, Salsac A-V, Leclerc E, Barthès-Biesel D, Wurtz H, Edwards-Lévy F. Comparison between measurements of elasticity and free amino group content of ovalbumin microcapsule membranes: discrimination of the cross-linking degree. J Colloid Interface Sci 2011;355:81–8. doi:10.1016/j.jcis.2010.11.038.
[26] Dawson G, Häner E, Juel A. Extreme deformation of capsules and bubbles flowing through a localised constriction. Proc IUTAM 2015;16:22–32. doi:10.1016/j.piutam.2015.03.004.
[27] De Cock LJ, De Koker S, De Geest BG, Grooten J, Vervaet C, Remon JP, et al. Polymeric multilayer capsules in drug delivery. Angew Chem 2010;49:6954–73. doi:10.1002/anie.200906266.
[28] Leclerc E, Kinoshita H, Fujii T, Barthès-Biesel D. Transient flow of microcapsules through convergent–divergent microchannels. Microfluid Nanofluid 2012;12:761–70. doi:10.1007/s10404-011-0907-1.
[29] Gires P-Y, Barthès-Biesel D, Leclerc E, Salsac A-V. Transient behavior and relaxation of microcapsules with a cross-linked human serum albumin membrane. J Mech Behav Biomed Mater 2016;58:2–10. doi:10.1016/j.jmbbm.2015.09.008.
[30] Zhu L, Rorai C, Mitra D, Brand L. A microfluidic device to sort capsules by deformability: a numerical study. Soft Matter 2014;10:7705–11. doi:10.1039/C4SM01097C.
[31] Edwards-Lévy F, Andry M-C, Lévy M-C. Determination of free amino group content of serum albumin microcapsules using trinitrobenzenesulfonic acid: effect of variations in polycondensation pH. Int J Pharmaceut 1993;96:85–90. doi:10.1016/0378-5173(93)90215-2.
[32] Whitesides GM, Ostuni E, Takayama S, Jiang X, Ingber DE. Soft lithography in biology and biochemistry. Annu Rev Biomed Eng 2001;3:335–73. doi:10.1146/annurev.bioeng.3.1.335.
[33] Hu X, Cubaud T. Inertial destabilization of highly viscous microfluidic stratifications. Phys Rev Fluids 2016;1:044101. doi:10.1103/PhysRevFluids.1.044101.
[34] Yamada M, Nakashima M, Seki M. Pinched flow fractionation: continuous size separation of particles utilizing a laminar flow profile in a pinched microchannel. Anal Chem 2004;76:5465–71. doi:10.1021/ac049863r.
[35] Nie Z, Seo M, Xu S, Lewis PC, Mok M, Kumacheva E, et al. Emulsification in a microfluidic flow-focusing device: effect of the viscosities of the liquids. Microfluid Nanofluid 2008;5:585–94. doi:10.1007/s10404-008-0271-y.
[36] Garstecki P, Fuerstman MJ, Stone HA, Whitesides GM. Formation of droplets and bubbles in a microfluidic T-junction-scaling and mechanism of break-up. Lab Chip 2006;6:437–46. doi:10.1039/b510841a.
[37] Cubaud T, Masson TG. Capillary threads and viscous droplets in square microchannels. Phys Fluids 2008;20:053302. doi:10.1063/1.2911716.
[38] Maenaka H, Yamada M, Yasuda M, Seki M. Continuous and size-dependent sorting of emulsion droplets using hydrodynamics in pinched microchannels. Langmuir 2008;24:4405–10. doi:10.1021/la703581j.

Oral communications

International conferences :

D. Vesperini, and A. Le Goff, "A microfluidic method to sort capsules and cells according to their mechanical properties", *8^{th} World Congress of Biomechanics*, (Poster) 2018, Dublin, Ireland.

D. Vesperini, I. Bihi, and A. Le Goff, "A microfluidic method for capsule and cell sorting based on mechanical properties", *Cell Physics*, 2017, Saarbrücken, Germany.

D. Vesperini, N. Meunier, P. Maire, A.-V. Salsac , and A. Le Goff, "Deformability- and size-based capsule sorting", *5^{th} Micro and Nano Flow Conference*, 2016, Milan, Italy.

D. Vesperini, and A. Le Goff, "Deformability- and size-based microcapsule sorting", *Active Complexe Matter Summer school*, (Poster) 2016, Cargèse, France.

National conferences :

D. Vesperini, A.-V. Salsac, and A. Le Goff, "Deformability- and size-based microcapsule sorting", *1^{re} Journée de la Matière et des Systèmes Complexes*, 2016, Saclay.

D. Vesperini, and A. Le Goff, "Trajectoires de capsules plus ou moins souples", *36^{me} Journées de Physiques Statistiques*, 2016, Paris.

Bibliography

[1] R. Kirschstein and L. R. Skirboll, "Stem cells: Scientific progress and future research directions," tech. rep., Department of Health and Human Services, June 2001.

[2] N. He, L. Zhang, J. Cui, and Z. Li, "Bone marrow vascular niche: home for hematopoietic stem cells," *Bone marrow research*, 2014.

[3] T. Junt, H. Schulze, Z. Chen, S. Massberg, T. Goerge, A. Krueger, D. D. Wagner, T. Graf, J. E. Italiano Jr., R. A. Shivdasani, and U. H. von Andrian, "Dynamic visualization of thrombopoiesis within bone marrow," *Science*, vol. 317, pp. 1767–1770, Sep 2007.

[4] E. Lefrançais, G. Ortiz-Muñoz, A. Caudrillier, B. Mallavia, F. Liu, D. M. Sayah, E. E. Thornton, M. B. Headley, T. David, S. R. Coughlin, M. F. Krummel, A. D. Leavitt, E. Passegué, and M. R. Looney, "The lung is a site of platelet biogenesis and a reservoir for haematopoietic progenitors," *Nature*, vol. 544, pp. 105–109, April 2017.

[5] A. C. Brown, S. E. Stabenfeldt, B. Ahn, R. T. Hannan, K. S. Dhada, E. S. Herman, V. Stefanelli, N. Guzzetta, A. Alexeev, W. A. Lam, L. A. Lyon, and T. H. Barker, "Ultrasoft microgels displaying emergent, platelet-like, behaviors," *Nat Mater*, vol. 13, pp. 1108–1114, December 2014.

[6] A. Baigger, R. Blasczyk, and C. Figueiredo, "Towards the manufacture of megakaryocytes and platelets for clinical application," *Transfusion medicine and hemotherapy*, vol. 44, pp. 165–173, 2017.

[7] C. Dunois-Lardé, C. Capron, S. Fichelson, T. Bauer, E. Cramer-Bordé, and D. Baruch, "Exposure of human megakaryocytes to high shear rates accelerates platelet production," *Blood*, vol. 114, pp. 1875–1883, August 2009.

[8] A. Blin, A. Le Goff, A. Magniez, S. Poirault-Chassac, B. Teste, G. Sicot, K. A. Nguyen, F. S. Hamdi, M. Reyssat, and D. Baruch, "Microfluidic model of the platelet generating organ: beyond bone marrow biomimetics," *Scientific Reports*, vol. 6, p. 21700, 2016.

[9] K. R. Machlus and J. E. Italiano Jr., "The incredible journey: from megakaryocyte development to platelet formation," *The Journal of Cell Biology*, vol. 201, no. 6, pp. 785–796, 2013.

[10] D. Barthès-Biesel, "Motion and deformation of elastic capsules and vesicles in flow," *Annual Review of Fluid Mechanics*, vol. 48, pp. 25–52, Jan 2016.

[11] R. M. Kleinberger, N. A. Burke, K. Dalnoki-Veress, and H. D. Stöver, "Systematic study of alginate-based microcapsules by micropipette aspiration and confocal fluorescence microscopy," *Materials Science and Engineering C*, vol. 33, pp. 4295–4304, 2013.

[12] A. Walter, H. Rehage, and H. Leonhard, "Shear-induced deformations of polyamide microcapsules," *Colloid Polymer Science*, vol. 278, pp. 169–175, 2000.

[13] P. Erni, P. Fischer, and E. J. Windhab, "Deformation of single emulsion drops covered with a viscoelastic adsorbed protein layer in simple shear flow," *Applied Physics Letters*, vol. 87, p. 244104, Dec 2005.

[14] F. Edwards-Lévy, M.-C. Andry, and M.-C. Lévy, "Determination of free amino group content of serum albumin microcapsules using trinitrobenzenesulfonic acid: effect of variations in polycondensation pH," *International Journal of Pharmaceutics*, vol. 96, pp. 85–90, 1993.

[15] C. Xu, S. Hu, and X. Chen, "Artificial cells: from basic science to applications," *Materials Today*, vol. 19, pp. 516–532, November 2016.

[16] E. Karsenti, "Self-organization in cell biology: a brief history," *Nature Reviews Molecular cell biology*, vol. 9, pp. 255–262, 2008.

[17] B. Alberts, A. Johnson, J. Lewis, M. Raff, K. Roberts, and P. Walter, *Molecular Biology of the Cell*. Garland Science, 4th ed., 2002.

[18] F. Casanova and L. Santos, "Encapsulation of cosmetic active ingredients for topical application – a review," *Journal of Microencapsulation*, vol. 33, pp. 1–17, November 2015.

[19] P. Karthik, P. Ezhilarasi, and C. Anandharamakrishnan, "Challenges associated in stability of food grade nanoemulsions," *Critical Reviews in Food Science and Nutrition*, vol. 57, pp. 1435–1450, May 2017.

[20] B. G. De Geest, G. B. Sukhorukov, and H. Möhwald, "The pros and cons of polyelectrolyte capsules in drug delivery," *Expert Opinion Drug Delivery*, vol. 6, no. 6, pp. 613–624, 2009.

[21] D. W. Inglis, "Efficient microfluidic particle separation arrays," *Applied Physics Letters*, vol. 94, p. 013510, 2009.

[22] L. R. Huang, E. C. Cox, R. H. Austin, and J. C. Sturm, "Continuous particle separation through deterministic lateral displacement," *Science*, vol. 304, pp. 987–990, May 2004.

[23] M. Yamada, M. Nakashima, and M. Seki, "Pinched flow fractionation: Continuous size separation of particles utilizing a laminar flow profile in a pinched microchannel," *Analytical Chemistry*, vol. 76, no. 18, pp. 5465–5471, 2004.

[24] A. A. S. Bhagat, H. W. Hou, L. D. Li, C. T. Lim, and J. Han, "Pinched flow coupled shear-modulated inertial microfluidics for high-throughput rare blood cell separation," *Lab on a Chip*, vol. 11, pp. 1870–1878, 2011.

[25] S. S. Kuntaegowdanahalli, A. A. S. Bhagat, G. Kumar, and I. Papautsky, "Inertial microfluidics for continuous particle separation in spiral microchannels," *Lab on a Chip*, vol. 9, pp. 2973–2980, 2009.

[26] D. Di Carlo, "Inertial microfluidics," *Lab on a Chip*, vol. 9, pp. 3038–3046, 2009.

[27] D. Di Carlo, D. Irimia, R. G. Tompkins, and M. Toner, "Continuous inertial focusing, ordering, and separation of particles in microchannels," *PNAS*, vol. 104, pp. 18892–18897, November 2007.

[28] J. Zhang, S. Yan, D. Yuan, G. Alici, N.-T. Nguyen, M. Ebrahimi Warkiani, and W. Li, "Fundamentals and applications of inertial microfluidics: A review," *Lab on a Chip: miniaturization for chemistry, physics, biology, materials science and bioengineering*, vol. 16, 10-34 2016.

[29] K. Sinha and M. D. Graham, "Shape-mediated margination and demargination in flowing multicomponent suspensions of deformable capsules," *Soft Matter*, 2016.

[30] A. Kumar and M. D. Graham, "Margination and segregation in confined flows of blood and other multicomponent suspensions," *Soft Matter*, 2012.

[31] A. Leyrat-Maurin and D. Barthès-Biesel, "Motion of a deformable capsule through a hyperbolic constriction," *Journal of Fluid Mechanics*, vol. 279, pp. 135–163, 1994.

[32] G. Dawson, E. Häner, and A. Juel, "Extreme deformation of capsules and bubbles flowing through a localised constriction," *Procedia IUTAM*, vol. 16, pp. 22–32, 2015.

[33] B. Kaoui, M. Lauricella, and G. Pontrelli, "Mathematical modelling of drug release from multi-layer capsules," *Medical Physics*, 2017.

[34] A. Le Goff, B. Kaoui, G. Kurzawa, B. Haszon, and A.-V. Salsac, "Squeezing bio-capsules into a constriction: deformation till break-up," *Soft Matter*, 2017.

[35] S. C. Hur, N. K. Henderson-MacLennan, E. R. B. McCabe, and D. Di Carlo, "Deformability-based cell classification and enrichment using inertial microfluidics," *Lab on a Chip*, vol. 11, pp. 912–920, 2011.

[36] M. Masaeli, E. Sollier, H. Amini, W. Mao, K. Camacho, N. Doshi, S. Mitragotri, A. Alexeev, and D. Di Carlo, "Continuous inertial focusing and separation of particles by shape," *Physical Review X*, vol. 2, p. 031017, 2012.

[37] A. Kilimnik, W. Mao, and A. Alexeev, "Inertial migration of deformable capsules in channel flow," *Physics of Fluids*, vol. 23, p. 123302, 2011.

[38] C. Schaaf and H. Stark, "Inertial migration and axial control of deformable capsules," *Soft Matter*, vol. 13, pp. 3544–3555, 2017.

[39] M. M. Villone, M. Trofa, P. L. Maffettone, and M. A. Hulsen, "Numerical design of a T-shaped microfluidic device for deformability-based separation of elastic capsules and soft beads," *Physical Review E*, 2017.

[40] J. P. Arata and A. Alexeev, "Designing microfluidic channel that separates elastic particles upon stiffness," *Soft Matter*, vol. 5, pp. 2721–2724, 2009.

[41] G. Wang, W. Mao, R. Byler, K. Patel, C. Henegar, A. Alexeev, and T. Sulchek, "Stiffness dependent separation of cells in a microfluidic device," *Plos One*, vol. 8, p. e75901, October 2013.

[42] E. S. G. Shaqfeh, J. A. Bernate, and M. Yang, "Numerical simulation of the deterministic vector separation of particles flowing over slanted open cavities," *Physical Review Fluids*, vol. 1, p. 084101, Decembre 2016.

[43] T. A. Sulchek, A. Alexeev, and G. Wang, "Microfluidic device for separation of particles." United States patent, January 2013.

[44] L. Zhu, C. Rorai, D. Mitra, and L. Brandt, "A microfluidic device to sort capsules by deformability: A numerical study," *Soft Matter*, vol. 10, no. 39, pp. 7705–7711, 2014.

[45] G. M. Whitesides, E. Ostuni, S. Takayama, X. Jiang, and D. E. Ingber, "Soft lithography in biology and biochemistry," *Annual Review of Biomedical Engineering*, vol. 3, pp. 335–373, 2001.

[46] D. B. Goldstein, "Effect of alcohol on cellular membranes," *Annals of Emergency Medicine*, vol. 15, no. 9, pp. 1013–1018, 1986.

[47] F. Zirbel and J. E. Kinsella, "Effects of thiol reagents and ethanol on strength of whey protein gels," *Food Hydrocolloids*, vol. 2, no. 6, pp. 467–475, 1988.

[48] G. Prado, A. Farutin, C. Misbah, and L. Bureau, "Viscoelastic transient of confined Red Blood Cells," *Biophysical Journal*, vol. 108, pp. 2126–2136, 2015.

[49] P. Marchetti, D. Decaudin, A. Macho, N. Zamzami, T. Hirsch, S. A. Susin, and G. Kroemer, "Redox regulation of apoptosis: impact of thiol oxidation status on mitochondrial function," *European Journal of Immunology*, vol. 27, pp. 289–296, 1997.

[50] A. Drochon, "Rheology of dilute suspensions of red blood cells: experimental and theoretical approaches," *The European Physical Journal Applied Physics*, vol. 22, pp. 155–162, 2003.

[51] T. Chu, A.-V. Salsac, E. Leclerc, D. Barthès-Biesel, H. Wurtz, and F. Edwards-Lévy, "Comparison between measurements of elasticity and free amino group content of ovalbumin microcapsule membranes: Discrimination of the cross-linking degree," *Journal of Colloid and Interface Science*, vol. 355, pp. 81–88, 2011.

[52] X. Hu and T. Cubaud, "Inertial destabilization of highly viscous microfluidic stratifications," *Physical Review Fluids*, vol. 1, no. 4, p. 044101, 2016.

[53] T. Cubaud and T. G. Mason, "Capillary threads and viscous droplets in square microchannels," *Physics of Fluids*, vol. 20, p. 053302, May 2008.

[54] P. He, D. Barthès-Biesel, and E. Leclerc, "Flow of two immiscible liquids with low viscosity in Y shaped microfluidic systems: effect of geometry," *Microfluidics Nanofluidics*, vol. 9, pp. 293–301, August 2010.

[55] P. Marmottant and J.-P. Raven, "Microfluidics with foams," *Soft Matter*, vol. 5, pp. 3385–3388, 2009.

[56] J. Berthier, V.-M. Tran, F. Mittler, and N. Surrut, "The physics of a coflow micro-extractor: Interface stability and optimal extraction length," *Sensors and Actuators A: Physical*, vol. 149, pp. 56–64, 2009.

[57] J. Scoffoni, E. Lajeunesse, and G. M. Homsy, "Interface instabilities during displacements of two miscible fluids in a vertical pipe," *Physics of Fluids*, vol. 13, pp. 553–556, March 2001.

[58] M. d'Olce, J. Martin, N. Rakotomalala, D. Salin, and L. Talon, "Pearl and mushroom instability patterns in two miscible fluids' core annular flows," *Physics of Fluids*, vol. 20, p. 024104, 2008.

[59] D. Vesperini, O. Chaput, N. Munier, P. Maire, F. Edwards-Lévy, A.-V. Salsac, and A. Le Goff, "Deformability- and size-based microcapsule sorting," *Medical Engineering and Physics*, vol. 48, pp. 68–74, 2017.

[60] S. K. Sia and G. M. Whitesides, "Microfluidic devices fabricated in poly(dimethylsiloxane) for biological studies," *Electrophoresis*, vol. 24, pp. 3563–3576, 2003.

[61] Z. Li, S. Y. Mak, A. Sauret, and H. C. Shum, "Syringe-pump-induced fluctuation in all-aqueous microfluidic system implications for flow rate accuracy," *Lab on a Chip*, vol. 14, pp. 744–749, 2014.

[62] T. Ward, M. Faivre, M. Abkarian, and H. A. Stone, "Microfluidic flow focusing: drop size and scaling in pressure *versus* flow-rate-driven pumping," *Electrophoresis*, vol. 26, pp. 3716–3724, Oct 2005.

[63] S. Lignel, A.-V. Salsac, A. Drelich, E. Leclerc, and I. Pezron, "Water-in-oil droplet formation in a flow-focusing microsystem using pressure- and flow rate-driven pumps.," *Colloids and Surfaces A*, vol. 531, pp. 164–172, 2017.

[64] E. O. Häner, *Microfluidic segregation of capsules*. PhD thesis, University of Manchester, 2017.

[65] G. L. Klement, T.-T. Yip, F. Cassiola, L. Kikuchi, D. Cervi, V. Podust, J. E. Italiano, E. Wheatley, A. Abou-Slaybi, E. Bender, N. Almog, M. W. Kieran, and J. Folkman, "Platelets actively sequester angiogenesis regulators," *Blood*, vol. 113, no. 12, 2009.

[66] J. E. Aslan, A. Itakura, J. M. Gertz, and O. J. McCarty, *Platelets and Megakaryocytes*, vol. 3, ch. Platelet shape change and spreading. Humana Press, 2012.

[67] S. Suresh, "Biomechanics and biophysics of cancer cells," *Acta Materialia*, vol. 55, pp. 3989–4014, 2007.

[68] V. Swaminathan, K. Mythreye, E. T. O'Brien, A. Berchuck, G. C. Blobe, and R. Superfine, "Mechanical stiffness grades metastatic potential in patient tumor cells and in cancer cell lines," *Cancer Research*, vol. 71, pp. 5075–5080, August 2011.

[69] M. M. Yallapu, K. S. Katti, D. R. Katti, S. R. Mishra, S. Khan, M. Jaggi, and S. C. Chauhan, "The roles of cellular nanomechanics in cancer," *Medicinal Research Reviews*, 2015.

[70] P. E. Lindahl, "Principle of a counter-streaming centrifuge for the separation of particles of different sizes," *Nature*, vol. 161, no. 4095, pp. 648–649, 1948.

[71] T. G. Pretlow II and T. P. Pretlow, "Centrifugal elutriation (counterstreaming centrifugation) of cells," *Cell Biophysics*, vol. 1, pp. 195–210, 1979.

[72] R. G. Miller and R. A. Phillips, "Separation of cells by velocity sedimentation," *Journal of Cell Phisiology*, vol. 73, pp. 191–202, 1969.

[73] D. English and B. R. Andersen, "Single-step separation of red blood cells, granulocytes and mononuclear leukocytes on discontinuous density gradients of Ficoll-Hypaque," *Journal of Immunological Methods*, vol. 5, pp. 249–252, Aug 1974.

[74] Sino Biologie, "http://www.sinobiological.com/flow-cytometry-fcm-facs-technology-center.html , Flow cytometry (FCM) / FACS technology center," 2016.

[75] R. C. Willis, "Sorting out the mess: Researchers are using a variety of methods to isolate specific cell types," *Modern drug discovery*, pp. 29–32, 2004.

[76] S. Miltenyi, W. Müller, W. Weichel, and A. Radbruch, "High gradient magnetic cell separation with MACS," *Cytometry*, vol. 11, pp. 231–238, 1990.

[77] P. Chen, Y.-Y. Huang, K. Hoshino, and X. Zhang, "Multiscale immunomagnetic enrichment of circulating tumor cells: from tubes to microchips," *Lab on a Chip*, vol. 14, no. 3, pp. 446–458, 2014.

[78] R. Handgretinger, P. Lang, M. Schumm, G. Taylor, S. Neu, E. Koscielnak, D. Niethammer, and T. Klingebiel, "Isolating and transplantation of autologous peripheral $CD34^+$ progenitor cells highly purified by magnetic-activated cell sorting," *Bone Marrow Transplantation*, vol. 21, pp. 987–993, 1998.

[79] A. A. Powell, A. A. H.Talasaz, H. Zhang, M. A. Coram, A. Reddy, G. Deng, M. L. Telli, R. H. Advani, R. W. Carlson, J. A. Mollick, S. Sheth, A. W. Kurian, J. M. Ford, F. E. Stockdale, S. R. Quake, R. F. Pease, M. N. Mindrinos, G. Bhanot, S. H. Dairkee, R. W. Davis, and S. S. Jeffrey, "Single cell profiling of circulating tumor cells: Transcriptional heterogeneity and diversity from breast cancer cell lines," *Plos One*, vol. 7, p. e33788, May 2012.

[80] K. Makker, A. Agarwal, and R. K. Sharma, "Magnetic activated cell sorting (MACS): Utility in assisted reproduction," *Indian Journal of Experimental Biology*, vol. 46, pp. 491–497, 2008.

[81] P. S. Dittrich, M. Jahnz, and P. Schwille, "A new embedded process for compartmentalized cell-free protein expression and on-line detection in microfluidic devices," *ChemBioChem*, vol. 6, pp. 811–814, Apr 2005.

[82] A. Fallah-Araghi, J.-C. Baret, M. Ryckelynck, and A. D. Griffiths, "A completely *in vitro* ultrahigh-throughput droplet-based microfluidic screening system for protein engineering and directed evolution," *Lab on a Chip*, vol. 12, no. 5, pp. 882–891, 2012.

[83] A. Y. Fu, C. Spence, A. Scherer, F. H. Arnold, and S. R. Quake, "A microfabricated fluorescence-activated cell sorter," *Nature Biotechnology*, vol. 17, pp. 1109–1111, 1999.

[84] S.-Y. Teh, R. Lin, L.-H. Hung, and A. P. Lee, "Droplet microfluidics," *Lab on a Chip*, vol. 8, no. 2, pp. 198–220, 2008.

[85] M. Curcio and J. Roeraade, "Continuous segmentated-flow polymerase chain reaction for high-throughput miniaturized DNA amplification," *Analytical Chemistry*, vol. 75, pp. 1–7, 2003.

[86] M. T. Guo, A. Rotem, J. A. Heyman, and D. A. Weitz, "Droplet microfluidics for high-throughput biological assays," *Lab on a Chip*, vol. 12, no. 12, pp. 2146–2155, 2012.

[87] L. Mazutis, J. Gilbert, W. L. Ung, D. A. Weitz, A. D. Griffiths, and J. A. Heyman, "Single-cell analysis and sorting using droplet-based microfluidics," *Nature Protocols*, vol. 8, no. 5, pp. 870–891, 2013.

[88] J.-C. Baret, O. J. Miller, V. Taly, M. Ryckelynck, A. El-Harrak, L. Frenz, C. Rick, M. L. Samuels, J. B. Hutchison, J. J. Agresti, D. R. Link, D. A. Weitz, and A. D. Griffiths, "Fluorescence-activated droplet sorting (FADS): efficient microfluidic cell sorting based on enzymatic activity," *Lab on a Chip*, vol. 9, pp. 1850–1858, July 2009.

[89] N. Pamme and C. Wilhelm, "Continuous sorting of magnetic cells *via* on-chip free-flow magnetophoresis," *Lab on a Chip*, vol. 6, no. 8, pp. 974–980, 2006.

[90] M. Zborowski, G. R. Ostera, L. R. Moore, S. Milliron, J. J. Chalmers, and A. N. Schechter, "Red blood cell magnetophoresis," *Biophysical Journal*, vol. 84, pp. 2638–2645, 2003.

[91] K.-H. Han and A. B. Frazier, "Diamagnetic capture mode magnetophoretic microseparator for blood cells," *Journal of microelectromechanical systems*, vol. 14, no. 6, pp. 1422–1431, 2005.

[92] K. Cushing, E. Undvall, Y. Ceder, H. Lilja, and T. Laurell, "Reducing WCB background in cancer cell separation products by negative acoustic contrast particle immuno-acoustophoresis," *Analitica Chimica Acta*, vol. 1000, pp. 256–264, 2018.

[93] D. R. Gossett, W. M. Weaver, A. J. Mach, S. C. Hur, H. T. K. Tse, W. Lee, H. Amini, and D. Di Carlo, "Label-free cell separation and sorting in microfluidic systems," *Analytical Bioanalytical Chemistry*, vol. 397, pp. 3249–3267, 2010.

[94] F. Petersson, L. Aberg, A.-M. Swärd-Nilsson, and T. Laurell, "Free flow acoustophoresis: Microfluidic-based mode of particle and cell separation," *Analytical Chemistry*, vol. 79, pp. 5117–5123, July 2007.

[95] F. Petersson, A. Nilsson, C. Holm, H. Jönsson, and T. Laurell, "Separation of lipids from blood utilizing ultrasonic standing waves in microfluidic channels," *The Analyst*, vol. 129, no. 10, pp. 938–943, 2004.

[96] C. W. Shields, L. M. Johnson, L. Gao, and G. P. López, "Elastomeric negative acoustic contrast particles for capture, acoustophoretic transport, and confinement of cells in microfluidic systems," *Langmuir*, vol. 30, pp. 3923–3927, 2014.

[97] X. Ding, Z. Peng, S.-C. S. Lin, M. Geri, S. Li, P. Li, Y. Chen, M. Dao, S. Suresh, and T. J. Huang, "Cell separation using tilted-angle standing surface acoustic waves," *PNAS*, vol. 111, pp. 12992–12997, Aug 2014.

[98] E. Ozkumur, A. M. Shah, J. C. Ciciliano, B. L. Emmink, D. T. Miyamoto, E. Brachtel, M. Yu, P. i Chen, B. Morgan, J. Trautwein, A. Kimura, S. Sengupta, S. L. Stott, N. M. Karabacak, T. A. Barber, J. R. Walsh, K. Smith, P. S. Spuhler, J. P. Sullivan, R. J. Lee, D. T. Ting, X. Luo, A. T. Shaw, A. Bardia, L. V. Sequist, D. N. Louis, S. Maheswaran, R. Kapur, D. A. Haber, and M. Toner, "Inertial focusing for tumor antigen–dependent and –independent sorting of rare circulating tumor cells," *Science Translational Medicine*, vol. 5, p. 179ra47, April 2013.

[99] A. A. S. Bhagat, H. Bow, H. W. Hou, S. J. Tan, J. Han, and C. T. Lim, "Microfluidics for cell separation," *Medical and Biological Engineering and Computing*, vol. 48, pp. 999–1014, 2010.

[100] J. P. Beech, S. H. Holm, K. Adolfsson, and J. O. Tegenfeldt, "Sorting cells by size, shape and deformability," *Lab on a Chip*, vol. 12, pp. 1048–1051, 2012.

[101] R. Huang, T. A. Barber, M. A. Schmidt, R. G. Tompkins, M. Toner, D. W. Bianchi, R. Kapur, and W. L. Flejter, "A microfluidics appoach for the isolation of nucleated red blood cells (NRBCs) from the peripheral blood of pregnant women," *Prenatal Diagnosis*, vol. 28, no. 10, pp. 892–899, 2008.

[102] J. Takagi, M. Yamada, M. Yasuda, and M. Seki, "Continuous particle separation in a microchannel having asymmetrically arranged multiple branches," *Lab on a Chip*, vol. 5, no. 7, pp. 778–784, 2005.

[103] S. S. P. Nathamgari, B. Dong, F. Zhou, W. Kang, J. P. Giraldo-Vela, T. McGuire, R. L. McNaughton, C. Sun, J. A. Kessler, and H. D. Espinosa, "Isolating single cells in a neurosphere assay using inertial microfluidics," *Lab on a chip*, vol. 15, pp. 4591–4597, 2015.

[104] M. Islam, H. Brink, S. Blanche, C. DiPrete, T. Bongiorno, N. Stone, A. Liu, A. Philip, G. Wang, W. Lam, A. Alexeev, E. K. Waller, and T. Sulchek, "Microfluidic sorting of cells by viability based on differences in cell stiffness," *Scientific Reports*, vol. 7, p. 1997, 2017.

[105] S. Zheng, H. Lin, J.-Q. Liu, M. Balic, R. Datar, R. J. Cote, and Y.-C. Tai, "Membrane microfilter device for selective capture, electrolysis and genomic analysis of human circulating tumor cells," *Journal of Chromatography A*, vol. 1162, pp. 154–161, Aug 2007.

[106] P. Preira, V. Grandné, J.-M. Forel, S. Gabriele, M. Camara, and O. Theodoly, "Passive circulating cell sorting by deformability using a microfluidic gradual filter," *Lab on a Chip*, vol. 13, no. 1, pp. 161–170, 2013.

[107] M. M. Wang, E. Tu, D. E. Raymond, J. M. Yang, H. Zhang, N. Hagen, B. Dees, E. M. Mercer, A. H. Forster, I. Kariv, P. J. Marchand, and W. F. Butler, "Microfluidic sorting of mammalian cells by optical force switching," *Nature Biotechnology*, vol. 23, pp. 83–87, Jan 2005.

[108] S. M. Hosseini and J. J. Feng, "How malaria parasites reduce the deformability of infected red blood cells," *Biophysical Journal*, vol. 103, pp. 1–10, July 2012.

[109] J. P. Mills, M. Diez-Silva, D. J. Quinn, M. Dao, M. J. Lang, K. S. W. Tan, C. T. Lim, G. Milon, P. H. David, O. Mercereau-Puijalon, S. Bonnefoy, and S. Suresh, "Effect of plasmodial RESA protein on deformability of human red blood cells harboring *Plasmodium falciparum*," *PNAS*, vol. 104, pp. 9213–9217, May 2007.

[110] Y. Alapan, Y. Matsuyama, J. A. Little, and U. A. Gurkan, "Dynamic deformability of sickle red blood cells in microphysiological flow," *Technology*, vol. 4, pp. 71–79, June 2016.

[111] M. Nishino, H. Tanaka, H. Ogura, Y. Inoue, T. Koh, K. Fujita, and H. Sugimoto, "Serial changes in leukocyte deformability and whole blood rheology in patients with sepsis or trauma," *The journal of Trauma*, vol. 59, pp. 1425–1431, 2005.

[112] B. Yap and R. D. Kamm, "Cytoskeletal remodeling and cellular activation during deformation of neutrophils into narrow channels," *Journal applied physiology*, vol. 99, pp. 2323–2330, 2005.

[113] K. Yoshida, R. Kondo, Q. Wang, and C. M. Doerschuk, "Neutrophil cytoskeletal rearrangements during capillary sequestration in bacterial pneumonia in rats," *American journal of respiratory and critical care medicine*, vol. 174, pp. 689–698, 2006.

[114] A. E. Ekpenyong, N. Toepfner, E. R. Chilvers, and J. Guck, "Mechanotransduction in neutrophil activation and deactivation," *Biochimica et Biophysica Acta*, vol. 1853, pp. 3105–3116, 2015.

[115] A. E. Ekpenyong, N. Toepfner, C. Fiddler, M. Herbig, W. Li, G. Cojoc, C. Summers, J. Guck, and E. R. Chilvers, "Mechanical deformation induces depolarization of neutrophils," *Science Advances*, vol. 3, p. e1602536, 2017.

[116] D. Di Carlo, "A mechanical biomarker of cell state in medicine," *Journal of Laboratory Automation*, vol. 17, no. 1, pp. 32–42, 2012.

[117] C. Cupelli, T. Borchardt, T. Steiner, N. Paust, R. Zengerle, and M. Santer, "Leukocyte enrichment based on a modified pinched flow fractionation approach," *Microfluidics and Nanofluidics*, vol. 14, pp. 551–563, Nov 2013.

[118] S. Gabriele, A.-M. Benoliel, P. Bongrand, and O. Theodoly, "Microfluidic investigation reveals distinct roles for actin cytoskeleton and myosin II activity in capillary leukocyte trafficking," *Biophysical Journal*, vol. 96, pp. 4308–4318, May 2009.

[119] S. Greenberg, D. Rosenthal, T. Greeley, R. Tantravahi, and R. Handin, "Characterization of a new megakaryocytic cell line: the Dami cell," *Blood*, vol. 72, pp. 1968–1977, 1988.

[120] H. Maenaka, M. Yamada, M. Yasuda, and M. Seki, "Continuous and size-dependent sorting of emulsion droplets using hydrodynamics in pinched microchannels," *Langmuir*, vol. 24, pp. 4405–4410, 2008.

[121] J. C. Alves-Filho, A. de Freitas, F. Spiller, F. O. Souto, Fernando, and Q. Cunha, "The role of neutrophils in severe sepsis," *Shock*, vol. 30, no. 7, 2008.

[122] J. H. Kang, M. Super, C. W. Yung, R. M. Cooper, K. Domansky, A. R. Graveline, T. Mammoto, J. B. Berthet, H. Tobin, M. J. Cartwright, A. L. Watters, M. Rottman, A. Waterhouse, A. Mammoto, N. Gamini, M. J. Rodas, A. Kole, A. Jiang, T. M. Valentin, A. Diaz, K. Takahashi, and D. E. Ingber, "An extracorporeal blood-cleansing device for sepsis therapy," *Nature Medicine*, vol. 20, pp. 1211–1216, Sep 2014.

[123] J.-J. Lee, K. J. Jeong, M. Hashimoto, A. H. Kwon, A. Rwei, S. A. Shankarappa, J. H. Tsui, and D. S. Kohane, "Synthetic ligan-coated magnetic nanoparticles for microfluidic bacterial separation from blood," *Nano Letters*, vol. 14, no. 1, pp. 1–5, 2014.

[124] J. J. Hoffmann, "Neutrophil CD64: a diagnostic marker for infection and sepsis," *Clinical Chemistry and Laboratory Medicine*, vol. 47, Jan 2009.

[125] M.-L. Rol, F. Venet, T. Rimmele, V. Moucadel, P. Cortez, L. Quemeneur, D. Gardiner, A. Griffiths, A. Pachot, J. Textoris, and G. Monneret, "The REAnimation Low Immune Status Markers (REALISM) project: a protocol for broad characterisation and follow-up of injury-induced immunosuppression in intensive care unit (ICU) critically ill patients," *BMJ Open*, vol. 7, p. e015734, Jun 2017.

[126] J. F. V. Vincent, *Structural Biomatrials*. The Macmillan Press LTD, 1982.

[127] C. Martinez Torres, *Structure and dynamics of single living cells: comparison of non intrusive coherent microscopicmethods and AFM indentation experiments*. PhD thesis, Université Claude Bernard Lyon 1, 2015.

[128] N. Caille, O. Thoumine, Y. Tardy, and J.-J. Meister, "Contribution of the nucleus to the mechanical properties of endothelial cells," *Journal of Biomechanics*, vol. 35, pp. 177–187, 2002.

[129] M. Staykova, D. P. Holmes, C. Read, and H. A. Stone, "Mechanics of surface area regulation in cells examined with confined lipid membranes," *PNAS*, vol. 108, pp. 9084–9088, May 2011.

[130] J. Guck, F. Lautenschlager, S. Paschke, and M. Beil, "Critical review: cellular mechanobiology and amoeboid migration," *Integrative Biology*, vol. 2, pp. 575–583, 2010.

[131] M. Carin, D. Barthès-Biesel, F. Edwards-Lévy, C. Postel, and D. C. Andrei, "Compression of biocompatible liquid-filled HSA-alginate capsules: Determination of the membrane mechanical properties," *Biotechnology and Bioengineering*, vol. 82, pp. 207–212, April 2003.

[132] O. Thoumine and A. Ott, "Time scale dependent viscoelastic and contractile regimes in fibroblasts probed by microplate manipulation," *Journal of Cell Science*, vol. 110, pp. 2109–2116, 1997.

[133] A. Ashkin, J. M. Dziedzic, J. E. Bjorkholm, and S. Chu, "Observation of a single-beam gradient force optical trap for dielectric particles," *Optics Letters*, vol. 11, pp. 288–290, May 1986.

[134] T. T. Perkins, S. R. Quake, D. E. Smith, and S. Chut, "Relaxation of a single DNA molecule observed by optical microscopy," *Science*, vol. 264, pp. 822–826, May 1994.

[135] J. Guck, R. Ananthakrishnan, H. Mahmood, T. J. Moon, C. C. Cunningham, and J. Käs, "The optical stretcher: A novel laser tool to micromanipulate cells," *Biophysical Journal*, vol. 81, pp. 767–784, August 2001.

[136] D. R. Gossett, H. T. K. Tse, S. A. Lee, Y. Ying, A. G. Lindgren, O. O. Yang, J. Rao, A. T. Clark, and D. Di Carlo, "Hydrodynamic stretching of single cells for large population mechanical phenotyping," *PNAS*, vol. 109, no. 20, pp. 7630–7635, 2012.

[137] P. B. Bareil, Y. Sheng, Y.-Q. Chen, and A. Chiou, "Calculation of spherical red blood cell deformation in a dual-beam optical stretcher," *Optics express*, vol. 15, p. 16030, November 2007.

[138] F. Wottawah, S. Schinkinger, B. Lincoln, R. Ananthakrishnan, M. Romeyke, J. Guck, and J. Käs, "Optical rheology of biological cells," *Physical Review Letters*, vol. 94, p. 098103, 2005.

[139] J. P. Shelby, J. White, K. Ganesan, P. K. Rathod, and D. T. Chiu, "A microfluidic model for single-cell capillary obstruction by *Plasmodium falciparum*- infected erythrocytes," *PNAS*, vol. 100, no. 25, pp. 14618–14622, 2003.

[140] H. W. Hou, Q. S. Li, G. Y. H. Lee, A. P. Kumar, C. N. Ong, and C. T. Lim, "Deformability study of breast cancer cells using microfluidics," *Biomedical Microdevices*, vol. 11, pp. 557–564, 2009.

[141] S. She, C. Xu, X. Yin, W. Tong, and C. Gao, "Shape deformation and recovery of multilayer microcapsules after being squeezed through a microchannel," *Langmuir*, vol. 28, pp. 5010–5016, 2012.

[142] P. Preira, J.-M. Forel, P. Robert, P. Nègre, M. Biarnes-Pelicot, F. Xeridat, P. Bongrand, L. Papazian, and O. Theodoly, "The leukocyte-stiffening property of plasma in early acute respiratory distress syndrome (ARDS) revealed by a microfluidic single-cell study: the role of cytokines and protection with antibodies," *Critical Care*, vol. 20, Dec 2015.

[143] Y. Lefebvre, E. Leclerc, D. Barthès-Biesel, J. Walter, and F. Edwards-Lévy, "Flow of artificial microcapsules in microfluidic channels: A method for determining the elastic properties of the membrane," *Physics of Fluids*, vol. 20, p. 123102, 2008.

[144] G. Binnig, C. F. Quate, and C. Gerber, "Atomic force microscopy," *Physical Review Letters*, vol. 56, pp. 930–934, March 1986.

[145] H. Hertz, *Miscellaneous papers*. Macmillan and Co. Ldt., 1896.

[146] K. L. Johnson, K. Kendall, and A. D. Roberts, "Surface energy and the contact of elastic solids," *Proceedings of the Royal Society of London*, vol. 324, pp. 301–313, 1971.

[147] I. N. Sneddon, "The relation between load and penetration in the axisymmetric boussinesq problem for a punch of arbitrary profile," *International Journal of Engineering Science*, vol. 3, pp. 47–57, 1965.

[148] G. G. Bilodeau, "Regular pyramid punch problem," *Journal of applied mechanics*, vol. 59, pp. 519–523, 1992.

[149] G. Thomas, N. A. Burnham, T. A. Camesano, and Q. Wen, "Measuring the mechanical properties of living cells using atomic force microscopy," *Journal of Visualized Experiments*, vol. 76, p. e50497, Jun 2013.

[150] C. Goldsbury and S. Scheuring, "Introduction to atomic force microscopy (AFM) in biology," *Current Protocols in Protein Science*, 2002.

[151] T. E. Fisher, A. F. Oberhauser, M. Carrion-Vazquez, P. E. Marszalek, and J. M. Fernandez, "The study of protein mechanics with the atomic force microscope," *Trends In Biochemical Sciences*, vol. 24, 1999.

[152] S. Sen, S. Subramanian, and D. E. Discher, "Indentation and adhesive probing of a cell membrane with AFM: Theoretical model and experiments," *Biophysical Journal*, vol. 89, pp. 3203–3213, November 2005.

[153] J. Alcaraz, L. Buscemi, M. Grabulosa, X. Trepat, B. Fabry, R. Farré, and D. Navajas, "Microrheology of human lung epithelial cells measured by atomic force microscopy," *Biophysical Journal*, vol. 84, pp. 2071–2079, March 2003.

[154] S. Nawaz, P. Sánchez, K. Bodensiek, S. Li, M. Simons, and I. A. T. Schaap, "Cell visco-elasticity measured with AFM and optical trapping at sub-micrometer deformations," *Plos One*, vol. 7, p. e45297, September 2012.

[155] K. Haase and A. E. Pelling, "Investigating cell mechanics with atomic force microscopy," *Journal of Royal Society Interface*, vol. 12, 2015.

[156] C. M. Franz and P. H. Puech, "Atomic force microscopy: A versatile tool for studying cell morphology, adhesion and mechanics," *Cellular and Molecular Bioengineering*, 2008.

[157] H. Liu, J. Wen, Y. Xiao, J. Liu, S. Hopyan, M. Radisic, C. A. Simmons, and Y. Sun, "*In Situ* mechanical characterization of the cell nucleus by atomic force microscopy," *ASCNano*, vol. 8, no. 4, pp. 3821–3828, 2014.

[158] M. Lekka, D. Gil, K. Pogoda, J. Dulińska-Litewka, R. Jach, J. Gostek, O. Klymenko, S. Prauzner-Bechcicki, Z. Stachura, J. Wiltowska-Zuber, K. Okoń, and P. Laidler, "Cancer cell detection in tissue sections using AFM," *Archives of Biochemistry and Biophysics*, vol. 518, pp. 151–156, 2012.

[159] W. A. Ducker, T. J. Senden, and R. M. Pashley, "Direct measurement of colloidal forces using an atomic force microscope," *Letters to nature*, vol. 353, pp. 239–241, September 1991.

[160] A. Fery and R. Weinkamer, "Mechanical properties of micro- and nanocapsules: Single-capsule measurements," *Polymer*, vol. 48, pp. 7221–7235, 2007.

[161] J. P. Best, M. P. Neubauer, S. Javed, H. H. Dam, A. Fery, and F. Caruso, "Mechanis of pH responsive hydrogel capsules," *Langmuir*, vol. 29, pp. 9814–9823, 2013.

[162] K.-T. Wan, V. Chan, and D. A. Dillard, "Constitutive equation for elastic indentation of a thin-walled biomimetic microcapsule by an atomic force microscope tip," *Colloids and Surfaces B*, vol. 27, pp. 241–248, 2002.

[163] E. M. Darling, M. Topel, S. Zauscher, T. P. Vail, and F. Guilak, "Viscoelastic properties of human mesenchymally-derived stem cells and primary osteoblasts, chondrocytes, and adipocytes," *Journal of Biomechanics*, vol. 41, pp. 454–464, Jan 2008.

[164] D. Wirtz, "Particle-tracking microrheology of living cells: Principles and applications," *Annual Review Biophysics*, vol. 38, pp. 301–326, 2009.

[165] S. Yamada, D. Wirtz, and S. C. Kuo, "Mechanics of living cells measured by laser tracking microrheology," *Biophysical Journal*, vol. 78, pp. 1736–1747, 2000.

[166] J. C. Crocker and B. D. Hoffman, "Multiple particle tracking and two-point microrheology in cells," *Methods in Cell Biology*, vol. 83, pp. 141–178, 2007.

[167] A. Pai, P. Sundd, and D. F. J. Tees, "*In situ* microrheological determination of neutrophil stiffening following adhesion in a model capillary," *Annals of Biomedical Engineering*, vol. 36, pp. 596–603, April 2008.

[168] T. P. Kole, Y. Tseng, and D. Wirtz, "Intracellular microrheology as a tool for the measurement of the local mechanical properties of live cells," in *Intermediate Filament Cytoskeleton*, vol. 78 of *Methods in Cell Biology*, pp. 45 – 64, Academic Press, 2004.

[169] M. Puig-De-Morales, M. Grabulosa, J. Alcaraz, J. Mullol, G. N. Maksym, J. J. Fredberg, and D. Navajas, "Measurement of cell microrheology by magnetic twisting cytometry with frequency domain demodulation," *Journal applied physiology*, vol. 91, pp. 1152–1159, 2001.

[170] B. Fabry, G. N. Maksym, J. P. Butler, M. Glogauer, D. Navajas, and J. J. Fredberg, "Scaling the microrheology of living cells," *Physical Review Letters*, vol. 87, no. 14, p. 148102, 2001.

[171] R. M. Hochmuth, "Micropipette aspiration of living cells," *Journal of Biomechanics*, vol. 33, pp. 15–22, Jan 2000.

[172] J.-Y. Shao, H. P. Ting-Beall, and R. M. Hochmuth, "Static and dynamic lengths of neutrophil microvilli," *Proceedings of the National Academy of Sciences*, vol. 95, pp. 6797–6802, June 1998.

[173] M. A. Tsai, R. S. Frank, and R. E. Waugh, "Passive mechanical behavior of human neutrophils: Effect of cytochalasin B," *Biophysical Journal*, vol. 66, pp. 2166–2172, June 1994.

[174] A. Sawicka, A. Babataheri, S. Dogniaux, A. I. Barakat, D. Gonzalez-Rodriguez, C. Hivroz, and J. Husson, "Micropipette force probe to quantify single-cell force generation: application to T-cell activation," *Molecular Biology of the Cell*, vol. 28, pp. 3229–3239, 2017.

[175] M. Sato, D. Theret, L. Wheeler, N. Ohshima, and R. Nerem, "Application of the micropipette technique to the measurement of cultured porcine aortic endothelial cell viscoelastic properties," *Journal of Biomechanical Engineering*, vol. 112, pp. 263–268, 1990.

[176] T. Boudou, J. Ohayon, Y. Arntz, G. Finet, C. Picart, and P. Tracqui, "An extended modeling of the micropipette aspiration experiment for the characterization of the Young's modulus and Poisson's ratio of adherent thin biological samples: Numerical and experimental studies," *Journal of Biomechanics*, vol. 39, pp. 1677–1685, 2006.

[177] R. Zhao, K. Wyss, and C. A. Simmons, "Comparison of analytical and inverse finite element approaches to estimate cell viscoelastic properties by micropipette aspiration," *Journal of Biomechanics*, vol. 42, pp. 2768–2773, Dec 2009.

[178] E. Shojaei-Baghini, Y. Zheng, and Y. Sun, "Automated micropipette aspiration of single cells," *Annals of Biomedical Engineering*, vol. 41, pp. 1208–1216, June 2013.

[179] M. J. Rosenbluth, W. A. Lam, and D. A. Fletcher, "Force microscopy of nonadherent cells: A comparison of leukemia cell deformability," *Biophysical Journal*, vol. 90, pp. 2994–3003, April 2006.

[180] A. C. Shieh and K. A. Athanasiou, "Dynamic compression of single cells," *Osteoarthritis and Cartilage*, vol. 15, pp. 328–334, Mar 2007.

[181] B. Lincoln, S. Schinkinger, K. Travis, F. Wottawah, S. Ebert, F. Sauer, and J. Guck, "Reconfigurable microfluidic integration of a dual-beam laser trap with biomedical applications," *Biomedical Microdevices*, vol. 9, pp. 703–710, May 2007.

[182] J. R. Lange, J. Steinwachs, T. Kolb, L. A. Lautscham, I. Harder, G. Whyte, and B. Fabry, "Microconstriction arrays for high-throughput quantitative measurements of cell mechanical properties," *Biophysical Journal*, vol. 109, pp. 26–34, July 2015.

[183] M. Kovács, J. Tóth, C. Hetényi, A. Málnási-Csizmadia, and J. R. Sellers, "Mechanism of blebbistatin inhibition of myosin II," *The Journal of Biological Chemistry*, vol. 279, no. 34, pp. 35557–35563, 2004.

[184] J. A. May, H. Ratan, J. R. Glenn, W. Lösche, P. Spangerberg, and S. Heptinstall, "GPIIb-IIIa antagonists cause rapid disaggregation of platelets pre-treated with cytochalasin D. evidence that the stability of platelet aggregates depends on normal cytoskeletal assembly," *Platelets*, vol. 9, pp. 227–232, 1998.

[185] C. Quéguiner and D. Barthès-Biesel, "Axisymmetric motion of capsules through cylindrical channels," *Journal of Fluid Mechanics*, vol. 348, pp. 349–376, 1997.

[186] A. Diaz and D. Barthès-Biesel, "Entrance of a bioartificial capsule in a pore," *Computer Modeling in Engineering Sciences*, vol. 3, no. 3, pp. 321–337, 2002.

[187] T.-X. Chu, *Fabrication et caractérisation de populations de microcapsules avec une technique microfluidique*. PhD thesis, Université de Technologie de Compiègne, 2011.

[188] X.-Q. Hu, B. Sévénié, A.-V. Salsac, E. Leclerc, and D. Barthès-Biesel, "Characterizing the membrane properties of capsules flowing in a square-section microfluidic channel: Effects of the membrane constitutive law," *Physical Review E*, vol. 87, Jun 2013.

[189] M. Malafosse, "Déformation de capsules dans des canaux microfluidiques à section rectangulaire de rapport 3/2," Master's thesis, Ecole des Ponts Paris Tech, 2015.

[190] S. Kuriakose and P. Dimitrakopoulos, "Deformation of an elastic capsule in a rectangular microfluidic channel," *Soft Matter*, vol. 9, no. 16, pp. 4284–4296, 2013.

[191] C. J. Chan, A. E. Ekpenyong, S. Golfier, W. Li, K. J. Chalut, O. Otto, J. Elgeti, J. Guck, and F. Lautenschläger, "Myosin II activity softens cells in suspension," *Biophysical Journal*, vol. 108, pp. 1856–1869, Apr 2015.

[192] M. P. Stewart, A. W. Hodel, A. Spielhofer, C. J. Cattin, D. J. Müller, and J. Helenius, "Wedged AFM-cantilevers for parallel plate cell mechanics," *Methods*, vol. 60, pp. 186–194, 2013.

[193] D. A. D. Flormann, *Physical characterization of red blood cell aggregation*. PhD thesis, Universität des Saarlandes and Université Grenoble Alpes, 2017.

[194] H.-J. Butt and M. Jaschke, "Calculation of thermal noise in atomic force microscopy," *Nanotechnology*, vol. 6, pp. 1–7, 1995.

[195] J. L. Hutter, "Comment on tilt of atomic force microscope cantilevers: effect on spring constant and adhesion measurements," *Langmuir*, vol. 21, no. 6, pp. 2630–2632, 2005.

[196] I. Spector, N. R. Shochet, D. Blasberger, and Y. Kashman, "Latrunculins novel marine macrolides that disrupt microfilament organization and affect cell growth: I. comparison with cytochalasin D," *Cell motility and the Cytoskeleton*, vol. 13, pp. 127–144, 1989.

[197] K. D. Nyberg, K. H. Hu, S. H. Kleinman, D. B. Khismatullin, M. J. Butte, and A. C. Rowat, "Quantitative deformability cytometry: Rapid, calibrated measurements of cell mechanical properties," *Biophysical Journal*, vol. 113, pp. 1574–1584, 2017.

[198] A. P. Somlyo and A. V. Somlyo, "Signal transduction by G-proteins, Rho-kinase and protein phosphatase to smooth muscle and non-muscle myosin II," *Journal of Physiology*, vol. 522, 177-185 2000.

[199] J. K. Liao, M. Seto, and K. Noma, "Rho kinase (ROCK) inhibitors," *Journal of Cardiovascular Pharmacology*, vol. 50, pp. 17–24, Jul 2007.

[200] L. Fabian, J. Troscianczuk, and A. Forer, "Calyculin A, an enhancer of myosin, speeds up anaphase chromosome movement," *Cell and Chromosome*, vol. 6, no. 1, 2007.

[201] A. Suzuki and T. Itoh, "Effects of calyculin A on tension and myosin phosphorylation in skinned smooth muscle of the rabbit mesenteric artery," *British Journal of Pharmacology*, vol. 109, pp. 703–712, 1993.

[202] A. Pietrzyk-Nivau, S. Poirault-Chassac, S. Gandrille, S.-M. Derkaoui, A. Kauskot, D. Letourneur, C. Le Visage, and D. Baruch, "Three-dimensional environment sustains hematopoietic stem cell differentiation into platelet-producing megakaryocytes," *Plos One*, vol. 10, p. e0136652, Aug 2015.

[203] C. Gullekson, *Effect of Cell-Substrate Interactions on Epithelial Cell Mechanics*. PhD thesis, University of Ottawa, 2018.

[204] N. Blumberg, J. M. Heal, and G. L. Phillips, "Platelet transfusions: trigger, dose, benefits, and risks," *F1000 Medicine Reports*, vol. 2, p. 5, Jan 2010.

[205] E.-J. Lee, P. Godara, and D. Haylock, "Biomanufacture of human platelets for transfusion: rationale and approaches," *Experimental Hematology*, vol. 42, pp. 332–346, 2014.

[206] "Rapport d'activité de l'EFS 2016," 2016.

[207] J. E. Italiano Jr., P. Lecine, R. A. Shivdasani, and J. H. Hartwig, "Blood platelets are assembled principally at the ends of proplatelet processes produced by differentiated megakaryocytes," *The journal of cell biology*, vol. 147, pp. 1299–1312, December 1999.

[208] A. Balduini, I. Pallotta, A. Malara, P. Lova, A. Pecci, G. Viarengo, C. L. Balduini, and M. Torti, "Adhesive receptors, extracellular proteins and myosin IIA orchestrate proplatelet formation by human megakaryocytes," *Journal of Thrombosis and Haemostasis*, vol. 6, pp. 1900–1907, Nov 2008.

[209] Y. Li, D. A. Kniss, L. C. Lasky, and S.-T. Yang, "Culturing and differentiation of murine embrionic stem cells in a three-dimensional fibrous matrix," *Cytotechnology*, vol. 41, pp. 23–35, 2003.

[210] B. Sullenbarger, J. H. Bahng, R. Gruner, N. Kotov, and L. C. Lasky, "Prolonged continuous in vitro human platelet production using three-dimensional scaffolds," *Experimental Hematology*, vol. 37, pp. 101–110, Jan 2009.

[211] L. C. Lasky and B. Sullenbarger, "Manipulation of oxygenation and flow-induced shear stress can increase the *In Vitro* yield of platelets from cord blood," *Tissue Engineering Part C: Methods*, vol. 17, pp. 1081–1088, Nov 2011.

[212] Y. Nakagawa, S. Nakamura, M. Nakajima, H. Endo, T. Dohda, N. Takayama, H. Nakauchi, F. Arai, T. Fukuda, and K. Eto, "Two differential flows in a bioreactor promoted platelet generation from human pluripotent stem cell–derived megakaryocytes," *Experimental Hematology*, vol. 41, pp. 742–748, 2013.

[213] J. N. Thon, L. Mazutis, S. Wu, J. L. Sylman, A. Ehrlicher, K. R. Machlus, Q. Feng, S. Lu, R. Lanza, K. B. Neeves, D. A. Weitz, and J. E. Italiano Jr, "Platelets bioreactor-on-a-chip," *Blood*, vol. 124, pp. 1857–1867, September 2014.

[214] A. Aguilar, F. Pertuy, A. Eckly, C. Strassel, D. Collin, C. Gachet, F. Lanza, and C. Léon, "Importance of environmental stiffness for megakaryocyte differentiation and proplatelet formation," *Blood*, vol. 128, no. 16, pp. 2022–2032, 2016.

[215] C. A. Di Buduo, L. S. Wray, L. Tozzi, A. Malara, Y. Chen, C. E. Ghezzi, D. Smoot, C. Sfara, A. Antonelli, E. Spedden, G. Bruni, C. Staii, L. De Marco, M. Magnani, D. L. Kaplan, and A. Balduini, "Programmable 3D silk bone marrow niche for platelet generation *ex vivo* and modeling of megakaryopoiesis pathologies," *Blood*, vol. 125, pp. 2254–2264, 2015.

[216] K. Eto, "Platelet biogenesis wears silkworm cocoons," *Blood*, vol. 125, pp. 2181–2182, April 2015.

[217] Z. Ruggeri, "Von Willebrand factor, platelets and endothelial cell interactions," *Journal of Thrombosis and Haemostasis*, vol. 1, pp. 1335–1342, 2003.

[218] J. N. Thon, A. Montalvo, S. Patel-Hett, M. T. Devine, J. L. Richardson, A. Ehrlicher, M. K. Larson, K. Hoffmeister, J. H. Hartwig, and J. E. Italiano Jr, "Cytoskeletal mechanics of proplatelet maturation and platelet release," *The Journal of Cell Biology*, vol. 191, pp. 861–874, Nov 2010.

[219] M. Bender, J. N. Thon, A. J. Ehrlicher, S. Wu, L. Mazutis, E. Deschmann, M. Sola-Visner, J. E. Italiano, and J. H. Hartwig, "Microtubule sliding drives proplatelet elongation and is dependent on cytoplasmic dynein," *Blood*, vol. 125, no. 5, pp. 860–868, 2015.

[220] M. Valko, D. Leibfritz, J. Moncol, M. T. Cronin, M. Mazur, and J. Telser, "Free radicals and antioxidants in normal physiological functions and human disease," *The International Journal of Biochemistry and Cell Biology*, vol. 39, pp. 44–84, Jan 2007.

[221] S. Chen, Y. Su, and J. Wang, "ROS-mediated platelet generation: a microenvironment-dependent manner for megakaryocyte proliferation, differentiation and maturation," *Cell Death and Disease*, vol. 4, p. e722, Jul 2013.

[222] J. J. O'Brien, S. L. Spinelli, J. Tober, N. Blumberg, C. W. Francis, M. B. Taubman, J. Palis, K. E. Seweryniak, J. M. Gertz, and R. P. Phipps, "15-deoxy-$\Delta^{12,14}$-PGJ_2 enhances platelet production from megakaryocytes," *Blood*, vol. 112, no. 10, pp. 4051–4060, 2008.

[223] M. Lebsir, "Analyse des trajectoires de cellules adhérentes en voie d'élongation: Etude des élongations de mégacaryocytes capturés dans un dispositif de flux," Master's thesis, Université Paris Est Créteil, 2017.

[224] J. E. Italiano Jr., S. Patel-Hett, and J. H. Hartwig, "Mechanics of proplatelet elaboration," *Journal of Thrombosis and Haemostasis*, vol. 5, pp. 18–23, 2007.

[225] S. Shiozaki, S. Takagi, and S. Goto, "Prediction of molecular interaction between platelet glycoprotein Ibα and von Willebrand factor using molecular dynamics simulations," *Journal of Artherosclerosis and Thrombosis*, vol. 23, no. 4, pp. 455–464, 2016.

[226] K. Sadoul, "New explanations for old observations: marginal band coiling during platelet activation," *Journal of Thrombosis and Haemostasis*, vol. 13, pp. 333–346, 2015.

[227] S. Patel-Hett, J. L. Richardson, H. Schulze, K. Drabek, N. A. Isaac, K. Hoffmeister, R. A. Shivdasani, J. C. Bulinski, N. Galjart, J. H. Hartwig, and J. E. Italiano Jr, "Visualization of microtubule growth in living platelets reveals a dynamic marginal band with multiple microtubules," *Blood*, vol. 111, no. 9, pp. 4605–4616, 2008.

[228] A. Vogel and V. Venugopalan, "Mechanisms of pulsed laser ablation of biological tissues," *Chemical Review*, vol. 103, pp. 577–644, 2003.

[229] A. Pais, "Einstein and the quantum theory," *Review of modern physics*, vol. 51, no. 4, pp. 863–914, 1979.

[230] T. H. Maiman, "Stimulated optical radiation in ruby," *Nature*, vol. 187, pp. 493–494, 1960.

[231] J. Neddersen, G. Chumanov, and T. M.Cotton, "Laser ablation of metals: a new method for preparing SERS active colloids," *Applied Spectroscopy*, vol. 47, no. 12, pp. 1959–1964, 1993.

[232] A. M. Morales and C. M. Lieber, "A laser ablation method for the synthesis of crystalline semiconductor nanowires," *Science*, vol. 279, pp. 208–211, 1998.

[233] R. L. Amy and R. Storb, "Selective mitochondrial damage by a ruby laser microbeam: an electron microscopic study," *Science*, vol. 150, pp. 756–758, 1965.

[234] M. Berns, J. Aist, J. Edwards, K. Strahs, J. Girton, P. McNeill, J. Rattner, M. Kitzes, M. Hammer-Wilson, L.-H. Liaw, A. Siemens, M. Koonce, S. Peterson, S. Brenner, J. Burt, R. Walter, P. Bryant, D. van Dyk, J. Coulombe, T. Cahill, and G. Berns, "Laser microsurgery in cell and developmental biology," *Science*, vol. 213, pp. 505–512, 1981.

[235] J. S. Becker, M. V. Zoriy, C. Pickhardt, N. Palomero-Gallagher, and K. Zilles, "Imaging of copper, zinc, and other elements in thin section of human brain samples (hippocampus) by laser ablation inductively coupled plasma mass spectrosmetry," *Analytical Chemistry*, vol. 77, no. 10, pp. 3208–3216, 2005.

[236] K. K. McCampbell and R. A. Wingert, "New tides : using zebrafish to study renal regeneration," *Translational research*, vol. 163, no. 2, 2014.

[237] R. Darwood, N. Theivacumar, D. Dellagrammaticas, A. Mavor, and M. Gough, "Randomized clinical trial comparing endovenous laser ablation with surgery for the treatment of primary great saphenous varicose veins," *British Journal of Surgery*, vol. 95, pp. 294–301, 2008.

[238] C. Li, N. Hisamoto, P. Nix, S. Kanao, T. Mizuno, M. Bastiani, and K. Matsumoto, "The growth factor SVH-1 regulates axon regeneration in *C. elegans* via the JNK MAPK cascade," *Nature Neuroscience*, vol. 15, no. 4, pp. 551–557, 2012.

[239] W. C. Chang, E. Hawkes, C. G. Keller, and D. W. Sretavan, "Axon repair: surgical application at a subcellular scale," *Wiley interdisciplinary reviews. Nanomedicine and nanobiotechnology*, vol. 2, pp. 151–161, 2010.

[240] M. Harsch, K. Bendrat, G. Hofmeier, D. Branscheid, and A. Niendorf, "A new method for histological microdissection utilizing an ultrasonically oscillating needle," *American Journal of pathology*, vol. 158, no. 6, pp. 1985–1990, 2001.

[241] D. M. Suter, "Live cell imaging of neuronal growth cone motility and guidance *in vitro*," *Methods in Molecular Biology*, vol. 769, pp. 65–86, 2011.

[242] T. Tani, R. D. Allen, and Y. Naitoh, "Periodic tension development in the membrane of the *in vitro* contractile vacuole of *Paramecium multimicronucleatum*: modification by bisection, fusion and suction," *The journal of Experimental Biology*, vol. 203, pp. 239–251, 2000.

[243] N. V. G. Vegesna, P. Ronchi, S. Durdu, S. Terjung, and R. Pepperkok, *Light Microscopy Methods and Protocols*, ch. Targeted Ablation using laser nanosurgery. No. 8, Springer Nature, Humana Press ed., 2017.

[244] N. Shen, D. Datta, C. B. Schaffer, P. LeDuc, D. E. Ingber, and E. Mazur, "Ablation of cytoskeletal filaments and mitochondria in live cells using a femtosecond laser nanoscissor," *Molecular and Cellular Biology*, vol. 2, no. 1, pp. 17–25, 2005.

[245] N. M. Wakida, C. S. Lee, E. T. Botvinick, L. Z. Shi, A. Dvornikov, and M. W. Berns, "Laser nanosurgery of single microtubules reveals location-dependent depolimerization rates," *Journal of Biomedical Optics*, vol. 12, no. 2, p. 024022, 2007.

[246] E. Botvinick, V. Venugopalan, J. Shah, L. Liaw, and M. Berns, "Controlled ablation of microtubules using a picosecond laser," *Biophysical Journal*, vol. 87, pp. 4203–4212, 2004.

[247] K. R. Strahs and M. W. Berns, "Laser microirradiation of stress fibers and intermediate filaments in non-muscle cells from cultured rat heart," *Experimental Cell Research*, vol. 119, pp. 31–45, 1979.

[248] J. Colombelli, A. Besser, H. Kress, E. G. Reynaud, P. Girard, E. Caussinus, U. Haselmann, J. V. Small, U. S. Schwarz, and E. H. K. Stelzer, "Mechanosensing in actin stress fibers revealed by a close correlation between force and protein localization," *Journal of Cell Science*, vol. 122, pp. 1665–1679, 2009.

[249] E. Kassianidou, C. A. Brand, U. S. Schwarz, and S. Kumar, "Geometry and network connectivity govern the mechanics of stress fibers," *PNAS*, vol. 114, no. 10, pp. 2622–2627, 2017.

[250] J. Wu, R. B. Dickinson, and T. P. Lele, "Investigation of *in vivo* microtubule stress fiber mechanics with laser ablation," *Integrative Biology*, vol. 4, no. 5, pp. 471–479, 2012.

[251] R. Fernandez-Gonzalez, S. de Matos Simoes, J.-C. Röper, S. Eaton, and J. A. Zallen, "Myosin II dynamics are regulated by tension in intercalating cells," *Developmental Cell*, vol. 17, pp. 736–743, November 2009.

[252] S. Kumar, I. Z. Maxwell, A. Heisterkamp, T. R. Polte, T. P. Lele, M. Salanga, E. Mazur, and D. E. Ingber, "Viscoelastic retraction of single living stress fibers and its impact on cell shape, cytoskeletal organization, and extracellular matrix mechanics," *Biophysical Journal*, vol. 90, pp. 3762–3773, 2006.

[253] A.-J. Jimenez, P. Maiuri, J. Lafaurie-Janvore, S. Divoux, M. Piel, and F. Perez, "ESCRT machinery is required for plasma membrane repair," *Science*, vol. 343, p. 1247136, 2014.

[254] W. Tao, R. J. Walter, and M. W. Berns, "Laser-transected microtubules exhibit individuality of regrowth, however most free new ends of the microtubules are stable," *The journal of cell biology*, vol. 107, pp. 1025–1035, 1988.

[255] L. Coburn, H. Lopez, B. J. Caldwell, E. Moussa, C. Yap, R. Priya, A. Noppe, A. P. Roberts, V. Lobaskin, A. S. Yap, Z. Neufeld, and G. A. Gomez, "Contact inhibition of locomotion and mechanical cross-talk between cell-cell and cell-substrate adhesion determine the pattern of junctional tension in epithelial cell aggregates," *Molecular Biology of the cell*, vol. 27, pp. 3436–3448, 2016.

[256] A. Ratheesh, G. A. Gomez, R. Priya, S. Verma, E. M. Kovacs, K. Jiang, N. H. Brown, A. Akhmanova, S. J. Stehbens, and A. S. Yap, "Centralspindlin and α-catenin regulate Rho signalling at the epithelial zonula adherens," *Nature Cell Biology*, vol. 14, no. 8, pp. 818–828, 2012.

[257] X. Liang, M. Michael, and G. A. Gomez, "Measurement of mechanical tension at cell-cell junctions using two-photon laser ablation," *Bio-Protocol*, vol. 6, no. 24, p. e2068, 2016.

[258] J.-Y. Tinevez, U. Schulze, G. Salbreux, J. Roensch, J.-F. Joanny, and E. Paluch, "Role of cortical tension in bleb growth," *PNAS*, vol. 106, no. 44, pp. 18581–18586, 2009.

[259] K. Vukušić, R. Buda, A. Bosilj, A. Milas, N. Pavin, and I. M. Tolić, "Microtubule sliding within the bridging fiber pushes kinetochore fibers apart to segregate chromosomes," *Developmental Cell*, vol. 43, pp. 11–23, 2017.

[260] J. Lafaurie-Janvore, P. Maiuri, I. Wang, M. Pinot, J.-B. Manneville, T. Betz, M. Balland, and M. Piel, "ESCRT-III assembly and cytokinetic abscission are induced by tension release in the intercellular bridge," *Science*, vol. 339, pp. 1625–1629, March 2013.

[261] J.-W. Shin, A. Buxboim, K. R. Spinler, J. Swift, D. A. Christian, C. A. Hunter, C. Léon, C. Gachet, P. D. P. Dingal, I. L. Ivanovska, F. Rehfeldt, J. A. Chasis, and D. E. Discher, "Contractile forces sustain and polarize hematopoiesis from stem and progenitor cells," *Cell Stem Cell*, vol. 14, pp. 81–93, 2013.

[262] M. R. Bubb, I. Spector, B. B. Beyer, and K. M. Fosen, "Effects of jasplakinolide on the kinetics of actin polymerization," *The Journal of Biological Chemistry*, vol. 275, no. 7, pp. 5163–5170, 2000.

[263] E. Pertussini, J. Ratajczak, M. Majka, D. Vaughn, M. Z. Ratajczak, and A. M. Gewirtz, "Investigating the platelet-sparing mechanism of paclitaxel/carboplatin combination chemotherapy," *Blood*, vol. 97, no. 3, pp. 638–644, 2001.

[264] G. Lukinavičius, L. Reymond, E. D'Este, A. Masharina, F. Göttfert, H. Ta, A. Güther, M. Fournier, S. Rizzo, H. Waldmann, C. Blaukopf, C. Sommer, D. W. Gerlich, H.-D. Arndt, S. W. Hell, and K. Johnsson, "Fluorogenic probes for live-cell imaging of the cytoskeleton," *Nature Methods*, vol. 11, pp. 731–733, May 2014.

[265] A. Suzuki, J.-W. Shin, Y. Wang, S. H. Min, M. Poncz, J. K. Choi, D. E. Discher, C. L. Carpenter, L. Lian, L. Zhao, Y. Wang, and C. S. Abrams, "RhoA is essential for maintaining normal megakaryocyte ploidy and platelet generation," *Plos One*, vol. 8, p. e69315, Jul 2013.